PhD-FSTC-2019-29
The Faculty of Sciences, Technology and Communication

DISSERTATION

Defence held on 29/04/2019 in Esch-sur-Alzette

to obtain the degree of

DOCTEUR DE L'UNIVERSITÉ DU LUXEMBOURG

EN BIOLOGIE

by

Marco ALBRECHT
Born on 20 September 1989 in Magdeburg (Germany)

MATHEMATICAL HISTOPATHOLOGY AND SYSTEMS PHARMACOLOGY OF MELANOMA

Dissertation defence committee

Prof Thomas Sauter, dissertation supervisor
Professor, Université du Luxembourg

Prof Stephanie Kreis, chairwoman
Professor, Université du Luxembourg

Prof Stéphane Bordas
Professor, Université du Luxembourg

Prof Joost van den Oord
Professor, Universitair Ziekenhuis Leuven

Dr Giuseppe Sciumé
Maître de Conférences, Université de Bordeaux

The host institution and three internship locations

Dissertation Defence Committee:

Head of jury	Prof. Stephanie Kreis	Molecular melanoma research (University of Luxembourg)
Supervisor:	Prof. Thomas Sauter	Systems Biology (University of Luxembourg)
Jury members:	Prof. Stéphane Bordas	Computational mechanics (University of Luxembourg)
	Prof. Joost van den Oord	Dermatopathology (Universitair Ziekenhuis Leuven)
	Dr. Giuseppe Sciumè	Civil engineering & porous media (University of Bordeaux)

Affidavit

I hereby confirm that the PhD thesis entitled "Mathematical Histopathology and Systems Pharmacology of Melanoma" has been written independently and without any other sources than cited.

Luxembourg, _____ _____

Marco Albrecht

Acknowledgement

I want to thank my supervisor Prof. Thomas Sauter for giving me the chance to work on such an ambitious and exciting project. I enjoyed the privilege of enormous freedom in tackling the tasks and could not imagine a better mentor. I was Inwardly and too often openly torn between the present and the post-dissertation-normalcy, between the surreal expectation and my ability, between my detail-obsession and dead-line-pragmatisms, and between so many locations in various countries. I was neither a diplomat nor the best writer and might not have been the easiest PhD student to supervise, but Prof. Thomas Sauter was always there to listen and to support me.

I furthermore want to thank two strong scientists for their intellectual generosity. Prof. Dagmar Kulms and Prof. Zvia Agur gave me the chance to perform non-standard experiments and approaches in Dresden and Israel and never dread an open and honest exchange of opinion. I am glad I lived up to their expectations. I want to thank Dr. Ines Müller for her patience and support, and I want to thank Yuri Kogan for being such an amazing, polite, patient, and supportive supervisor.

I want to thank Dr. Giuseppe Sciumé, who entrusted me with his source code and kindly taught me so much about multi-phase flow, mechanics, and porous media. He forged my view on what cancer might be.

I want to thank my CET supervisory board with Prof. Stéphane Bordas and Dr. Alexander Skupin. Especially Prof. Stéphane Bordas provided me with so many additional opportunities from which I learned a lot.

I am glad to have such a diverse defence defence committee with Dr. Giuseppe Sciumé, Prof. Joost van den Oord, Prof. Stéphane Bordas, Prof. Thomas Sauter, and Dr. Stephanie Kreis. I enjoyed a critical and controversial discussion with all committee members during my PhD candature and appreciate the time each committee member invested in me.

I want to thank Dr. Lina Prasmickaite for a fruitful collaboration, which resulted in a paper.

I am also grateful to my colleges Dr. Panuwat Trairatphisan, Dr. Lasse Sinkkonen, Dr. Maria Pires Pacheco, Dr. Déborah Gerard, Dr. Jochen Ohnmacht, Dr. Philippe Lucarelli, Dr. Thomas Pfau, Dr. Luana Presta, Dr. Patricia Martins Conde, Marios Gavriil, Sébastien De Landtsheer, Tamara Bintener, Yujuan Gui, Borja Gomez Ramos, Sergio Helgueta Romero, and Julia Becker.

An extraordinary gratitude goes out to the European Union for providing funding and diverse reporting opportunities, which thought me patience, focus, and presenting skills.

I want to acknowledge also our all beloved research programme manager Dr. Isabela Aparicio and our very much respected Mel-Plex coordinator Prof. Markus Morrison. From all not yet mentioned principle investigators, I want to especially thank the pathologist Prof. Joost van den Oord, whom I tried to convince the most.

And most importantly, I admire the most childlike, craziest, most rebellious, funniest, and most successful Mel-Plex community with the best carbonara-cook and grand dame of apoptosis Greta Del Mistro, the party-girl and immunology expert Nicole Rufo, the newbie Anna Zinoveva, the academic-career-rider Biswajit Podder, the project manager and master of mice Valéry Bodemeyer, the pole-dance-queen Vesna Vetma, the businessman Jan Rožanc, the pub-night-master Živa Frangež, the guru Sébastien De Landtsheer, the elegant professor of fun and success Francesca Bosisio, the motorcycle-fan Christiano Guttà, the Nordic fairy Katja Palonen, the cheerful happiness Neta Tsur, the revolutionist and hippo-enthusiast Estefanía Chiquero-Leon, and our English-mother-tongue-talent Romina Silva. See you all in our postdoc holiday event!

I also want to thank all the training staff of Mel-Plex and the Doctoral Programme in Systems and Molecular Biomedicine, doctoral school administrator Magali Guillaume, our secretary Caroline Herfroy, and the kind cleaning lady Cindy Bombardier who prevented the complete dilapidation of my office.

I also thank my students, which were a fantastic, diligent, and inquisitive group. They accepted to be my pedagogical guinea pigs and did not regret it, at least not always.

I also want to say thanks to my fiancée Mohammed al Khasraje, who always supported my path, rebuked me where necessary, silently abide my temporary weight gain of 35 kg, and accepted my long work-trips as well as all the lost evenings and weekends.

And last but not least, I would like to acknowledge my mother, who always spend moral support, unfortunately, did not see me much, and who helped me with small loans to overcome the inevitable organisational challenges accompanied with the location changes.

All in all, I became personally and professionally more maturated, and I experienced very intense four years with big mountains to climb, broad valleys to endure, and many scientific plants to seed. I received the opportunity to reflect on nature, science, humans, the value of success, and myself, and I will carry a bunch of great memories to my next life stages. I want to thank all the people I met and who accompanied my path. As a Systems Biologist would say: we are not only single elements - we are embedded in a network. May the feedback be with us.

Dedication

I dedicate the work to the European Union.

It arose after a time where I, as a member of a minority, had only one possible future: dust in Hitler‘s crematoria.

It was there, behind a wall, as I was born in a dictatorship where one party decided what truth is.

It was there as symbols on the scaffolding, as my neighbourhood was modernised to catch up with Western Europe.

It maturated during multiple crises while I have studied natural science and engineering.

And finally, the European Union financed my research and the wonderful time in various European countries, San Francisco, and Israel.

Contents

List of abbreviations

All biomolecule names in this thesis are approved by the HUGO Gene Nomenclature Committee (HGNC) of the Human Genome Organisation (HUGO).

HGNC abbreviations

AKT1 AKT serine/threonine kinase 1

AGRN agrin

AMPK AMP kinase

AQP1 aquaporin 1 (Colton blood group)

AQP3 aquaporin 3 (Gill blood group)

BCAR1 BCAR1 scaffold protein, Cas family member

BRAF b-Raf proto-oncogene

CD44 CD44 molecule (Indian blood group)

CDH1 cadherin 1

CDH2 cadherin 2

CDH3 cadherin 3

CNKSR1 connector enhancer of kinase suppressor of Ras 1

CRB3 crumbs cell polarity complex component 3

CTLA4 cytotoxic T-lymphocyte associated protein 4

CTNNB1 catenin beta 1

CYP cytochrome P450s

CYP1A2 cytochrome P450 family 1 subfamily A member 2
CYP2B6 cytochrome P450 family 2 subfamily B member 6
CYP2C8 cytochrome P450 family 2 subfamily C member 8
CYP2C9 cytochrome P450 family 2 subfamily C member 9
CYP2C19 cytochrome P450 family 2 subfamily C member 19
CYP3A4 cytochrome P450 family 3 subfamily A member 4
DDR2 discoidin domain receptor tyrosine kinase 2
DLL1 delta like canonical Notch ligand 1
DLL3 delta like canonical Notch ligand 3
EBPRs elastin binding protein receptors
EGF epidermal growth factor
EGFR epidermal growth factor receptor
ELN elastin
EPAS1 endothelial PAS domain protein 1
EPN epsin
FBN1 fibrillin 1
FLNA filamin A
FGF fibroblast growth factors
GAPDH glyceraldehyde 3-phosphate dehydrogenase
GNAQ G protein subunit alpha q
HIF1A hypoxia inducible factor 1 subunit alpha
IDH1 isocitrate dehydrogenase (NADP(+)) 1, cytosolic
IL21 interleukin 21
ILK integrin linked kinase
JAG2 jagged canonical Notch ligand 2
JUN jun proto-oncogene, AP-1 transcription factor subunit
KDR kinase insert domain receptor
LMNA lamin A/C
LMNB1/2 lamin B1/2
LRP4 LDL receptor related protein 4
LOX lysyl oxidase
MAP2K mitogen-activated protein kinase kinases
MAPK1 mitogen-activated protein kinase 1
MAPK8 mitogen-activated protein kinase 8
MITF melanocyte inducing transcription factor

MMP	matrix metalloproteinases
MTOR	mechanistic target of rapamycin kinase
MUSK	muscle associated receptor tyrosine kinase
MYC	MYC proto-oncogene, bHLH transcription factor
NF1	neurofibromin 1
NF2	neurofibromin 2
NR1I2	NR1I2 nuclear receptor subfamily 1 group I member 2
NRAS	NRAS proto-oncogene, GTPase
NM2A	nonmuscle myosin 2 A
NM2B	nonmuscle myosin 2 B
NRAS	neuroblastoma RAS viral (v-ras) oncogene homolog
PDCD1	programmed cell death 1
PDE1	phosphodiesterase 1
PIK3CA	phosphatidylinositol-4,5-bisphosphate 3-kinase catalytic subunit alpha
PIEZO1	piezo type mechanosensitive ion channel component 1
PIEZO2	piezo type mechanosensitive ion channel component 2
PKA	cAMP-dependent protein kinase
PRKAA2	protein kinase AMP-activated catalytic subunit alpha 2
PTEN	phosphatase and tensin homolog
PTK2	protein tyrosine kinase 2
PXN	paxillin
RAC1	Rac family small GTPase 1
RAF1	Raf-1 proto-oncogene, serine/threonine kinase
RAS	RAS type GTPase family
RHO	rhodopsin
ROCK1	Rho associated coiled-coil containing protein kinase 1
RPS6	ribosomal protein S6
SAV1	salvador family WW domain containing protein 1
SLC9A1	solute carrier family 9 member A1
SLC16A1	solute carrier family 16 member 1
SNAI1	snail family transcriptional repressor 1
SRC	SRC proto-oncogene, non-receptor tyrosine kinase
STAT3	signal transducer and activator of transcription 3
TAZ	tafazzin
TCF/LEF	TCF/LEF transcription factor family

TEAD TEA domain transcription factors

TGFB transforming growth factor beta family

TGFB1I1 transforming growth factor beta 1 induced transcript 1

TLN1 talin 1

TNC tenascin C

TNFRSF9 TNF receptor superfamily member 9

TP53 tumor protein p53

TWIST1 twist family bHLH transcription factor 1

VASP vasodilator stimulated phosphoprotein

VCL vinculin

VEGFA vascular endothelial growth factor A

WWC1 WW and C2 domain containing 1

YY1AP1 YY1 associated protein 1

ZYX zyxin

Chemicals and other biological abbreviations

ATP adenosine triphosphate

BGN biglycan

BM basement membrane

BSA bovine serum albumin

CD cell degradable polyethylene glycol peptide conjugate

ChS chondroitin-sulfate

CSD cumulative sun damage

DNA deoxyribonucleic acid

DTIC dacarbazine

ECAR extracellular acidification rate

ECM extracellular matrix

EGTA egtazic acid

EMT epithelial–mesenchymal transition

FBS fetal bovine serum

FCCP carbonyl cyanide-4-(trifluoromethoxy)phenylhydrazone

GaG glycosaminoglycans

GFP green fluorescent protein

GTP guanosine-5’-triphosphate

HC host cells phase

HPMC hypromellose

IF interstitial fluid

IFF interstitial fluid flow

IFP interstitial fluid pressure

ILM inner limiting membrane

LLC large latent complex

mRNA messenger ribonucleic acid

NADH nicotinamide adenine dinucleotide

NK natural killer cell

TC tumour cells phase

OCR oxygen consumption rate

OEM osmotic engine model

PBS phosphate-buffered saline

PDMS polydimethylsiloxane

PEG polyethylene glycol

PGs proteoglycans

PPR proton production rate

RTK receptor tyrosine kinase

SDS sodium dodecyl sulfate

SSM superficial spreading melanoma

TBST tris-buffered saline + polysorbate 20

Technical and physical abbreviations

2D two-dimensional

3D three-dimensional

AEI augmented entropy inequality

CEI constrained entropy inequality

CIT classical irreversible thermodynamics

DDI drug-drug-interaction

MATLAB® matrix laboratory

mmHg millimetre of mercury

ODE ordinary differential equations

NDF numerical differentiation formula

PD proportional derivative

PDE partial differential equations

PET photo induces electron transfer

PK pharmacokinetics

REV representative elementary volume

RSS residual sum of squares

SEI simplified entropy inequality

SEM scanning electron microscope

SI international system of units

TCAT thermodynamically constrained averaging theory

UV ultraviolet light

UVB ultraviolet B

VSVO variable-step, variable-order

Institutions and databases

EMA European Medicines Agency

HGNC HUGO Gene Nomenclature Committee

HUGO Human Genome Organisation

MGDB Melanoma Gene Database

MMMP Melanoma Molecular Map Project

RPMI Roswell Park Memorial Institute

TCGA The Cancer Genome Atlas

Summary

Treated metastatic melanoma often becomes resistant and relapses whereby resistance mechanisms can be found at the level of biochemical, histological, and pharmacological data. By using this data in a mathematical form, an integrative understanding of tumour progression can be gained that reveal the functionality of more complex and hidden recurrence mechanisms. The aims of this thesis were

- to investigate how a new engineering concept on tumour growth, based on porous media theory, can be leveraged to support medicine and cancer biology research,
- to identify suitable tests for cancer growth model validation,
- to study how elements of biochemical cancer pathways are linked to the elements of physical growth, and
- to establish a pharmacokinetics module for the melanoma cancer drug dabrafenib.

The studied engineering concept is qualitatively suitable to represent late-stage metastatic melanoma in irregular fibrous tissue types, whereby all equations are tested for biological relevance and parametrisation. The framework allows modelling of tissue-specific growth, and the thesis shows that the simulated tumour can shift between compact growth with ECM displacement and invasive growth with ECM circumvention as a consequence of cell plasticity/viscosity change. This is unique among continuous models of tumour growth. However, the investigation also shows that the pressure-saturation relationships are not biologically motivated and can be replaced by a swelling polymer model which captures the water absorbing effect of glycans.
The thesis addresses a biologically and computationally reasonable strategy to validate the tumour growth model as complete as possible. A suitable way to validate a part of the tumour growth model is using time course data of spheroid growth in hydrogels of different

stiffness values. Spheroids generated from the LU451 melanoma cell line mainly grow due to extracellular matrix (ECM) degradation, have a time-variant growth rate increasing with gel rigidity, and the confined environment renders the melanoma cell line drug-resistant upon dabrafenib dose escalation. This setting reveals the interplay between mechanical and biochemical development over time.

The dependency between biological elements of cancer pathways and the mechanical elements of the engineering concept on tumour growth were clarified. Therefore, the literature on mechanoregulation has been reviewed and serves as a computational link between systems biology and physical oncology. Finally, the thesis provides preliminary steps and a concept toward a serious interdisciplinary methodology to understand tumour growth, although this cannot be considered a final model for any of the known melanoma growth settings.

Additionally, the thesis provides a novel quantitative systems pharmacology approach to consider liver-enzyme-induction and drug-drug-interaction. The finding is that the potent dabrafenib metabolite desmethyl-dabrafenib accumulates with consequential efficacy loss in a confined tumour environment. The PhD project was structured in three parallel paths, as depicted in Figure 1. All codes and scripts are available upon request.

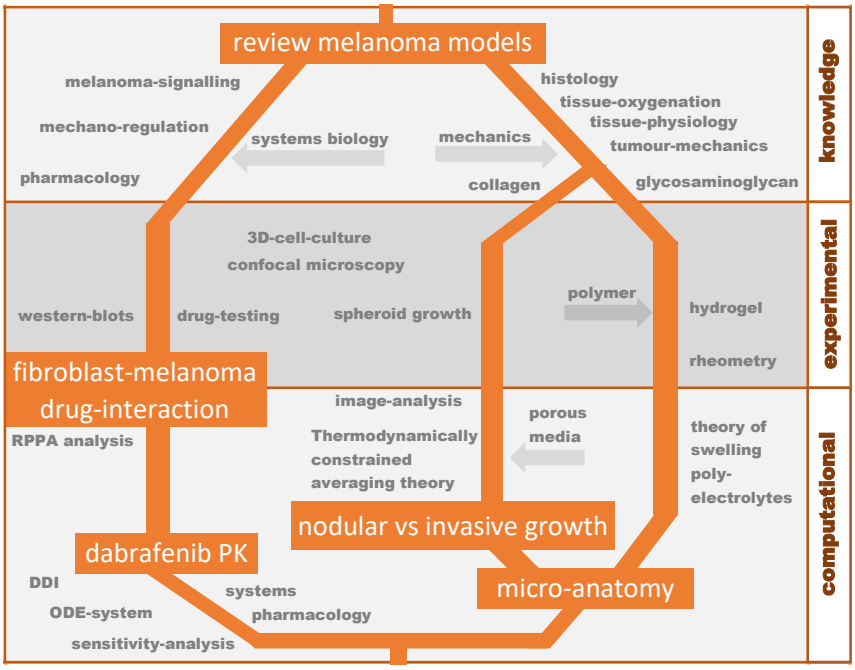

Figure 1: The PhD-project organisation of content. Papers are represented in orange boxes. The PhD project encompasses three parallel development paths which branch out and reunite. The branches are systems pharmacology and drug testing, tissue modelling with porous media theory, and hydrogel or glycan modelling with the theory of absorbent polymers. The paper on fibroblast-melanoma-drug-interaction was based on a collaboration with the Oslo University Hospital and is not integrated into this thesis [1]. From the remaining papers, the paper on nodular versus invasive growth is published [2]. Gray keywords specify the different fields of study and experiments performed.

Papers and manuscripts

Systems Biology Approaches and Computational Models for Cutaneous Melanoma

This review has been submitted to *Theoretical Biology and Medical Modelling* on 4th July 2019 together with Dr. Philippe Lucarelli, Prof. Dagmar Kulms, and Prof. Thomas Sauter. PL and DK provided initial text blocks. MA wrote and collected the majority of references and were responsible for the manuscript writing. All authors were involved in the review planning, guidance, and writing of the manuscript. The paper can be found in chapter 5.

Thermodynamically constrained averaging theory for cancer growth modelling

This original research paper has been published in *IFAC-Papers* in December 2018: *Albrecht, Marco, Giuseppe Sciumè, Philippe Lucarelli, and Thomas Sauter. "Thermodynamically constrained averaging theory for cancer growth modelling." IFAC-PapersOnLine 49, no. 26 (2016): 289-294.* MA wrote the manuscript and adjusted the code to generate the simulation results. GS wrote the original code. PL and TS ensured the quality of script writing. The paper can be found in chapter 6.

An evolutionary perspective on mechanobiology in context of melanoma

The **review paper** describes how the various mechanical cues in a tissue environment influence intracellular signalling pathways and how this relates to melanoma. This review paper will be submitted to a not yet selected journal together with Prof. Thomas Sauter. The paper can be found in chapter 7.

Stroma-induced phenotypic plasticity offers phenotype-specific targeting to improve melanoma treatment

This original research paper has been published in *Cancer letters* in December 2018:
Seip, Kotryna, Kjetil Jørgensen, Marco Vincent Haselager, Marco Albrecht, Mads Haugland Haugen, Eivind Valen Egeland, Philippe Lucarelli et al. "Stroma-induced phenotypic plasticity offers phenotype-specific targeting to improve melanoma treatment." Cancer letters 439 (2018): 1-13.
MA made the analysis of reverse phase protein assay, two-way Anova analysis, and reproduced the data clustering. The paper is not included in the present thesis. Further experiments can be found in chapter 8.

Quantitative systems pharmacology of dabrafenib metabolism: drug interaction, CYP3A4 enzyme induction, and efficiency loss in hydrogels

This original research paper has been submitted to *npj Systems Biology and Applications* on 2nd April 2019 together with Mr. Yuri Kogan, Prof. Dagmar Kulms, Prof. Thomas Sauter. No reviewer decision was received until the 20th July (almost 4 months), because the Nature journal has "some difficulties in securing the right reviewers" for the manuscript. MA made the concept, the model, the model fit, performed all experiments, wrote all codes, and drafted the manuscript. YK, DK, TS were involved in the research planning, guidance, and writing of the manuscript. All authors have critically read, understood, and approved the manuscript. The paper can be found in chapter 9.

MelPlex training network

This PhD project was part of the Marie SkŁodowska-Curie Innovative Training Networks (ITN-ETN) with the name *Exploiting MELanoma disease comPLEXity to address European research training needs in translational cancer systems biology and cancer systems medicine* and the acronym Mel-PLEX (grant agreement no: 642295). The sub-project presented here is located between molecular markers, drug-testing, pathology, and whole body physiology. The original title of sub-project three was "establishing a multi-scale modelling environment for pro-survival and proliferation signalling to understand melanoma growth arrest and recurrence". An integral part of the training network were secondments at the Technical University of Dresden and Optimata ltd. Additional secondments at the University of Bordeaux were necessary to acquire advanced knowledge in cancer growth modelling.

TREFLE at the University of Bordeaux

From September 21 to October 23, 2015 as well as from June 1 to July 6, 2017, Mr Marco Albrecht has completed his internship within the department TREFLE of the I2M (Institut de Mécanique et d'Ingénierie de Bordeaux, UMR 5295 CNRS). His internship encompassed the following topics:

- Tumour modelling with TCAT (Thermodynamically Constrained Averaging Theory);
- Basis of Solids and Fluids Mechanics needed for the adopted multiphase model;
- Numerical solution of PDEs by means of the Finite Element Methods;
- Programming language of Cast3M (FE code of the CEA, the French Alternative Energies and Atomic Energy Commission);
- Modelling of angiogenesis and rheological tests with TCAT

Experimental Dermatology at TU Dresden

From July 1 to December 31, 2016, Mr Marco Albrecht successfully completed a methodological rotation with Prof. Dagmar Kulms in the framework of the mandatory Mel-Plex lab exchanges. His secondment has been conducted at the Laboratory of Experimental Dermatology at the Center of Regenerative Therapies Dresden (CRTD) of the TU Dresden, 01307 Dresden, Fetscherstraße 105. During his 6 months secondment, Mr. Marco Albrecht's major business comprised:

- Cell culture techniques and appropriate use of antibiotics - Generation of tumour spheroids from melanoma cell lines A375 and LU451 - Handling and modification of Cellendes dextran hydrogels;
- Confocal microscopy (Zeiss, LSM 780/FCS, inverse) and image analysis using ImageJ software;
- Western Blot techniques; and
- Dynamic mechanical testing of gels in cooperation With Prof. Uwe Freudenberg at the Institute of Biofunctional Polymer Materials at the MPI Dresden.

Optimata Ltd

From January 1 to March 31, 2017, Mr Marco Albrecht successfully completed a methodological rotation with Prof. Zvia Agur and Mr. Jury Kogan in the framework of the mandatory Mel-Plex lab exchanges. His secondment has been conducted at Optimata Ltd., 60991 Israel, Bene-Atarot, HeTe´ene street. During his 3 months secondment, Mr. Marco Albrecht's major business comprised the pharmacokinetics of dabrafenib.

Introduction

1. From melanocytes to melanoma

A thesis on cancer growth modelling should start with the aetiology of cancer, the different growth mechanism, and where a particular cancer type grows. In the most basic view, cancer originates from the body's own cells [7], and in case of melanoma, the cancer cells descend from melanocytes. Melanocytes reside, *e.g.*, in the skin which is roughly shown in Figure 1.1 as a first orientation. How melanocytes transform and arising melanoma progress will be the subject of this section.

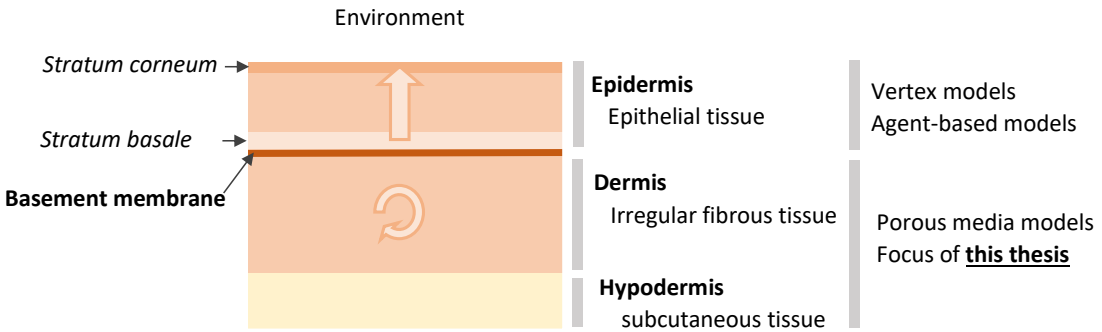

Figure 1.1: Simplified skin scheme. The skin can be subdivided into epidermis, dermis, and hypodermis. The epidermis is an epithelial tissue where kerationcytes (major skin cell) proliferate (cell-division) at the *stratum basale* and migrate (upward pointing arrow) to the dead keratinised *stratum corneum*. The epidermis is separated by the basement membrane from the dermis, where cell renewal has no directionality. The epidermis is dominated by cell-cell contacts and might be modelled with the vertex model strategy or agents [3–5] while the irregular fibrous or loose connective tissue might be modelled with porous media theory [6].

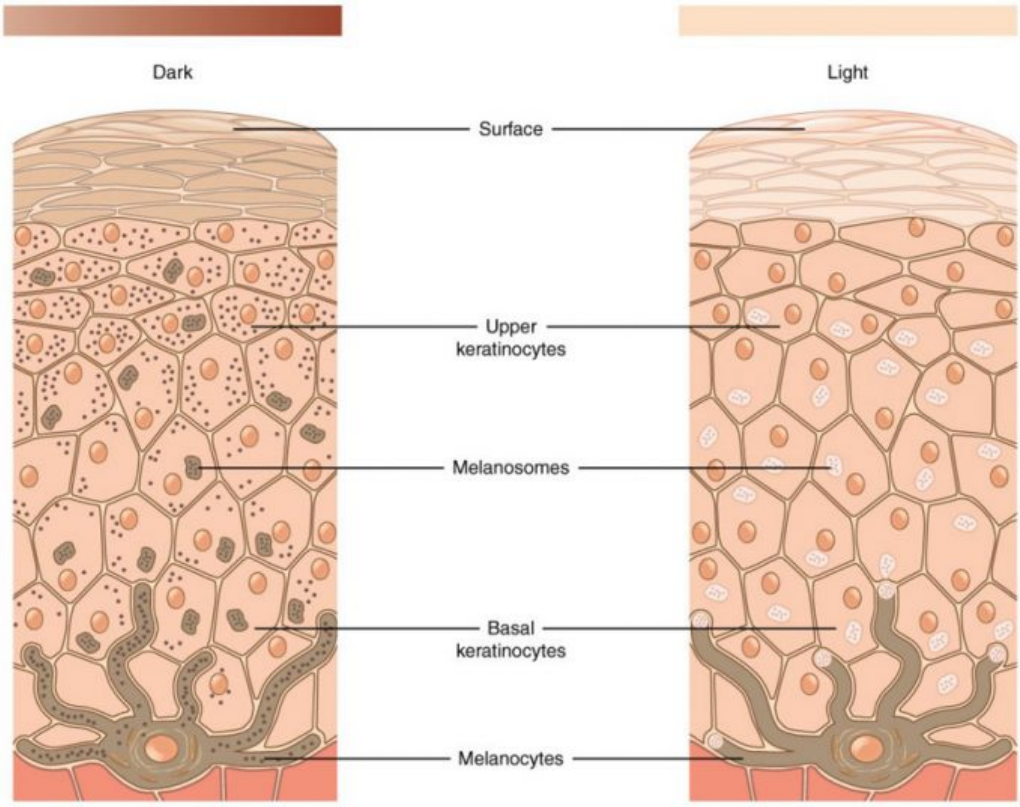

Figure 1.2: Melanoma develops from melanocytes, which are located in the stratum basale at the dermo-epidermal junction. Healthy melanocytes produce the pigment melanin that accumulates within the keratinocytes of the epidermis to shield the skin from DNA damaging UV-light. Figure source: [8].

1.1 Melanocytes

Melanocytes have their embryonic origin in the neural crest and reside more specifically in the *stratum basale* of the epidermis, where they produce the pigment melanin [9] as symbolised in Figure 1.2. Melanin is subsequently distributed by the melanocytes to the 30-40 adjacent keratinocytes[1] to protect the DNA content of the nucleus[2] from DNA damaging ultraviolet radiation [9].

1.2 BRAF and NRAS mutations

Melanoma is known to have the highest mutation rate among all cancer types, whereby around 50%-60% of melanoma patients harbour the b-Raf proto-oncogene (BRAF) mutation and 22% the neuroblastoma RAS viral (v-ras) oncogene homolog (NRAS) mutation [10]. An overview of occurring mutations in melanoma pathways is given in Figure 1.3 whereby the BRAF pathway via mitogen-activated protein kinase kinases (MAP2K) and proliferation marker mitogen-activated protein kinase 1 (MAPK1) is

[1] Keratinocytes are the dominant cell type of the epidermis.

[2] The nucleus is a separate space within a cell and contains genetic information. Small melanin carrying vesicles, so-called melanosomes, are stored all over the nucleus and act like a "cap" to protect from UV light.

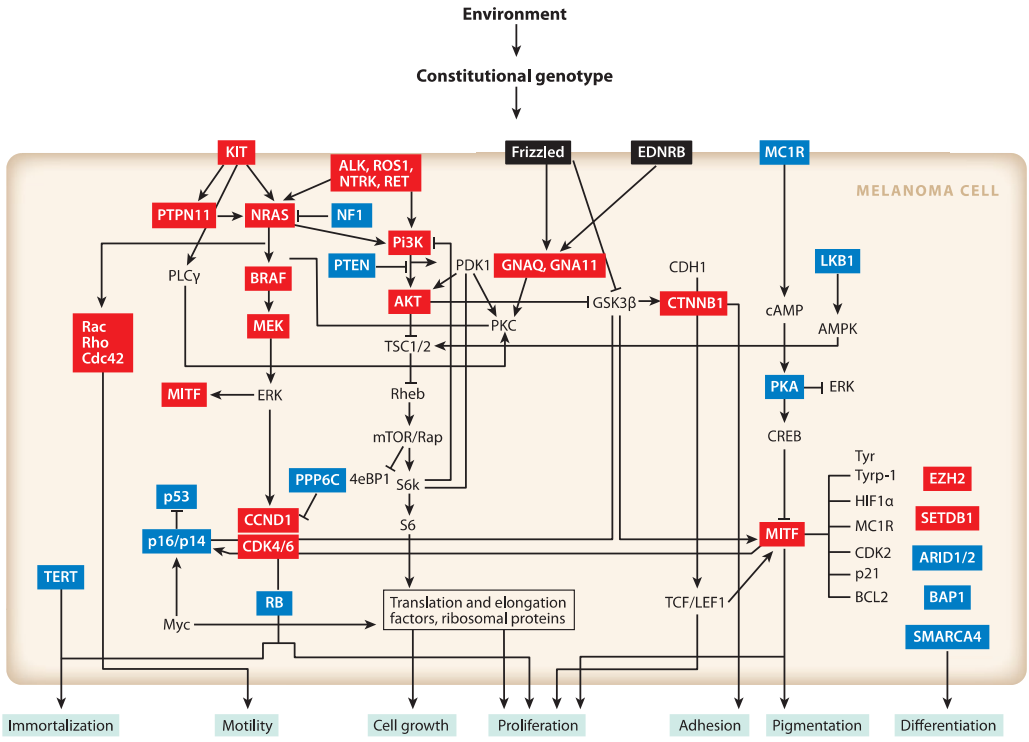

Figure 1.3: Several pathways are mutated. Proteins in red often have a gain-of-function mutation and proteins in blue often have a loss-of-function mutation [11].

often inhibited in clinical practice [11]. Of particular interest in this thesis is the compensatory proliferation pathway via phosphatidylinositol-4,5-bisphosphate 3-kinase catalytic subunit alpha (PIK3CA), AKT serine/threonine kinase 1 (AKT1), mechanistic target of rapamycin kinase (MTOR), and proliferation marker ribosomal protein S6 (RPS6), because it can also be induced by mechanical cues and fibroblasts in the environment [12, 13].

1.3 Melanoma progression stages

In alignment with the high mutation rate, melanoma progression trajectories are diverse and occasionally skip intermediate stages [14]. While many cancer types have a degenerative cascade with following subsequent steps, it has never been proved for melanoma, and lesions like a dysplastic naevus seem not to derive from common naevi. Thus, only categories can be defined such as naevus, dysplastic naevus, melanoma *in situ*, and invasive melanoma. Moreover, pathologists classify a radial growth pattern within the epidermis and a vertical growth pattern with melanocytic lesions in the dermis.

1.3.1 Growth patterns of melanocytes in benign and malignant lesions

The occurrence of melanocytic tumours depends on the body site. Sun-exposed sides can be distinguished into more hidden sides such as the torso, lower legs, and upper back[3], and sides which are prone to cumulative sun damage (CSD) such as the face [15]. CSD is diagnosed by the degree of solar elastosis, or more specifically by the degree of elastin (ELN) fibre accumulation within the skin ECM. High-CSD melanocytic tumours, such as the lentigo maligna melanoma, grow in a lentiginous growth pattern and harbour the neurofibromin 1 (NF1), the NRAS, or a BRAF mutation being different from the $BRAF^{V600E}$ -mutation[4] [15]. Lentiginous growth is restricted to the *stratum basale*[5] of the epidermis. Low-CSD tumours, such as superficial spreading melanoma (SSM), represent almost two-thirds of cases in Caucasians and harbour most frequently the $BRAF^{V600E}$ mutation [15]. SSM grow in a pagetoid growth pattern, which is characterised by scattered enlarged melanocytes and nests throughout all epidermal layers [15]. Besides lentiginous and pagetoid growth, nodular melanoma is a separate entity of melanoma growth and is characterised by the absence of a preceding radial growth phase [15].
Pagetoid growth is associated with melanoma *in situ* [14] and describes melanocytic tumours, which are restricted to the epidermis and are considered to be the first stage of cancer. Other growth patterns can be at the dermo-epidermal junction (junctional), in the dermis (dermal), or both (compound).
Some authors use also the term congenital growth pattern to describe grow in deeper dermis around appendages such as hair follicles [14]; however, many pathologists would not use the term as the word congenital mainly describes lesions since birth. Moreover, lentigo maligna melanoma also goes deep in the follicles, which points to an unclear and thus impractical classification of growth pattern.

1.3.2 Naevus size is in a fragile balance between growth and shrinkage

The described growth patterns are not static but change with time. Mutated melanocytes may develop a naevus that often reveals a fragile size balance. Naevi are often acquired until adolescence, stop growth, and remain then in a senescence-like state for years, but might expand suddenly in case of immune system suppression [14, 16]. The sudden expansion of eruptive naevi often arise in different parts of the body [16], which makes sense as the suppressive effect of the immune system is reduced systemically. The balance between naevi growth and regression can also tip over into the other direction if the general growth rate diminishes with increased age. Naevi often disappear after the sixth life decade probably by increasing impact of attrition [14], an effect that is systemic as well. However, the disappearance of naevi at an advanced age is also often associated with the process of maturation. Histological maturation describes the movement of melanocytes

[3] These sides are, however, often exposed in tanning beds
[4] Code indicates that the amino acid position 600 is occupied by a glutamic acid (E) instead by the default monomer valine (V).
[5] also known as *stratum germinativum*

into deeper dermal areas, whereby the morphology evolves from epitheloid (type-A) to lymphocyte-like (type-B) to spindled or fibroblast-like (type-C) [17]. Modellers might help clarify whether emigration of maturating cells causes the naevi shrinkage or whether the maturation is an independent process that does not change the force balance in naevi. If this force balance determines the naevi size instead, emigrating cells are replaced after they left a gap behind. With the mechanisms described later, it will raise the question of whether the morphology change during melanoma maturation is a consequence of local mechano-biological adjustments.

These examples highlight the dynamics of melanocytic lesions, which modellers should acknowledge, and motivate computational tools in this area as many effects, such as naevi dysplasia, are not well understood [18]. The growth balance is important information to a computational scientist, as it shows that assuming a constant growth rate or a simple growth law might belie expectations of the observed diversity of melanoma. Conversely, the fact that the aetiology of growth arrest and senescence[6] is unclear might motivate computational scientists to study the system equilibrium condition and the mechanical restriction during melanocytic expansion.

A nevus must not but might be the origin of melanoma. To become melanoma, nevus cells must develop invasive behaviour. Then, in the invasive radial growth phase, melanoma cells penetrate the basement membrane as single cells or small, non-expansive clusters. As soon as they form expansive nests and clusters, the vertical growth phase commences, and the malignancy cannot be as easily managed as melanoma *in situ* anymore.

1.3.3 Invasive stage

Invasive melanoma is characterised by the disruption and penetration of the basement membrane (BM). The BM is a double-sided dense ECM layer [19, 20]. As soon as the invasion has started, cells begin to escape from the tissue-depth-dependent UV radiation intensity, and the mutation rate declines [14]. However, the increase in copy number alteration suggests that the previously acquired mutations unfold their potential and become manifest [14]. New mutations at the later stage are rare in melanoma and concern mainly tumor protein p53 (TP53) and phosphatase and tensin homolog (PTEN) [14]. Not only genetic mutations but also oscillating transcriptome changes between proliferative and invasive stages can support the invasive progression, which is known as the phenotype switch [21]. Nodular[7] invasive growth can occur suddenly without visible precursor in the epidermis, which suggests, *e.g.*, a source in melanocytes with several driver-mutations but lack of the crucial proliferation-initiating mutations [14].

In summary, the high mutation rate of melanoma originates mainly in the epidermis, favourable mutations consolidate during the invasion, and only a few important mutations

[6] senescence is the loss of function or the absence of cell division. Alternatively, the term quiescence is used which means cell cycle arrest. Quiescence, however, is temporary in contrast to senescence that indicates permanent loss of renewal capacity.

[7] Nodular melanoma is specifically defined as a vertical growth phase without visible radial growth phase.

occur at later stages.

1.3.4 Metastatic stage

Metastatic melanoma occurs first in lymph nodes: earlier at the draining area of the primary tumour and later at visceral[8] sites. The resection of the sentinel lymph node[9] does not prevent spreading as indicated by undistinguishable patient survival data [22]. Departure and formation of new metastasis have been linked to the activity of catenin beta 1 (CTNNB1) and Wnt signalling, while recurrent driver-mutations have not been found [14]. The molecules CTNNB1 and Wnt will be set in context with mechanoregulation.

This section gave a fundamental insight into the complex histopathology of melanoma. Melanoma can occur at many sides without precursor and can push away host tissue to expand. Wherever tissue contortions appear, forces come into play; and wherever forces are, mechanical laws must be considered. Without a sufficient description of the development of forces within a tissue, neither mechanoregulation can be sufficiently understood nor can we understand which mechanisms counteract tumour expansion. Therefore, the next step is the introduction into tissue and tumour mechanics.

[8] inner organs

[9] The sentinel lymph node is the lymph node, which is closest to the cancer side. The sentinel lymph node consequently represents a gate to the lymph system.

2. Tissue and tumour mechanics

2.1 Mutations initiate but mechanics forms malignancy

It is clear that genetic mutations initiate and drive malignancy, but mechanical phenomena interfere with virtually every characteristic of cancer and stromal cells, and mechanics can be linked almost to all hallmarks of cancer [23]. The growth of cancer is not dependent on a constant growth rate which has been set after a mutation. To a greater degree, growth is a highly context-dependent process with phenotype switch, interaction with other cell types, time-variant growth rates, and modifications of the mechanical properties. Mechanical forces - like compression, tension, hydrostatic pressure and shear stress - modify the way tumour grows, develop, invade and metastasise [24]. Moreover, forces propagate faster than diffusive mediators, have thereby a crucial part in spatio-temporal development of tissue [25], and interfere directly with the chromosomal organisation and gene expression in the nucleus [26]. Consequently, it is difficult to decide whether molecular patterns are cancer gene related and are driven by mechanical cues as a consequence of cancer growth and tissue contortion. After describing different tissue modelling philosophies, the introduction gives an overview on growth control and the physical forces, which counteract malignant expansion.

2.2 Tissue modelling philosophies

Tissues are subject to a complex interplay of physical phenomena. Two incompatible research fields provide theories to tackle the mechanical dimension. Firstly, the cell oriented tissue modelling community, which focuses on the coexistence of deformable individual cells and extracellular fibres as biochemical signals. Secondly, the organ oriented

tissue modelling community, which focuses on the externally inflicted tissue deformations with extracellular fibres as dispersed structural elements. Cells are thereby neglected.
Both tissue modelling strategies underestimate vital tissue components such as the stroma complexity or the cells, and both invest much computational power into either single cell resolution or in the molecular simulation of ECM fibre networks. A valuable compromise might be porous media systems as explained below.

2.2.1 Organ oriented tissue modelling community

The organ oriented tissue modelling community is mainly interested in simple tissue models as an element for complex organ models and surgery-guidance. Their theories treat fibrous tissues primarily as biphasic poroelastic systems [27, 28], or as monophasic materials with isotropic or anisotropic fibre dispersion [29–33]. Some authors link molecular fibre dispersion at the microscale to the mechanical properties at the monophasic macroscale without the impact of water [34], or with consideration of hydration dynamics [35]. The impact of altering single structural constitutes is intensively discussed [36, 37], but the resulting models represent rather hydrogels than biological tissues.
Organ oriented tissue models ignore both ECM voids caused by cells and cells themselves. The problem is that cells act as spherical inclusions in polymer networks and contribute to the nonlinear stress-strain response in soft tissues and Poisson's ratios above 0.5 [38]. Moreover, cells modify their mechanical environment in response to mechanical cues in sufficient long time periods [39, 40]. Therefore, cells cannot always be ignored if accurate tissue modelling is to be achieved.
Another methodology is provided with the mixture theory [41], which includes several fluids representing different tissues. But because the mixture theory ignores micro velocity fields and forces all fluids to follow more or less strict a mysterious velocity of the whole mixture, it does not necessarily provide more biologically meaningful and mathematically sound models [42–44]. Moreover, mixture theory frequently ignores structural informations [36] and uses modelling parameter which cannot be determined experimentally. Consequently, establishing and validating sound computational tissue models is non-trivial when facing the complex independent regulated components observed in internally transformed tissues [45].
When cancer growth in host tissues is modelled, a tissue surface tension and a distinct boundary between different tissues is often hypothesised and biologically discussed [46]. However, such a boundary seem to be very inflexible, and it is not clear which molecular biology can be associated with it. In contrast, this thesis will tackle the force interactions at the microscale and averages them to the macroscale where a kind of boundary appears. Instead emphasising boundaries between tissues, this thesis will explore tissues in themselves.

2.2.2 Cell oriented tissue modelling community

Contrarily, the cell oriented tissue modelling community understands tissues as a coexistence of deformable cells [47], where external ECM fibres are seen as a cell internal characteristic. The gap size-dependent gate function of the extracellular matrix is only occasionally considered [48]. Cell oriented tissue models are used to study chemical communication either in fibrous tissues without deformation or in deformable but not fibrous epithelial, muscle, and nervous tissues. The pericellular space is often only a simplified space with constant diffusion.

2.2.3 Porous media oriented modelling community

A less detailed but more complete tissue theory [42, 50] came up with thermodynamically constrained averaging theory (TCAT) to describe multiphase flow in porous materials [51]. The concept comes originally from geo- and soil mechanics. Applied to organic tissues, the deformable porous media resembles the ECM ultrastructure in which multiple fluids can flow in different directions. The cell population fluid is represented as a viscous phase with adhesion to the ECM. The phase for interstitial fluid (IF), the liquid between cells [52], flows through the porous network and carries soluble factors.

The change of the cell viscosity determines the interplay between the cells and the ECM [2]. Well-differentiated cell populations act like highly viscous fluids and push the ECM ultrastructure until pores close and internal tissue blockades occur. However, less differentiated and more versatile cells pass the ECM without causing remarkable ECM contortions [2]. The growth induces ECM compaction might be comparable with the compaction being observed at a lower spatial scale when cartilage is exposed to an external hydrostatic pressure gradient [53].

Compared to mixture theory, the TCAT modelling strategy fills better the gap between advanced cell orientated tissue models and the continuous organ oriented tissue models in the raw mono- or biphasic representation. However, TCAT models explain neither the stiffening of organic tissues after dehydration nor the absence of interstitial fluid flow (IFF) in some observations. In addition, obtained interstitial fluid pressure (IFP) values seem to be quite low. One obvious reason in irregular fibrous tissues is that the phases of the solid ECM and the IF phase are not clearly separated and that the pericellular space is a porous medium itself. Moreover, the cell phases are "compressible", in the sense of osmotic regulation, and are consequently not so static as current TCAT models suggest. All these effects are general questions of tissue modelling and will be discussed in more detail later, but a look at Figure 2.1 shows that these effects need to be tailored to different body sides as the the skin structure is highly body side dependent.

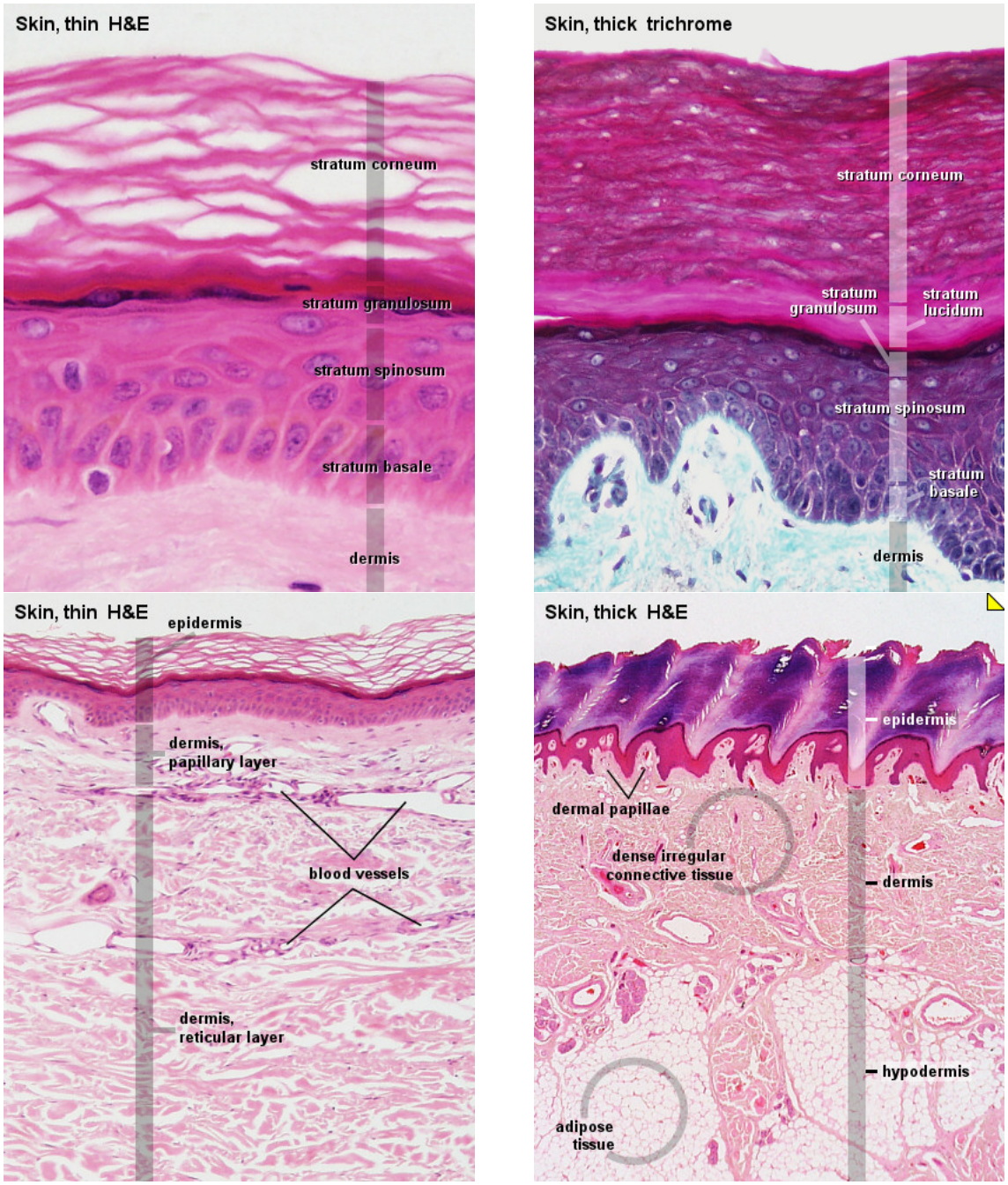

Figure 2.1: Histological sections of non-acral (thin) and acral (thick) skin with a focus on the epithelium or all skin layers. The *stratum corneum* is a stratified dead area that computational scientists would interpret as a homogeneous material. It could be modelled monophasic, or biphasic if transepidermal water loss is studied. Interesting is the variable thickness of the *stratum corneum*, which depends on the anatomical origin of the section. The increased *stratum corneum* in acral skin has to be kept in mind if atmospheric oxygen is used for a boundary condition. The epithelium is composed of cells with well-developed tight-junctions. Epithelial and embryonic tissues require computational tools not discussed in this thesis. Tumour expansion in dense irregular or loose ECM is the modelling aim of this thesis. Growth simulations require good image segmentation algorithms and a statement about the depicted skin side. Figure source: [49].

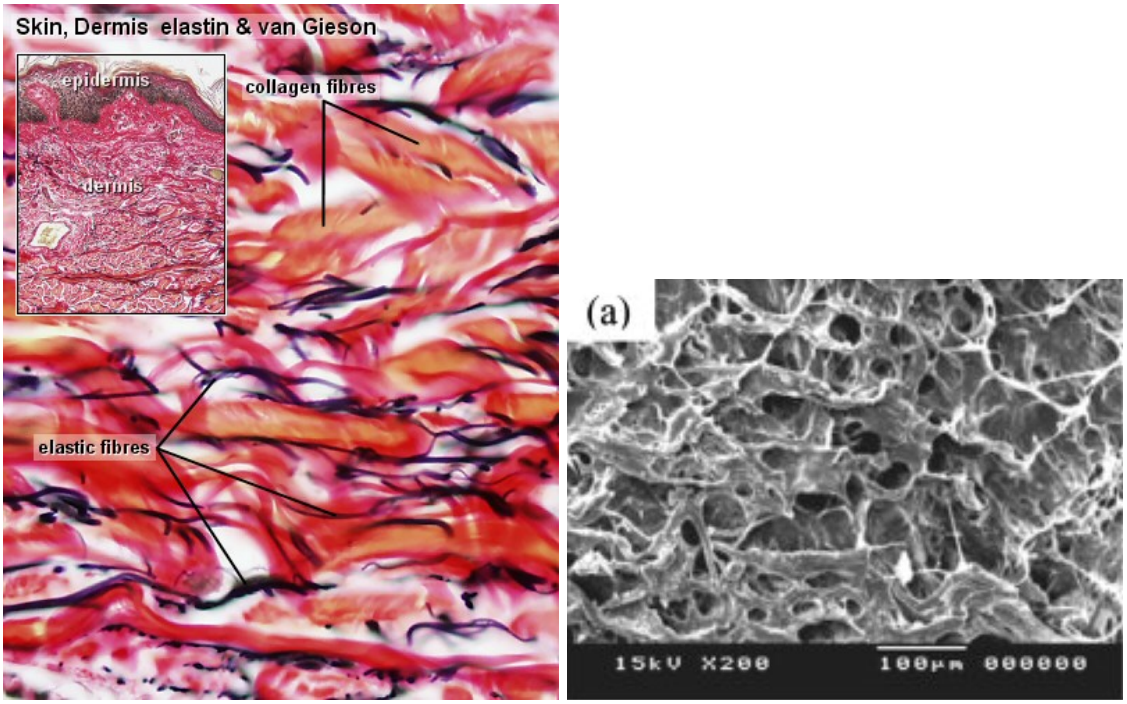

Figure 2.2: The extracellular matrix of the dermis falls within the category of irregular dense ECM. **Left:** histological section treated with Van Gieson's stain to highlight collagen and either Verhoeff's stain or Weigert's elastic stain to visualise ELN [49]. The white areas represent the ground substance made of GaG. GaG are water soluble and are lost during sample preparations with the most common solvents. **Right:** scanning electron microscope (SEM) image of decellularised porcine dermis with lower magnification [54]. Most SEMs of gels and decellularized tissues show the single fibres at high magnification, which miss the mesoscale micro-anatomy.

2.3 Irregular fibrous tissue has a porous ECM scaffold

Within the skin, the dermis represents irregular fibrous or loose connective tissue. Figure 2.2 reveal the porous structure of the ECM in the dermis. In both, the histological section with ECM staining and the decellularised dermis under a SEM, the irregular composition and porous-like gaps become imaginable. The porous structure relates to decellularised tissues [56–58] with voids in the size of cells and larger. As one can see in Figure [49] bottom left, the dermis consists of two quite different areas: a superficial papillary dermis which is more fluid than firm and rich in thin elastic fibres; and a deeper reticular dermis which is (regular) stiff and shows more prominent and thick collagen fibres. Both parts are composed of different types of collagen. Hence, invasion in the papillary dermis will have different features compared to invasion in the reticular dermis. The mechanics of the extracellular matrix is a geometrically complex problem with three spatial scales: the macroscale, the microscale, and the molecular scale.

At the macroscale, one can describe the mechanical deformation of the porous anatomical ultrastructure of the ECM. Deformed ECM scaffolds are frequently observed in mechanopathology [58–60] and are associated with pore pressure as known for both

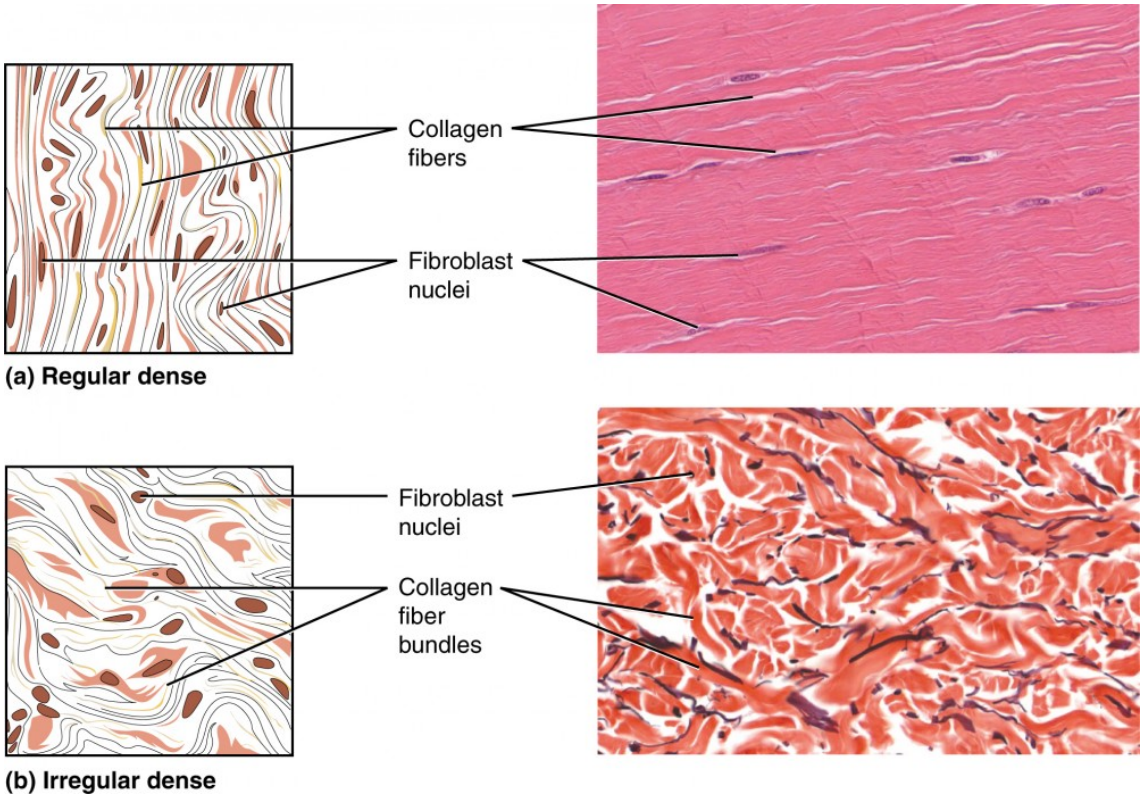

Figure 2.3: Difference between regular and irregular dense matrix. The stained nuclei represent ECM producing cells. Pathologists donate the inactive form fibrocyte and the active form fibroblast. While the fibres are parallel in the regular dense matrix, the fibres are seemingly randomly orientated in the irregular dense matrix. For modellers, the information is relevant to consider the anisotropy of materials and growth directions. Figure source: [55].

mechanical and physicochemical systems [61].

At the microscale, one can describe the mechanical deformation of the ECM polymer network within the pericellular space. Here, the inter-fibre gap size defines the voids of the porous material. Rules of hydrogels and absorbent polymers might apply. A certain directionality of the collagen fibres can occur and might have to be considered with a mathematical anisotropy term.

At the molecular scale, ECM molecules might represent an incompressible solid phase. The bulk modulus of the solid phase at the molecular scale is assumed to be infinite, which means that molecules cannot be compressed in its volume.

Thus, this thesis differs between ECM ultrastructure at the macroscale, ECM polymer network structure at the microscale, and ECM molecule structure at the molecular scale. The matrix components cannot be seen as diffusive species in an ideally mixed medium and can thus not be modelled as a node in a typical biochemical reaction network with mass action law. As a solid interconnected continuum, the ECM is highly dependent on constitutive material laws, keeps the tendency to return to the original position after displacement, and gives a geometry dependent pattern. In the biological perspective,

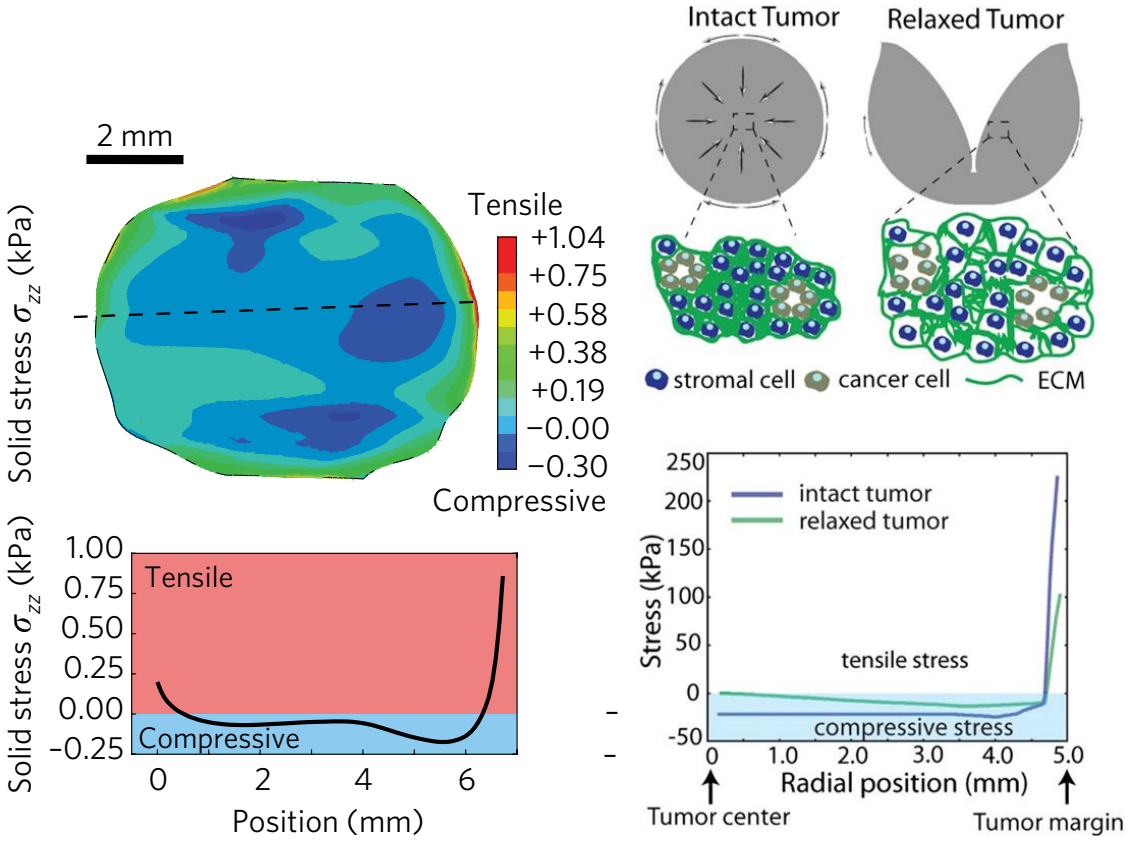

Figure 2.4: Stress field in a tumour caused by growth-induced stress. The solid stress is negative in the tumour and positive at the tumour margin. Figure Source: [59, 60].

geometry dependency might provide cells with information on their spatial localisation with subsequent triggering of the locally appropriate differentiation programme. The consequential heterogeneous pattern of cellular differentiation is, *e.g.*, observed in tissue morphogenesis [25, 62]. .

2.4 Dissecting the role of collagen and glycan

The ECM is a part of the tumour environment and is composed of a "core matrisome" with around 300 protein types [64]. Albeit ECM-omics[1] data for poorly and highly metastatic melanoma xenografts[2] exists [65], a three-dimensional growth model requires a simplified ECM representation. A simple subdivision of the "core matrisome" is into glycoproteins, collagens, and proteoglycans (PGs) [65] whereby in this thesis, collagen is set apart from the glycan fraction.

[1] Quantitative measurement of many molecules to extract relevant subgroups or to understand the collective characteristics

[2] transfer from biological material from one species to another, like human cancer cells in mice

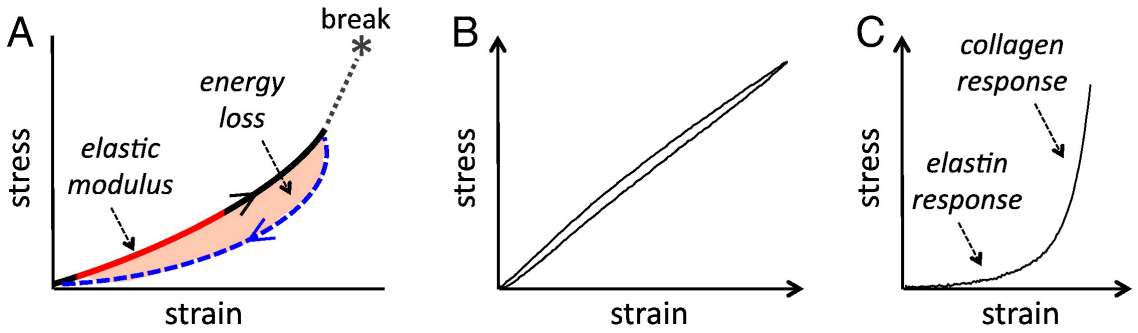

Figure 2.5: Mechanical properties of the extracellular matrix in the form of stress-strain-relationships. If the material is ideal elastic, the stress is preserved, and the material returns to the original position. If the material does not fully return, a viscous response is partly present. A: Stress-strain curve of ECM. Arrow indicates the direction of loading (back) and unloading (blue). Strong deformation leads to changes in molecular structure and thus energy loss. Excessive stress can lead to material break. B: Strain of ideal elastic material correlates linearly with stress load. C: Collagen and ELN show together an assembled curve with elastic and plastic behaviour. Figure source: [63].

2.4.1 Collagen resists tensile stress

The collagenous fraction resists tensile stress and can be modelled as a porous solid phase, which physically counteracts the growth potential of tumours. The dermis contains irregular dense ECM as shown in Figure 2.2 and 2.3. The collagen fibre orientation is tissue specific and can have a parallel fibre positioning in other tissues.

Most tumours show circumferential tensile stress at the tumour margin [59] as shown in Figure 2.4. It is also relevant because some cells react on tensile stress with proliferation [66]. Tensile stress might be associated with collagen bundles, which wrap around the nodular growing mass and become increasingly parallel[3]. Consequently, collagen acts like an annular ligament[4] that encapsulate the neoplasm. Collagen fibres exposed to tensile stress show two stages. As long as the fibres are undiluted during entropic stretching[5], the stress increases mildly with the strain. As soon as the fibres are taut in enthalpic stretching[6], the stress increases exponentially with the strain [67]. The stress-strain curve, shown in Figure 2.5 C, displays how the ECM components collagen and ELN deform when strained. Collagen becomes meaningful for larger strains while ELN damps small and repetitive strains. Hence, collagen provides strength and ELN elasticity, whereby the degree of pre-stress crucially determines the collagen response.

If tissues are in focus instead of single molecules; ELN and collagen fractions are believed to determine the elastic response, while IF contributes to the viscous response [68]. Elastomeric tissues show visco-elastic behaviour in stretch and relaxation cycles as shown in Figure 2.5 A. The trajectory indicates that the stress is lower for the relaxation than

[3] Fibres are not necessarily parallel to the tumour surface as the polymeric network is biologically remodelled and migration tracks realign the ECM perpendicular to the tumour surface

[4] An annual ligament is a medical term for a strong band of fibres that encircles an anatomical structure.

[5] Polymers are wound, and entropic laws control the organisation within the polymeric network.

[6] Bounds between monomers determine the mechanical properties

for stretching, which indicates energy loss due to heating. If the material is viscous and the strain remains constant, the material will readjust, and the stress relaxes in a plastic response. In this is the case, the surrounding tissue will not return to the original position after removal of a tumour. The ability of some biopolymers to relax is highly biologically relevant. For instance, the formation of intestinal organoids with a lumen[7] initially requires a non-degradable stiff matrix, which subsequently relaxes [69].

2.4.2 Glycan modulates compressive stress

The glycan fraction is a swelling polymer that accounts for compressive stress, cushions the cells [63], and determines the remaining space in which chemicals, drugs, and nutrients can diffuse [70]. Compressive stress emerges, *e.g.*, in the tumour core [59]. Glycans can bind water up to 1000 times the molecular weight of GaG, so that 90% of the water in the skin is in the bound form [71]. Glycans achieve a swelling effect with the negatively charged chondroitin-sulfates, which attracts water and repels the glycans from each other. This mutual repelling force span the GaG[8]. The negatively charged gel collapses if the counter-ion concentration increases or the pH decreases [72].

The ion-sensitive de-swelling effect theoretically allows cells to migrate easily through the stroma, given they release cations into the environment and the polymer network mesh-size is not limiting. Thus, glycans are likely responsible for the local control of transport processes within the remaining unbound IF. Moreover, the de-swelling effect might improve the penetration by stromal cells such as fibroblasts or cells of the immune surveillance. The histological perspective complements the description of glycans. In conventional histological sections, the glycan fraction is called the ground substance and is lost in the sample preparation with the most comment solvents so that white gaps remain (Figure 2.2 left).

In conclusion, glycan is a flexible filling material that is highly ion-sensitive and is thus likely to facilitate critical biological functions such as migration but is also able to control the volume fraction of IF by the absorption capacity.

2.4.3 Collagen to GaG ratio is higher in dermis than in brain

A careful decellularisation process can extract tissue ECM with physical, biological, and chemical methods, which have minimal impact on mechanical properties [57]. The obtained ECM ultrastructure can be analysed with imaging software to obtain fibre diameters, fibre orientation, porosity, connectivity, spatial intersection density, and volume proportion [73]. It also builds a good base for scaffold mechanical modelling [34, 73]. The ECM of porcine dermis has a composition of 0.85 $\pm$ 0.04 mg collagen/mg ECM (dry wt.) and 1.11 $\pm$ 0.06 μg sulfated GaG /mg ECM (dry wt.) [74]. Collagen concentration of porcine brain ECM was 537.5 $\pm$ 26.9 μg collagen/mg ECM (dry wt.) and 5.1 $\pm$ 1.4 μg

[7] Inner space of a tubular structure

[8] GaGs contain charged chondroitin-sulfates and belong thus to polyelectrolytes. Polyelectrolytes are charged polymers.

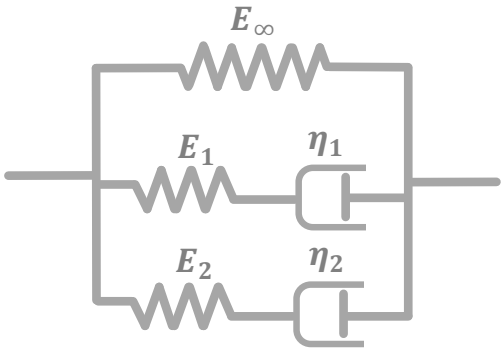

Figure 2.6: A two-element-Wiechert model has two Maxwell liquids and a spring element in parallel. A Maxwell liquid has a spring and a dash-pod in sequence. A composition of springs and dash-pods help mechanical engineers characterise material properties. In cancer, LOX cross-links collagen and thus increases the spring constant E_∞, while MMP decrease either the ratio of E_n to ν_n by degrading polymers or the spring constant E_∞ by degrading crosslinker.

sulfated GaG /mg ECM (dry wt.) [75]. Consequently, the dermis has a much higher relative collagen content while the brain is relative richer of GaGs. It might be that melanoma uses different mechanisms to colonise these tissues.

2.4.4 Polymer-network theory describes collagen and glycan behaviour

The polymeric network structure of biomaterials mediate the glycan swelling phenomenon and the physical effects for the collageneous solid phase. The stretching of the collagen network can be modelled with a constitutive material law, while the latter phenomenon can be described with two coupled equations of the swelling behaviour [72], which will be described in more details later.

An appropriate mechanical material law for a polymeric collagen network is the two-element-Wiechert model [76] sketched in Figure 2.6. If intertwined polymers are strained, polymers unravel to reduce the internal stress. A Maxwell-element represents unravelling with a sequence of one elastic spring and a viscosity representing dash-pod. Two Maxwell-elements in parallel might represent several polymer types. The dash-pod could symbolise unravelling polymers sliding across each other. Cross-links inhibit the unravelling process, and an additional spring is placed in parallel to the Maxwell elements to restrict the dash-pods. Crosslinking by ions (alginate), a second polymer type, or the enzyme lysyl oxidase (LOX) increases the stiffness in hydrogels. Also, relaxation is a crucial characteristic of cell-ECM interaction to achieve growth and development [77]. Taken together, the Wiechert model is a good representative for the visco-elastic behaviour of cross-linked polymers and is thus biologically meaningful.

Another effect is the swelling behaviour of polymeric networks, which requires another modelling strategy. After initial successes in rubber research [78], the absorbent polymer field developed [79] and resulted finally in specialised models for the swelling of GaG

networks [72]. Such networks have fibres that absorb the solvent, but the polymeric network crosslinks counteract the complete dissolution. The osmotic pressure pulls solvent into the material while the polymeric network cross-links restrict solvent influx.
While collagen can be seen as an independent phase that resist tensile stress, the swelling effect of glycans mediates how forces are interchanged between ECM, cells, and IF. The glycans swell and pre-stress collagen fibres and contribute in this way to tissue stability. The ion-dependent deswelling effect of glycans might facilitates migration.

2.4.5 Tissues and hydrogels are difficult to compare

Hydrogels gently nestle up to the cells and provide the mechanical cues, living cells require. Simultaneously, hydrogels are water-rich, allow cellular expansion, and dissolve with time so that residing cells can substitute the hydrogel polymers with native ECM. In contrast, dermis shows a stable porous structure [54] and contain distinctly more polymer with 170 - 190 mg collagen per g wet skin tissue weight [52] than the 1-7 mg/ml collagen used in labs to form hydrogels [80]. In experimental gels, polymers can homogeneously cross-link in all directions and achieve high stability. In tissues, however, polymers cross-link and gelate in the space around cells, which limits the stability toward all sides.
Moreover, experimental hydrogels are often much weaker and might lead to inflation of false positives. For example, Matrigel™ is often used for invasion assays but is, with an elastic modulus of 0.41 kPa [81], much weaker than a basement membrane derived from the inner limiting membrane (ILM) between vitreous body and retina of a human eye. This basement membrane is the only basement membrane that can be separated from adjacent tissues and has an elastic modulus between 250-500 kPa [20].
In addition, *in vivo* tissues are daily exposed to compression and relaxation cycles, which might compact ECM fibres to a septum between cells and a stable ECM ultrastructure. Flow and diffusion might be possible between a compacted ECM partition and the cell membrane despite the high collagen concentration.
Thus, transfer of properties from polymer networks to homogeneous tissues [34] neglects mechanical phenomena based on mesoscale mechanics of the ECM ultrastructure and underestimates the increased polymer content in tissues.

2.5 Dissecting the role of ECM, interstitial fluid, and cell phase

The dissection of fluid and solid stress as well as the dissection of externally applied and internal growth-induced stress is a key to understand both the functioning of tissues and the proper use of therapeutics for mechanical stress relieve [45].

2.5.1 Solid and fluid stress play different roles in cancer

Mechanical forces in a tumour can be subdivided into two main parts: fluid and solid stress. Both can be measured separately [83] and will be discussed in the following.

The total solid stress is the sum of externally applied stress and growth-induced stress. Externally applied stress is the stress that is applied from the environment on the tumour and can be entirely removed. Depending on the environment, stress levels are between 28 millimetre of mercury (mmHg) and 120 mmHg but can theoretically exceed 150 mmHg in mice [45]. Growth induced stress is accumulated during tumour progression, remains stored after resection and contributes to total stress with less than 30%. Growth-induced stress can partially be released by a cut as shown in Figure 2.4. Through a cut on the most extensive site, the tumour unfolds and releases the energy: The centre swells, and the cutting edge retracts. The growth-induced stress level is 0-10 mmHg in avascular tumour spheroids, 2-60 mmHg in mice tumours and 35-142 mmHg in human tumours [45].

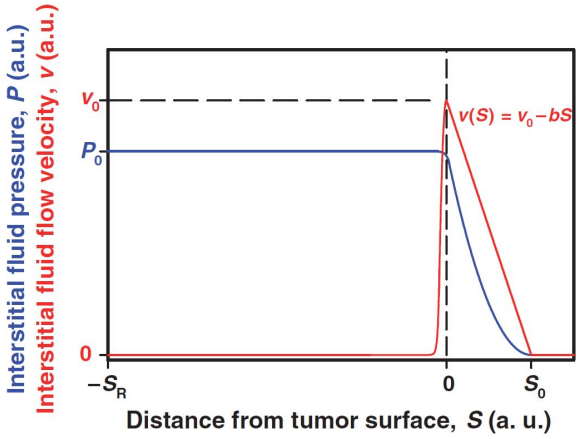

Figure 2.7: The blue IFP curve and the red IFF velocity curve vary along the tumour radius in arbitrary units. The curves are displayed from the tumour centre ($\mathrm{S_R}$) to the tumour surface (0) and also show the following drop within the tumour environment up to the point of normalising physiology ($\mathrm{S_0}$). Figure source: [82].

Along with solid stress, fluid stress contributes to the forces in tumours. Interstitial fluid is not only a carrier of chemical molecules but also serves as mechanical pressure coupling between distinct tumour sites, tumour and stroma, and tumour and cardiovascular system. IFP was first measured in 1884, whereby the less precise term "tissue pressure" was used [84]. Tumour tissue was found to exhibit a higher interstitial pressure than healthy tissue, and since the first exact measurements on rabbits in 1950 by Young [85], several publications have shown that IFP increases with tumour size, in the direction to tumour centre, and with decreasing blood flow [86]. With the wick-in-needle technique, it was possible to show that human metastatic melanoma exhibits increasing IFP from normal skin (0.4 ± 1.7 mmHg, $n = 5$), over small lesions (5.8 ± 2.2 mmHg, $n = 6$, $0.1 - 4\ \mathrm{cm}^3$) to larger tumours (22.8 ± 13 mmHg, $n = 6$, $8 - 106\ \mathrm{cm}^3$). The highest value in the study was 48 mmHg $(6.4\ \mathrm{kPa})$, and a sharp pressure drop at the tumour-stroma interface has been observed similar to the representation in Figure 2.7 [86]. Pressures up to 107 mmHg $(14.3\ \mathrm{kPa})$ and intratumoral oedema were reported in another study with the same technique and larger tumours [45, 87].

Furthermore, patients who had responded to treatment showed decreasing IFP values down to 0 mmHg while non-responders developed heightened pressure. However, a correlation between pressure and tumour size was not found in this study [87]. Rofstad studied IFP by letting melanoma cell lines grow in xenografts. He did not find a correlation with the fraction of necrotic cells, but he found a correlation of increasing IFP with increasing propensity of cell lines to growth denser [88], with decreasing mean capillary diameter [89] and high blood flow resistance caused by tumour-line specific vascular abnormalities [90]. While IFP correlates well with tumour size up to a particular grade [86], the vascular network dominates the IFP in larger tumours [89]. Whether an IFP gradient results in IFF or not will be discussed in the following section.

2.5.2 Material transport occurs at the micro- and macroscale

Transport of interstitial fluid, nutrients, and gases occur at the microscale and the macroscale. Convective and diffusive transport through a polymer occurs at the microscale while movement of tissue components contributes to the viscous response at the macroscale. The flow within the blood and lymph vessels is not considered in this section.

Interstitial fluid: from pressure gradients to flow

Whether IFP differences result in IFF or not is still an open research question. Only a few studies show experimental evidence and report IFF from 0.1 to 10 μm per second [91]. Because this relationship is thought to be important metastatic dissemination, a study investigated the relationship between IFP and IFF with dynamic contrast-enhanced MRI [82] and the spatial behaviour in Figure 2.7. One perspective is that the fluid does not remain static but begins to move through the tortuous pores of the ECM and around cells and causes shear stress. This shear stress can be locally strong even if the overall flow is weak [92].

Macroscale mechanics depends on free IF

The ratio between accessible IF and IF bound to polymers can influence tissue mechanics in following imaginable cases.
Tissue dehydration, tissue compression, ECM production, and GaG upregulation reduces the IF supply or increases the binding capacity. The transport of IF is detained, and thus tissue becomes stiffer. The decrease of ECM pores reduces energy dissipation and the viscous response in tissues. Instead, energy is transferred to the ECM ultrastructure and is finally intercepted by the elastic response.
On the other side, tissue hydration, cell lysis, ECM degradation, and GaG downregulation increase the fluid supply, or decreases the solvent binding capacity. This might lead to cell shift, polymer relocation, and IFF. As a consequence, energy dissipates, and tissues show a less elastic and a more viscous characteristic.

Convective transport through a polymer

The convective transport of fluid in tissues can occur through cells via aquaporins [93] k_1 or through steric hindering polymers. The second way was tried to be approximated with an array of cylinders [94, 95] but especially the fibrillar structure of ECM proved this concept not applicable [96]. Additionally, lipids reduce further the conductivity [97]. The most appropriate way to model this might be the most general form of the Carman-Kozeny model [98]:

$$k_2 = \frac{(1-\omega_f)^3}{G \cdot S}$$

with Kozeny factor for geometry G, the wetted surface area density S, and the oxygen volume fraction in the interstitial fluid ω^f.
A third way describes water flow through channels. In case of water flow along fibre tracts and pulsating vessels [99] in a particular direction, the Hagen-Poiseuille equation can be applied. A newer approach in engineering might be more appropriate if undirected channels emerge in case of oedema or if the pericellular ECMs build a compacted septum with adjacent water channels due to repetitive tissue compressions. The recently published model is based on large-scale interconnected pipes through which water might flow. The water permeability through a system of interconnected pipes reads [100]:

$$k_3 = C_k(\sigma) R^2 (\frac{R}{l})^2 [z - z_c]^{\beta(\sigma)}$$

with the functions C_k and β of pore size variability σ, the pore connectivity z, and percolation threshold defining the threshold to disconnection z_c. Another scale-free variable is the ratio of mean pore radius to mean pore separation distance $\frac{R}{l}$.
In short, IFF occurs in three ways: either through the cells via aquaporins, through a pericellular polymer or through a channel between a pericellular polymer and the cells if present.

Diffusive transport through a polymer

The bound water is assumed to diffuse along the fibre network and tend to outbalance ECM network moisture. Diffusive transport is more dominant than convective transport in tissues and is strongly correlated with tissue anisotropy [101]. Diffusion in polymer networks D is related to diffusion in the not hindered case D_o. In polymer networks, it depends on hydrodynamic F and steric S contributions [102–104]:

$$D = F \cdot S = e^{(-\pi\omega^f)^{0.174 ln(\frac{59.6}{\lambda})}} \cdot e^{-0.84((1+\lambda)^2)\omega^f)^{1.09}}$$

with the ratio of solute diameter to fibre diameter λ.

2.5.3 Tissue physiology is influenced by osmotic forces

The awareness of the osmotic potential based on compressed polymers has consequences on tissue physiology. If IF would be isotonic, the mixture of compressed polymer and IF has to be consequentially hypertonic and thus potentially cytotoxic. Thereby, charged molecules can outbalance the effect by relocation as long the polymer density contains an exclusion volume bigger than the size of mobile ions and molecules [105]. This section discusses the effect of charged molecules.

Isotonic fluids are not the same as isotonic spaces

An old rule implies that all body fluids are isotonic fluids with an osmolarity of almost $c_f = 300\ \mathrm{mOsm/L} = 300\ \mathrm{mol/m^3}$ and an osmotic pressure of $\Pi_\mathrm{f} = c_f R\Theta = 500\ kPa$ according Van't Hoff's law. This rule might only be valid for the space around cells in dynamic equilibrium with sufficient free IF but not specific to body fluids moving in it. After complete draining of free water, the osmotic pressure might not be outbalanced anymore and rises with further compression.

Colloid osmotic pressure is negligible

The colloid osmotic pressure plays a minor role in human IF. It increases from 1.8 kPa for children below seven years to 2.8 kPa in adults, while the value in the latter group is body height dependent [106, 107]. The colloid osmotic pressure decreases from thorax level to the ankle below waist level from 1.6-2.5 kPa to 0.9-1.7 kPa [108, 109].

Polymers determine local control while motile elements determine systemic control

While crosslinked polymers remain at the initial location and determine local set points, diffusive molecules might control systemic adjustments. As a consequence, a paradigm shift is currently occurring in physiology. Polymer structures are increasingly seen as strong static and local regulators, which can probably be actuated by locally residing cells. Consequently, body-wide control of ions and colloids has less impact on clinical relevant fluid and volume regulation than previously thought. Polymer structures such as the GaG in stroma [52, 110], the actomyosin cortex in cells [111, 112], and the intravascular glycocalyx layer [113–116] are strong contributors in the tissue fluid management.

Motile ions and molecules outbalance polymer charges

Two mechanisms outbalance charged polymers. Molecules with the same charge as the polymer leave the tissue while counter ions are attracted.

Albumin is negatively charged like GaG, is excluded from many interstitia, and its concentration is inverse proportional to the concentration of GaG [105].

Positively charged electrolytes and small hydrophilic molecules build probably a countercurrent mechanism [117] based on electro-mechanical coupling [118] to reduce the energy in the whole system. It might be energetically favourable to neutralise the negative charges of GaG with Na^{2+} and to relocate osmotically active substances into adjacent tissues with lower swelling ECM content or into the lymph, which becomes

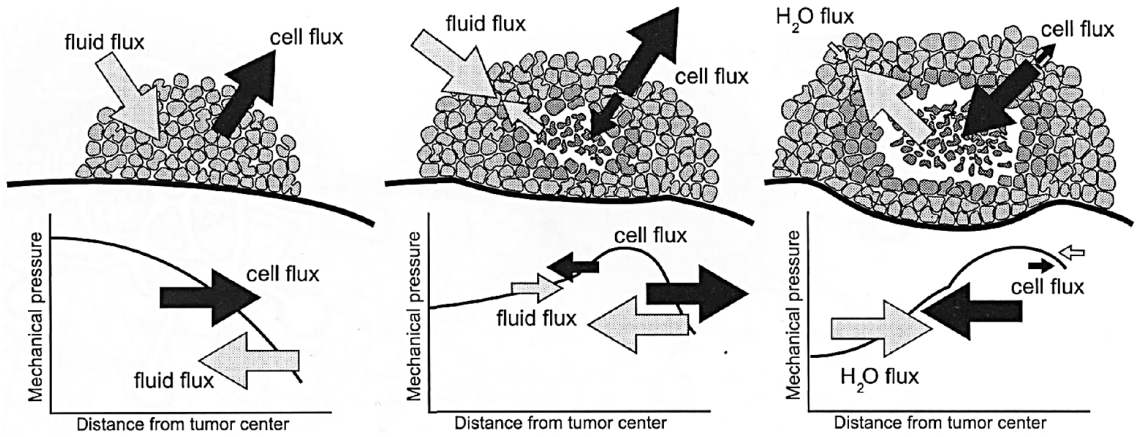

Figure 2.8: Cell and fluid flux in a tumour spheroid. While in the beginning, the spheroid grows at the expense of environmental IF, the fluid source comes increasingly from the dissolving necrotic core. The IFF changes from influx to outflux, and cells, which were initially pushed out, are falling into the gap that the dissolving necrotic core left behind. Figure source: [120, (p.19)].

hypertonic. Small molecules such as hygroscopic urea [119] eschew areas with high swelling pressure and accumulate in the epidermis, while the GaG-rich dermis stores Na^{2+} [9] during high-salt diet [110].

2.5.4 Oxygen deprivation dissolves the cell phase and affects tissue stability

Oxygen permeates human tissues and is indispensable for the life of aerobic organisms. Therefore, the following text give some quantitative orientation points. Circumambient air has a proportion of 21% of oxygen with a partial pressure of 150 mmHg while most mammalian tissues have a proportion of 2% - 9% oxygen with a partial pressure 40 mmHg. Tissue with oxygen levels below 2% become hypoxic and below 0.02% anoxic [121]. Oxygen diffuses up to 145 micrometres into the tissue, and tumour cells become necrotic if they are 100 - 200 micrometres apart from the blood vessels [120, 121].
Oxygen deprivation causes necrosis and changes the mechanical integrity of tumour spheroids as shown in Figure 2.8. In the beginning, the tumours expand by attracting IF from the surrounding tissue. The outward pointing cell flux is high as well as the inward pointing IF flux. With the lysis of necrotic cells, increasingly more fluid comes from the core and less from the surrounding tissue. The growth pressure weakens. At the maximum size, the tumour is in a steady state; the fluid flux from necrotic cells equals the fluid absorbed by proliferating tumour cells [120]. This kind of treadmill effect within harsh conditions might accelerate both the mutation rate and evolutionary selection.
For tissue explants and cancer tissues, collective necrotic swelling over hours and

[9] Retention of Na^{2+} might also explain the hyperchloraemic acidosis after therapy with unbalanced 0.9% saline in the clinical practice [114].

subsequent slow shrinking over weeks[10] might follow sudden energy shut down and thus ion pump outage [122]. Necrotic swelling might impact the viscous response as both cells and GaG compete for IF.

2.5.5 Vasculature influences the body-fluid distribution

A cardiovascular system is required to ensure oxygen supply. The fluid and substance exchange between vasculature and tissue does not follow the classical Starling equation and depends instead on the filtration through the glycocalyx at the luminal side of the blood vessel endothelium [113, 115, 116]. The excess volume seeps as IF through the tissue, enters the lymph vessel system, and comes back to the general circulation via the subclavian veins to ensure a balance of the body fluids. How easily cancer impairs the body fluid balance, has been shown in mice with spreading B16-F10 melanoma. The mice experienced 20-30 times higher lymph flow through tumour-draining lymph nodes, and lymphangiogenesis is triggered before melanoma colonise the lymph system [123]. Cancer tends to have leaky blood vessels and thus an excess of IF. One can expect that the proximal drainage system extends accordingly.

Impaired body-fluids are associated with therapy resistance

Disturbances of the body fluids lead to tissue swelling due to increased volume fractions of IF known as oedema. The solid stress of growing tumours tends to clamp lymph vessels and block the fluid drainage which results in increased IFP up to the levels of the microvascular pressure [124]. A tumour can also clamp blood vessels which reduces the tumour perfusion. Vessel impairment and high IFP are associated with accelerated tumour progression, immunosuppression, inflammation, invasion, and metastasis with reduced impact of chemo-, radio-, and immunotherapies [60]. Tumour perfusion can be improved by depleting cancer cells, fibroblasts, collagen, or hyaluronan [60].

Vasculature might be normalised to achieve controlled drug therapy

Angiogenesis is required to develop larger tumours, which inspired the invention of drugs against angiogenesis to destroy the tumour. Unfortunately, the impairment of drug delivery and susceptibility to radiotherapy are undesired consequences so that the attention moved to the normalisation of blood vessels [125]. Modelling efforts showed that tumour necrosis leads to tumour instability and fragmentation with an increased likelihood of invasive behaviour [126]. The vascular, interstitial, and lymphatic fluid dynamic in growing or shrinking tumours were already mathematically modelled. Simulation results suggest that the vasculature and interstitium must be normalised to overcome physical resistance to drugs [127]. It might be better to use drugs that normalise the vasculature to ease drug availability as well as to make the tumour compact and stable [126, 128].

[10] The paper explains that the slow shrinkage let calcium react with nuclear phosphor [122], which causes the calcification of tumours not observed in melanoma.

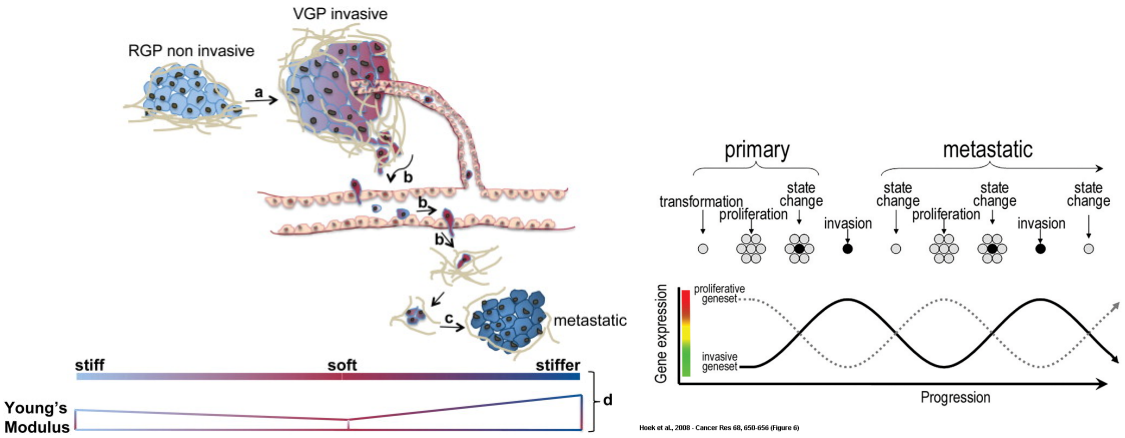

Figure 2.9: A notable hypothesis is that the elastic modulus of melanoma cells change at different progression stages [130], which fall in line with the observation that the transcriptome switches between a proliferative and an invasive phenotype [131].

Furthermore, hypoxic cancer cells make the interstitium acidic[11] and the tumour resistant to therapeutic radiation. The switch to anaerobe glycolysis releases acid lactate, and in this acidic environment, adjusted cancer cells have a survival benefit against host cells [120].

Vessels path the way for metastasis

Melanoma uses both lymphatic and blood vessels to spread [129]. In this perspective, it is interesting to investigate how the disturbance of body fluids and the consequential extension of the drainage system promote tumour growth. This section emphasised the necessity to treat the IF as an independent phase in computational models.

2.5.6 Cells adapt to overcome obstacles: the phenotype switch

Cell plasticity is another vital factor, and it seems that each melanoma stage prefers another stiffness or cell configuration. Cancer cells might adopt the plasticity that helps best overcome a particular physical obstacle [130, 133]. This has been hypothesised for melanoma to explain the shift from the radial to vertical growth phase as shown in Figure 2.9 left [130]. This seems to agree with observations *in vivo* and in gene expression suggesting an oscillating switch between invasive and proliferative stage with a corresponding change in melanocyte inducing transcription factor (MITF) expression [21, 131] as shown in Figure 2.9 right. This smooth sway between proliferative and invasive melanoma phenotypes is commonly known as phenotype switch [134]. But a periodic change in phenotype also seems to be the case for other cancer types [132] with correlating changes of other factors, as shown in Figure 2.10.
Cell adhesion and cell viscosity are decoupled cell controlled variables. The cell-specific

[11] Prodrugs, which become cytotoxic under hypoxic conditions, are more cancer specific, but the reduced oxygen partial pressure in the core is associated with a higher metabolic turnover and thus accelerated degradation of drugs [128].

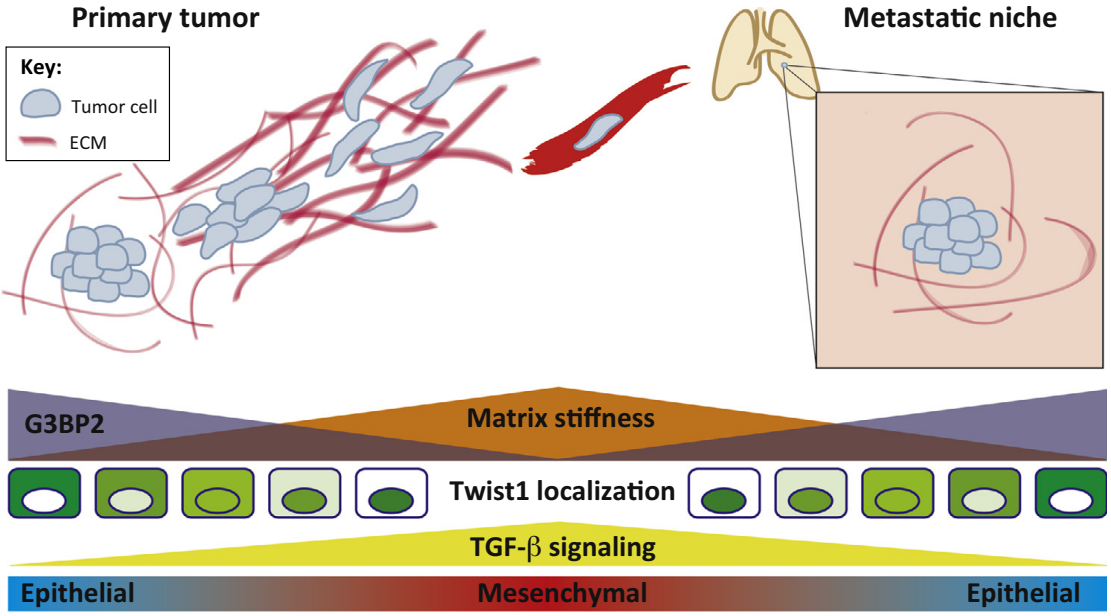

Figure 2.10: The internal change of stiffness and EMT is correlated with molecular marker and associated with different progression stages. Figure source: [132].

permeability depends on cell adhesion [135, 136] and the dynamic cell viscosity depends on the cytoskeleton state [133, 137, 138].

2.5.7 Passive and active cell migration

Invasiveness is closely connected with migration. Migration of cells can be passive or active. But only passive migration can be considered for the TCAT framework.

Active cell migration is too complex for this thesis

An experimentally validated mechanical cell model calculates the final active migration velocity of the melanoma cellline A375 based on adhesion, surface condition, or matrix anisotropy, gap size between fibres, cell contractility, and cell protrusions [139]. In addition, nucleus size, cell stiffness, and blebs influence migration [140, 141]. The migration velocity depends on several parameters [139], can use six different migration modes [140], and requires a right balance between amoeboid and mesenchymal plasticity, controlled by the mechanosensitive balance of the proteins paxillin (PXN) and transforming growth factor beta 1 induced transcript 1 (TGFB1I1)[12] [142]. As a consequence, active cell migration is out of the scope of this thesis, and implementing active migration requires an independent research work.
Because migration in confined materials differs fundamentally from migration behaviour observed on flat Petri-dishes, two-dimensional (2D)-cell culture migration data is inappropriate for the computational approach presented in this thesis.

[12] Also known as hydrogen peroxide-inducible clone-5 (Hic-5)

Passive cell migration is part of this thesis

Previous TCAT models and other cancer modelling frameworks assume increasing cell pressure when the cell density increases within the voids. The cells migrate subsequently along the declining cell pressure gradient. However, this kind of passive migration has never been observed in confined three-dimensional (3D) structures and can rather be seen as pressing out of cells if pore pressure transcends the adhesion strength threshold. The main force in the pore, to press out cells, might be the stress of the pericellular polymer network and the hydrostatic pressure of the IF. The stress might occur either via external load on the tissue, increased cellularity, or via leaky blood vessels. However, cells are not just passive objects, which react to pressure differences. Instead, cells are known to migrate toward stiffer areas with durotaxis [143, 144]. This is especially true for cancer cells who migrate on fibronectin substrate into areas of elevated stiffness where they might increase proliferative potential [145].

Another passive migration strategy works without cytoskeleton contribution and is based on the osmotic engine model (OEM) [146]. Given that the osmotic pressure gradient exists, a confined environment is present, cells are polarised, and the cell-phase allows water permeation through the cells via aquaporins, the OEM becomes relevant [146]. The water flows in the direction of increasing osmolarity, and in reverse, cells move in the opposite direction toward lower osmolarity. Cell proliferation might increase the relative polymer volume fraction within the pericellular space. This might increase the ECM solid stress and the osmotic polymer pressure. Whether such confined porous structures and this kind of osmotic pressure lead to activation of the OEM after disruption of tumour or spheroid integrity is thinkable but unknown [59, 140].

Both passive migration possibilities, pressing out cells and OEM, force cells away from the crowded areas. Because stroma stress and osmotic pressure are additive for cells, while both are compensatory for IF, IF might flow around the cells. Thus, a kind of place switch or evagination of cells might take place. Thus transport of water might not always be more likely than cell movement under local compressive stress.

II Methods

3. Computational methods

The thesis encompasses computational methods from swelling polymer physics, rheology, imaging, and tumour growth modelling.

3.1 Hydrogel and tissue rheology

In this thesis, a plate rheometer was implemented in Cast3M in cooperation with Dr. Giuseppe Sciumé as shown in Figure 3.1 and serves as possibility to determine parameters of the microstructure and physiology of tissues. The theory on the underlying rheology can be found in Appendix A.

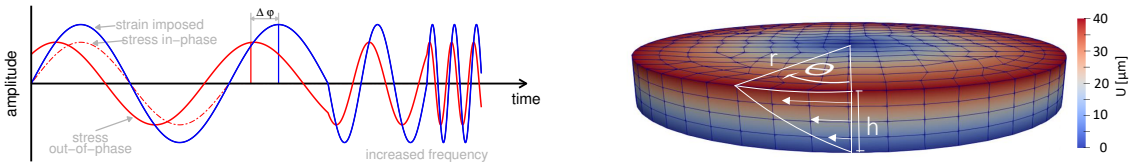

Figure 3.1: Rotational plate rheometer with imposed strain delivers sinusoidal stress-strain curves. Ideal elastic materials have stress in-phase. The stress of materials with increasing viscosity is increasingly out-of-phase with increasing phase shift $0 < \Delta\varphi < \frac{\pi}{2}$. The strain is represented by a displacement field $\mathbf{U}$ with colour code from blue for weak to red for strong displacements. The cylindrical shape with angular deflection Θ of the upper surface, radius r, and height h defines the geometry of the material to be tested.

3.2 Tumour modelling

The thesis built up on the work of Giuseppe Sciumé *et al.* [6, 50, 147, 148]. The underlying porous theory is TCAT and summarized in Appendix B.1. The derivation of a generic irregular fibrous tissue model from TCAT can be found in the Appendix B.2. The continuous modelling approach with TCAT is a very detailed representation of the growth process and differs from the mixture approach [42]. While the mixture theory assumes a homogeneous tumour fluid within a host cell fluid environment without a distinctly defined ECM. Instead of a free boundary problem at the macroscale, TCAT describes an ECM that spans the whole tissue and the healthy and the malignant cell fluids squeeze via local rules through the solid but deformable porous ECM network and share the pore space with an independent moving interstitial fluid phase. All tissue components obey their own rules for movement and have a tissue specific volume fraction, which additionally change how the tissue will behave. A visible tumour mass at the macroscale emerges due to averaging of local properties. The modelling of swelling glycans in the interstitial space is explained in the Appendix C, and potential experimental sources to initiate TCAT cancer growth models are summarised in Appendix D.

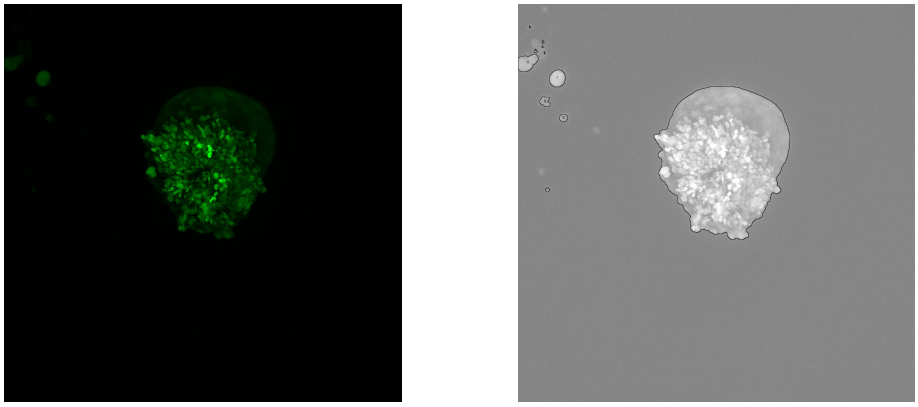

Figure 3.2: Image quantification takes the original image (left), quantifies the area and returns the control figure (right). The control figure contains the original image and the boundary of the image segmentation for a fast visual quality check.

3.3 Spheroid imaging

Spheroids were imaged with LSM 780/FCS confocal microscope and 10x magnification after 3 h and daily imaged for 9 days. Images were recorded, the z-stacks were projected into a single plane, and a colour threshold was defined to access the area as shown in Figure 3.2. Image quantification was performed with Fiji in batch process using the following custom-made code:

```
t=getTitle();
Stack.setChannel(2)
run("Delete Slice", "delete=channel");
run("Z Project...", "projection=[Max Intensity]");
run("16-bit");
run("Green");
run("Gamma...", "value=0.50");
close("\\Others")
run("Enhance Contrast", "saturated=0.35");
run("Apply LUT", "slice");
run("8-bit");
run("Duplicate...", " ");
run("Smooth", "slice");
run("Smooth", "slice");
run("Smooth", "slice");
run("Smooth", "slice");
setAutoThreshold("Intermodes dark");
run("Convert to Mask");
run("Analyze Particles...", "size=2-Infinity show=Outlines clear include summarize");
run("Images to Stack", "name=Stack title")
run("Next Slice [>]");
run("Delete Slice");
run("Z Project...", "projection=[Sum Slices]");
rename(t);
saveAs("Jpeg", "E:\\ResultImageQuant\\");
```

4. Experimental methods

4.1 Preparing dextran hydrogels

Cellendes' slow gelling 3D Life Dextran hydrogel was prepared to achieve a degradable and a not degradable gel type with four different stiffness values. The different stiffness values represent different tissue environments or different degrees of tumour growth induced environmental stiffening. The dextran polymer is a fluid solution until contact with crosslinking molecules induces the solidification. The 3D Life Biomimetic Hydrogel System from Cellendes was prepered with increasing concentration of thiol-reactive dextran polymer (2 µL, 4 µL, 6 µL, and 8 µL dextran solution for 30 µL final gel) to mimic different stiff matrices. The dextran polymer was cross-linked with either non-degradable polyethylene glycol (PEG) or cell degradable polyethylene glycol peptide conjugate (CD), which is sensitive to metallo-matrix proteases (MMP1, MMP3, MMP7 and MMP9). The gel was functionalized with fibronectin solution from

Table 4.1: Pipette scheme for Cellendes' dextran hydrogel with fibronectin coating. The increased polymer and cross-linker concentration increases the related shear modulus G' determined with a rheometer.

CD: G'($\omega = 1$ rad/s)	0.5	2.6	3.9	4.6	kPa
PEG: G'($\omega = 1$ rad/s)	0.4	1.3	2.0	3.0	kPa
Water	33.1	23.9	12.7	1.6	μL
10xCB PH 7.2	5.4	5.6	5.6	5.6	μL
Thiol-reactive polymer	4.5	8.9	13.4	17.9	μL
Fibronectin solution	4.0	4.0	4.0	4.0	μL
RPMI	13.4	11.2	11.2	11.2	μL
CD or PEG Link	6.7	13.4	20.1	26.8	μL

human fibroblasts (0.5mg/mL,1.8 µL per gel drop, Sigma) and prepared with Roswell Park Memorial Institute (RPMI)1640 medium + GlutaMax supplemented with 10% fetal bovine serum (FBS) and 1% penicillin/streptomycin. 25 µL pre-gel solution had been prepared on each glass bottom dish before the spheroid with 5 µL media was injected. After gelatinisation, 2 mL media with penicillin and streptomycin were added and glass bottom dishes were incubated at 37 $^{\circ}\mathrm{C}$.

4.2 Experimental rheometry of hydrogels

For the mechanical analysis, 67 µl gel solution was injected between hydrophobic glass slices (9 mm diameter, Sigmacode) and polymerised for 60 min at room temperature. Glass cover has been removed. Gel discs were swollen to equilibrium overnight in medium and subsequently punched out with an 8 mm biopsy puncher. Gel discs had a height of 0.774-1.260 mm and were subjected to a frequency sweep test over a range of 0.01 to 100 rad/s at room temperature with an applied rotational strain of 5% and a compression strain of 10% on an Ares LN2 rheometer (TA Instruments) with an 8 mm parallel plate geometry.

4.3 Cell line

The established metastatic $\mathrm{BRAF}^{\mathrm{V600E}}$ melanoma cellline LU451 is used in this thesis and has been derived from lymph nodes of a 22 years old male.The green fluorescent protein (GFP) positive melanoma cellline LU451 was cultured in RPMI media with 10 % (v/v) FBS.

4.4 Preparing spheroids

Spheroids are generated by pipetting 25 µL cell suspension drops on a Petri dish lit. The cell suspension contained 250 cells per 25 µL media with 20% (v/v) methylcellulose solution. The spheroids grew in hanging drops over 18 mL 1x phosphate-buffered saline (PBS) for 7 days. Cells were feeded at day 4 and 6 with 10 µL media per drop.

4.5 Spheroids in hydrogel

To understand how tumours grow, cell lines were formed to spheroids and then injected into hydrogels of known rigidity. An imaging procedure accessed then the spheroid size. Spheroids were imaged with LSM 780/FCS confocal microscope and 10x magnification after 3 h and daily imaged for 9 days.

4.6 Western Blot

Harvested cells were lysed in IP lysis buffer (50 mM Hepes pH 7.5, 150 mM NaCl, 10% glycerol, 1% triton-X-100, 1.5 mM $\mathrm{MgCl_2}$, 1 mM egtazic acid (EGTA), complete

protease inhibitor cocktail (Sigma Aldrich), PhoSTOP (Sigma Aldrich)). The bovine serum albumin (BSA) test was used for protein quantification (Pierce BCA Protein Assay Kit, Thermo Scientific, USA). Protein solution was mixed with 2x Laemmli buffer (125 mM Tris/HCl pH 6.8, 4% sodium dodecyl sulfate (SDS), 10% glycerol, 0.02% bromphenol blue), sonificated and kept at 95 $^{\circ}\mathrm{C}$ for 10 minutes. LU451 and HeLa protein solution run on Criterion TGX 8-16% gels (BioRAd, USA) with 150 V for 45 min. The protein transfer form gel to TransBlot Turbo nitrocellulose membrane (BioRad, USA) was made with TurboBlot for 7 min. Subsequently, 0.5 % blocking reagent (Roche, Switzerland) was used for 1 h at room temperature. Membranes were incubated with each primary antibodies at 4 $^{\circ}\mathrm{C}$ for at least 10 h. Utilized antibodies were tailored to following targets: MAPK1 (1:1000, Cell signalling) and glyceraldehyde 3-phosphate dehydrogenase (GAPDH). Antibodies are separately listed in Table 4.2. Membranes were washed after each antibody application with tris-buffered saline + polysorbate 20 (TBST)[1] 3 times for 10 min and incubated with anti-mouse or anti-rabbit secondary antibodies (1:5000). Membranes were activated with Super Signal West Dura chemiluminescent substrate and read with Fuji LAS 4000 CCD system. ImageQuant TL software was used for densitometry.

Table 4.2: Antibody overview

target protein	manufactorer	ID	dilution	type	protein size
MAPK1	Cell signaling	9102S	1:1000	Rabbit	42/44 kDa
pMAPK1	Cell signaling	4376S	1:1000	Rabbit	42/44 kDa
GAPDH	Cell signaling	2118L	1:2500	Rabbit	36 kDa

[1] Polysorbate 20 is also known as Tween 20

II Results

5. Existing melanoma models reviewed

Having an overview of models for a particular disease is helpful to see where models are still missing and which kind of models are already in place. The **review paper** "Systems Biology Approaches and Computational Models for Cutaneous Melanoma" was submitted to *Theoretical Biology and Medical Modelling* with the authors Marco Albrecht, Philippe Lucarelli, Dagmar Kulms, and Thomas Sauter.

5.1 Abstract

Genes, proteins, or cells influence each other and consequently create patterns, which can be increasingly better observed by experimental biology and medicine. Thereby, descriptive methods of statistics and bioinformatics sharpen and structure our perception. However, additionally considering the interconnectivity between biological elements promise a deeper and more coherent understanding of melanoma. For instance, integrative network-based tools and well-grounded inductive research *in silico* reveal disease mechanisms, stratify patients, and support treatment individualisation. This review gives an overview of different modelling techniques beyond statistics, shows how the approaches relate to each other, and identifies possible areas of new computational melanoma research.

5.2 Introduction

Melanoma is a neoplasm of the skin and originates from transformed melanocytes. It causes the loss of 1.6 million disease-adjusted life-years worldwide, and the incidence rate will increase in the next decades [149]. After the discovery of the high prevalence of

BRAF and NRAS mutations in melanoma [150, 151], small-molecule inhibitors such as dabrafenib and vemurafenib were developed to target the downstream MAPK pathway specifically. More recently, immunotherapies, with antibodies directed against oncogenes or immune receptors like the cytotoxic T-lymphocyte associated protein 4 (CTLA4) or the programmed cell death 1 (PDCD1)[1], have proven clinically effective [152]. The two-year survival rate is 53.5% for combined BRAF + MAP2K inhibitors and 63% for combined CTLA4 + PDCD1 immunotherapy [153]. For both targeted therapy and immunotherapy, a comprehensive list of resistance mechanisms has been revealed [154–156]. The biochemical pathways can shift to alternative ways, and the stromal environment causes non-genetic phenotype switches between proliferative and mesenchymal stages [131, 157]. Consequently, increasing interest emerges in targeting [158] and modelling [6] the stroma. Environmental tumour-associated fibroblasts are suspected of playing thereby an essential role in melanoma progression [159].

The review is structured as follows. Melanoma-specific databases are briefly mentioned in section one, and network-based approaches are explained in section two. The complex interaction between molecular players requires network-based approaches to suggest novel key intervention strategies, to stratify patients, and to individualise patient treatment. In the next step, the interplay of different melanoma cell types with immune cells and fibroblasts is reviewed. These methods enable therapy individualisation and patient stratification. Melanoma in a confined, spatial, and physiological tissue environment is topic in section four and is relevant for tumour growth prognosis, drug delivery, surgery, and dermoscopic pattern recognition. All available computational melanoma models are listed in Supplemental Table 1 and organised as shown in Figure 5.1.

In this review, we tried to gather all published computational models of melanoma and describe them along with their contribution to the field. Even when they seem simplistic, they often represent technically difficult stepping-stones for more biologically meaningful models in the future.

5.3 Tools and repositories

Published knowledge in the form of structured and centralised searchable databases facilitates model development. Beside general sources for System Biologists [160], melanoma-specific databases are available (Table 5.1). The Melanoma Molecular Map Project (MMMP) is an open-access, participative project that structures published knowledge about molecules, genes, and pathways to enable translational perspectives [161]. The MelGene project provides an easily searchable database of genetic association studies of cutaneous melanoma, as well as a meta-analysis for many polymorphisms [162]. The MelanomaDB database lists published genomic datasets including clinical and molecular information and allows the creation of gene lists from the merging of selected studies [163]. The Melanoma Gene Database (MGDB) provides

[1] Also known as PD1

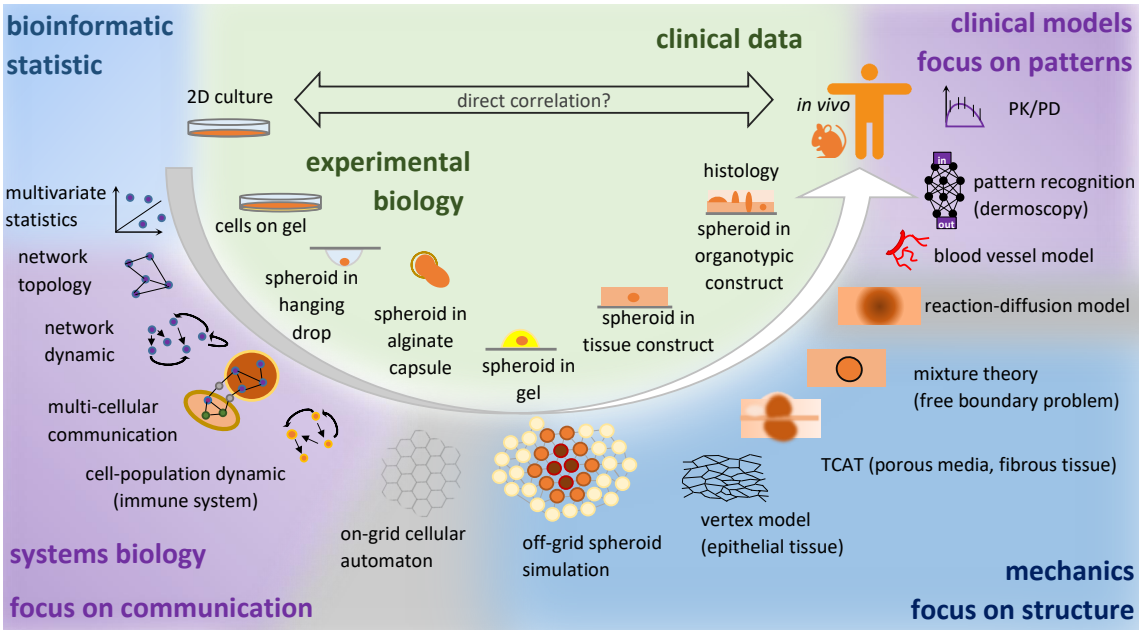

Figure 5.1: Computational and experimental approaches to understand cancer. Experimental approaches span from 2D cell culture to complex cell culture and clinical data. Computational models change accordingly in scale and approach. Methods are classified counter-clockwise beginning at the top left corner. Descriptive methods of statistics and bioinformatics focus on the identification of single features. Systems Biology increasingly connects different elements and focuses on dynamic effects and networks. If these interconnections are spatially distributed, on-grid and off-grid cellular automatons, vertex models, and reaction-diffusion models become relevant. Deformed tissue structures and anatomical obstacles require increasing integration of mechanical information. The more the approaches move from cell data to clinical images, the more pattern recognition becomes relevant. The upper half of the figure pronounce the statistical significance; the bottom half of the figure shows models, which pronounce the importance of physical and mechanistic dependencies. In conclusion, a direct correlation between *in vitro* and *in vivo* data might be straight-forward, but might be also too simplistic. The laborious indirect way with step-wise experimental and computational extension of knowledge might be harder and more expensive, but more insightful in the long term.

Table 5.1: Data bases that contain melanoma data.

Databases	Information	Last update	Source
Melanoma Molecular Map Project	Information about single molecules molecular profiles and molecular pathways involved in melanoma progression	2015	[161]
MelGene	83,343 CM cases and 187,809 controls and reported on 1,114 polymorphisms in 280 different genes	2016	[162, 165]
MelanomaDB	Published melanoma genomic datasets including clinical and molecular information	20 May 2013	[163]
Melanoma Gene Database	Relationship between melanoma protein-coding genes, microRNAs and lncRNAs	02 Nov 2016	[166]

extensive entries about 527 genes (422 protein-coding) showing association with melanoma, including epigenetic and drug-related evidence. Attention is required when using these databases, which agglomerate data from multiple sources, sometimes in an automated manner, and are thus susceptible to perpetuating the biases and errors of the data source [164].

5.4 Molecular networks and pathway modules

Molecular networks represent larger sets of molecules in an interconnected manner, which goes beyond the statistical significance of single features and the gene-set enrichment analysis paradigm [167]. Network science shows how biological functions emerge from the interactions between the components of living systems and how these emergent properties enable and constrain the behaviour of those components [168]. In order to explore this rich information source, System Biology provides different computational frameworks which are adjusted to the characteristics of genomic, transcriptomic, proteomic, and metabolomic data. Melanoma-specific -omics data can be obtained from genomic [169, 170] and proteomic studies [171] but also from the secretome [172] or the metabolome [173, 174]. Multiple -omics data are rarely integrated with a systems-centered approach [175] so that the following studies are only a beginning. We present melanoma-specific modelling studies across the omics-data types and begin with an approach based on genomic data.

5.4.1 Models for melanoma genomics

The mutation pattern in the genome of metastatic melanoma can be used to find mutually exclusive gene modules [176]. If two proteins are related in an interaction network and their genes are mutated in a way that one gets amplified while the other gets deleted or only one gets modified without the other, one could presume that this happens to intensify cancer pathways on the protein level under given evolutionary pressure. Consequently, one can conclude whether a protein inhibits or activates the other in a known interaction network. The evolutionary pressure on cancer protein pathways select mutation patterns with survival benefit. One analysis of The Cancer Genome Atlas (TCGA) melanoma samples integrates somatic mutations with copy number alterations and found concerted

deregulation of the G-protein and MAPK signalling pathways [177]. Similarly, integrated genomic and epigenomic analyses have been used to classify melanoma brain metastases in different mutually exclusive molecular subtypes [178].

5.4.2 Models for melanoma transcriptomics

The melanoma transcriptome is more context-specific than the genome and easier to measure than the proteome. The pattern changes can be used to stratify patients or to identify drug targets. But it can also give an impression of the re-wiring of pathways. Barter *et al.* applied three different strategies (single genes, gene sets, and network analysis) to 47 melanoma microarray datasets. They concluded that network methods do not perform better overall, that these different approaches tend to classify patients not consistently, and that the optimal method might have to be identified patient-specifically [179]. Wang *et al.* performed 45 siRNA screens of the A375 cellline, whole-genome sequencing, and Bayesian gene network interference to enable directional and synergenic conclusions. Similar to Barter's findings, the network hubs alone were not sufficient to stratify patients better. However, if the network hubs are contextualised with cell-cycle and DNA-repair function, the prediction of an individual prognosis is possible [180]. The concept of pathway re-wiring bases on the following reasoning. Some mutations can cause modified protein structures, which in turn can alter the links between the proteins without a change in protein concentration levels. Two proteins are interacting if the protein level change of one protein correlates or anti-correlates with the level change of another protein. When this co-expression gets lost, the connection gets lost, and the connectivity reduces. When two unrelated proteins show a new co-expression in the next progression stage, the connectivity increases and a pathway re-wiring can be assumed. This network analysis can be performed independent of significantly changed differential expression and fold changes. Kaushik *et al.* followed this strategy and meta-analysed 632 melanoma microarray samples with melanoma progression stages: normal skin, non-metastatic (radial and vertical growth phase), metastatic, and lymph node metastases [181]. They diversified the clinical relevant groups by pooling the data of tissue samples with untreated and cisplatin-treated melanoma celllines and melanocytes. The extracted re-wired pathway hubs were subsequently checked for drugability.

5.4.3 Models for melanoma proteomics

The proteome directly mirrors cellular function. Genomic and transcriptomic data do not show the post-transcriptional, translational, and further epigenetic changes which the proteom passed and are thus limited in their representation of the final physical processes. Proteomic data is, *e.g.*, very beneficial for modelling the signal transduction such as MAPK or PIK3CA pathway [182]. In the context of melanoma, most studies aim either at understanding resistance mechanisms or the responses to particular compounds. For example, it was possible to predict with high accuracy the apoptosis susceptibility of 11 melanoma celllines to TRAIL and dacarbazine (DTIC) using 17 protein measurements.

This was achieved by grouping the measurements in pathway-inspired functional groups and using these in the multivariate statistical analysis [183]. Resistance in melanoma celllines was studied with data-driven modelling and multivariate statistics. 21 phosphoproteins were measured over time in a panel of 10 celllines subjected to different doses of five different RAF/MAP2K inhibitors [184]. This led to the identification of an early down-regulation of the mitogen-activated protein kinase 8 (MAPK8)[2]/jun proto-oncogene, AP-1 transcription factor subunit (JUN) pathway upon RAF/MAP2K inhibition, but an up-regulation in six celllines at later time points. This study showed that a fraction of treated cells become quiescent and apoptosis-resistant. The same group further validated these results and suggested targeting MAPK8, protein tyrosine kinase 2 (PTK2), or SRC proto-oncogene, non-receptor tyrosine kinase (SRC) to inhibit this particular drug-resistant phenotype [185]. Bernardo-Faura *et al.* used Fuzzy Logic to investigate the temporal network re-wiring in A375 cells in response to different kinase inhibitors. The authors used a prior-knowledge network to simulate the behaviour of the cells over time, and detect discrepancies at specific time-points between the model predictions and the measurements. This work, as well, underlines the importance of the MAPK8 pathway in early drug-induced changes in signalling pathways [186]. Another comprehensive study studied the impact of MYC proto-oncogene, bHLH transcription factor (MYC) on the proteome and drug resistance, which lead to the identification of a co-targeting strategy [187]. Especially this paper raised some interest. However, the interactions with the environment, the restriction to only one cellline, and the limited appropriateness of the used drugs for clinical purposes show that it is still a long way to support physicians in decision-making [188].

5.4.4 Models for melanoma metabolomics

The metabolic state is the consequence of proteomic function and environmental conditions such as nutrient and oxygen shortages. Metabolite concentrations can be obtained with robust measurements, and well-established methods are available (Antoniewicz, 2015). Notably, Scott *et al.* used metabolic flux analysis to characterise the response of seven melanoma celllines to hypoxia [189]. They showed the crucial roles of both Warburg and Pasteur effects in melanoma and paved the way for the therapeutic targeting of metabolism. To date, studies in which the metabolism is integrated with other omics-data do not exist for melanoma.

5.4.5 Mechanistic network models for melanoma

Validated mechanistic network models of melanoma do not exist yet, but a valid Boolean model of melanogenesis covers both keratinocyte and melanocyte signalling. Lee *et al.*, thereby, imposed increasing ultraviolet B (UVB) light intensity and modelled the cellular response to it. The simulated profiles of the protein levels were individually compared to

[2]Also known as c-Jun N-terminal kinases JNK

literature to check qualitative plausibility. Lee *et al.* demonstrated the central role of CTNNB1 in the regulation of both melanogenesis and apoptosis. This prediction was then validated using UVB-exposed reconstituted human skin equivalents [190]. Moreover, a system of ordinary differential equations (ODE) was used to model the MAPK, PIK3CA/AKT1, and other pathways with in total 48 species and 48 biochemical reactions [191]. The model was an extension of the model of PC-12 (rat adrenal gland) cells from Brown *et al.* [192]. The model shows that increasing dabrafenib concentrations cause declining pERK concentration but in unphysiological ranges. Future ODE-based modelling of melanoma signalling would ideally improve the balance between model size and melanoma-specific data (Akaike information criterion) to enable robust predictions. Sensitivity analyses and model selection procedure might help to suggest key mechanisms and intervention strategies.

Network information can be used to stratify patients, to find drugable targets, and to understand the impact of therapy on the biochemical pathways. The next section describes models to inter-connect cells instead of molecules. Cell population models are used to find coherencies between cell culture and clinical patient populations or to understand the immune system on the whole-body level.

5.5 Cell population models: bridging cell culture to clinics

Melanoma cells are not isolated entities and interact with keratinocytes, fibroblasts, and the various cells of the immune system. Moreover, melanoma cells might be divided into subtypes or phenotypes. Population models often describe the interaction between them, *e.g.*, how the abundance of one cell population influences the abundance of another cell population. A subset of these models integrate cell culture data; another subset of these models are experimentally adjusted with human or murine *in vivo* data.

5.5.1 Melanoma models can mimic the interplay of cell types

Flach *et al.* studied the interplay of melanoma cells, stromal fibroblasts, and stromal fibronectin. It is rather a simple ODE model of spheroid growth. Free melanoma cells at the stromal interface activate fibroblasts to get mechanical support. The mechanically supported cells proliferate until they become blocked due to space limitations [193]. Several studies point to the crucial role of ECM remodelling, fibronectin, and PTK2 signalling in driving resistance to BRAF inhibitors [12, 194]. This conceptual model of Flach *et al.* has been refined, validated, and extended to BRAFi and PTK2i therapy [195]. These results allowed a deeper understanding of the role of stroma during acquired resistance and its potential role during targeted therapy in drug-resistant patients [193, 195]. The same group worked on a dynamic autophagy model with AKT1i therapy for melanoma [196]. After cell culture and clinical patient data had been integrated into the autophagy model, key stratification parameters were identified. Stratification parameter could either

accompany clinical trials or support treatment choice. Another melanoma cell population model is provided by Sun *et al.* with an excellent description of the parameter origin. The considered cell types are primary BRAFi sensitive, and BRAFi resistant, and which may or may not enter the metastatic cell state after the initiation of drug treatment. Cells grow until a maximum cell burden. The set of stochastic differential equations with 19 parameters is experimentally adjusted via circulating tumour cell DNA and melanoma cell line data. Progression-free survival is bravely set equal with the melanoma cell concentration for simplicity [197]. Future models with integrated pharmacokinetic elements might consider clinically relevant pharmacokinetic models [198].

5.5.2 Cell interplay is studied for melanoma immunology

Cell population models for the interplay of melanoma cells with immune cells are helpful as melanomas are highly immunogenic tumours [199]. This high immunogenicity is the reason for the success of therapies based on immune activation in this tumour type. Indeed, melanoma was the first cancer type for which an immune checkpoint inhibitor and an oncolytic virus were approved [200, 201]. As such, several computational models have been specially developed to study the interplay between the immune and melanoma cells. For example, several ODE systems were devised to model the tumour relationship with Th1 and Th2 helper lymphocytes [202], with natural killer cell (NK) cells in the context of interleukin 21 (IL21) therapy [203], with M1 and M2 macrophages [204], or both macrophages and helper lymphocytes [205]. Also, vaccine strategies based on dendritic cell therapy for melanoma were modelled with a multi-compartment ODE system to define adequate doses and schedules [206]. However, one drawback of these models is that the patients' intrinsic variables, key determinants in immune-related therapies, are not taken into account [207]. One study took into account the genetic signatures associated with resistance to immunotherapies, which helped the parametrisation of an ODE model and suggested co-adjuvants for successful anticancer vaccine therapies [208]. In another study, Pappalardo *et al.* implemented an on-grid cellular automaton model of melanoma, in which melanoma cells interact with macrophages, T cells, and dendritic cells in different cellular states. Pappalardo *et al.* highlighted the role of TNF receptor superfamily member 9 (TNFRSF9) for successful therapy and adjusted their model with experimental mice data of activated or resting OT1 T-cells and anti-TNFRSF9 antibodies in B16 melanoma [209]. Given the size of the model, additionally experimental data would further improve model parametrisation and robustness [210].

Cell-population models can combine clinical and cell culture data and might support the determination of individualised drug regimen based on cellular dynamics. While these models are suitable for freely acting cells, tumours are frequently restricted by the ECM and anatomical space limitations. These effects were simplified by some models mentioned above [193, 195, 209]. While the first two refer to 3D spheroid growth in collagen gel, the latter refers to tumour size in mice. Tumour growth is more complex and

will be addressed in the next section.

5.6 Spatial models for melanoma

Revealing the molecular networks within cells is an important step to develop appropriate drug combination therapies for melanoma. Cell population models are an additional way to stratify patients and to individualise the therapeutic regimen. However, the spatial tumour expansion in tissue has played a subsidiary role heretofore, and physical barriers modify the expansion rate. Consequently, the biological interactions with spatially distributed environmental factors are addressed in the following.

5.6.1 Dissecting parameters in spatial models is a challenge

Fully experimentally validated models of melanoma expansion are still limited to simple Petri dish experiments. In a series of reports, Treloar *et al.* use a lattice cellular automaton model and an experimental approach to identify different parameters of MM127 colony growth where cell motility, cell–to–cell adhesion, and cell proliferation influence the same: the expansion of the cell colony [211, 212]. These parameters were also estimated using a Bayesian framework coupled with a stochastic model of 2D melanoma growth [213]. Using melanoma and fibroblast monocultures as well as different co-culture systems, Haridas *et al.* have parametrised a partial differential equations (PDE) model of the interactions of cancer cells and fibroblasts [214]. Continuous modelling of melanoma cells under different osmotic pressures was performed with a 2D lattice model to simulate scratch assays [215]. The aim was to distinct migration/invasion between primary and metastatic cells. New vertex modelling strategies [216] and scratch assay analysis tools [217] might further improve this approach.

5.6.2 Spatial organisation of skin and confined spaces

The previously described spatial parameter determination strategy for cell-lines is especially helpful for the epidermal skin layer. However, the skin is more complex and contains also irregular fibrous tissue. The epidermal layer is separated from the lower dermis by a collagenous basement membrane [218], on which keratinocytes are generated and migrate through the epidermis up to the skin surface where they keratinise to the stratified protective barrier called *stratum corneum*. The epidermal layer is also the most common location for melanoma initiation. Residing melanocytes can become benign neoplasms and appear as innate or acquired naevi [14]. Further changes and appearing atypical cells constitute the first malignant stage: the radial growth phase. From the clinical perspective and the perspective of modelling, the basement membrane is crucial. Invasion through the basement membrane indicates the vertical growth phase, which requires surgical treatment. Pharmacological therapy is indicated for metastatic growth in secondary tissues. Within the dermis and secondary host tissues, interactions with fibroblasts occur. In contrast to the epidermis, the dermis layer is streaked with collagen

and elastin fibres synthesised by fibroblasts [219], and these ECM fibres restrict tumour expansion [59]. Using colony growth in 2D cell culture experiments does not lead to quantitative parameters for spatial models representing stromal processes. For example, migration velocity depends on the ECM fibre geometry [139], the migration process is fundamentally different in confined structures [140], and depend on the PXN and TGFB1I1 balance related to PTK2 [142]. Moreover, BRAF inhibition promotes MMP activity and cell migration in three dimensions [220]. A consequent experimental parametrisation of realistic melanoma growth models does not exist and is aggravated by the diversity of parameter origin and their mutual dependency as shown by Treloar *et al.* [211, 212].

Not only the parametrisation is challenging, but also the computational framework is tedious if the correct physiological modelling of the host tissues is required. Physical models are used to understand the progression of melanoma, the contortion of the tumour tissue, and the drug penetration of tumour tissue. Physical models are also used for surgery guidance and might give conclusions about the activity of cancer pathways in particular tumour locations in the future.

5.6.3 Impact of mechanoregulation

In three dimensions, additional factors impair drug sensitivity [12, 221] and increase or decrease tumour growth rate [222]. Mechanical melanoma models consider the growth induced deformation of the ECM rich environment. The more the proliferating mass expands, the more counterforce is generated by the connected ECM fibres. The elastic energy is conserved and geometry dependent [59]. The mechanical deformation of tissues and mechanical stress influence intracellular signalling by mechano-sensors like PTK2 [223] or YY1 associated protein 1 (YY1AP1)/tafazzin (TAZ) [224], which are discussed as drug resistance mechanism for BRAF-mutant melanoma cells [12, 185, 225] or progression marker for cutaneous and G protein subunit alpha q (GNAQ) mutant uveal melanoma [226–228]. Proximity to mechano-regulating fibroblasts can induce pathway changes to PIK3CA/MTOR and switch the phenotype of melanoma cells to the mesenchymal state [13]. Consequently, melanoma cells reduce the inherent stiffness to facilitate invasion [130, 132]. Additionally, the skin, being the primary site for cutaneous melanoma, is a mechano-sensitive organ. Skin can grow when it is stretched, and rete ridges, projections of the epidermis into the dermis, were recently suspected to form according to mechanical characteristics [219]. The skin has inspired many computational models describing dermal transport processes as well as providing a mechanical understanding of the skin's optical, functional, and structural characteristics [229].

5.6.4 Mechanical models of melanoma

Mechanical models of melanoma are build up with the mixture theory, the thermodynamically constrained averaging theory (TCAT), or the discrete ansatz with

cross-linked elastic cells.

Mixture theory

Two mixture theory models exist. One describes the skin surface, and one mimics the vertical section [230, 231]. Balois *et al.* consider interstitial fluid pressure, a mechanically optimal cell density, and friction between naevi and the surrounding. Ciarletta *et al.* represent melanoma in the radial growth phase in the ECM free epidermis as a viscous fluid sliding on a basement membrane with friction dependent growth velocity. In a second step, this friction is neglected and instead considered between the basement membrane and an additional keratinocyte representing fluid adjacent to the melanoma cells. The tumour front is a moving interface/ free boundary problem subjected to stability analysis.

TCAT theory

A TCAT model [6], however, represents a multi-phase approach, which is different from mixture theory and circumvents the free boundary problem. TCAT models do not have a defined tumour boundary at the macro-scale, but the ECM spans the whole tissue, with a higher concentration at the basement membrane. The interstitial fluid, the healthy and the malignant cells squeeze via local rules through the solid but deformable porous ECM network. Averaging of local properties causes a macroscale behaviour which resembles the distortion of the tissue and the invasion of the basement membrane. By adjusting the cancer cell plasticity but not ECM integrity, the model changes from solid to invasive growth [2].

Disordered lattice model

The discrete model [232] describes individual cells on a 2D disordered lattice. Cells are represented as spheres, which are connected via breakable springs, and mimic the extracellular matrix and cell-cell contacts. MMP activity is modelled by a higher probability of spring breaking near melanoma cells. Despite the simple mechanical and geometrical laws, the simulation results give a realistic impression. Because discrete models are more computationally demanding than continuous models, they allow only limited upscaling. However, the benefit of this single-cell modelling approach is the potential discrimination between compressive and tensile stress, which can differ strongly across the ECM biopolymer types [67] and tumour locations [59]. The model by Taloni *et al.* was validated with 2D experiments. The experiments were performed under osmotic pressure without fibronectin, the linker between mechanics and intracellular signalling.

Difficulties in determining mechanical parameters

Mechanical parameters are difficult to measure, and tissue is already complex without any malignant contortions [36]. Mechanical tissue parameters span up to 5 log steps depending on tissue moisture and experimental setting [68]. Some recent developments in experimental strategies are hardly known by experimental and computational scientist but can help improving computational models. Experimental mechano-sensors enable the

measurement of sub-molecular force transmissions [233], and fluorescent oil microdroplets allow the measurement of anisotropic stress fields in 3D tissues [234]. Tunable alginate microcapsules can be used to determine the mechanical growth-pressure of spheroids [235], and high throughput mechanical testing of cells is possible with optical deformation of cells [236]. If direct measurement of stiffness is not possible, the lamin A/C (LMNA) to lamin B1/2 (LMNB1/2) ratio serves as an appropriate biomarker [237]. The clinical imaging technology elastography gives direct access to the tissue stiffness fields and thus tumour locations in vivo [238]. Elastography can also be used for the *in vivo* staging of melanoma [239]. The integration of elastography and melanoma mechano-signalling could visualise the stiff areas where mechano-sensors influence melanoma pathways. This could facilitate the translation of these research models into clinical relevant predictive models.

5.6.5 Oxygenation of melanoma in skin and brain

Impaired oxygen and nutrient delivery cause necrotic cores, which is a widespread assumption. A necrotic core can be modelled explicitly [6] or indirectly via nutrient concentration reduction [231]. However, Thibaut Balois & Martine Ben Amar question the existence of necrotic cores in epidermal melanoma and take the atmospheric oxygen source into account [230, 240]. If oxygen came only from the dermis, the oxygen partial pressure would drop to around eight mmHg at the skin surface[3] [241]. Mild hypoxic conditions are present around the basement membrane, promoting melanocyte proliferation [242] as well as melanoma progression [243]. Interestingly, the brain, a common location for metastasised melanoma, has with 35 mmHg also a low tissue oxygen concentrations [244]. Most established melanoma celllines are cultured under atmospheric oxygen and are therefore evolutionarily adjusted to these artificial conditions. Molecular oxygen sensors for 3D settings [245] are as possible as advanced hypoxia sensors [246] to improve the validation of computational models. Oxygen consumption rates of cells can be obtained with the Seahorse technology [247] and were determined for melanocytes and melanoma celllines [248].

5.6.6 Models of melanoma-associated vascularisation

The tumour-associated vascularisation is a consequence of oxygen limitations and influenced by mechanical cues [249, 250]. Mathematical blood vessel models define an independent computational research field [251]. Notably, Welter and Rieger combined the discrete modelling of vasculature remodelling with the continuous gradients of melanoma cells, oxygen, nutrients, and drugs [252]. They used melanoma-specific data for the vasculature [253], and this excellent model is useful for blood flow and simple drug diffusion simulations. Wang *et al.* created an agent-based model with both melanoma and endothelial cells with a focus on angiogenesis. They tested the combined effect of doxorubicin chemotherapy and kinase insert domain receptor (KDR)[4] inhibition with

[3] Skin surface was sealed with paraffin oil

[4] Also known as vascular endothelial growth factor receptor 2 (VEGFR)

sunitinib [254]. It might be interesting to see a follow-up model with improved use of biological data for parameter, synergy, and validation. Dzwinel *et al.* coupled several continuous sub-models of melanoma growth to increase modelling quality and efficiency. They used a single phase continuum for growth accompanied by angiogenesis, vascular remodelling, and tumour ECM interactions. The model was embedded in a realistic skin structure environment, and the melanoma progression resembled nodular, lentigo maligna, and acral lentiginous melanoma [255]. The same group extended the model by a discrete vascularisation dynamic, which was coupled intermittently [256]. The used super-modelling approach is a theory on model synchronisation [257]. However, the connection coefficients seem untrained in comparison to other application areas, and the coupling remains weak [257]. In general, while these models provide valuable insight into the vasculature, much work is needed to ensure adequate melanoma-specific parametrisations and validations of the various models. Einar Rofstads' group provides excellent data sets on melanoma-associated vascularisation and might be considered for further modelling projects [258].

5.6.7 Drug delivery models

Blood vessels are an important route for drugs to the location of action, and pharmacokinetics is studied to determine the drug concentration in local blood plasma. However, the transport from the blood vessels or skin surface to the melanoma cells depends on the diffusion coefficient of the microanatomical structures. Drug delivery models are available for both the penetration of spherical tumours with melanin-binding antibodies for radioimmunotherapy [259] and SPACE-EGF mediated transdermal delivery of MYC siRNA [260]. The impact of biomechanics and tumour physiology on drug delivery is not considered by those models but discussed for MU89 Melanoma in mice [60, 261]. A proliferating mass makes fibrous tissue crowded and compressed. This might lead to a reduced interstitial fluid volume fraction and thus impaired drug transport. Such a phenomenon might be best modelled with the multi-phase flow in porous media [6].

5.6.8 Pattern recognition of melanoma

The pattern of naevi and melanoma *in situ* are the physical consequence of the above-described processes in the epidermis and are usually assessed and classified in dermatology. The regular differentiation between harmless naevi and potential melanomas by a dermatologist enables early therapy. The related patterns can be modelled in two dimensions using a mixture theory model [230]. The study shows how different patterns of malignant cells can form within a healthy cell environment. 2D patterns of naevi and melanoma can also be subjected to planar linear transformations using two subsequent dermoscopy pictures. Those pictures allow the classification of melanoma growth rates and naevi symmetry [262]. The ABCD criteria for melanoma have been mathematically considered too [263]. Automated optical classification of naevi and melanomas is a fast-growing field and employs machine learning methods for the image

recognition. The sensitivity and specificity of these models are comparable with the decisions of dermatologists [264–266]. Specific features in 2D dermoscopy pictures can also be used to determine the Breslow depth with specificity and sensitivity of almost 100%, which has direct prognostic value [267]. The depth of invasion is an important prognostic marker for patient survival, and the Breslow index can be determined manually or automatically from histopathological images [265, 268].

5.6.9 Models of surgical treatment

Surgical treatment is the consequence of early identified melanomas. Wide excision of primary melanoma can have counter-intuitive ramifications according to the reaction-diffusion model of Eikenberry *et al.* The surgical resection of primary melanomas might include tumour-associated immune cells, which lead to an accelerated outgrowth of local metastasis due to reduced immune suppression [269]. Computational models are also used to assist image-guided and computer-assisted surgery mainly for the brain [270]. The brain, besides lung and lymph nodes, is a preferred host tissue for metastatic melanoma [14].

Spatially resolved models can give us further insight into surgical interventions and drug delivery but also about the interactions between melanoma cells and stroma. Tissues can promote and constrain tumour progression via the extracellular matrix or the blood vessel system. The modelling of the tumour microenvironment has to consider additional factors like extracellular matrix stiffness and topography, interstitial fluid pressure, oxygen and nutrients gradients [271]. How difficult the parameter determination can be, has been shown with the colony growth [212] and with the section on mechanical cues. Parameters are crucial to have a falsifiable test hypothesis for model selection. Only in this way, a deeper understanding of the complex relationships can be achieved. Unfortunately, many publications work with uncurated parameter lists, and interested readers are recommended to trace back parameter values to the original source to judge the validity. At the moment, the field of physical oncology is still in transition. Modellers focus on computational frameworks creating patterns which are qualitatively comparable with *in vivo* observations. A more sophisticated way might be the stepwise model development accompanied by advanced cell culture strategies as suggested by Figure 5.1. 3D cell culture techniques from spheroids to organotypic skin reconstructs are briefly presented in the next section.

5.7 Spatial melanoma models need specific experiments

Although modelling promises to become more and more prominent in melanoma research, and continuous improvements in computational power make more complex and realistic models accessible, experimentally validated parametrisation remains a crucial bottleneck. To produce high-quality mathematical models, quantitative data under standardised operating procedures are required [272, 273]. Tumour spheres and spheroids in general [274], and organotypic *in vitro* models for melanoma [275] in

particular offer more realistic experimental conditions. Fully functional organotypic skin constructs [276] can mimic all melanoma progression stages. 3D constructs are not just a carrier of cells; they modify the experimental outcome. Thus a quantification of the hydrogel system parameter, such as the shear or Young's modulus becomes standard. The shear modulus G or the roughly three times higher Young's modulus E of the gel system is stated with the unit kPa (E=2G(1+υ); υ: Poisson's ratio) [12, 223, 277]. For example, the often used matrigel for invasion assays is with the elastic modulus of 0.45 kPa a weaker obstacle than the basement membrane with 250-500 kPa [20, 81]. Additionally, the impact of stress relaxation should be not underestimated [77]. A range of hydrogel systems is available [278] and can also be used for automated drug testing [279] albeit questions of standardisation of 3D cell culture models remain [280]. The complexity of tumour cell environment interactions requires a step-wise understanding with a multitude of experimental techniques [281] and related computational efforts. Computational scientists must incorporate the experimental context to develop meaningful computational melanoma progression models.

5.8 Discussion

Cancer is a highly complex, heterogeneous disease, characterized by a series of genetic, metabolic, and functional changes at both the cell and tissue levels [282], and melanoma-specific dynamics along tumour progression stages in both plasticity [130] and genetics [283] highlight the need for integrative models to understand disease mechanisms of melanoma better. Computational tools are needed to make large data sets more consistent and accessible to cancer researchers [7] and are required to integrate existing knowledge. The model-building community works across different scales and comprises studies centred on signalling pathways and gene regulation [160], metabolism [284, 285], epithelial tissue mechanics [286], tumour physiology [287], or the immune system [288].

Mathematical modelling of melanoma presents several specificities. The high mutation load, signalling network plasticity, and cellline heterogeneity make the fitting of mechanistic ODE systems or straightforward network inference from patients biopsies difficult. Instead, most studies focus on well-characterised cellline collections to carefully extract specific regulatory network motifs with multivariate statistics. In the future, the integration of genomic information with gene expression, metabolomics, and tumour mechanics might improve our understanding of melanoma progression and resistance acquisition. By relating molecular characteristics of celllines with their functional properties, mathematical network models hold the potential to advance personalised oncology. These models require close collaboration between experimental, clinical, and computational scientists in an iterative procedure. Modelling generates hypotheses, which can be tested in vitro, and experimental results inform the design of better models and allow the falsification of theories [289].

A general problem in the interdisciplinary work in biology and medicine is that the more

demanding the necessary mathematical and physical framework become, the more disconnected it becomes from the experimental and theoretical knowledge in biology, medicine, and pharmacology. The gap between the different disciplines is not closed yet, which leads to both conceptual problems in the models and inappropriate parameter choices. Context and tissue-specific modelling of melanoma would be more helpful than the usual generic cancer growth models with unclear parameter sources. The unique oxygen patterns in skin [240, 241], the tendency of melanocytes to proliferate better in mild hypoxic conditions [242], and the strong oxygen consumption of melanoma cells [248] found a rare propagation in the modelling community, which too often copies concepts and parameters from other cancer types.

Moreover, better quality standards in both biomedical [290] and computational [291] research need to be developed and adopted. On the one hand, computational groups cannot reproduce and test the diverse parameter sources in their own labs, lacking the time and expertise to embrace the whole complexity of biological relationships and experimental methods, and on the other hand, biologists and clinicians find it difficult to help, as the more developed computational procedures are likewise difficult to apply successfully.

The creation of a mechanistic and predictive model is a serious and work-intensive endeavour that forces all participants to think deeper [168]. Ultimately, the reward is more aim-tailored research but also the discovery of hidden causalities, which would otherwise have rendered explorative research inconclusive or contradictory. Recent progress in devising experimental procedures for parameter determination have fueled the work of several computational groups, and the understanding of non-cell autonomous and non-genetic resistance mechanisms [157] emphasise the importance of complex *in vitro* models for the parametrisation of computational counterparts. In particular, biomechanics is now recognised as a central pillar of our understanding of tumour progression and metastasis. However, our knowledge of mechanosensitive pathways is far from complete [132, 277, 292, 293]. The future promises us an unmatched insight if all disciplines improve the inter-disciplinary collaboration.

6. TCAT mimics the phenotype switch

The following **original paper** shows the ability of a TCAT cancer growth model to switch between invasive and nodular growth. This ability of the model is essential because melanoma conducts phenotype switches with accompanied high plasticity in the cellular stiffness. The paper was published very early in the PhD project period and can be found with the reference:
Marco Albrecht, Giuseppe Sciumè, Philippe Lucarelli, and Thomas Sauter. "Thermodynamically constrained averaging theory for cancer growth modelling." IFAC-PapersOnLine 49, no. 26 (2016): 289-294.
The subsequent text was heavily edited after publication to make it readable. However, the poor language makes the original publication hard to understand, and also the following text does not reflect the improved quality, which has been achieved towards the end of the training period.

6.1 Abstract

Biochemical network models are often used to describe intracellular mechanisms at the cellular level. The obtained results are difficult to translate into three dimensional biological systems. The multiplicity and time dependency of mechanical phenomena and spatial concentration gradients affect the intercellular biochemical networks. These environmental effects can be integrated with our promising cancer modelling environment, which is based on the thermodynamically constrained averaging theory (TCAT). Especially, the TCAT parameter viscosity can be used as a critical player in tumour evolution. Strong cell-cell contacts and a high degree of differentiation make cancer cells viscous, support compact tumour growth, increase tumour cell density, and displace the extracellular material. In

contrast, dedifferentiation and cell-cell contact unbinding make cancer cells more fluid and lead to an infiltrating tumour growth behaviour without resistance by the ECM. The fast-expanding tumour front of the invasive type consumes oxygen. The limited oxygen availability behind the invasive front results surprisingly in a lower tumour cell density in the tumour core. The proposed modelling technique is most suitable for tumour growth phenomena in irregular fibrous tissue.

6.2 Introduction

The biological field experiences an enormous boost in mathematical and quantitative methods within the last decades. Systems biology has emerged in the interface of molecular biology, mathematics, informatics, and engineering. Besides this movement, physical oncology has been developed by clinicians, mathematicians, and civil engineers [294]. These interdisciplinary fields coalesce.

The mechanical properties of cancer are more and more related to biochemical counterparts during the last five years [295]. Tensile and compressive stress within the tumour arise upon expansion of the tumour mass [60], and cells sense these mechanical cues [296]. Some cancer cells responded to elevated extracellular matrix stiffening with the reinforcement of their cytoskeleton and increased actin-myosin contractility [297]. This facilitates squeezing through the endothelium of blood vessels - a step toward the metastatic aggressive cancer type [298]. The internal cell stiffness follows the stiffness of the environment, *e.g.*, via PTK2 mediated mechanotransduction. The mechanical homeostasis is thereby regulated by positive and negative feedback loops [40]. Guck *et al.* established a fluidics device that stretches cells with lasers, and he points to the softness of several cancer celllines, especially of cells with metastatic origin [299]. This soft conformation might help cells squeezing through the tight and small channels within the ECM. The stiffness of the melanoma cells changes along the different progression [130]. The phenotype switch finds its equivalent in the transcriptomic pattern. The melanoma cell state oscillates between a proliferative but non-invasive and a non-proliferative and invasive phenotype, controlled by the differentiation marker MITF [131]. Consequently, melanoma might always switch to the optimal mechanical invasion strategy to circumvent anatomical obstacles.

Understanding the optimal mechanical environment might improve the therapeutic regimen as stiff environments make cancer cells resistant [12]. Chemotherapy removes the poorly adjusted cancer cells first, but resistant cancer clones often remain [300]. These evolutionarily selected cells can take up space, which results in a more aggressively growing cancer. Limiting the available space for tumour growth with cytostatics might turn cancer into a chronic disease as an alternative. To better analyse these findings, a mathematical model might be helpful to understand the mechanical feedback and the concentration gradients to minimise the risk and to maximise the therapy success.

In this paper, we demonstrate the benefits of using TCAT as a base for cancer modelling. After briefly summarising the TCAT framework, it will be demonstrated how the tumour cell parameter viscosity can be used to switch between the invasive and the non-invasive tumour type. The model could integrate network models of biochemical signalling pathways according to the paradigms in systems biology. Cellular mechanosensors are therefore considered. Moreover, cellular functions are discussed when they modify the mechanical state of tissues.

6.3 Thermodynamically constrained averaging theory

The TCAT is explained to understand the roots of the framework. Porous media, in which multiphase flows occur, is common in geology, hydrology, petroleum engineering, and technology. Gases and immiscible liquids flow faster than the solid bulk material or stone. Usually, Darcy's law is applied. But this is a formulation on the macroscale only. Several microscale phenomena like wettability have a significant impact on the macroscale but are not mathematically considered [42]. These inconsistencies are frequently bridged with pure mathematical constructs without physical relations. The TCAT, as developed by [51], is a rigorous methodology to interconnect conservation equations across different length scales. Conservation equations of phases, interphases, common curves, and common points are represented in material derivative form and considered in the entropy inequality equation. The entropy inequality is then maximised in a Lagrangian framework and thereby constrained by conservation equations to obtain a constrained entropy inequality. Variational methods and force-flux pairs are used to find closure relations near equilibrium. Averaging theorems are used to transfer microscale equations to macroscale equivalents, and evolution equations account for the maintenance of geometric properties. The framework allows a straight-forward model extension and employs partial differential equations with maximum second order derivatives in time and space, while other continuous modelling techniques operate with complicated fourth order Cahn Hilliard equations, which cannot be easily extended [42].

6.4 TCAT tissue model deformed by tumour growth

Giuseppe Sciumè *et al.* applied the TCAT framework to investigate the impact of mechanical stress on diabetic foot ulceration [50] and to explain tumour growth within healthy tissues. This section summarises the latest model of melanoma growth in skin [6] with some minor modifications as detailed below.

The ECM is a protein network, secreted by the cells, which establishes a stable cell environment and can be seen as a solid porous medium. It contains tortuous interconnected gaps, whose combined volume is called porosity ϵ. The saturation degree S^α states how these pores are saturated with three immiscible liquids α. The liquids represent either interstitial fluid (IF,l), host cells (host cells phase (HC),h), or tumour cells

(tumour cells phase (TC),t). Favourable growth conditions for the tumour cells lead to TC mass expansion by converting IF to TC. The expanding TC liquid presses against the other fluids and the ECM. The ECM has a general permeability $\mathbf{k}$ for liquids, depending on the tissue characteristic. A relative permeability k_{rel}^{α} controls the movement of a cell phase in relation to the others, while IF moves last as it is more attached to the ECM (high wettability or hydrophilicity). The relationship between the fluid velocity $\mathbf{v}^{\overline{\alpha}}$ relative to the ECM scaffold velocity $\mathbf{v}^{\overline{s}}$

$$\mathbf{v}^{\overline{\alpha}} - \mathbf{v}^{\overline{s}} = \frac{k_{rel}^{\alpha}\mathbf{k}}{\mu^{\alpha} S^{\alpha}\epsilon} \cdot (-\nabla p^{\alpha}) \qquad (\alpha = h, t, l). \tag{6.1}$$

can be derived from the TCAT momentum equation. The velocity difference depends on the pressure gradient $(-\nabla p^{\alpha})$. The dynamic viscosity μ^{α} of the cell population represents their ability to be moved. This movement is inhibited by cell-cell contacts, which maintain a high cell mixture viscosity. However, if the pressure gradient becomes large enough, cell-cell contacts unbound and the viscosity gradually reduce by a factor of ten.
The tissue model can be formulated at the macroscale and is derived from TCAT mass conservation and momentum conservation equations. The five primary variables are the oxygen concentration $\omega^{\overline{ol}}$, the pressure of the IF phase p^{l}, the pressure difference between IF and HC phase p^{hl}, and the pressure between TC and HC phase p^{th}. The sum of these pressures corresponds to the tumour pressure $p^{t} = p^{l} + p^{hl} + p^{th}$. The displacement of the extracellular matrix $\mathbf{u}^{s}$ is the fifth primary variable.
The momentum balance equation of the extracellular matrix is

$$\nabla \cdot \left(\frac{\partial \mathbf{t}_{\mathsf{eff}}^{\overline{\overline{s}}}}{\partial t} - \frac{\partial p^{s}}{\partial t} \right) = 0. \tag{6.2}$$

The effective stress rate is defined as $\dot{\mathbf{t}}_{\mathsf{eff}}^{\overline{\overline{s}}} = \mathbf{D}_{s} : \dot{\mathbf{e}}_{\mathsf{el}}^{\overline{\overline{s}}} = \mathbf{D}_{s} : (\dot{\mathbf{e}}^{\overline{\overline{s}}} - \dot{\mathbf{e}}_{\mathsf{vp}}^{\overline{\overline{s}}})$, where the strain rate $\dot{\mathbf{e}}^{\overline{\overline{s}}} = \mathbf{S}\frac{\partial \mathbf{u}^{s}}{\partial t}$ is of visco-plastic (vp) and elastic (el) origin. The tangent matrix $\mathbf{D}_{s}$ represents the mechanical properties of the ECM and links the stress with the strain, whereas the tensor $\mathbf{S}$ links the strain with the displacement. The solid pressure is coupled with the proportionately considered liquid pressures $p^{s} = p^{l} + (1 - S^{l})p^{hl} + S^{t}p^{th}$. The saturation degree S^{α} within the pores are assumed to represent the Bishop parameter. The result is the pressure-strain relationship $\frac{\tilde{\alpha}}{K}\frac{\partial p^{s}}{\partial t} = \mathbf{1} : \mathbf{d}_{sp}^{\overline{\overline{s}}}$. Each liquid and solid component is not compressible but the deformation of the ECM scaffold is taken into account by bulk modulus K. The final governing ECM displacement equation

$$\nabla \cdot (\mathbf{D}_{s} : (\mathbf{S}\frac{\partial \mathbf{u}^{s}}{\partial t})) - \nabla \cdot (\mathbf{D}_{s} : \dot{\mathbf{e}}_{vp}^{\overline{\overline{s}}}) = \nabla \cdot (\mathrm{K}(1 : \dot{\mathbf{e}}_{sp}^{\overline{\overline{s}}})). \tag{6.3}$$

is based on Equation 6.2. The mass balance equation of the solid phase is integrated into the following mass balance equations of three immiscible liquids: The IF phase

$$\begin{aligned}
&\left[\frac{1}{K}(S^t + p^{th}\frac{\partial S^t}{\partial p^{th}})\right]\frac{\partial p^{th}}{\partial t} \\
&+ \left[\frac{1}{K}(1 - S^l - p^{hl}\frac{\partial S^l}{\partial p^{hl}})\right]\frac{\partial p^{hl}}{\partial t} + \left[\frac{1}{K}\right]\frac{\partial p^l}{\partial t} \\
&= \nabla\cdot\left[\frac{k^t_{rel}\mathbf{k}}{\mu^t}\cdot\nabla p^{th}\right] + \nabla\cdot\left[\left(\frac{k^t_{rel}\mathbf{k}}{\mu^t} + \frac{k^h_{rel}\mathbf{k}}{\mu^h}\right)\cdot\nabla p^{hl}\right] \\
&+ \nabla\cdot\left[\left(\frac{k^t_{rel}\mathbf{k}}{\mu^t} + \frac{k^h_{rel}\mathbf{k}}{\mu^h} + \frac{k^l_{rel}\mathbf{k}}{\mu^l}\right)\cdot\nabla p^{l}\right] \\
&- \left[\mathbf{1}:(\dot{\mathbf{e}}^{\overline{\overline{s}}} - \dot{\mathbf{e}}^{\overline{\overline{s}}}_{sp})\right] + \frac{\rho^l - \rho^t}{\rho^t\rho^l}\overset{l\to t}{\mathrm{M}},
\end{aligned} \tag{6.4}$$

the host cell phase

$$\begin{aligned}
&\left[\frac{S^h}{K}(S^t + p^{th}\frac{\partial S^t}{\partial p^{th}}) - \epsilon\frac{\partial S^t}{\partial p^{th}}\right]\frac{\partial p^{th}}{\partial t} \\
&+ \left[\frac{S^h}{K}(1 - S^l - p^{hl}\frac{S^l}{p^{hl}}) - \epsilon\frac{\partial S^l}{\partial p^{hl}}\right]\frac{\partial p^{hl}}{\partial t} + \left[\frac{S^h}{K}\right]\frac{\partial p^l}{\partial t} \\
=&\nabla\cdot\left[\frac{k^h_{rel}\mathbf{k}}{\mu^h}\cdot\nabla(p^l + p^{hl})\right] - S^h\left[\mathbf{1}:(\dot{\mathbf{e}}^{\overline{\overline{s}}} - \dot{\mathbf{e}}^{\overline{\overline{s}}}_{sp})\right] - \epsilon\mathbf{v}^{\overline{s}}\nabla S^h,
\end{aligned} \tag{6.5}$$

and the tumour cell phase

$$\begin{aligned}
&\left[\frac{S^t}{K}(S^t + p^{th}\frac{\partial S^t}{\partial p^{th}}) + \epsilon\frac{\partial S^t}{\partial p^{th}}\right]\frac{\partial p^{th}}{\partial t} \\
&+ \left[\frac{S^t}{K}(1 - S^l - p^{hl}\frac{\partial S^l}{\partial p^{hl}})\right]\frac{\partial p^{hl}}{\partial t} + \left[\frac{S^t}{K}\right]\frac{\partial p^l}{\partial t} \\
=&\nabla\cdot\left[\frac{k^t_{rel}\mathbf{k}}{\mu^t}\cdot\nabla(p^l + p^{hl} + p^{th})\right] - S^t\left[\mathbf{1}:(\dot{\mathbf{e}}^{\overline{\overline{s}}} - \dot{\mathbf{e}}^{\overline{\overline{s}}}_{sp})\right] \\
&- \epsilon\mathbf{v}^{\overline{s}}\nabla S^t + \frac{1}{\rho^t}\overset{l\to t}{\mathrm{M}}.
\end{aligned} \tag{6.6}$$

The tumour cell phase can be partitioned into two miscible liquids accounting for the living tumour cell fraction $(1 - \omega^{\overline{Nt}})$ and the necrotic tumour cell fraction

$$\frac{\partial\omega^{N\bar{t}}}{\partial t} = \frac{1}{\epsilon S^t\rho^t}\left[\epsilon S^t r^{Nt} - \omega^{N\bar{t}}\underset{\text{growth}}{\overset{l\to t}{\mathrm{M}}} - \epsilon S^t\rho^t\mathbf{v}^t\cdot\nabla\omega^{N\bar{t}}\right], \tag{6.7}$$

which arises with a low oxygen mass fraction ω^{ol}. The oxygen distribution is described by the species mass conservation equation

$$\epsilon S^l\frac{\partial\omega^{ol}}{\partial t} = \nabla\cdot(\epsilon S^l D^{\overline{ol}}_0(\epsilon S^l)^\sigma\nabla\omega^{ol}) + \frac{1}{\rho^l}(\omega^{ol}\overset{l\to t}{\mathrm{M}} - \overset{ol\to t}{\mathrm{M}}) \tag{6.8}$$

with the oxygen diffusion coefficient $D_0^{\overline{ol}}$. The mass transfer from the IF phase to the TC phase $\mathrm{M}^{l\to t}$ represent tumour growth. The related oxygen species transfer $\mathrm{M}^{ol\to t}$ accounts for oxygen consumption. Cell death due to oxygen limitation is modelled as species transfer r^{Nt} between two miscible liquids. The living tumour mass is transferred to the fraction of dead tumour mass within the immiscible tumour cell phase. These three transfer terms are composed of cosine functions 6.9 to 6.12. These functions contain threshold parameters, which describe the transition zones between the minimum and and maximum tumour growth rate, oxygen consumption, and tumour cell death rates.

$$G_1(\omega^{\overline{ol}}) = \begin{cases} 0 & \text{for } 0 \le \omega^{\overline{ol}} \le \omega^{\overline{ol}}_{\text{crit}} \\ \frac{1}{2} + \frac{1}{2}\cos\left[\pi\left(1 + \frac{\omega^{\overline{ol}} - \omega^{\overline{ol}}_{\text{crit}}}{\omega^{\overline{ol}}_{\text{env}} - \omega^{\overline{ol}}_{\text{crit}}}\right)\right] & \text{for } \omega^{\overline{ol}}_{\text{crit}} \le \omega^{\overline{ol}} \le \omega^{\overline{ol}}_{\text{env}} \\ 1 & \text{for } \omega^{\overline{ol}} \ge \omega^{\overline{ol}}_{\text{env}} \end{cases} \tag{6.9}$$

$$G_2(p^t) = \begin{cases} 1 & \text{for } 0 \le p^t \le p^t_{\text{cr1}} \\ \frac{1}{2} + \frac{1}{2}\cos\left[\pi\left(1 + \frac{p^t - p^t_{\text{cr1}}}{p^t_{\text{cr2}} - p^t_{\text{cr1}}}\right)\right] & \text{for } p^t_{\text{cr1}} \le p^t \le p^t_{\text{cr2}} \\ 0 & \text{for } p^t \ge p^t_{\text{cr2}} \end{cases} \tag{6.10}$$

$$R(\omega^{\overline{ol}}) = \begin{cases} \frac{1}{2} + \frac{1}{2}\cos\left[\pi\left(1 + \frac{\omega^{\overline{ol}}}{\omega^{\overline{ol}}_{\text{crit}}}\right)\right] & \text{for } 0 \le \omega^{\overline{ol}} \le \omega^{\overline{ol}}_{\text{crit}} \\ 1 & \text{for } \omega^{\overline{ol}} \ge \omega^{\overline{ol}}_{\text{crit}} \end{cases} \tag{6.11}$$

$$N_1(\omega^{\overline{ol}}) = \begin{cases} \frac{1}{2} + \frac{1}{2}\cos\left(\frac{\omega^{\overline{ol}}}{\omega^{\overline{ol}}_{\text{crit}}}\pi\right) & \text{for } 0 \le \omega^{\overline{ol}} \le \omega^{\overline{ol}}_{\text{crit}} \\ 0 & \text{for } \omega^{\overline{ol}} \ge \omega^{\overline{ol}}_{\text{crit}} \end{cases} \tag{6.12}$$

Below the oxygen threshold $\omega^{\overline{ol}}_{\text{crit}}$, tumour cells start to become necrotic and operate on a reduced basic respiratory or metabolic turnover rate with the basic oxygen consumption rate $R(\omega^{\overline{ol}})$. Above this threshold, tumour cells start growing until they reach the maximum proliferation rate at the environmental oxygen concentration $\omega^{\overline{ol}}_{\text{env}}$. The proliferation rate is maximal if tumour pressure is below p^t_{cr1}. Above this threshold, cells have a reduced growth rate to mimic contact inhibition.

Necrosis shuts down the work of cellular ion pumps due to energy shortage [122]. Osmotic water influx let the cells swell within three hours to the doubled size before the cells lose water through a stretched and leaky cell membrane. The concentrated cytoplasm builds calcified crystals, which accumulate in the necrotic core of tumours [122]. Accordingly, the swelling can be modelled with a factor of two in the necrosis rate equation

$$\epsilon S^t r^{N^t} = 2 \cdot [\gamma^t_{\text{necrosis}} N_1(\omega^{\overline{ol}})](1 - \omega^{N\bar{t}})\epsilon S^t - \gamma^t_{\text{clear}} \omega^{N\bar{t}} \epsilon S^t. \tag{6.13}$$

Equation 6.13 contains the maximal necrosis rate $\gamma^t_{\text{necrosis}}$ and an additional term that describes cell degradation with the clearance rate γ^t_{clear}. Because this is only a transfer within the tumour phase, the tumour growth rate has to be adjusted. The necrotic swelling

arises from the IF and not from the living tumour mass $(1-\omega^{N\bar{t}})\epsilon S^t$. The mass transfer term

$$\begin{aligned}\underset{\text{growth}}{\overset{l\to t}{\mathrm{M}}} =&[\gamma^t_{\text{growth}} G_1(\omega^{\overline{ol}}) G_2(p^t)](1-\omega^{\overline{Nt}})\epsilon S^t \\ &+ [\gamma^t_{\text{necrosis}} N_1(\omega^{\overline{ol}})](1-\omega^{N\bar{t}})\epsilon S^t \\ &- \gamma^t_{\text{clear}}\omega^{N\bar{t}}\epsilon S^t \end{aligned} \tag{6.14}$$

with the maximal growth rate γ^t_{growth} can be increased by the swelling of the necrotic fraction and can be reduced by shrinkage and degradation of the necrotic material. The swelling and degradation of necrotic material are extensions of the previous model [6], while Equations 6.9 - 6.12 replace former used Heaviside step functions for a better numeric stability. The model equations are discretised in space with the Galerkin method and in time with the approach of Crank-Nicolson and the Wilson's Theta method. The equations are implemented in Cast3M (www-cast3m.cea.fr) and solved with a finite element method. The mathematical model contains two blocks: One describes pressure and diffusion with Equations 6.4, 6.5, 6.6, and 6.8; and one takes into account the solid mechanics with Equation 6.3. Both blocks are solved iteratively until convergence is reached at each single time step.

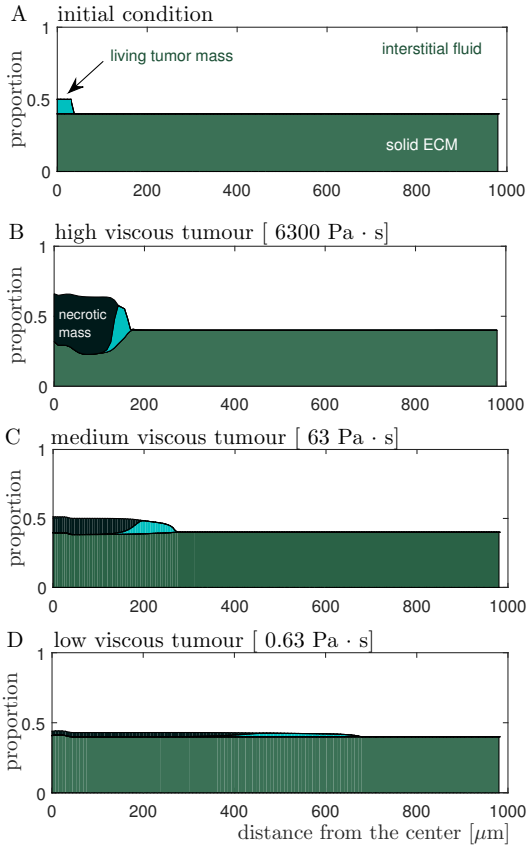

Figure 6.1: The simulation shows the volume proportions of solid ECM (dark green), IF (white), living tumour mass (cyan), and necrotic cells (black). The volumes are well mixed, and their relative change is tracked along the spheroid radius. The tumour core is at the left side, and the border of a hypothetical tissue spheroid is at the right side. **A:** Initial condition. **B-D:** Model simulation of tumour growth with high (B), medium (C) and low (D) viscosity after 31 days. The change of the viscosity is comparable with a switch between benign and malignant tumour growth.

6.5 Simulation results

A physical model of cancer growth should explain biological phenomena observed experimentally. One important experimental observation is the change from a compact growing tumour to an invasive tumour with reduced growth. In this paper, the tumour

evolution is investigated when cell-cell contacts are weakened, and intracellular stiffness is decreased. Accordingly, three different viscosities are simulated for the tumour cell phase: the high viscous tumour ($\mu^t = 6300\ \mathrm{Pa \cdot s}$), the medium viscous tumour ($\mu^{\mathrm{t}} = 63\ \mathrm{Pa \cdot s}$), and the low viscous tumour ($\mu^{\mathrm{t}} = 0.63\ \mathrm{Pa \cdot s}$).

The starting conditions are illustrated in Figure 6.1 A. An initial tumour mass (radius: 50 $\mu\mathrm{m}$) is assumed within a 3D hydrogel spheroid (radius: 1000 $\mu\mathrm{m}$). After the simulation of 31 days, three different viscosities yield three different tumour phenotypes. Exact values are listed in Table 6.1.

Table 6.1: Final results after 31 days of simulation. The space infiltrated by the tumour contains, besides the tumour cells, IF and ECM. The cytoplasm volume of all dead and living tumour cells (TC) or of all living tumour cells (LTC) is reduce with cell viscosity. The displacement of the ECM increases with viscosity.

	high viscous tumour	medium viscous tumour	low viscous tumour
Radius infiltrated $[\mu\mathrm{m}]$	199	291	695
Volume infiltrated $[\mathrm{mm}^3]$	33	103	1408
Volume of TC $[10^{-3}\mathrm{mm}^3]$	8.55	8.73	33.32
Volume of LTC $[10^{-3}\mathrm{mm}^3]$	2.86	5.31	23.67
Max displacement $[\mu\mathrm{m}]$	18.8	2.68	0.49

The high viscous tumour grows slowly, 33.5 % of the cells are alive, and the tumour has a compact form as shown in Figure 6.1 B.
The medium viscous tumour infiltrates a 46% larger radius and a 3 times bigger volume. The total tumour cell volume remains almost constant, while the fraction of living cells is with 60.8% distinctly larger. The tumour cell density is according to Figure 6.1 C smaller.
The low viscous tumour infiltrates a 3.5 times larger radius than the high viscous tumour, and it infiltrates a 42.7 times larger volume. The total tumour mass increases by a factor of 3.9. Figure 6.1 D indicates the very small tumour cell density. The low viscous tumour has the largest necrotic core, with a radius of around 400 $\mu\mathrm{m}$, and the thickest living tumour front, with 295 $\mu\mathrm{m}$. 71% of the low viscous tumour mass belongs to the living tumour cell mass.
The correlation between viscosity and tumour cell density can be explained by oxygen delivery. The oxygen profiles of all three cases are shown in Figure 6.2 A, and the profile of each case can be separated into three sections. The first section is located in the necrotic core zone, in which the oxygen mass fraction is constant at a minimum level. The second section is in the zone of the living tumour cell front. Here, the biggest change of the oxygen mass fraction is observed. The third section is the zone without tumour cells. The profile of the oxygen mass fraction in the third zone is diffusion dependent. The oxygen mass fraction increases from the invasive front to the boundary of the hydrogel spheroid, which has the fixed oxygen value of $4.2 \cdot 10^{-6}[-]$. The more viscous the tumour

is, the more time the tumour has to grow locally. In the low viscous case, the living tumour front changes the position quickly. At the new position, the living tumour front consumes oxygen and interrupts the supply of oxygen for the old position behind. The tumour becomes faster necrotic than in the viscous case, and the cell density remains small.
Figure 6.2 B shows the displacement of the ECM due to the growing tumour. The high viscous tumour displaces the surrounding ECM by almost 20 μm. This could explain the lower oxygen level in the necrotic core in comparison to the less viscous cases. The compressed matrix reduces the pore space for diffusion, and the sharp living tumour front draw on oxygen from the tumour core instead from the tumour environment.
The displacement decreases according to Table 6.1 from the high viscous to the medium viscous tumour by a factor of 7 and from the medium viscous to the low viscous tumour by a factor of 5.5. Within low and medium viscous tumours, cells can squeeze easier through the ECM and the solid ECM has a lower resistance to tumour growth. While the ECM is impactful in the solid tumour, the displacement of the ECM for the medium and low viscous growth is negligible and no limitation of oxygen delivery is expected by ECM compression.

6.6 Discussion

The change of the viscosity is like the change between benign and malign tumour growth. The question is, whether it is easier for the tumour to displace or to flow through the ECM. The highly viscous tumour represents stiff and highly differentiated cancer cells with strong cell-cell contacts and cannot penetrate the ECM scaffold. The low viscous tumour can infiltrate the tissue and consequently affects a much larger space with a lower cell density than the highly viscous tumour. The observed smoothness in cancer celllines [299] has in our simulation a profound benefit for tumour progression. The low cancer cell density might be associated with the invasive and low proliferative profile of mesenchymal melanoma cells [131]. Our model predicts a much lower cancer cell density in accordance with the related oxygen profile for the invasive tumour. The lower cancer cell density and the reduced cancer-specific staining of mesenchymal cells might contribute to the measurement of smaller tumour sizes with vernier callipers. The calliper measurement might be limited to a small visible subpart of the infiltrated area. Interestingly, this has been observed, albeit the molecular link between dedifferentiation and growth rate were neglected [131].
The proposed model is easy to extend. For instance, cells produce ECM reducing MMP, or they change the metabolism to an oxygen-independent but acidic lactate producing modus. Both weaken the mechanical properties of the ECM. The first reduces the amount of solid material; the second changes the material properties of the solid phase due to an acidic environment [301]. Mass exchange terms can easily be added to take the degradation of solid material into account. Besides the cells' impact on the environment, the environmental feedback on the cells can be considered. The model calculates the IF

pressure as well as the oxygen concentration to any discrete time step. The increasing IFP does not have only an effect on the drug efficiency [302] but is also connected to the pressure induced crosslinking of ECM molecules. The model calculates the IFP as well as the oxygen concentration to any discrete time step. The increasing IF pressure does not have only an effect on the drug efficiency [302] but is also connected to the pressure induced crosslinking of ECM molecules. This crosslinking activates the mechanotransduction, which activates SRC [303], a protein that is also triggered by limited oxygen concentration [243]. This will be modelled in subsequent papers as concentration of active SRC depending on ECM displacement $[SRCa] \propto \mathbf{u}^s$. SRC is directly responsible for cell-cell contact unbinding and migration [304], which we can, in turn, consider as viscosity change. SRC activates MAPK1, which is, with its interacting partners, a central player in cancer biology and a target for pharmaceuticals.

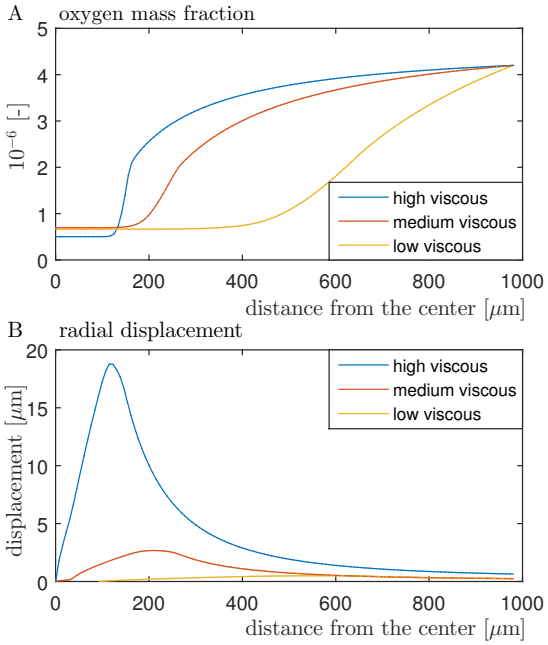

Figure 6.2: Spatial profile along the radius after 31 days. **A:** Oxygen mass fraction (unitless). **B:** ECM displacement. Positive displacement means a displacement in the direction of the spheroid surface while a negative sign indicates a compression in direction tumour centre.

Moreover, our model provides at any time the relation between IF, tumour cytoplasm, and host cell cytoplasm, which can be used to relate the intracellular pathways quantitatively to each other, *e.g.*, based on the input-output behaviour of molecular network models. The per cell production rate of any molecule can be directly translated to the actual concentration in the limited interstitial volume.

6.7 Conclusion

The thermodynamically constrained averaging theory has been used to model cancer growth in 3D collagen gels or tissues. The benefit of our modelling approach is that the ECM and the HC can be actuated separately by the TC, while most other continuous modelling approaches treat the environment as a mixture with averaged material properties. This allows us to use the advantages of continuous and biomechanical modelling but also reaching advantages of agent-based modelling. While the agent-based models define clearly the reaction volume of each cell, we define precisely the reaction volumes of

the cytoplasm within a representative elementary volume (REV). This can be justified if neither single cell information is available nor cellular memory must be tracked. While in agent-based systems, the number of cell types is nearly unlimited, our described cell liquids can be subdivided into several miscible and cell-type-specific liquids. Our approach shifts the focus from inter-cell communication to an extended view with cell-ECM interplay. This improved cancer growth model is a valuable supplement to agent-based models, which work with collections of mechanically deformable beads. Our approach has the potential to outperform other continuous models, which do not have a clear definition of reaction spaces to which molecular networks can be related.

The reduction of cell-cell contacts and the reduction of the intracellular stiffness reduce the overall viscosity of the tumour cell population. The TCAT parameter viscosity is a central player for the tumour growth shape and the overall tumour volume. A low viscosity reduces the displacement of the ECM, and the tumour cells infiltrate a much larger volume. Due to a changed oxygen profile in the low viscous tumour, the cancer cell density within the tumour remains small. The parameter viscosity can be linked with several biologically meaningful sub-systems or molecules, and the proposed model has the potential to extend network orientated models, which were formulated in the field of Systems Biology.

7. Melanoma and Mechanoregulation

After the cancer model was presented and its ability to switch between solid and invasive growth was emphasized, the following section tries to find direct links from this mechanical model to the intracellular signalling of melanoma. The **review paper** "An evolutionary perspective on mechanobiology in context of melanoma" will be submitted to a not yet selected journal together with Prof. Thomas Sauter.

7.1 Abstract

Mechanical forces are increasingly linked to various biochemical pathways which are tightly linked to diseases. This review takes an evolutionary perspective on different modules of mechanoregulation and complements it with related melanoma biology.

7.2 Cells sense mechanical cues and adjust accordingly

The ECM structure and composition is under permanent control by the residing cells, and cells are susceptible to the ECM. A well-balanced interplay preserves the mechanical homoeostasis [40]. It becomes increasingly clear that mechanical forces play a crucial role in tissue and cell biology [305, 306], whereby the field develops very fast. The allocation of mechanosensors to the different mechanical cues is an achievement of the last three years after methods for the dissection of mechanical triggers, and the quantification of related sensor signals became available [306, 307].

7.3 An evolutionary perspective on mechanoregulation

This section focuses on mechano-regulation in tumour progression and reorganises the current melanoma knowledge along these lines. This help identifying crucial proliferation and pro-survival pathways, which control growth arrest and recurrence of cancer. In the following, tissue mechanics is explained according to an evolutionary process in Figure 7.1 with stepwise added elements: the element for osmotic regulation (1), the element for general mechanosensing (2), the element for cell-cell contact sensing (3), the element for collagen sensing (4), the element for GaG sensing (5), and the vascular element (6).

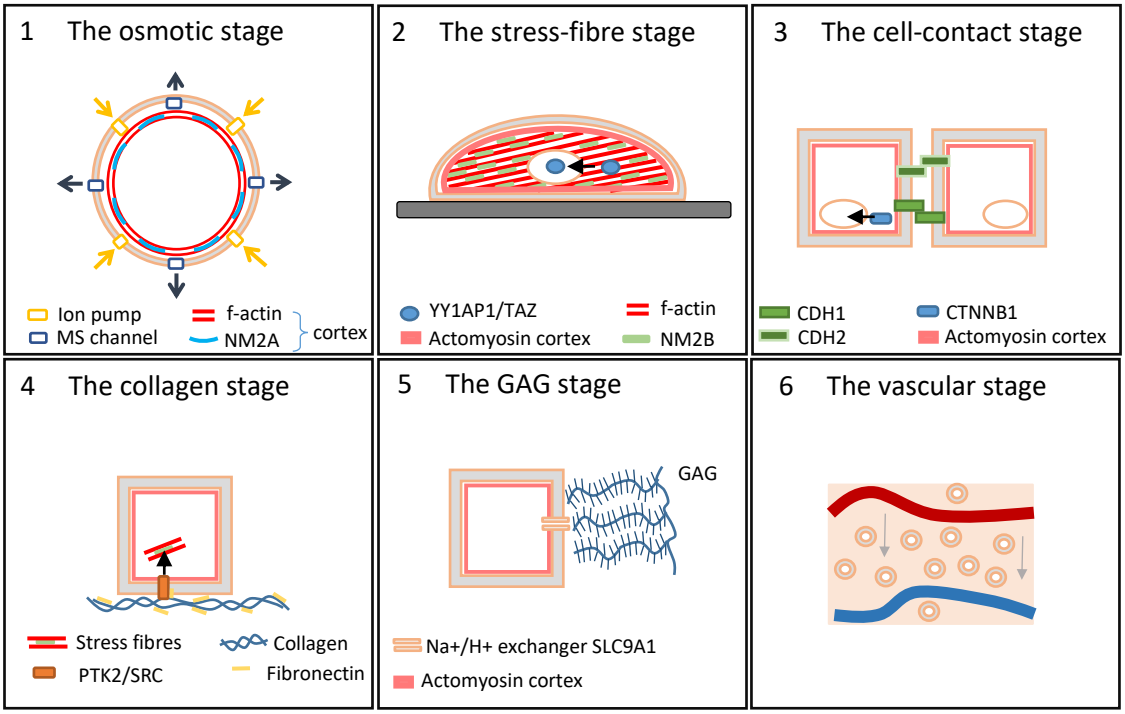

Figure 7.1: An evolutionary orientated perspective on biomechanical modules as a new hypothesis. Single cells cope with osmotic changes (1) and sense the mechanical environment via f-actin stress fibres (2). Then, cells build connections and make their fate dependent on their cellular neighbours (3). Subsequently, cells learn to detect collagen (4). Collagen sensing (4) is coupled directly to stress fibres (2), while environmental GaG (5) challenge the osmotic regulation (1). Finally, the vascular system is a source of IF and enables large tissues, organs, and organisms.

7.3.1 Osmotic stage

The cellular volume regulation is connected to a multitude of biological relevant functions, like proliferation, apoptosis, necrosis, and migration [308, 309]. The regulation is thereby highly dependent on cell-type and environment [310]. The volume regulation of single cells is well understood and depends on mechanosensitive ion channels, ion pumps, and an actomyosin cortex [112, 311]. It is known for both cells in suspension during osmotic shocks [112] and for cells on different stiff surfaces [312]. However, the cell volume regulation

in embedded hydrogels or tissues remains elusive. The volume regulation depends on ion channels on the fast time scale ($\sim$ s) with relevant intracellular ion concentration changes within minutes. Water permeation dominates upon slow mechanical deformations ($\sim \mu\mathrm{m/min}$) and cells adapt to external changes and recover within tens of minutes [112, 308]. Thus, volume regulation responds fast to osmotic changes of the environment and external loads to preserve cell volume. To avoid cell death upon compressive loads, actin-polymerisation and the solute carrier family 9 member A1 (SLC9A1)[1] are required [313, 314]. The motor protein nonmuscle myosin 2 A (NM2A) can contract cortical actin very fast for a short time [315]. NM2A dissociates readily from actin, allows a fast *de novo* formation of cytoskeletal networks, is calcium dependent, integrin-independent, and has the necessary head-domain for pulsing contractions in the cortical cytoskeleton [297]. Thereby, snail family transcriptional repressor 1 (SNAI1) expression regulates the cortex contraction while twist family bHLH transcription factor 1 (TWIST1) expression stabilises the cortex [316]. SNAI1 and TWIST1 link PIK3CA/PTEN signalling with the cadherin switch from cadherin 1 (CDH1)[2] to cadherin 2 (CDH2)[3] in melanoma progression [317, 318]. Single cells came evolutionary before multicellular organism, which suggests that the cell cortex is the oldest and probably dominant mechanism. It has been shown that cell-shape is dominant over substrate stiffness in 3D cell culture [319].

7.3.2 Stress fibre stage

For the osmotic stage, cortical actomyosin with NM2A is relevant, but the medially orientated F-actin stress fibres have an independent impact on cell mechanosensing and bind nonmuscle myosin 2 B (NM2B). In contrast to NM2A, NM2B is tightly bound to actin, is slower, and therefore more suitable for maintaining a high static tension[4] [315].

Cell stiffness follows substrate stiffness

The actin-network tension follows the substrate stiffness closely and is regulated by the balance of perinuclear $\beta 1$ to cortical $\beta 2$ integrins in single cells [320], whereby the perinuclear LMNA to LMNB1/2 ratio is a general indicator for micro stiffness [237]. Cells on soft substrate become soft and viscous, while cells become more elastic with an isotropic actin organisation on stiffer substrates. Hard substrates make cells stiff, elastic, and cause a nematic[5] actin organisation in the cell [321]. The cell rheology can be measured with magnetic beads [138] or via high-throughput optical stretching [299].

[1] Also known as sodium hydrogen exchanger NHE1
[2] Also known as E-cadherin
[3] Also known as N-cadherin
[4] Tension is here defined as the pulling forces acting on actin filaments upon the activity of myosin motors [306]
[5] parallel orientation of fibres like in a liquid crystal

Cell stiffness lead to YY1AP1/TAZ activation

Cell shape tend to flatten on a plane area, but the actomyosin cortex counteracts

On a flat and stiff surface, strong cell-surface adhesion increases actomyosin contractility with consequential water and ion efflux. The volume loss reaches 40-50%, whereas the spread-area get three-fold [312]. The actomyosin cortex counteracts these forces during mitosis to obtain a rounder shape but still low cell volume [111]. These observations further substantiate the different and partly contrary functionality of cortical and medial stress fibres which are of importance as they are directly considered responsible for BRAF inhibitor resistance in melanoma [225].

7.3.3 Cell-cell-contact stage

Epithelial and embryonic tissues are characterised by tight cell-cell contacts and might be best described by computational vertex models [322] and mechanical agent-based models [5]. Having a mechanical model for epithelial cells is an excellent prerequisite to understand the cellular regulation of cell-cell contacts and their purpose. As described above, actin-cytoskeleton tension activates YY1AP1/TAZ, but the contraction of either compressed cell-cell contacts or the apical actin-cortex in polarised cells suppress the YY1AP1/TAZ nuclear localisation in a neurofibromin 2 (NF2)[6]-dependent manner [306]. This suggests that tumours rather growth at the tumour margin under tensile stress than sides without cell-cell contacts or within the compressed tumour centre.

Calcium dependent cadherins control cell-cell-contact integrity

Crucial elements of cell-cell contacts are membrane standing glycoproteins commonly known as cadherins [323]. Cadherins require Ca^{2+} to establish homophilic bonds between cells and respond to extracellular Ca^{2+} on a rapid time scale [324]. Heterotypic bindings are possible [325] such as between fibroblast CDH2 and cancer-cell CDH1 which enables collective cell migration and thus invasion [326]. The dynamic behind cadherin and cytoskeleton interaction and their importance for responses to mechanical cues became recently more accessible [327]. CDH1, CDH2, and cadherin 3 (CDH3)[7] are scrutinised further in the following to extract the major signalling events.

CDH1 sets the rate and CDH3 the set-point

CDH1 stands for cell-cell contacts, prevents invasion and metastasis, and keeps the regulator for cortical actomyosin contraction SNAI1 low [316, 328]. The catch bonds between the membrane standing CDH1 become stronger under moderate stress, are stabilised by the actomyosin cortex [329], and are in balance with oligomerised immobile CDH1 clusters being relevant for intercell-contact strength [328]. CDH1 controls thereby the rate of intercellular force adjustment, whereas CDH3 determines the mechanical

[6] Also known as merlin
[7] Also known as P-cadherin

set-point [330]. This represents a proportional derivative (PD) control[8] of intercellular tension in alignment with classical control theory.
Moreover, CDH1 has a higher affinity to mechano-signaltransduction but can be compensated by CDH3 at low concentration levels of CDH1. CDH1 and CDH3 are jointly expressed in the basal layer of stratified epithelia. However, when they together come up in cancer context, an aggressive tumour is expected, while expression of only one type suppresses invasion [330]. The rate of inter-cell-contact strength might require fast and effective control, but the slow diffusion of CDH1 molecules on the membrane is rather limited. Indeed, fast CDH1 availability is achieved by clathrin- and caveolin-dependent endocytosis [328].

CDH1/CTNNB1 signalling contemplates YY1AP1/TAZ signalling

Stretched CDH1 can release CTNNB1, which is like YY1AP1/TAZ, a master-regulator of mechanical strain-induced cell proliferation [331]. However, while YY1AP1/TAZ localisation is detectable after one hour, peaks around six hours, and swiftly disappears, the accumulation of CTNNB1 in the nucleus comes after six hours and remains stable for over one day [331]. YY1AP1/TAZ indirectly facilitate CTNNB1 degradation and Wnt-signalling [332], a pathway that targets TWIST1 and is believed to be regulated by mechanical forces [306]. The target transcription factor of YY1AP1/TAZ is TEA domain transcription factors (TEAD), which is responsible for the cell-cycle entry to G_1; however, the target-transcription factor of CTNNB1 TCF/LEF transcription factor family (TCF/LEF) is required to enter the S phase. Both transcription-factors TEAD and TCF/LEF have to be activated to enable both G_1 and S cell-cycle entry as none of the transcription factors alone is sufficient initiate proliferation [331].

CDH2 lowers stiffness sensing, but keratinocytes inhibit CDH2

CDH2 is another important cell-cell contact molecule. CDH2 attenuates integrin-dependent mechanosensing of environmental stiffness, reduces cell contractility, nuclear YY1AP1/TAZ localisation, and focal adhesion formation [333]. CDH2 achieves this probably by inhibiting Rac family small GTPase 1 (RAC1) and guanosine-5'-triphosphate (GTP) dependent accumulation of cortical NM2A in focal adhesions [333]. The levels of CDH2 between A375 melanoma cells is reduced by calcium regulation of adjacent keratinocytes [334]. Disruption of CDH2 binding is discussed as a clinical option to treat melanoma as it increases vascular permeability and drug diffusion but has also lead to downregulation of PTEN being correlated with AKT1, which is known to increase cell proliferation, invasion, and survival [335]. PTEN inhibition and AKT1 increase is however also a sign for increased stiffness sensing mediated by integrin signalling.
Cell-cell contacts build adheres-junctions and allow both tissue integrity and tissue

[8]The proportional element sets the set-point while the derivative element prevents overshooting during the approach of the setpoint. Often memory is considered with an integrator leading to a PID-control being a standard tool in engineering.

dynamics [306]. Thereby CDH1, CDH2, and CDH3 are essential regulators of the cellular response. Swelling pressures in the interstitium might also challenge epithelial cell-cell contacts. Recent studies revealed that dissolved interstitial polymers spread the pericellular space between epidermal cells with strong cell-cell adhesion [336, 337]. The effect of interstitial polymers will be addressed in the following sections.

7.3.4 Collagen stage

Epithelial tissue is adjacent to a dense two-layered BM [19] which separates the epithelial tissue from the subjacent fibrous tissue. ECM rich fibrous tissues are mainly generated by fibroblasts [338], whereby collagen is recognised by discoidin domain receptor tyrosine kinase 2 (DDR2), and ELN is recognised by elastin binding protein receptors (EBPRs) [339]. The stiffness increases with enhanced ECM deposition and by new collagen crosslinks established by, *e.g.*, LOX. The mechanical behaviour of the ECM is an essential factor, and local sensing of its stiffness is a function of integrin signalling.

Fibronectin is crucial for stiffness sensing

Lack of filamin A (FLNA) prevents collagen stiffness sensing in M2 melanoma cells if fibronectin is not present [340]. However, $BRAF^{V600E}$ mutant melanomas can produce fibronectin by themselves, which is associated with invasion [341] and abrogated BRAFi response [194].

PTK2 alias FAK is a vital mechano-sensor

The PTK2[9] requires fibronectin and is a mechano-sensor of the second kind as it senses the viscoelastic properties of the cell environment[10] [296]. Bell and Terentjev developed a mechanical two-spring-model of opening and closing rates depending on the stiffness and cytoskeletal pulling forces. They realised that PTK2 is a naturally adaptive sensor that shifts the setpoint and thus remains sensitive to changes in substrate stiffness [296].

A negative feedback loop exists between PTK2 and CDH1

PTK2 is involved in melanoma cell migration and metastasis. A crucial part is thereby cell-contact molecules such as CDH1 on which PTK2 has proven influence [328]. Integrin signalling is coupled via strong negative feedback with CDH1 signalling and stimulates cell contractility, which is believed to disrupt CDH1 binding physically [328]. Down-regulation of PTK2 increases MAPK1 and signal transducer and activator of transcription 3 (STAT3)-dependent CDH1 expression, while up-regulation of PTK2 decreases CDH1 [342]. It is not possible to bind CDH1 and PTK2 at the same time given the underlying matrix is stiff enough [328]. The PTK2 binding partner SRC might control CDH1 endocytosis. Additionally, PTK2 phosphorylates CTNNB1 and results in impaired adherens junctions [328]. In melanoma, PTK2 triggers the PIK3CA-PTEN pathway (cell-matrix contact,

[9] Also known as the focal adhesion kinase (FAK)
[10] Mechanosensors of the first kind react directly to external forces such as stretch-activated ion channels.

stiffness), regulates transcription of TWIST1 and SNAI1 (actomyosin cortex regulation), and thus support the CDH1 to CDH2 switch (cell-cell-contact reduction) [317].

PTK2 interacts with several other mechano-sensors

In the focal adhesions are several other mechanosensitive molecules associated such as talin 1 (TLN1), vinculin (VCL), PXN, zyxin (ZYX), ENAH/vasodilator stimulated phosphoprotein (VASP), and BCAR1 scaffold protein, Cas family member (BCAR1) [320]. They acting together with the integrin linked kinase (ILK) and small GTPases to regulate the balance between the migratory and non-migratory phenotype; either due to adherens junction stabilisation or due to the migration and invasion via adherens junction remodelling [320].

PTK2 signalling makes melanoma drug resistant

The CTNNB1 and PTK2-SRC cascade render BRAF-mutant melanomas vemurafenib resistant given cancer-associated fibroblasts are present, or more precisely, a stiff and fibronectin rich matrix is in contact with the melanoma cells [12]. The subsequently activated actin stress fibres are intensified by BRAF-inhibitor vemurafenib and cause YY1AP1/TAZ dependent vemurafenib resistance in $BRAF^{V600E}$ -mutant melanoma [225].

7.3.5 Glycosaminoglycan stage

GaG are polyelectrolytes with the ability to rapidly swell and de-swell in response to ions and pH changes [72, 343]. Interestingly, most of the literature reports cancer relevant glycans if it comes to the brain cancer type glioblastoma or alterations of ion channels in connection to brain diseases. The dominance of ion-channels and glycans in brain associated diseases is understandable as this tissue has a larger fraction of GaG and a lower fraction of collagen in comparison to the dermis [74, 75]. Tissue mechanics controls among others also the brain[11] [39]. Brain metastasis concern 44% of melanoma patients and is cause of death for 20% - 54% of them [345]. In the following, some mechanisms are listed to enable an understanding of the relationship of glycan abundance, stiffness, mechanoregulation, and growth signalling.

GaG challenges mechanisms of osmotic regulation

As the mechanical characteristic of water-absorbent glycans is very close to osmotic forces, the GaG stage couples directly to the osmotic stage. This is the same principle as the collagen stage that couples directly to the stress fibre stage. In the evolutionary perspective, it makes sense that nature extents pre-existing mechanism to refine cellular regulators instead to develop completely new pathways. In a third layer, sensors of chemicals couple directly to these mechanically stimulated pathways. Wnt-signalling is tightly linked to CTNNB1 signalling [346] which represents cell-cell contacts. The receptor tyrosine kinase (RTK) cross-talk with the PTK2/SRC-related BRAF-MAP2K-MAPK1 cascade and

[11] Another hint for mechanosensitivity comes from space. Astronaut brain change in long-duration flights by brain up-shift and narrowing both the central sulcus and cerebrospinal fluid space [344].

the PIK3CA-MTOR pathway to promote cell growth and proliferation [347]. Hence, two core mechanisms exist, osmoregulation and stress fibre tension, which are extended by cell-cell contact, mechanical cell-collagen, and mechanical cell-GaG sensors. These mechanisms are anon extended by receptors for chemicals such as growth factors and Wnt.

Compressed GaGs might cause hypotrophy in dysplastic lesions

Growing cancerous tissue occasionally reveal abnormal cell sizes, which is often characterised as dysplastic growth. Pathologists distinguish furthermore between hyperplasia indicating an increase in cell number, hypertrophy indicating an abnormally large cell state, and hypotrophy indicating an unusually small cell state. In water-absorbent, stiff, and photo-crosslinked methacrylate alginate, melanoma cells show a significantly reduced cell size [348].

As described in the section for the osmotic stage, cells are well adapted to regulate the ion concentration and the actomyosin cortex to keep the cell volume constant. However, in competition to the water-absorbent ground substance or dense water-absorbent hydrogel, cells might suffer from a limited regulatory capacity to achieve the anticipated cell volume. Dysplastic growth might be caused by elevated cellularity with consequential compression of pericellular polymers and thus elevated osmolarity. Mutation of ion-channels and components of the cytoskeleton might cause dysplastic lesions as well. If this can be confirmed, cells do not only need to outbalance osmotic forces from the IF but must also compete with swelling polymers, which increase osmolarity upon compression.

Osmotic forces upon polymer compression might also explain, why neoplastic cells have reduced cytoplasm and reduced pigmentation in high-CSD melanoma [15]. The CSD associated solar elastosis lead to accumulation of ELN fibres in the extracellular matrix. This increases the polymer density and consequently increases both stiffness and osmolarity. This might in turn support mechanical induced dedifferentiation and thus reduced melanin production.

Cells sense GaGs

Despite sensing the osmotic concurrence to glycans, cells have sensors to recognise specific glycans, *e.g.*, by hyaluronan receptor CD44 molecule (Indian blood group) (CD44) [339].

GaGs modulate growth factors

PGs bind growth factors like vascular endothelial growth factor A (VEGFA), epidermal growth factor (EGF), fibroblast growth factors (FGF), and transforming growth factor beta family (TGFB), which are released upon ECM degradation or deformation [349]. TGFB is non-covalently bound to the large latent complex (LLC) and interacts with fibronectin and PGs after secretion. Then, TGFB is mainly captured and thus modulated by the glycoprotein fibrillin 1 (FBN1), which is thought to intensify TGFB signalling by local enrichment [349, 350].

AGRN contemplates PTK2 signalling

The proteoglycan agrin (AGRN) is expressed in all tissues and triggers as mechanosensor the LDL receptor related protein 4 (LRP4)/muscle associated receptor tyrosine kinase (MUSK) receptor to increase the activity of YY1AP1/TAZ in a PTK2 dependent manner [351]. AGRN enhance PTK2 signalling, is probably relevant in softer tissues, and inhibits the suppressor function of NF2 [351]. NF2 suppression might lead to an increased proliferation in compressed tissue.

GaGs increase tissue stiffness

Glycans can also increase tissue stiffness and contribute in this way to the invasion, such as shown for melanoma with environmental expressed biglycan (BGN) [352]. If brain tissue is enriched with glycoprotein tenascin C (TNC), tissue stiffness increases which in turn increases TNC deposition. This positive feedback loop leads to aggressive glioblastoma and may be caused by reduced miR-203 suppression of hypoxia inducible factor 1 subunit alpha (HIF1A) as a consequence of isocitrate dehydrogenase (NADP(+)) 1, cytosolic (IDH1) dysregulation [353].
The piezo type mechanosensitive ion channel component 1 (PIEZO1) and the piezo type mechanosensitive ion channel component 2 (PIEZO2) belong to the stretch-activated ion channels [354, 355], which increase intracellular calcium levels when cells transfer from unconfined to confined spaces. They are dependent on cAMP-dependent protein kinase (PKA) but independent of NM2A. The PIEZO1/ calcium/ phosphodiesterase 1 (PDE1)/PKA pathway might be involved in confined migration of invasive melanoma cells [356]. Moreover, PIEZO1 is a predictor for worse outcome in glioblastoma, promotes glioma aggression, and interacts with the integrin-PTK2 pathway [357].

Stretch activated ion channels localise to mechanoregulators

Likewise, the SLC9A1[12] localises to integrins, TLN1, VCL and PXN and is required for melanoma cell motility during tumour associated acidosis [314], and SLC9A1 prevents cell death upon compressive loads [313]. Acidification and SLC9A1 overexpression reduce cell-cell adhesion strength while strengthening cell-matrix interactions in human melanoma [358].
To sum up, glycans absorb IF, modulate growth factors, increase tissue stiffness and PTK2 dependent stiffness sensing, and stimulate ion-channel dependent survival and migration.

7.3.6 Vascular stage

A certain fraction of the blood serum infiltrates tissues and is drained by the lymphatic system. A minimum transport of water through tissue must exist to allow the growth of avascular tumour spheroids. Whether this happens over the pericellular space or via aquaporin water channels [359] in the cell membrane is unclear. The water channel aquaporin 3 (Gill blood group) (AQP3) is strongly overexpressed in human skin squamous

[12] also known as sodium–hydrogen antiporter 1 (NHE1)

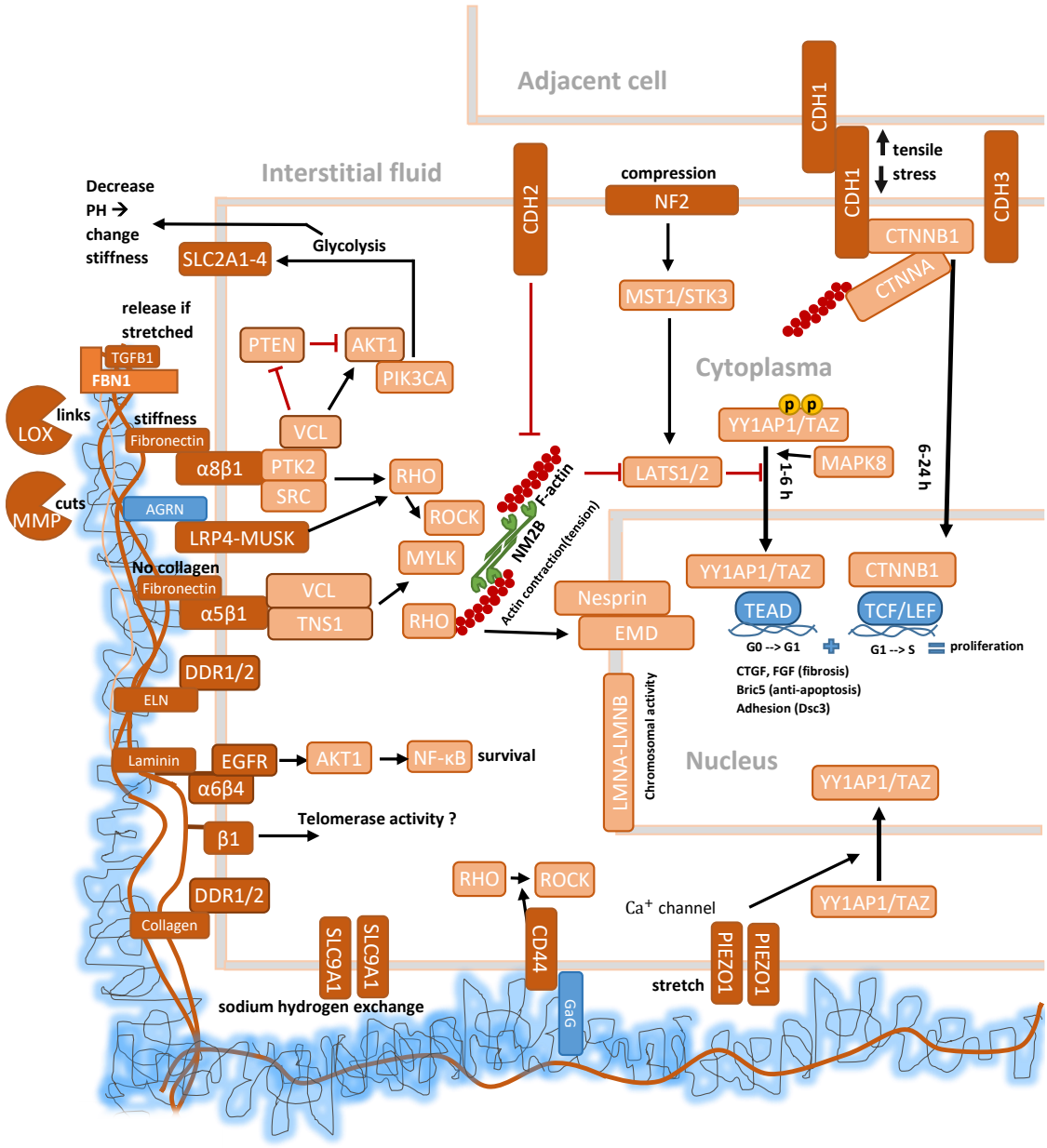

Figure 7.2: Summary of mechanosensitive pathways according to the literature cited in the text.

cell carcinoma, and blockage leads to tumour resistant mice [360]. A comparable effect was observed for aquaporin 1 (Colton blood group) (AQP1) in melanoma where obstruction leads to a reduction of tumour volume of 75 % [361]. Thus cellular molecules can influence the permeation of fluid through tissues.

The importance of the mechanical microenvironment as well as the identification of non-genetic and non-cell autonomous drug resistance mechanisms fill several translational research works on metastatic melanoma [157]. As a consequence, mechanical properties do not only influence the growth; they also affect the sensitivity to certain drugs. The reorganisation of mechano-regulatory mechanisms along an evolutionary motivated succession of steps, help modellers orientate in this field. The mentioned regulatory molecules are summarized in Figure 7.2.

7.4 Mechanics contributes to spatial growth control in epithelium

Links between mechanic sensors and mechanical elements on the tissue level were explained and illustrated with examples in the previous sections. This following section briefly summarises their direct impact on histological features and the spatial organisation of tissues. The spatial organisation of skin can vary along different body sides as shown in Figure 2.1 and requires a location-dependent adjustment of the geometric initial conditions. Skin homeostasis and growth control depend on mechano-regulation [219, 362]. Especially noteworthy are the regulators for cell-cell contacts and cell-ECM contacts.

CDH1 interferes with tight-junction positioning and EGF signalling

Cell-cell contact regulators such as CDH1 are involved in the adherens junction tension between cells [363]. The tension is the highest in the middle layers of the *stratum granulosum*, where the tight junctions become positioned. Tight junctions are selective gates, which separate the apical and basolateral membrane domains and control the diffusion of ions and solutes adjacent to tight junctions in the pericellular space [364]. Rübsam *et al.* show thereby how mechanical cadherin-signalling interacts with the epidermal growth factor receptor (EGFR) activity [363].

YY1AP1/TAZ signalling keeps the *stratum basale* undifferentiated

The nuclear localisation of the mechanical rheostat YY1AP1/TAZ requires the stiff BM and the absence of an apical side, which is given for the stratified squamous epithelium structure of the skin surface [365]. The stem-like *stratum basale* is characterised by YY1AP1/TAZ localisation in the nucleus, whereas cells with apical domain recruit crumbs cell polarity complex component 3 (CRB3), NF2, WW and C2 domain containing 1 (WWC1)[13], and salvador family WW domain containing protein 1 (SAV1) to prevent nuclear accumulation of YY1AP1/TAZ [365].

[13] Also known as KiBRA

For melanoma, Notch protein is interesting as it is present at distal keratinocytes and contact with Notch initiates invasive growth [366]. Nuclear localisation of YY1AP1/TAZ protects against Notch signalling by maintaining the undifferentiated state of epidermal progenitor cells due to YY1AP1/TAZ controlled up-regulation of delta like canonical Notch ligand 1 (DLL1), delta like canonical Notch ligand 3 (DLL3), and jagged canonical Notch ligand 2 (JAG2) [332]. Distal keratinocytes at the skin surface expose Notch-ligands[14], which trigger melanoma cell de-differentiation by impairing the binding of differentiation-marker MITF to the miR-222/221 promoter. De-repression of miR-222/221 is thought to induce invasion and the switch from the radial to vertical growth stage [366]. Notch signalling amplifies upon pulling forces and requires BAR domain-containing proteins such as epsin (EPN) [368, 369], which recognise and modifies membrane curvature [370].

7.5 Conclusion

Melanoma is known for phenotype switches and non-sell autonomous resistance mechanisms in a confined environment. Accordingly, this review structures different mechano-sensing mechanisms in a way that relates directly to cellular function.

[14] Notch1 itself is reported to be a mechanosensor responding to laminar shear stress and modelling calcium signalling [367]

8. Melanoma reacts to the environment

Mechanical cues influence many biological processes as described in the introduction. Consequently, the aim of the experimental, not yet published, part was the determination of melanoma growth trajectories and the effect of drugs in a confined environment. The experiments were performed within six months at the University Hospital Carl Gustav Carus (TU Dresden) under the supervision of Prof. Dagmar Kulms.

8.1 Stiffness enhances spheroid growth

8.1.1 Cellendes dextran hydrogel resembles a two element Wiechert model

Before studying the growth of spheroids within hydrogels, the mechanical properties of the experimental hydrogel system were studied. The experimental hydrogel system from Cellendes is a dextran polymer that is crosslinked by PEG or CD cross-linker and is kept moist in cell culture medium. Dynamical mechanical analysis was performed with a strain imposed rheometer to obtain the mechanical parameters as shown in Figure 8.1. The frequency sweep revealed a frequency dependent elastic shear

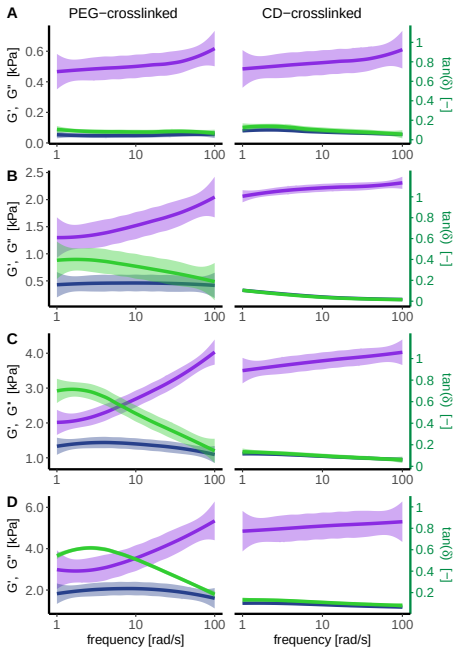

Figure 8.1: Frequency sweep test of hydrogels. Polymer content increases from A to D. Violet: shear storage modulus G' (elasticity). Gray: shear loss modulus G" (viscosity). Green: damping factor (right axis).

modulus and an increasing damping factor toward lower frequencies in the PEG-gel, but not in the CD-cross-linked gel. The mechanical behaviour of the PEG-gel suggests gel formation at the gel transition point[1] from the glassy to the rubbery state [76] and is comparable with a two element Wiechert model as shown in Figure 8.2.

8.1.2 LU451 cell line shields the confocal light

In order to track the growth, the size quantity was tracked to different times. The original plan was to determine the volume, which is more precise than the area. However, it turned out that the melanoma cell line shields the light so that the stimulation of GFP positive cells above the down-pointing cell layer was not possible. In order to test the suspicion, the sample had been screened upside down, which resulted in the same u-shape as shown in Figure 8.3. As melanoma produces melanin to protect skin from harmful light, this peculiarity is plausible.

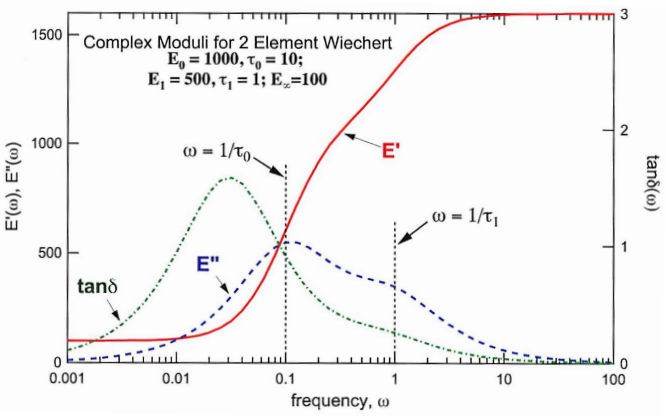

Figure 8.2: Theoretical behaviour for a two-element Wiechert model in frequency sweep with the young modulus E instead of the shear modulus G. Figure source [76].

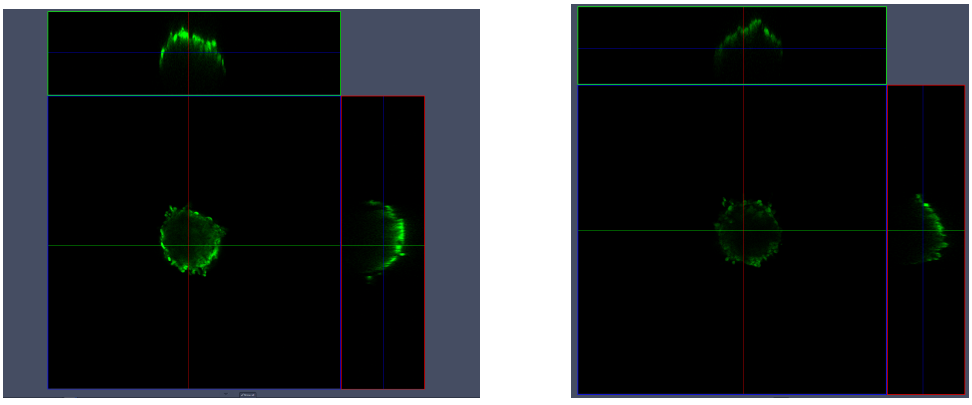

Figure 8.3: Z-stack of a spheroid at a chosen layer with the transverse section from two sides. The left figure for the standard position of the Petri dish and the right figure for the upside down position.

[1] Polymers can restructure in different organisational states and can crystallise with specific changes in the stress-strain response. Therefore, polymers behave differently to other materials such as concrete or metal [76].

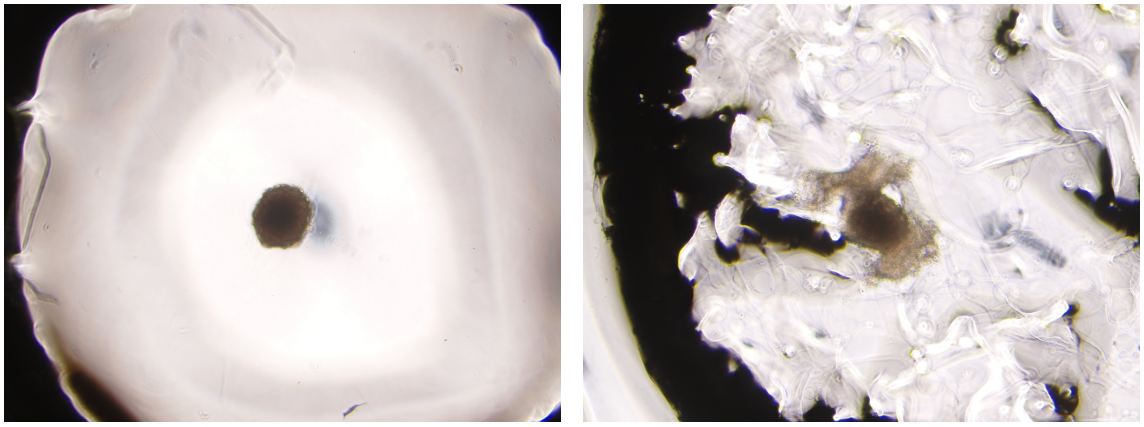

Figure 8.4: Light-microscopy image of two embedded spheroids after nine days. Left in the softest CD-gel and right in the stiffest CD-gel. The soft gel is homogeneous whereas the stiff gel is streaky.

8.1.3 Growth rate increases with the stiffness but is determined by polymer degradation

After the hydrogel was mechanically characterised and melanoma spheroid specific technical issues were identified, the spheroid growth of the LU451 cellline was tracked in different stiff environments. To understand the growth, spheroid expansion was tracked without any treatment as a starting point. LU451 Spheroids where grown in the hydrogel-drops as shown in Figure 11.1. The evolution of LU451 spheroids developed stiffness dependent as shown in Figure 8.5 for one replicate and averaged over more than three replicates in Figure 8.6.

In contrast to the spheroids in the cell degradable gel, spheroids in the not cell degradable gel show a decreased growth with increased hydrogel stiffness. Spheroids in the not degradable PEG gel tend to escape the gel and grow in an umbrella-like shape on the gel instead of within. The growth rate on the stiffer substratum is also higher compared to the soft. One spheroid in the $1.6\ \mathrm{kPa}$ PEG gel changed the cell morphology and reached after three days more than a doubled size, but remained then constant.

8.2 Dabrafenib increases pERK in spheroid but not in monolayer

Besides the understanding of cancer growth in general, the interaction with drugs is a cornerstone of this thesis. Therefore, drug efficacy is tested in three different experimental test settings: monolayer, hanging drop spheroids and embedded spheroids.

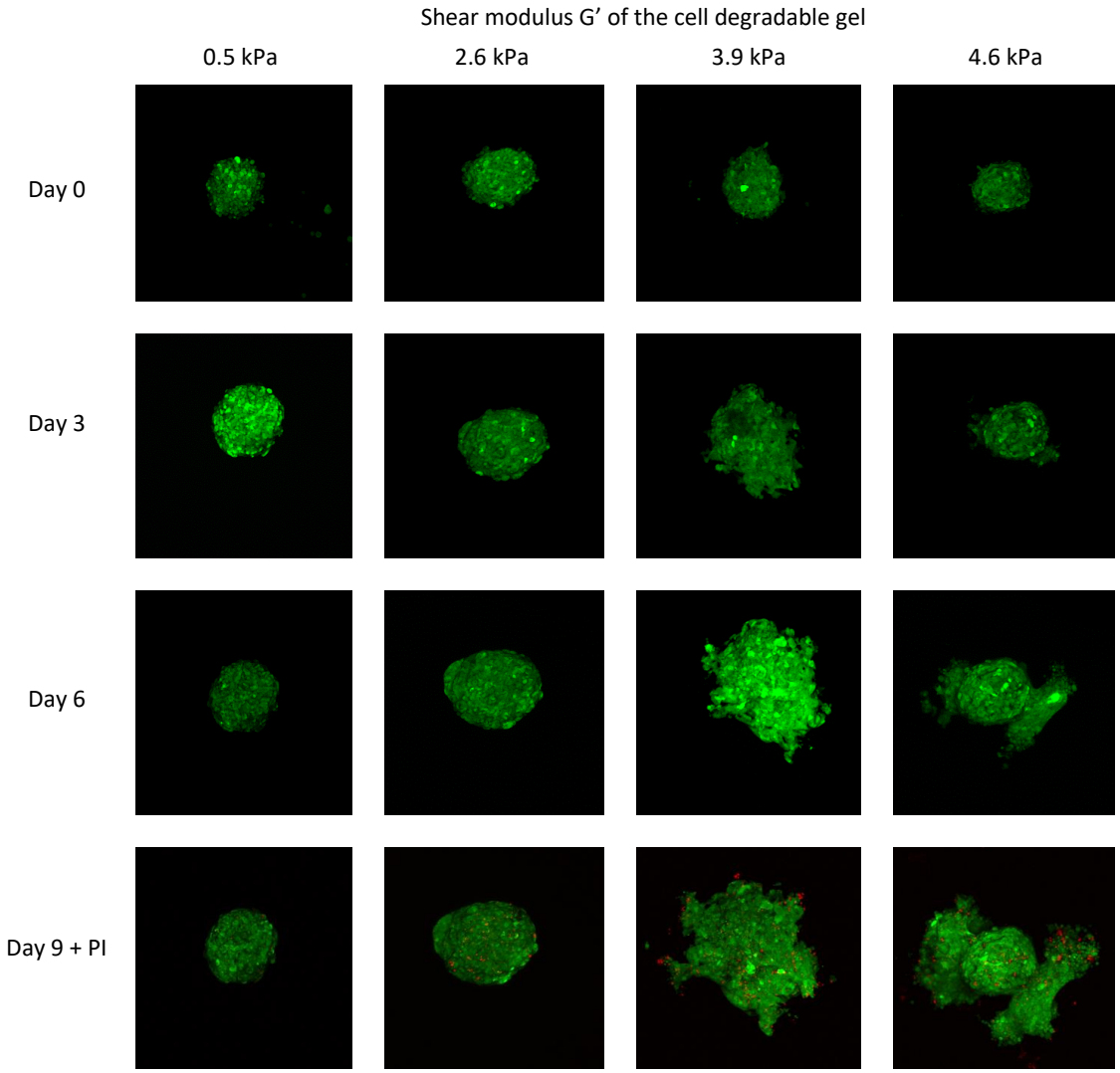

Figure 8.5: Growth of four selected spheroids with increasing stiffness/ polymer content. Propidium iodide (PI) stains dead cells red, whereby only a few cells are dead.

8.2.1 Phospho-ERK is increased in spheroids with 10 uM dabrafenib

After accessing the growth trajectories, differences in the phosphoproteins were assessed for the LU451 cellline in different experimental settings. Therefore, YY1AP1, PTK2, EGF and housekeeping proteins were planned to be measured in cell monolayer, spheroids, and embedded spheroids. It turned out that the embedded spheroids are difficult to be extracted fast enough in sufficient quantities, that the mechanosensor quantities were inconclusive, and that β-tubulin is an inappropriate control, probably because β-tubulin is a cytoskeleton protein and thus potentially mechanosensitive.

An unexpected finding is the recovery of the proliferation maker pERK in spheroids treated with 10 uM dabrafenib. As shown in Figure 8.7, the pERK level reduces after 3 h in dabrafenib treated spheroid as well as in the monolayer. However, after 48 h the proliferation marker seems to be reactivated after 48h in spheroids; an effect that has

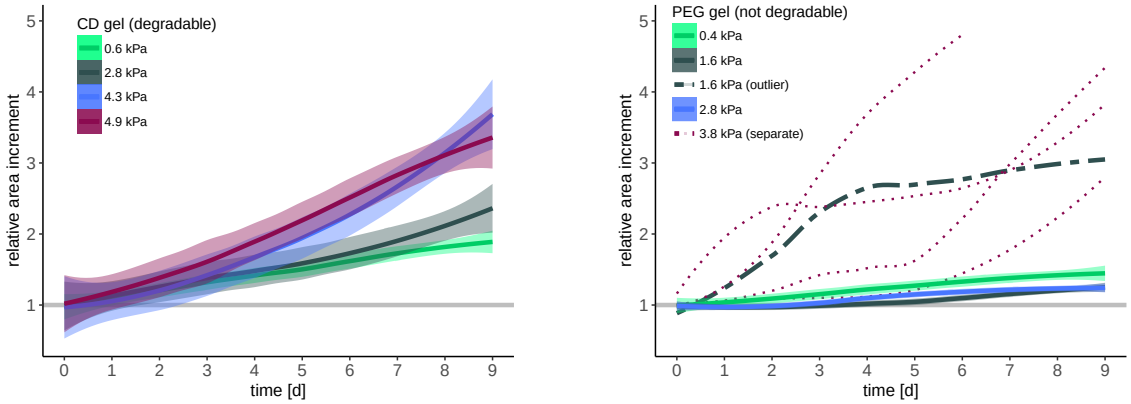

Figure 8.6: Spheroid size evolution over nine days normalised to the first day. Time course fitted with loess with 95% standard deviation. Left: Growth in the degradable gel. Right: Growth in the not degradable PEG gel with the separate depiction of outliers.

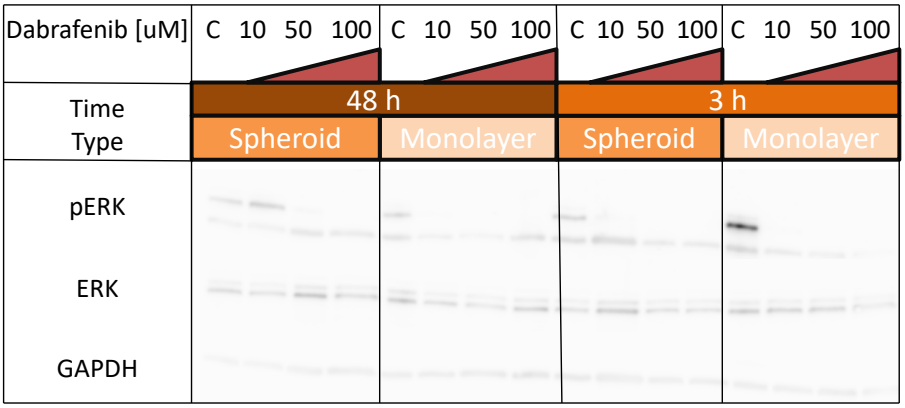

Figure 8.7: Proliferation marker level pERK is shown as a protein band in a Western blot. The proteome has been extracted from spheroids or monolayer after treatment with dabrafenib for either 3h or 48 h. The control protein is GAPDH. The additional band below pERK (42,44 kDa) is from the GAPDH traces (37kDa) of the previous anti-rabbit staining done by a clueless computational scientist.

been reproduced three times.

In addition, the drug effect on LU451 spheroids growth was measured and is shown in Figure 9.6. In contrast to monolayer and spheroids, embedded spheroids tend to become resistant with increased dabrafenib levels, and some spheroids seem even to expand more than spheroids in the control group.

9. PK identifies drug resistance

The ability of cells to recognise different mechanical cues in the environment and to modify the mechanical properties of tissues is tightly linked to melanoma biology *in vivo*. Also the experimental results above showed a strong relationship between mechanical environment, dabrafenib dose, and growth control. For this reason, a complete reassessment of dabrafenib pharmacokinetics is performed to find translational aspects of these mechanisms. This **original research** paper has been submitted to *npj Systems Biology and Applications* on 2nd April 2019 together with Mr. Yuri Kogan, Prof. Dagmar Kulms, Prof. Thomas Sauter. No reviewer decision was received until the 20th July (almost 4 months), because the Nature journal has "some difficulties in securing the right reviewers" for the manuscript.

9.1 Abstract

The oncogenic $BRAF^{V600E}$ -mutation is a leading cause for the excessive proliferation of metastatic melanoma and non-small-cell lung cancer. Both cancer types are commonly treated with the BRAF inhibitor dabrafenib. A crucial limitation of dabrafenib monotherapy is the high relapse rate, being caused by acquired drug resistance. Resistance is indicated by reactivation of the proliferation marker pMAPK1 as shown to be the case upon daily administration of more than 300 mg dabrafenib in a clinical drug-dose determination study. To clarify whether drug concentrations upon doses above 300 mg could be reached by a potential long-term drug accumulation upon administration of 300 mg dabrafenib, we developed an extended pharmacokinetics model. The proposed mechanistic model accounts for dabrafenib metabolism, cytochrome P450 family 3 subfamily A member 4 (CYP3A4) enzyme induction, and drug-drug interaction. Thereby, the model surmounts

the current methodological limitations with a refined systems pharmacological approach. The model predicts an eight-fold increase of the maximum concentration of both carboxy-dabrafenib and desmethyl-dabrafenib after four weeks for the recommended dose of 150 mg b.d. dabrafenib. For the almost likewise effective dose of 50 mg b.d. dabrafenib, the drug accumulation is predicted to be only two-fold. In the metabolic process, inactive carboxy-dabrafenib may be locally converted to active desmethyl-dabrafenib in an acidic tumour environment. We confirmed experimentally that high physiological dabrafenib concentrations fail to induce cell death in melanoma spheroids embedded into fibronectin supplemented hydrogels which demonstrates the potential relevance of the predicted metabolite accumulations.

9.2 Introduction

Dysregulation of the mitogen-activated (MAPK) RAS type GTPase family (RAS)-RAF-MAP2K-MAPK1 pathway presents a key driver of melanoma progression, especially when a constitutively activating point mutation of the proto-oncogene $BRAF^{V600E}$ exists [371]. Accordingly, the invention of targeted kinase inhibitors promised therapeutic benefit [372]. However, nearly all responses to targeted BRAF inhibitors are partial with a subpopulation of patients showing primary resistance [372], while about 50% of the patients acquire secondary resistance and consequentially present tumour relapse [373].

While tumour relapse can be directly associated with primary and secondary resistance on the molecular level, the dose determination study on dabrafenib indicates a proliferation marker increase for higher doses [374], indicating higher dabrafenib doses to be potentially associated with tumour relapse. The phosphorylated form of proliferation marker and downstream MAP-kinase MAPK1 were measured in human tissue samples. The most effective pMAPK1 downregulation of 80% was reached with the daily dose of 300 mg dabrafenib, being equivalent to the currently administered 150 mg twice a day (b.d). In contrast, elevated doses of 400 mg and 600 mg daily caused reduced pMAPK1 inhibition [374].

pharmacokinetics (PK) relates the drug dose to the drug concentration in blood plasma over time, and drug concentration in the blood plasma relates better to drug interactions with the proliferation marker pMAPK1. If periodically administrated dabrafenib accumulates in the blood plasma, it might come to the same reduced pMAPK1 inhibition as with elevated doses of 400 mg and 600 mg from the outset. Drug accumulation of dabrafenib can be precluded by an established dabrafenib PK model [198]. However, a PK model for dabrafenib metabolites in the blood plasma does not exist to our knowledge and might be useful to check for potential drug accumulations.

The dabrafenib peak levels do not accumulate, but rather decline with each subsequently given dose, which is caused by cytochrome P450s (CYP) [198]. CYPs deplete dabrafenib in the liver and intestine just like the majority of approved drugs in clinical use [375, 376].

The dabrafenib peak levels consequently decrease with an increase of the CYP enzyme level or decrease with a reduction of enzyme capacity. Thus, CYPs are a major source of PK variability [376] and cause two modelling problems: the enzyme level is time variant, and the enzyme capacity might decrease due to competing drugs.
Dabrafenib induces CYP3A4, and conversely, the CYP3A4 substrate dabrafenib is expected to deplete faster [374]. Dabrafenib triggers the CYP3A4 messenger ribonucleic acid (mRNA) production in liver cells [375], but CYP level change is also a general problem [376]. At least eight drugs can increase the CYP enzyme level [377, 378] and at least 36 drugs can lead to CYP inhibition [378, 379]. The lack of experience in mechanistic modelling for enzyme induction and inhibition led to the decision of the European Medicine Agency (EMA) to disregard PK models based on enzyme level changes [380], and thus such models are an open research problem.
Dabrafenib PK can also be affected by drug-drug-interaction (DDI) due to CYP3A4 targeting drugs such as the anti-fungal drug ketoconazole [376]. The enzyme kinetic for the competitive substrate inhibition [381] is often used to mimic the concentration profile of one drug under the influence of another. Such kinetic laws of enzymes are based on assumption sparse reaction networks with the mass-action law, which are simplified with the help of assumptions such as constant enzyme levels [382]. The restrictive assumption of a constant enzyme level for DDI analysis might be less dominant in the parameter-rich physiologically based PK (PBPK) [383] and might be outbalanced by additional terms in the sigmoidal maximum effect model itself [384]. However, a constant enzyme level is not the case for dabrafenib [375] and underlying assumptions of enzyme kinetic laws might be violated.
The current dabrafenib PK model does not account for dabrafenib metabolites and has only a phenomenological term to mimic enzyme induction [198]. This descriptive term is a dose and time-dependent clearance term which provides only little insight into enzyme regulation and is thus also not able to integrate DDI. Systematic and reliable integration of enzyme induction is therefore lacking.

To overcome the limitations of the current PK model and for a better understanding of dabrafenib dose-related tumour relapse, we constructed an integrative and mechanistic PK model of dabrafenib metabolism. It follows a workflow for the systematic integration of enzyme induction and enables the identification of possible upper limits of metabolite concentrations. Furthermore, we consider drug-drug interactions with ketoconazole to improve the parameter robustness of our model and to increase the usefulness for patients with multiple medications.

9.3 Results

We propose a PK model for dabrafenib metabolism represented by the verbal model in Figure 9.1. The verbal model is a graphical representation of a set of ordinary differential

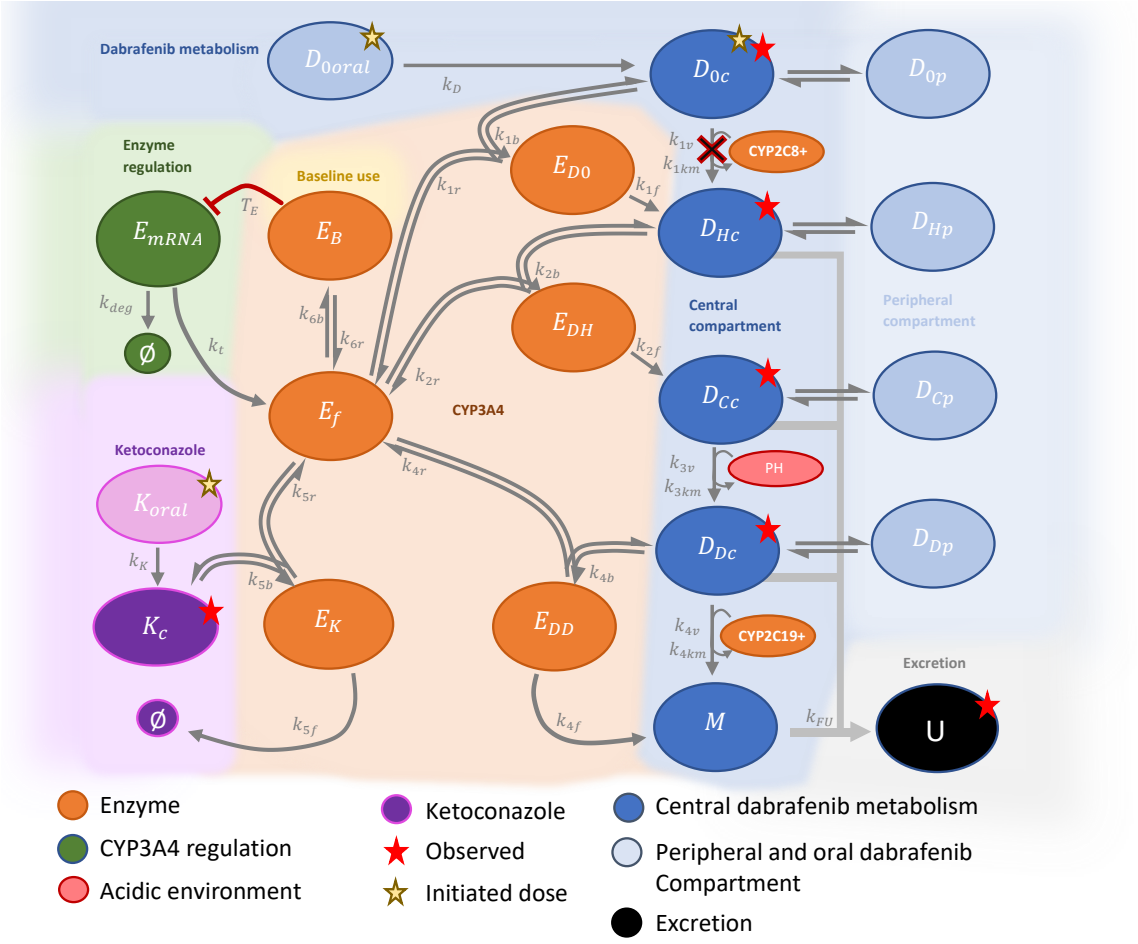

Figure 9.1: The verbal model of dabrafenib metabolism is a graphical representation of the underlying mathematical equations and serves as a communication tool between the modeller and the experts of the system. Dabrafenib is administrated orally and appears as a separate element if given as solution D_{0oral} or appears as a part of the central compartment if given as a pill D_{0c}. The index 0 indicates unprocessed dabrafenib. Dabrafenib is metabolised by the CYP3A4 to hydroxy-dabrafenib D_{Hc}. The enzyme pool CYP2C8+ turned out to prevent a good data fit and is thus neglected. Hydroxy-dabrafenib turns by CYP3A4 to carbo-dabrafenib D_{Cc}. Carbo-dabrafenib turns by an acidic environment into desmethyl-dabrafenib D_{Dc} which anon turns by CYP3A4 and the enzyme pool CYP2C19+ to metabolites, which are pooled to the element M. The individually donated metabolites are exchanged with the peripheral compartments ($D_{0c}, D_{Hc}, D_{Cc}, D_{Dc}$) and excreted via faeces and urine U. Ketoconazole is given orally K_{oral}. Ketoconazole in the central compartment K_c binds free CYP3A4 enzyme E_f to build a ketoconazole-CYP3A4 complex E_K releasing depleted ketoconazole into a mathematical sink $\emptyset$. A part of the free enzyme builds the substrate-CYP3A4 complex representing the enzyme baseline use. If the enzyme for the baseline use falls below the threshold T_E, CYP3A4 mRNA E_{mRNA} is produced, which is required to produce more CYP3A4 protein with translation rate k_t. A part of the mRNA is degraded with the rate k_{deg}.

equations (ODEs), which can be found in the methods part. Each ellipse in the verbal model stands for one model element, and each model element represents the concentration of a chemical, an enzyme, or an enzyme-substrate complex. Several model-elements form a network-module representing a functional part of the whole model. To obtain a useful model, several steps were performed and will be described in the following subsections and by reference to Figure 9.2. We used the original PK model [198] not only for the parent drug dabrafenib but also for the metabolites. The mechanistic links between the dabrafenib metabolites where modelled based on a *in vitro* experiment with recombinant CYPs. The dabrafenib metabolism model contains the CYP3A4 enzyme, which serves also as a central element of a ketoconazole PK module used to constrain the dabrafenib model further. The resulting model is fitted in various contexts representing diverse clinical datasets on dabrafenib, ketoconazole and dabrafenib-ketoconazole interaction. To refine the model fit, an enzyme induction motif had to be identified. Therefore, the total enzyme concentration was varied for each dose period until the model aligned with the data. The so obtained insight into the time behaviour of CYP3A4 and other model elements enabled the design of a network motif that mimics enzyme induction. Several refits of the model with enzyme induction completed the modelling procedure.
The in-depth discussion of model assumptions and modelling decisions was prerequisite for the validity of the subsequent following model prediction. The predicted metabolite accumulations were finally set in context with experimental drug testing. Drug efficiency loss for higher dabrafenib doses underlined the meaningfulness of our modelling approach.

Model of Ouellet *et. al.* serves as a template for the metabolites

Ouellet *et. al.* has described the reversible transport reaction of dabrafenib between the central D_{0c} and the peripheral compartment D_{0p} [198]. The upper right corner of Figure 9.1 represents the original model, whereby the index 0 indicates unmodified dabrafenib. This model incorporates an oral and an inducible clearance term, whereby the inducible clearance must appear in both the central and the peripheral compartment to reproduce the published model (coded in *Supplementary_Code_1.m* and visualised in the Supplementary Figure 1). We used the computational model of Ouellet *et. al.* as a starting point of our model and replaced the descriptive clearance terms by mechanistic terms for enzyme dependent clearance in order to integrate dabrafenib metabolism later on.
The reversible reaction of the dabrafenib transport between the central and the peripheral compartment was copied three times to represent the dabrafenib metabolites hydroxy-dabrafenib D_{Hc}, carbo-dabrafenib D_{Cc}, and desmethyl-dabrafenib D_{Dc} being in balance with the allocated peripheral concentrations (D_{Hp}, D_{Cp}, D_{Dp}). The balance between dabrafenib metabolite and allocated peripheral compartment obey the model parameters of Ouellet *et. al.* The definition of disjunct models of the dabrafenib metabolites lack interconnections, which were modelled on the base of enzyme tests in the following

subsection.

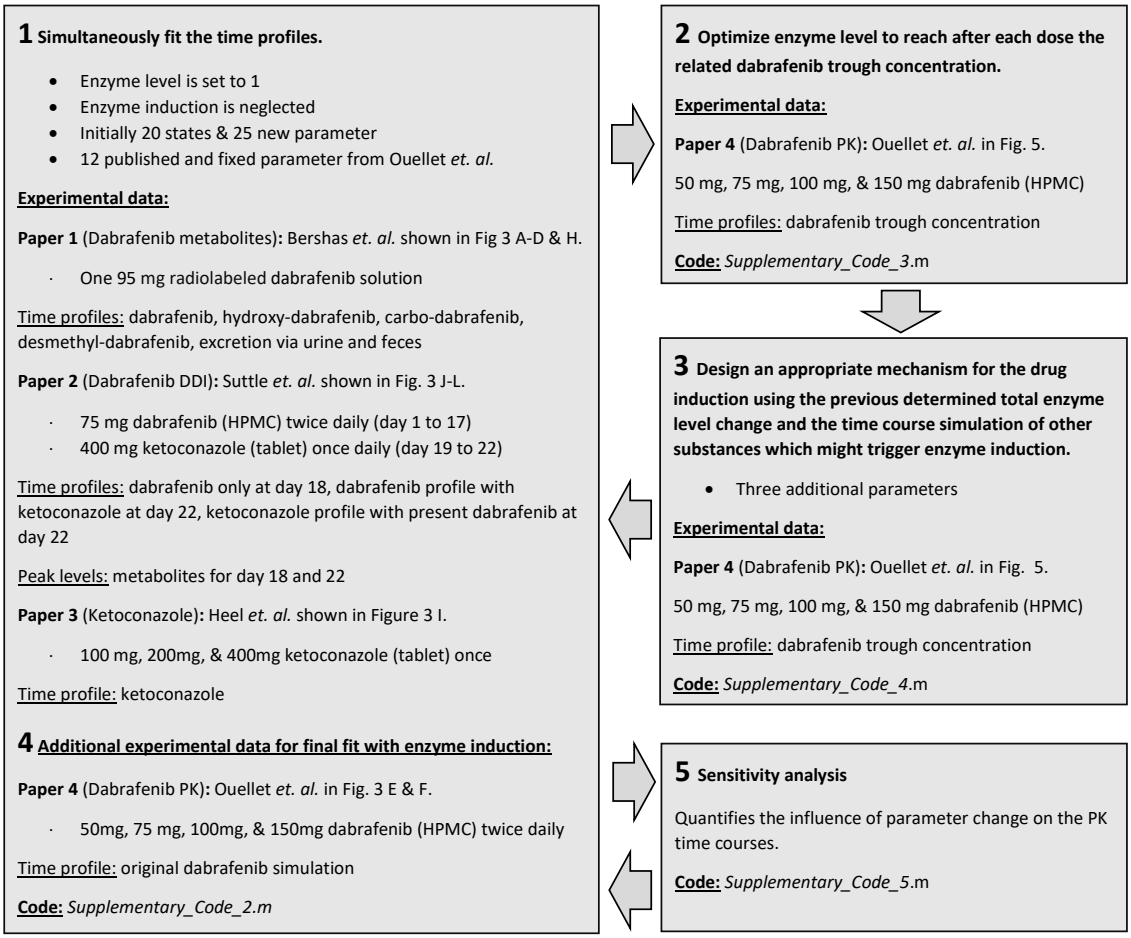

Figure 9.2: The workflow for an efficient dabrafenib PK model development with integration of CYP3A4 induction and DDI. First: the model is fitted simultaneously for dabrafenib metabolism alone [385], ketoconazole PK alone [386], and drug-drug interaction [387]. The first step does not consider enzyme level changes. Second: The published trough levels [198] are fitted. Therefore, the total enzyme concentration is varied while all other parameters are fixed. Third: an appropriate enzyme induction mechanism is designed, and the related parameters are estimated. Therefore, the parameters of the model step one are fixed, and profiles of step two serve as orientation. Fourth: the control design is introduced in the initial model, which is refitted. Fifth: the final model is subjected to sensitivity analysis to identify irrelevant model structures.

In vitro experiments guide the model structure on the biotransformation from one metabolite to another

A study using recombinant CYP enzymes and human liver microsomes determined the relative contribution of each tested CYP to the metabolite depletion [375], enabling the modelling of the metabolic flow from dabrafenib to the final metabolites. According to this study, CYP3A4 depleted 23% of dabrafenib. The enzymes cytochrome P450 family 1 subfamily A member 2 (CYP1A2) (1.9%), cytochrome P450 family 2 subfamily B member

6 (CYP2B6) (6.9%), cytochrome P450 family 2 subfamily C member 9 (CYP2C9) (10%), and CYP2C8 (56%) depleted 74,8 % of dabrafenib, and their activity was combined to the CYP2C8+ enzyme pool. In the next step, hydroxy-dabrafenib turns into carbo-dabrafenib by modification through CYP3A4 exclusively [375]. Carbo-dabrafenib converts to desmethyl-dabrafenib in an enzyme-independent but pH-dependent reaction [375, 385]. Subsequently, desmethyl-dabrafenib converts into several metabolites being united as element M. Desmethyl-dabrafenib depletion requires CYP3A4 (69%) as well as the enzymes CYP2C9 (9.6%) and CYP2C19 (22%) combined to the CYP2C19+ enzyme pool [375]. The dabrafenib metabolism is hereby fully described as shown in Figure 9.1.
To create a predictive and computational feasible model, a few modelling assumptions were made. First, we assumed that the pH-dependent turnover, as well as the enzyme pools CYP2C8+ and CYP2C19+, can be approximated by the Michaelis-Menten kinetics. Second, due to multi-functionality of the free enzyme CYP3A4, we assume that the reaction network model is the best representation of CYP3A4 function and experienced that a simplification to a kinetic law neither lead to fewer parameters nor facilitates DDI and enzyme induction modelling. In this network model, the total CYP3A4 amount subdivides in the free enzyme form E_f without any bound substrate and the CYP3A4-metabolite complexes with bound dabrafenib E_{D0}, hydroxy-dabrafenib E_{DH}, or desmethyl-dabrafenib E_{DD} as shown in Figure 9.1. Third, the enzyme CYP2C9 appears twice but accounts only for a proportion of around 10%. It is, therefore, reasonable to integrate its contribution into the two enzyme pools CYP2C8+ and CYP2C19+ instead to model it as detailed as CYP3A4. Fourth, A sensitivity analysis revealed that our model fit rendered the CYP2C8+ pool redundant, wherefore we removed the equation for the CYP2C8+ pool. Fifth, the unspecific characteristic of CYPs enables the reversible binding to all kind of substances, which can affect the time behaviour [388]. Thus, the enzyme product carbo-dabrafenib might inhibit CYP3A4 without being converted. This product inhibition is not the case because the allocated parameters do not influence the simulated time profiles in the sensitivity analysis. As a conclusion, we assumed instead that the pH-dependent change from carbo-dabrafenib to desmethyl-dabrafenib might be dominant over a potential product inhibition.

Other drugs, such as ketoconazole, influence CYP3A4 capacity and thus dabrafenib metabolism

The previously described mechanistic ODE model on dabrafenib metabolism depends only on dabrafenib and might lack parameter identifiability because of the abundance of parameters. Perturbation of the CYP3A4 network module by another drug may help to constrain the parameter set further. Additionally, the modelling of drug-drug interaction extends the model applicability for patients with multiple medications.
To improve both parameter robustness and the predictive power of the model, we used a PK model of ketoconazole, whereby interaction between dabrafenib metabolism and the anti-fungal drug ketoconazole is mediated by CYP3A4, which modifies both dabrafenib

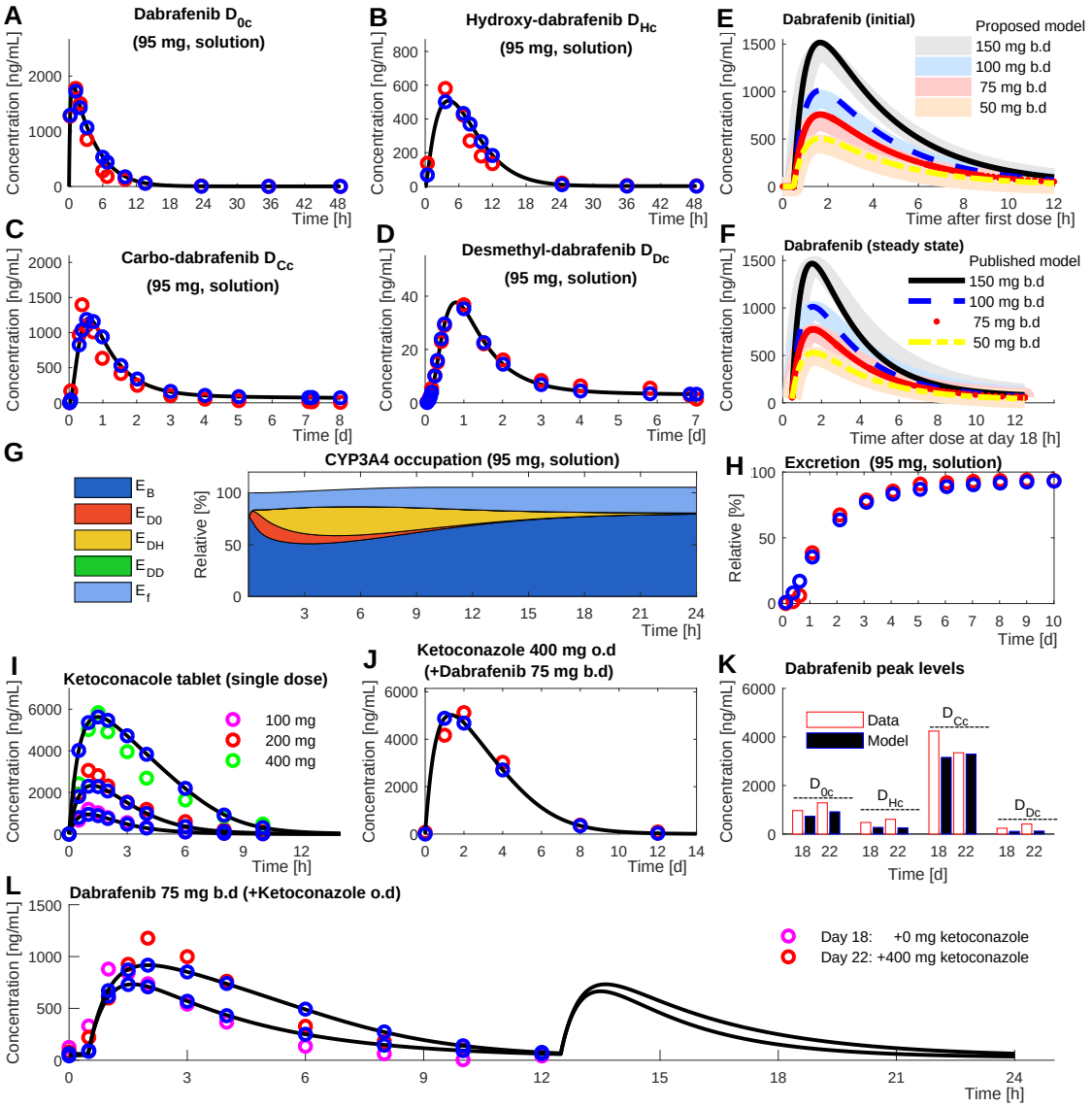

Figure 9.3: The original data sets with and the simulation result of the final model with enzyme induction. The black line with the blue circles represents the simulation result. Circles of different colour indicate experimental measurements. Bershas *et. al.* administrated once 95 mg of a [^{14}C]-dabrafenib solution to obtain the profiles of dabrafenib D_{0c} (A), hydroxy-dabrafenib D_{Hc} (B), carbo-dabrafenib D_{Cc} (C), desmethyl-dabrafenib (D), and excretion (H) [385]. The model shows the predicted enzyme occupation with slight enzyme induction (G). Ouellet *et. al.* administrated 50 mg, 75 mg, 100 mg, and 150 mg b.d dabrafenib as hypromellose (HPMC) capsule and measured the first dose (E) and steady-state (F) concentration profiles [198]. Heel *et. al.* administered once 100 mg, 200 mg or 400 mg ketoconazole in fastened patients (I). Suttle *et. al.* administrated 75 mg b.d dabrafenib for 18 days (K,L) and added 400 mg o.d ketoconazole until day 22 (J,K,L).

and ketoconazole. Each drug occupying CYP3A4 for modification reduces the enzyme capacity of CYP3A4 and thus causes an inhibitory effect. CYP3A4 converts ketoconazole into the major metabolite N-deacetyl-ketoconazole, which is consecutively metabolised by flavin-containing monooxygenase (FMO) [389]. This CYP3A4 dependent route lead to 6 ketoconazole metabolites, and we assume that the remaining 22 ketoconazole metabolites do not affect our system [389].
In order to integrate ketoconazole data, we constructed a two-compartment PK model, which describes the transfer from the oral to the central compartment, and the first step of ketoconazole catalysis. The ketoconazole module is sketched in Figure 9.1 bottom left.

Model and data align partially without enzyme induction

The model presented so far was fitted to clinical data for dabrafenib, ketoconazole, and DDI between dabrafenib and ketoconazole according to the workflow scheme (Fig 9.2), but excluded CYP3A4 enzyme induction. The total CYP3A4 enzyme concentration was initially assumed to be constant and set to one. The performed variation of all other model parameters changed the concentration levels of model elements until a maximal agreement between data and model was archived. Because each dataset has been generated under different conditions, the parameter set has to be universally valid for all experimental conditions. Therefore, each experimental condition was matched by a comparable model configuration encompassing initial concentration levels, dosage forms, and time-points of drug administration. All context-specific models were then fitted simultaneously. The following datasets have been selected and required minor model extensions for optimal data integration.
The first *in vivo* dataset showed how the blood plasma concentration of the dabrafenib metabolites changed over time [385]. In this clinical study, the dosage form was a drug solution with 95 mg radiolabeled dabrafenib. A drug solution is a dosage form that required an alternative three-compartment model, and therewith an oral compartment appeared on the top of Figure 9.1. The three-compartment model replaced the original model of Ouellet *et. al.*, which is based on the pill dosage form [198]. Moreover, the dataset contained the drug fraction measured in urine and faeces over time. The excreted end-products of dabrafenib metabolism appear as an element on the bottom right of Figure 9.1.
The second dataset about DDI between dabrafenib and ketoconazole shows time courses of dabrafenib metabolites at day 18 when administrated individually, and at day 22 if co-administrated with ketoconazole [387]. This data-set was crucial to linking the dabrafenib metabolism module with the ketoconazole module.
The third integrated dataset was used to determine the parameters of the ketoconazole pharmacokinetic module [386]. Several ketoconazole datasets were assessable whereby datasets based on patients with food intake had delayed ketoconazole peak concentrations [390]. In order to select a dataset being appropriate in the modelling context, we took into account that dabrafenib is chemically unstable and should be taken

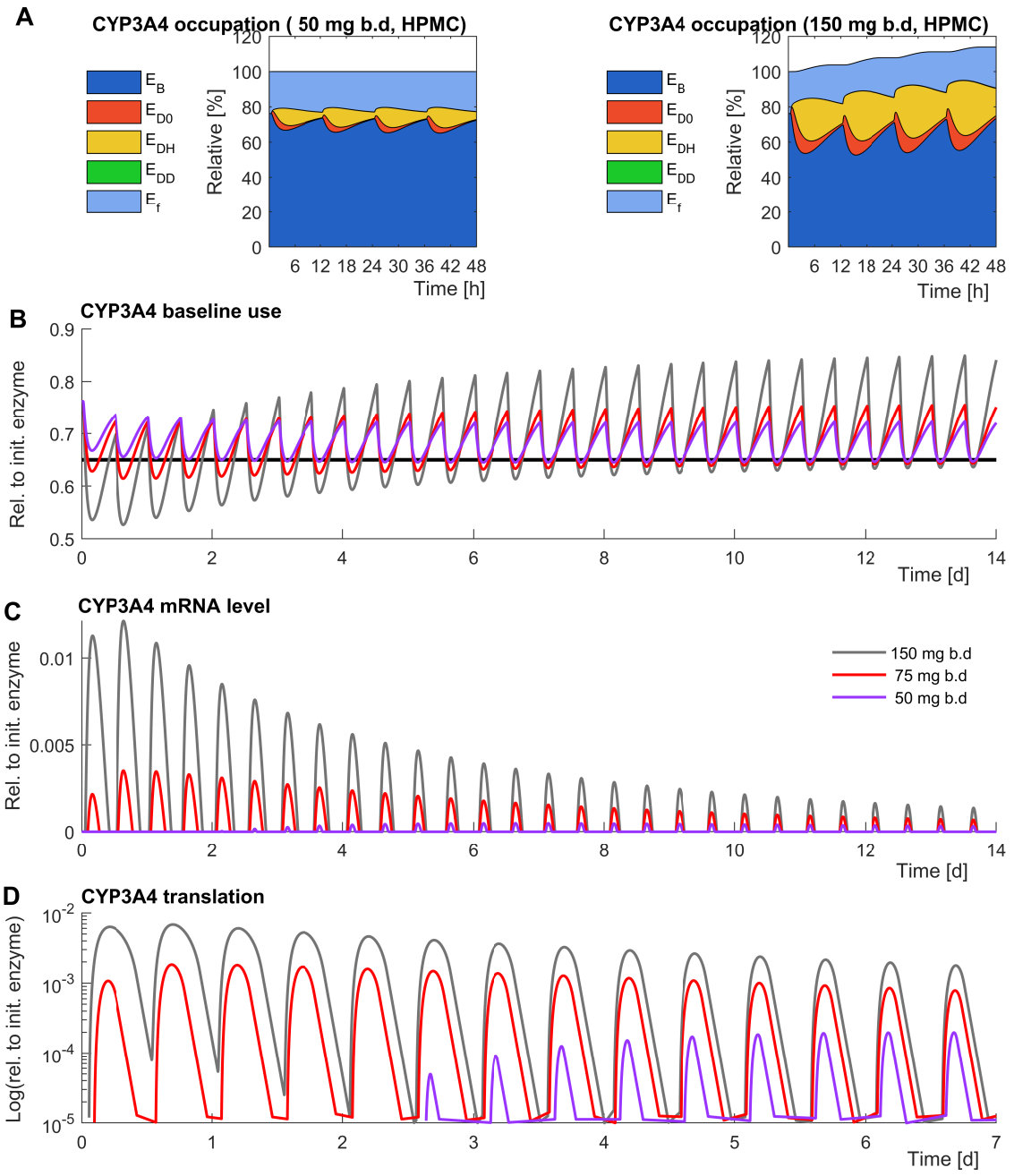

Figure 9.4: The final enzyme regulation describes the increase of CYP3A4 enzyme depending on the CYP3A4 baseline use. The enzyme occupation and induction differs for the administration of 50 mg or 150 mg b.d Dabrafenib (A). When the CYP3A4 baseline use (B) falls below the black threshold, CYP3A4 mRNA (C) is produced and finally translated to CYP3A4 protein (D). Gray: 150 mg b.d dabrafenib (HPMC). Red: 75 mg b.d dabrafenib (HPMC). Purple: 50 mg b.d dabrafenib (HPMC).

at least one hour before, or at least 2 hours after a meal according to EMA. Assuming that ketoconazole and dabrafenib are given together in the morning for the DDI study, the dataset for fasting patients has been taken as reference for the ketoconazole fit. In this study, 100 mg, 200 mg, or 400 mg ketoconazole in pill form were administrated as a single dose [386].

Identifying optimal CYP3A4 concentrations for each dose period reveals a simple enzyme up-regulation

After simultaneously fitting all profiles to the selected datasets, we obtained the preliminary fit in Supplemental Figure 2 and 3. The model underestimated dabrafenib concentrations for the first dose PK and overestimated ketoconazole and dabrafenib concentrations with periodic drug administration for two weeks. This misfit was expected under conditions omitting CYP3A4 induction. The CYP3A4 level was too high for the first-dose dabrafenib measurements and was too low for the drug levels after periodic drug administration for two weeks. In order to overcome the model inadequacy, the CYP3A4 level had to change over time, and an underlying mechanism for CYP3A4 enzyme induction had to be identified. In order to understand the underlying enzyme induction mechanism, it was necessary to identify the temporal change of CYP3A4 levels in workflow step two (Figure 9.2). Therefore, the parameter of the previously developed model got fixed, and the total CYP3A4 enzyme concentration was varied for each dose period. The resulting concentration change pattern of CYP3A4 and other model elements served as orientation for workflow step three.

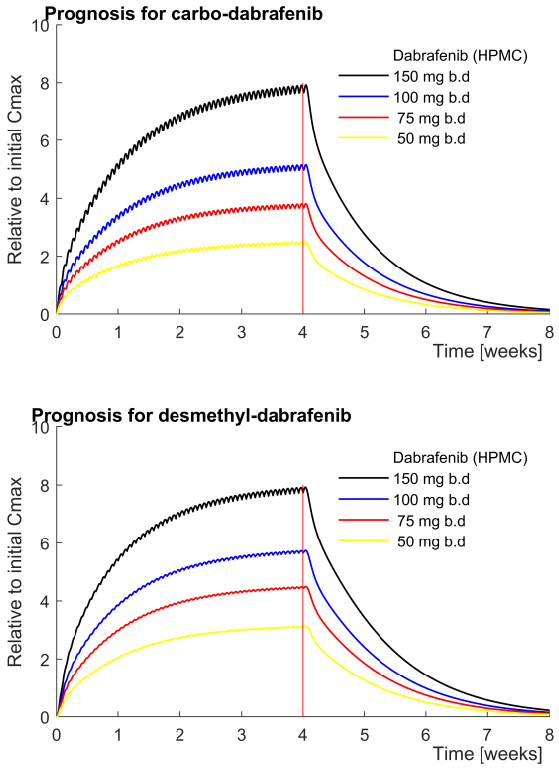

Figure 9.5: Model prediction and experimental outcome. The model shows the drug accumulation of carbo-dabrafenib and desmethyl-dabrafenib for clinical efficient doses of dabrafenib [374]. The maximal metabolite plasma concentration after 4 weeks is approximately doubled for 50 mg b.d dabrafenib compared to the first dose and is eight-fold for 150 mg b.d. dabrafenib. Four weeks after drug discontinuation, drug metabolites almost completely left the system.

The model was fitted to the trough concentration [198], which provided information about

a potential drug accumulation or a change in the clearance rate over time. The trough concentration is the lowest drug level reached in each dose period before the next dose is administrated, and it declines with an increased enzyme concentration. The dose period lasts 12 hours for dabrafenib. For 150 mg b.d dabrafenib, the trough concentration dropped immediately [198], indicating a fast induction of CYP3A4. Contrary, administration of 50 mg b.d dabrafenib caused an accumulation of the trough concentration for a couple of days before the trough concentration slowly declined [198], in this case suggesting a delayed and slow CYP3A4 induction.
In workflow step two, the total CYP3A4 concentration was adjusted for each drug period to reach the published trough concentration for 50 mg, 75 mg, 100 mg, and 150 mg b.d dabrafenib [198]. The determined enzyme levels revealed a simple saturation pattern with dose-dependent maximal levels of enzyme induction (Supplementary Figure 4). Because the CYP3A4 level pattern is less complex than the pattern of the trough concentration [198], the underlying regulatory mechanism must also be simpler than initially expected, which facilitated the control design in the next step.

A three-parameter model of enzyme regulation is sufficient to bring the whole PK model in agreement with the data

The identified saturation pattern of the enzyme increase might be best generated by a simple negative feedback loop with three parameters as shown in Figure 9.1 top left. Therefore, we assumed that a fraction of the total amount of CYP3A4 serves as catalyst for unknown metabolic processes *in vivo* E_B. The regulatory motif states that enough CYP3A4 must be dedicated to baseline processes to avoid the generation of additional CYP3A4. Accordingly, the difference between a threshold of minimal enzyme availability for baseline processes T_E and the actual level of enzyme performing baseline work correlated best with the change in total CYP3A4 enzyme level, being depend on the mRNA translation rate k_t (Supplementary Figure 4 E and F). This mechanism ensures an optimal CYP3A4 level, which depends on the situational demand of CYP3A4.
After rationalizing the assumption of a negative feedback loop as a mechanism for enzyme induction, the regulatory motif was implemented in the main model and several fitting circles refined the complete parameter set (Table 9.1). The three-parameter-model for the regulation brought the model in agreement with clinical data sets (Figure 9.3). The final model delivered the expected CYP3A4 occupation for different drug doses and the time behaviour of the CYP3A4 regulatory elements as shown in Figure 9.4. We obtained instant and strong CYP3A4 production in response to 150 mg b.d dabrafenib and a delayed and slower CYP3A4 production for 50 mg b.d dabrafenib. Both are in agreement with the published trough concentration [198]. The simulation showed a moderate underestimation of longtime metabolite concentrations in Figure 9.3 E and K, whereby the model remained qualitatively correct except for the carbo-dabrafenib bar in Figure 9.3 K [387].
The enzyme induction motif enabled a sufficient data fit and was based on both simulated profiles from workflow step two and experimental data on the trough concentration. The

assumed regulation finalizes the dabrafenib specific modelling process. Because the model assumptions and the data selection were comprehensively substantiated and the model size was kept small in relation to the data, the following model prediction gained creditability.

Table 9.1: Estimated parameter for dabrafenib metabolism

name	value	name	value	name	value
k_D (sol)	4.55	k_{1b}	8.63	k_{4f}	2.26
$VcFS$	40.1	k_{1r}	13.5	k_{4v}	1.18
$VpFS$	240.2	k_{1f}	2.72	k_{4km}	8.8
QFS	0.98	k_{2b}	39.4	k_{5b}	24.0
k_K	1.83	k_{2r}	11.1	k_{5r}	5.05
VcK	51.05	k_{2f}	0.62	k_{5f}	1.03
FU	0.02	k_{3v}	0.14	k_{6b}	5.76
T_E	0.65	k_{3km}	17.28	k_{6r}	1.79
k_t	0.61	k_{4b}	2.16		
k_{RNAdeg}	10.107	k_{4r}	20.2		

Model predicts substantial accumulation of carbo-dabrafenib and desmethyl-dabrafenib

The proposed model predicts the accumulation of inactive carbo-dabrafenib and active desmethyl-dabrafenib. As shown in Figure 9.5, the curves have a saturation profile, and while the accumulation occurred mainly in the first two weeks, the steady-state concentration was reached after four weeks. After therapeutic discontinuation of dabrafenib, four weeks are required to reach full clearance of carbo-dabrafenib and desmethyl-dabrafenib in the blood plasma. At the steady state values after 4 weeks, we obtained the following peak concentration fold-changes. For 150 mg b.d dabrafenib, Cmax for both carbo-dabrafenib and desmethyl-dabrafenib increased 8-fold, for 100 mg b.d dabrafenib increased 4-6 fold, and for 75 mg b.d increased 3-4 fold, respectively. The dose 50 mg b.d (100 mg daily) performed almost as good as 150 mg b.d. across various criteria in the dose selection study [374]. However, the accumulation of metabolites is only two-fold for 50 mg b.d dabrafenib and also the absolute concentrations are lower.

Higher dabrafenib concentrations have reduced killing potential and occasionally enhance tumour outgrowth in three-dimensional cell-culture

In order to underline the relevance of elevated active desmethyl-dabrafenib levels, we performed three-dimensional cell culture and evaluated the drug efficiency for higher dosages. Spheroids consisting of LU451 melanoma cells were embedded into fibronectin supplemented hydrogels and were left untreated for four days to ensure a physiologically realistic accommodation. Subsequently, spheroids were exposed to 10 nM, 50 nM, and 100 nM, respectively.

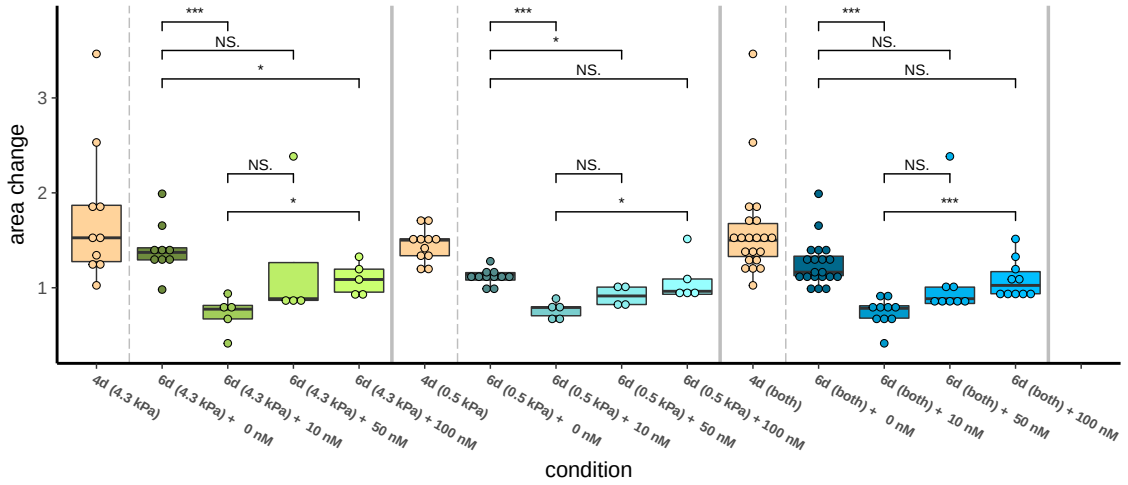

Figure 9.6: Higher doses of dabrafenib lose melanoma killing potential in three-dimensional cell culture. Melanoma spheroids being embedded in fibronectin-coated dextran hydrogel with a mechanical shear modulus of 0.5 kPa (soft) and of 4.3 kPa (hard). The right plot combines the data in the previous two plots. The drug administration on day 4 and the control at day 6 show the spheroid size normalised to day 0 and day 4 respectively. 10 nM dabrafenib result in a significant reduction in size while this effect gets lost for the higher doses of 50 nM and 100 nM dabrafenib. The source code for this figure is in the *Supplementary_Code_6.r*. The code for image quantification and the images of the two outlier are provided in the Supplementary Information. * * *: $p < 0.001$,**: $p < 0.01$, * < 0.05.

The concentration of 10 nM dabrafenib caused a significant reduction in the spheroid area as expected (Figure 9.6). However, 50 nM and 100 nM dabrafenib lacked a significant effect on spheroid area. Additionally, 100 nM dabrafenib was significantly less efficient than treatment with 10 nM dabrafenib. Two spheroids, exposed to high levels of dabrafenib, had an extended outgrowth compared to untreated spheroids and are shown in the Supplementary Figure 5; however, the reason for this occasional behaviour is unknown. The model predicted that desmethyl-dabrafenib accumulates in the blood plasma and needs four weeks to leave the system after treatment discontinuation. We showed that the parent drug loses efficiency in higher doses which raise concerns about elevated desmethyl-dabrafenib levels *in vivo*.

9.4 Discussion

We propose a mechanistic model of dabrafenib metabolism, which extends the dabrafenib model of Ouellet *et. al.* [198] to dabrafenib metabolites, mechanistic CYP3A4 induction, and drug interaction with ketoconazole. The previous model described four different drug doses for both the initial period and under steady-state conditions after periodic dabrafenib administration for two weeks [198]. The new model has 28 additional parameter but accounts therefore for 11 supplementary time courses on dabrafenib metabolism, ketoconazole, and ketoconazole-dabrafenib interaction (9.3) [198, 385–387].

The extended model is a single interacting system and coincides with the already published PK profiles in their respective experimental context. It is based on the reaction network theory and the mass action law, which allows a high degree of mechanistic detail. Mechanistic models can extrapolate, interpolate, and predict to the extent that is supported by the available data and constrained by the underlying model assumptions. This inductive research approach allows a deeper functional insight than descriptive methods [168, 391].

Drug-drug interactions depend on the balance between free enzymes and enzyme-substrate complexes.

The linear-independent tracking of enzymes or enzyme-substrate complex concentrations enables an independent investigation of the enzyme CYP3A4 induction and allows an impression of the substrate occupancy of CYPs. The substrate occupancy reduces the enzyme capacity, thus the drug depletion rate, and consequently allows the construction of causal relationships for DDI without considering inhibitory terms. Mechanistic models for DDI are highly appreciated for the care of patients under multi-medication and the elderly [392], and we can show that the utilisation of the enzyme alone can explain the DDI between dabrafenib and ketoconazole.

Model is sufficient to explain DDI data but PBPK might refine it

The proposed PK model is sufficient to explain DDI between dabrafenib and ketoconazole, and the regulatory motif for the enzyme induction was necessary to make it consistent with integrated data. Each assumption might be questioned, or new experimental insight allows a more detailed modelling of a model part. For this purpose, the model code is freely accessible. Moreover, an extension to a population model might improve the representation of patient variability, and coupling with physiologically based PK might further refine the model.

Physiological modelling would give us more insight into the impact of systemic parameters on the individual PK and might clearer differ between the experimentally determined kinetic parameter and both physiological and anatomical contributions. Then, patient-specific characteristics like unusual organ sizes or amputations can be considered in the prediction of individual PK. However, we assume that the transport physiology operates on a faster time scale (minutes) than the drug clearance (hours to days). We did not explicitly model the whole body physiology and assume that its potential effects, e.g., transport rates, fall technically into our kinetic model parameters k.

In vitro data guide the model structure but only *in vivo* data guide the model fit

The experimentally determined values *in vitro* were used to determine the model structure but the model adjusted was based only on clinical *in vivo* data. Quantitative *in vitro* data is inappropriate for our kinetic parameters not only because systemic transport rates modify them but also for the following reasons:
First, the CYP enzyme capacity *in vitro* remains unclear about the enzyme capacity for the drug of interest if the enzymes are exposed to the various substrates *in vivo*. The liver detoxifies various metabolites and each CYP type takes a different part of it with consequently less CYP capacity than *in vitro* for the drug of interest.
Second, the enzyme CYP3A4 is not only present in liver but also in the intestinal duodenum and jejunum processing, e.g., almost half of a CYP3A4 substrate denoted midazolam [393]. Hence, liver microsome capacity is not representative for CYP composition and capacity of both liver and intestine.
Third, the fixation of the experimentally determined ratio of CYP3A4 (23%) to CYP2C8+ (75 %) turnover *in vitro* [375] resulted in the underestimation of the drug-drug interaction effect in a preliminary simulation. The model shows only agreement with the data if CYP3A4 itself has more impact on the dabrafenib PK than the CYP2C8+ pool. Clinical data support the tendency of the model because the inhibition of CYP2C8 with gemfibrozil had less impact on dabrafenib PK than CYP3A4 inhibition with ketoconazole [387]. The sensitivity analysis revealed that the variation of the CYP2C8+ parameter was irrelevant for the simulation outcome.
In conclusion, *in vitro* data cannot be used to directly determine the kinetic model parameters of the proposed PK model but are needed to determine the model structure. The model structure offers the flexibility to align with data but not each structure is needed to achieve it. The CYP2C8+ pool allowed a CYP3A4 independent conversion from dabrafenib to hydroxy-dabrafenib *in vivo*, but the sensitivity analysis indicated a minor impact of this structure, which was consequentially removed.

More experimental evidence might allow the consideration of NR1|2

In order to model CYP3A4 induction, we assumed that CYP3A4 levels remain constant as long as dabrafenib let enough CYP3A4 enzyme depleting the baseline metabolites. Instead of xenobiotic drugs, such metabolic baseline processes might better substantiate the evolutionary appearance of unspecific CYPs in liver and intestine. The observed correlations of CYP3A4 mRNA increase with increasing levels of investigated drugs, such as dabrafenib [375], do not prove a direct causal relationship because the above-described regulation is also able to explain the experimental observation.
Ketoconazole inhibits CYP3A activity and can slightly increase CYP3A mRNA production [394]. The inhibitory effect may arise because ketoconazole uses CYP3A4 to turn into N-deacetyl-ketoconazole. Consequently, CYP3A4 capacity is reduced for baseline processes and other drugs such as dabrafenib. The inductive effect may arise because ketoconazole

might reduce the baseline commitment of CYP3A4 below the threshold. In cell culture, a minimal enzyme induction effect has been observed [394] and if other metabolites *in vivo* reduce the enzyme capacity even further, the enzyme induction effect might be more pronounced. Or PK model has the flexibility to do so but does not enforce ketoconazole dependent CYP3A4 enzyme induction.
It has been speculated that dabrafenib may trigger the NR1I2 nuclear receptor subfamily 1 group I member 2 (NR1I2)[1] as this receptor can bind xenobiotic drugs and subsequently induces CYP induction [387], but this is not necessarily the case [395]. It is not shown to our knowledge that dabrafenib or any of the dabrafenib metabolites bind NR1I2 to induce CYPs.
It has been shown that ketoconazole blocks NR1I2 dependent CYP3A4 induction [396], but clinical studies question its effect *in vivo* [397]. Ketoconazole reaches $6000\ {}^{\mathrm{ng}}/_{\mathrm{mL}}$ in blood plasma [386], which is equivalent to 11.3 $\mu\mathrm{M}$ ketoconazole. 6-25 $\mu\mathrm{M}$ ketoconazole blocks the binding of NR1I2 with its co-activator, which results in the absence of CYP3A4 mRNA production *in vitro* [396]. However, the ketoconazole plasma level remains only a few hours above 6 $\mu\mathrm{M}$ and questions the clinical relevance *in vivo* as well as the observation that the herbal substance St John's wort induces CYP3A4 despite the presence of ketoconazole [397]. In conclusion, the *in vivo* situation differs from the *in vitro* situation by the presence of competing substrates in the liver, which must be processed by CYP3A4, and the only temporary presence of enough drug to permanently block the NR1I2 coactivator binding. Systems Biologists always start with the simplest explanations of available observations. Model extensions with more parameters require more data and are only justified if simpler models conflict with the respective observations. Because we provide the code, NR1I2 can be considered for future model extension.

Accumulating carbo-dabrafenib and desmethyl-dabrafenib concentrations are plausible

The prediction of the model revealed an 8-fold accumulation of carbo-dabrafenib and desmethyl-dabrafenib based on the currently recommended drug dose of 150 mg b.d dabrafenib. The drug accumulation is plausible because the peak concentrations of these metabolites are delayed and coincide with the administration of the next dose (Figure 9.3 C-D). Several experimental findings support our model predictions. After 18 days of 150 mg dabrafenib administration in pill form, total exposure to carbo-dabrafenib is 13.5 times higher than to dabrafenib and also 18.4 - 20.9 times higher than to the other metabolites [387]. Even for a single dose with 95 mg radiolabeled dabrafenib solution, the total exposure (AUC) to carbo-dabrafenib is 4.9 times higher than to dabrafenib [385]. But not only the ratio from carbo-dabrafenib and desmethyl-dabrafenib to the parent drug dabrafenib reverses over time, also their ratio to the initial drug period increases distinctly. After 15 days with ≥ 70 mg b.d dabrafenib, total exposure to carbo-dabrafenib was 2.78

[1] Also known as pregnane X receptor (PXR)

to 8.77 times higher than at day one, and exposure to desmethyl-dabrafenib was 12.6 to 35.0 times higher than at day one [374].
The model is mostly quantitative with rather slightly underestimated than overestimated drug concentrations and is qualitative in Figure 9.3 K except for the carbo-dabrafenib bar [387]. The reason for less carbo-dabrafenib after concomitant administration of ketoconazole and dabrafenib is not known. We considered only acidity dependent carbo-dabrafenib depletion in our model. The rate constant in the pH-dependent Michaelis-Menten term might be time variant or location dependent, which explains that desmethyl-dabrafenib accumulates faster (2.8-8.8 fold increase) than carbo-dabrafenib (12.6-35 fold increase) [374].

Acidity might shift the local balance toward active desmethyl-dabrafenib

Carboxy-dabrafenib is not expected to contribute to the clinical activity because of the low potency of 1/22 of the parent drug [374]. The dabrafenib metabolites have the following declining potency: dabrafenib $>$ hydroxy-dabrafenib $\approx$ desmethyl-dabrafenib $\gg$ carboxy-dabrafenib [385]. However, acidity determines the turnover from inactive carboxy-dabrafenib to active desmethyl-dabrafenib [385]. This might lead to unknown local consequences at the tumours because tumours and cancer cells are known for their low pH environment [398]. And indeed the extracellular acidification rate of the melanoma celllines FM55-M2 and SK-MEL-28 is around 15 times higher than for melanocytes [248]. Local drug level measurements do not exist for dabrafenib metabolites to our knowledge, probably because drug measurements in tissues are currently not recommended [399].

Dabrafenib is inefficient if a high drug level and a fibronectin-supplemented environment concur

We demonstrated dabrafenib inefficiency in fibronectin-supplemented dextran hydrogel. In such conditions, high dabrafenib concentrations do not affect the metastatic melanoma cellline LU451 derived from lymph nodes. Two spheroids showed even accelerated growth compared to the control spheroids.
The administrated dabrafenib concentrations are in the physiological range. Dabrafenib reaches temporary 3000 nM in blood plasma, according to the reproduced dabrafenib PK [198] (Supplementary Figure 1). Concentration levels are likely lower in tissues and span from 3 to 100 nM dabrafenib in two-dimensional cell culture [400].
Local drug accumulations are not immediately dangerous because of the low drug toxicity of the targeted therapy [374], but adverse effects and protective environments can emerge [12]. A reactivation of pMAPK1 can be technically reproduced with melanoma spheroids embedded in stiff and fibronectin supplemented hydrogels following vemurafenib treatment [12]. Similar adverse effects of vemurafenib were found for a variety of cell lines and tissue microarrays in dependence on fibronectin [194] as well as in fibronectin supplemented three-dimensional collagen gels [221]. The adverse effect is thus known for vemurafenib, but we showed this effect also for dabrafenib albeit the effect is slightly weaker as we

worked with higher doses. But also *in vivo*, BRAF inhibitors can trigger growth behaviour to different extents. Vemurafenib, dabrafenib, and encorafenib were reported to cause neoplasia such as squamous cell carcinoma in 22%, 6%, and 3.7% of the cases, which is in alignment with our experimental observations. Squamous cell carcinoma can originate in BRAF wild-type expressing keratinocytes after a brief hyper-activation of pMAPK1 [401]. Drug resistance required either fibronectin supplemented three-dimensional cell culture or a *in vivo* model. Three-dimensional cell culture better mimics the architecture and behaviour of avascular metastasis *in vivo* than two-dimensional cell culture [Vörsmenn 2013; Müller 2018].
Recent developments in cancer research explain this effect by the matrix stiffness and the fibroblast product fibronectin [12]. Fibroblasts switch the phenotype of melanoma cells to the mesenchymal state by shifting the signalling to the PIK3CA/MTOR pathway [13]. The epithelial-mesenchymal transition and metastatic potential are affected by the mechanical characteristics of the environment [130, 132], whereby lack of differentiation between soft and hard gel indicates that the presence of a mechanical environment is sufficent. Fibronectin links the mechanical cues in the environment via the mechanosensor PTK2 into intracellular signals such as MAPK1, PIK3CA, Rho associated coiled-coil containing protein kinase 1 (ROCK1)-rhodopsin (RHO) whereby mechanical cues influence via other ways also Wnt and TGFB signalling and control the YY1AP1/TAZ mediated hippo signalling [277, 402]. It is increasingly accepted that cells reveal non-cell autonomous resistance mechanisms [157] which also require the targeting of the stroma [403]. The recent development shows the importance of three-dimensional cell-culture systems for drug testing before clinical trials are performed [404].

Dabrafenib might be overdosed

This study showed that the current dose of 150 mg b.d dabrafenib might be too high, which leads to counter-intuitive ramifications in the long term. The recommendations of the regulatory authorities might be re-evaluated. The drug dose could be reduced, and occasional therapy breaks might be considered to allow carbo-dabrafenib and desmethyl-dabrafenib to leave the system. According to the former drug selection study, 75 mg b.d is almost as efficient as 150 mg b.d. dabrafenib, whereby the low sample size, strong variability and occasional dose escalation requires the judgement of experienced clinical scientists [374]. Our model does not account for patient variability and has an incomplete explanatory power consequently for the individual dose decision, which can better be accounted for in physiologically based pharmacokinetics [383] and population models [198]. However, the paradigm to give rather more than less seem to be outdated. The model codes are attached and can be modified and extended depending on further research questions and regulatory expectations.

9.5 Methods

Model structure

The proposed model is based on the original model of dabrafenib PK [198] and the related parameter. The original model by Oeullet *et. al.* is reproduced and discussed in the Supplementary Information. We replaced the descriptive terms for drug clearance by the enzymatic clearance of dabrafenib in the central compartment $CL_{met}(D_{0c}, t)$:

$$\begin{aligned}\frac{dD_{0c}}{dt} &= -\frac{\frac{Q}{F}}{\frac{V_c}{F}}(D_{0c} - D_{0p}) + \frac{k_D \cdot D}{\frac{V_c}{F}} \cdot e^{-K_D \cdot (t - t_{lag})} \\ &\quad + CL_{met}(D_{0c}, t) \\ \frac{dD_{0p}}{dt} &= +\frac{\frac{Q}{F}}{\frac{V_c}{F}}(D_{0c} - D_{0p})\end{aligned}$$

The data on drug metabolism was obtained after administration of a dabrafenib suspension, which is expected to cause another PK profile. The alternative three-compartment model for a dabrafenib solution

$$\begin{aligned}\frac{dD_{0\text{oral}}}{dt} &= -k_D \cdot D_{0\text{oral}} \\ \frac{dD_{0c}}{dt} &= -\frac{Q_{Ds}}{V_{Dc}}(D_{0c} - D_{0p}) + \frac{k_D \cdot D_{0\text{oral}}}{V_{Dc}} + CL_{met}(D_{0c}, t) \\ \frac{dD_{0p}}{dt} &= +\frac{Q_{Ds}}{V_{Dc}}(D_{0c} - D_{0p})\end{aligned}$$

accounts for the concentrations in the oral $D_{0\text{oral}}$, central D_{0c}, and peripheral D_{0p} compartment.
We modelled the ketoconazole PK with a two-compartment model

$$\begin{aligned}\frac{dK_{oral}}{dt} &= -k_K \cdot K_{oral} \\ \frac{dK_c}{dt} &= \frac{k_K \cdot K_{oral}}{V_{Kc}} - k_{5b} \cdot E_f \cdot K_c + k_{5r} \cdot E_K\end{aligned}$$

representing the ketoconazole concentration in the oral K_{oral} and central K_c compartment. The time derivative d/dt on the left-hand side indicates the change of the substance over time as a consequence of the terms on the right-hand side of the equation. Each term on the right-hand side represent a quantity such as the amount of ketoconazole in the central compartment K_c that binds the free CYP3A4 enzyme E_f with the binding affinity k_{5b}. A negative sign at the term negatively influences the concentration change of the substance in the left-hand side of the equation. The quantity does not disappear because it is added to another equation representing the change of ketoconazole-CYP3A4 complex E_K. A part of the bound ketoconazole unbinds without turnover $k_{5r}E_K$. The processed part $k_{5f}E_K$ appears only in the equation for the free enzyme and the enzyme-ketoconazole

complex. The enzyme-ketoconazole-complex

$$\frac{dE_K}{dt} = k_{5b} \cdot E_f \cdot K_c - k_{5r} \cdot E_K - k_{5f} \cdot E_K$$

is modelled similar to the enzyme-dabrafenib-complex

$$\frac{dE_{D0}}{dt} = k_{1b} \cdot E_f \cdot D_{0c} - k_{1r} \cdot E_{D0} - k_{1f} \cdot E_{D0},$$

the enzyme-hydroxy-dabrafenib-complex

$$\frac{dE_{DH}}{dt} = k_{2b} \cdot E_f \cdot D_{Hc} - k_{2r} \cdot E_{DH} - k_{2f} \cdot E_{DH},$$

or the enzyme-desmethyl-dabrafenib-complex

$$\frac{dE_{DD}}{dt} = k_{4b} \cdot E_f \cdot D_{Dc} - k_{4r} \cdot E_{DD} - k_{4f} \cdot E_{DD}.$$

The unspecific nature of CYP3A4 enyzmes might lead to unfunctional competetive product binding [405] of carboxy-dabrafenib

$$\frac{dE_{DC}}{dt} = k_{3b} \cdot E_f \cdot D_{Cc} - k_{3r} \cdot E_{DC} \qquad \text{(neglected)}$$

while other dabrafenib derivatives are converted and do not represent a product competition. However, sensitivity analysis resulted in removal of these effect probably because the subsequent acidity dependent transformation

$$\frac{dD_{Dc}}{dt} = \frac{k_{3v} D_{Cc}}{(k_{3km} + D_{Cc})}$$

is dominant. The initially implemented function for E_{DC} has been removed and is not shown in Figure 9.1. Sensitivity analysis resulted also in the negligence of the CYP2C8+ pool.

$$\frac{k_{1v} \cdot D_{0c}}{(k_{1km} + D_{0c})} := 0$$

so that the enzymatic clearance of dabrafenib

$$CL_{met}(D_{0c}, t) = \underbrace{-k_{1b} \cdot E_f \cdot D_{0c} + k_{1r} \cdot E_{D0}}_{\text{CYP3A4}}$$

depends only on the enzyme CYP3A4. Thereby, hydroxy-dabrafenib is released. Hydroxy-dabrafenib depletion

$$\begin{aligned}\frac{dD_{Hc}}{dt} =& k_{1f} \cdot E_{D0} - k_{2b} \cdot E_f \cdot D_{Hc} + k_{2r} \cdot E_{DH} \\ & - \frac{Q}{V_c}(D_{Hc} - D_{Hp}) - k_{FU} \cdot D_{Hc}\end{aligned}$$

depends only on CYP3A4. The turnover from carboxy-dabrafenib to desmethyl-dabrafenib depends on an acidic environment probably in lysosomes [385]. This is also modelled with the Michaelis-Menten kinetic

$$\begin{aligned}\frac{dD_{Cc}}{dt} =& \underbrace{-\frac{k_{3v} \cdot D_{Cc}}{(k_{3km} + D_{Cc})}}_{\text{PH}} + k_{2f} \cdot E_{DH} \\ & - k_{3b} \cdot E_f \cdot D_{Cc} + k_{3r} \cdot E_{DC} \\ & - \frac{Q}{V_c}(D_{Cc} - D_{Cp}) - k_{FU} \cdot D_{Cc}.\end{aligned}$$

The final depletion of desmethyl-dabrafenib

$$\begin{aligned}\frac{dD_{Dc}}{dt} =& \underbrace{\frac{k_{3v} \cdot D_{Cc}}{(k_{3km} + D_{Cc})}}_{\text{PH}} - \underbrace{\frac{k_{4v} \cdot D_{Dc}}{(k_{4km} + D_{Dc})}}_{\text{CYP2C19+}} \\ & - k_{4b} \cdot E_f \cdot D_{Dc} + k_{4r} \cdot E_{DD} \\ & - \frac{Q}{V_c}(D_{Cc} - D_{Cp}) - k_{FU} \cdot D_{Dc}\end{aligned}$$

to other metabolites (M)

$$\frac{dM}{dt} = \underbrace{\frac{k_{4v} \cdot D_{Dc}}{(k_{4km} + D_{Dc})}}_{\text{CYP2C19+}} + k_{4f} \cdot E_{DD} - k_{FU} \cdot M$$

is mediated by CYP3A4 and the enzyme pool CYP2C19+ [375]. Each mentioned dabrafenib derivate has an allocated peripheral compartment

$$\begin{aligned}\frac{dD_{Hp}}{dt} &= \frac{Q}{V_p}(D_{Hc} - D_{Hp}) \\ \frac{dD_{Cp}}{dt} &= \frac{Q}{V_p}(D_{Cc} - D_{Cp}) \\ \frac{dD_{Dp}}{dt} &= \frac{Q}{V_p}(D_{Dc} - D_{Dp})\end{aligned}$$

equal to the classical dabrafenib model and with the original parameter as fixed values. The metabolites are excreted via faeces and urine

$$\frac{dU}{dt} = k_{FU} \cdot (D_{Hc} + D_{Cc} + D_{Dc} + M)$$

with the rate k_{FU}, whereby dabrafenib and ketoconazole are assumed to be faster metabolised than excreted. The free enzyme CYP3A4

$$\frac{dE_f}{dt} = -\frac{dE_K}{dt} - \frac{dE_{D0}}{dt} - \frac{dE_{DH}}{dt} - \frac{dE_{DC}}{dt} - \frac{dE_{DD}}{dt} - \frac{dE_B}{dt} + E_{reg}$$

can be regulated E_{reg} and does not further specified baseline work

$$\frac{dE_B}{dt} = k_{6b} \cdot E_f - k_{6r} \cdot E_B.$$

For the initial drug free condition, an index 0 is used. The free enzyme E_{f0} and the enzyme used for the baseline work E_{B0} are in balance before drugs are administrated. The analytic steady-state solution

$$E_{f0} = \frac{\frac{k_{6r}}{k_{6b}} E_{tot}}{(1 + \frac{k_{6r}}{k_{6b}})} \; ; \quad E_{B0} = E_{tot} - E_{f0} \; ; \quad E_{tot} = 1$$

was calculated and used as initial condition.
If the level of enzyme for the baseline use falls below the baseline work threshold T_E, CYP3A4 mRNA is produced to compensate for the enzyme shortage. The CYP3A4 mRNA

$$\frac{dE_{mRNA}}{dt} = \max((T_E - E_B), 0) - k_{mRNAdeg} \cdot E_{mRNA}$$

degrades with the rate $k_{mRNAdeg}$. The mRNA is translated into new CYP3A4 protein

$$E_{reg} = k_t \cdot E_{mRNA}$$

with the translation rate k_t. CYP3A4 mRNA level correlates moderately with CYP3A4 protein concentration ($\mathrm{R}^2 = 0.511$), which in turn correlates slightly better with CYP3A4 activity ($\mathrm{R}^2 = 0.64$) in a linear manner [406]. CYP3A4 protein degradation with a dependent baseline-production did not improve the model fit. Several control designs have been tested, but the number of additional parameters has not justified the improvement of fit.

Sensitivity analysis

The optimal parameter set brings model and dataset in agreement. For the sensitivity analysis, each parameter is incrementally decreased to 10% or increased to 1000% of the original parameter value. Consequentially, the time course profile and the fitting quality changes for sensitive parameters and changes not for not sensitive parameters. Two

versions for sensitivity analysis have been generated. The first version shows how the residual sum of squares (RSS) changes with the change of parameter values in respect to the measurement values. The displayed residuals are normalised by the residuals, which come from the fit with the optimal parameter set. The second version does not pay attention to true measurement values. It shows how the time profile pattern changes with the parameter change in comparison to the optimal fit time shape. Well-fitted profiles tend to have v shaped RSS profiles. Insensitive parameters have a perfectly flat RSS profile and an empty time course profile. The whole sensitivity analysis can be found in the Supplementary Information.

Optimisation and numerics

We optimised the parameter to bring the model in agreement with the PK data [198, 385–387]. We extracted the values from the publications with WebPlotDigitizer. Calculations were performed in matrix laboratory (MATLAB®) R2017b and the global optimisation toolbox. The ODE system was solved with the stiff variable-step, variable-order (VSVO) solver ode15s based on the numerical differentiation formula (NDF) with generous relative (1e-3) and absolute (1e-2) tolerances to accelerate computations. For the increasingly refined fit, absolute and relative tolerances were reduced (1e-5). Optimal enzyme concentrations were found in workflow step 2 with the single variable optimiser *fminbnd*. All other fits were reached with global optimisation, mainly with the genetic algorithm *ga*, which uses selection, crossover, and mutation rules to evolutionary approach an optimal solution. The population size was set to 20 times the number of parameters. Initial population was set in generous boundaries $0.001 < x = 0.5 < 30$. Peak concentrations were weighted considerably higher to comply with the importance of maximum concentration values for pharmacology. DDI data where weighted much higher at the beginning as it was the most difficult to achieve. Several runs were performed with boundaries being 100%, 50%, 20% and 10% around the previous solution. Each data series was seen as optimisation objective normalised to one, before the next genetic algorithm run. Occasional manual parameter adjustment for rough solution tweaking was necessary. Despite substantial progress in evolutionary multi-objective algorithms [407], an algorithm that deals with several subsequent time-courses and takes advantage of the overlapping small parameter subsets of each time course does not exist to our knowledge. This optimisation problem must be smoothed out from a central time-course along the others. Related dynamic time-course problems appear frequently in Systems Biology [408, 409].

Experimental Methods

Cellline: the GFP-positive and BRAF-mutant metastatic cell line LU451 was cultivated in RPMI-1640 + GlutaMax medium (Life Technologies, Karlsruhe, German) supplemented with 10% FBS (Thermo Scientific, Langenselbold, Germany) and 1% penicillin/streptomycin (Life Technologies). **Spheroids:** spheroids were generated in seven days with the hanging drop method. 250 cells were seeded in 25 μL RPMI

enriched with 20% methylcellulose [276]. Spheroids were injected into the hydrogel and covered with 2 mL RPMI. At day 4, spheroids were stimulated with 0, 10, 50 or 100 μM dabrafenib. **Hydrogel:** 3-D Life Dextran-CD Hydrogel SG (Cellendes, Reutlingen, Germany) was obtained by the subsequent addition of the following substances: water, 10XCB pH 7.2, dextran, fibronectin (human fibroblasts, 0.5 $\mathrm{mg/mL}$, Sigma), RPMI, CD-linker. The allocated amounts were 14.8, 2,4, 2, 1.8, 6 and 3 μL for a soft gel and 5.7, 2,5, 6, 1.8, 5 and 9 μL for a hard gel. For the determination of the shear modulus, cylindrical gel discs were cast. 67 μL gel solution polymerised for 60 min at room temperature between hydrophobic glass slices (9 mm diameter, Sigmacode). After removing the glass cover, gel discs were swollen to equilibrium overnight in medium and subsequently punched out with an 8 mm biopsy puncher. Gel discs had a height of 0.774-1.260 mm and were subjected to frequency sweep over a range of 0.01 to 100 rad/s at room temperature with an applied rotational strain of 5% and compression strain of 10% on an Ares LN2 rheometer (TA Instruments) with an 8 mm parallel plate geometry. **Imaging and analysis:** Spheroids where detected at day 0, 4 and 6 with confocal microscopy (LSM 710; Zeiss, Munich, Germany). Z-stacks were taken to quantify the area of the spheroid in a batch process with Fiji. The boundary of the detected area was projected on the original image to enable a manual quality check of the automated analysis. The Fiji code is in the Supplementary Information. A volume could not be computed because the cell line absorbed the light. Thus, only the down-pointed spheroid surface where detected. Spheroid areas of day 4 were normalised to areas at day 0, and spheroid areas of day 6 were normalised to areas at day 4 (day of treatment). Significance was accessed with the Welch's t-test implemented in the R-package *ggsignif*.

IV

Discussions and perspectives

10. Modelling irregular fibrous tissue

When thinking about cancer growth, computational scientists commonly consider the extension of an interface or volume, choose a kind of growth law, or think about an unstable dynamic system. However, tumour growth is a very tissue and cancer cell-specific process that might stop or accelerate in a complex interplay of intracellular pathways and mechanical elements. Instead of building a generic multi-scale model of melanoma, this thesis had first to re-conceptualise knowledge of several disciplines as available methods are not directly applicable to address molecular biological or medical questions. As for other interdisciplinary disciplines, such as systems biology or biomedical engineering, conceptual equivalence between mathematical description and biological observation is considered to be a top priority. Each model component needs a biological reflection to enable a decision whether a simulation behaviour is biologically reasonable or not. During the project term, it became increasingly clear that the multifariousness of the problem requires the interdisciplinary development of mathematical histology. Mathematical histology might help to study how biochemical pathways influence the mechanical, physiological, and structural state of tissues and how these anon influence biological pathways and drug resistance. Mathematical histology might also study the transferability of results from 2D or 3D cell culture to clinically relevant research questions, which also fulfil the justified high standards of pathologists. Therefore the elements have to be distinguishable present and not lumped to an abstract single or two-phase system. The thesis shows that tumours represented by the TCAT framework can switch between invasive and solid growth but many other considerations drove the project and may require evaluation:

- Tumour growth is slow and develops over days, months, or years. Challenging thermodynamic effects of non-equilibrium active matter might arise the faster the changes are. We assume that thermodynamic effects are sufficiently captured with methods being designed for slow non-equilibrium thermodynamics. Iteration steps of around 5 to 20 minutes might be justified.
- With a slow growth rate, biological regulation becomes a dominant factor whereby the quasi-steady-state assumption applies to signalling events. If the mechanical deformation is faster than the response time of cells, the system simplifies to typical engineering models, which do not require a deep understanding of biological regulation.
- Thermodynamic properties can be used to constrain metabolic pathways or molecular motors. However, tumours are living systems. Living systems have the ability for negative entropy at the expense of the environment. As tumours are often coupled with the cardiovascular system and obtain energy from there in the form of nutrients, it is not clear where the system's boundaries can be set to use an entropy constraint. Additionally, while physical supply might be restrictive and can be modelled, biological systems will dynamically adapt to outbalance shortages in ways that are not directly accessible. This dynamic self-regulatory capacity of living systems can prevent a useful physical description. If thermodynamic rules are employed, they might be restricted to the dead matter components such as the extracellular matrix, biochemical circuits, and molecular motors. Processes of living matter, however, like cells or tissues obey laws of biology, especially the genetic information in the DNA. A combination of the thermodynamic description of dead matter and biologically description of living matter might be required to describe tumour growth, while the modeller has to decide whether a phenomenon behaves predominantly physically (dead matter) or biologically (living matter).
- Moving tumour interphases itself might be useful to achieve real-time simulations of tissue to guide surgeons, but they are not suitable to understand potential drug interventions and tumours itself. Biological cells usually have no feeling for larger scale geometry. Thus, cellular signalling and adjustments are microscale-effects and respond to local physical cues, which requires the attention to the effects in the tumour volume, not to the tumour interface geometry.
- Crucial information of the ECM such as the relaxation modulus, the elastic modulus, and the differentiation between compressive and tensile stress are biologically meaningful.
- Each tumour is unique and does not obey a generic master growth model. Each cancer type is further classified into different cancer sub-types.
- Tumour growth is tissue specific. Melanoma is expected to grow within brain in another way than within dermis or epidermis.
- Growth is cell line specific and depends on the mutation status.
- Growth is environment specific and is partly driven by mechanisms of tissue

homoeostasis.

- Growth is spatially and temporarily different and is reflected by tumour heterogeneity and the unique histological representation. Also the different progression stages or categories are meaningful.
- Understanding the conditions of proliferation and renewal in healthy tissue is key to understand growth in malignant tissue. In a first step, a causal growth model should be able to mimic dynamic tissue equilibrium without cancer cells. For example, the constant turnover of keratinocytes within the epidermis might be mimicked.
- A causal growth model should prioritise the characterisation of obstacles to growth and then consider how a tumour circumvent these obstacles. Cellular growth potential is essential but is not necessarily sufficient to enable growth, and the model should reflect this by default. Only if enough obstacles are defeated, the model should allow the growth potential to turn into physical growth.
- A causal growth model has to be thought twice. One needs a mechanical growth model to represent the histology and a cellular control unit to steer this mechanical model. The cellular control unit is a biochemical reaction network that actively responds to external cues. The endpoints of cellular signalling need representation in the mechanical growth model, and each element in the mechanical model has to be investigated for potential control by the cells.
- Cells matter in growth models. From the mechanical engineering perspective, they might be too weak to resist stress compared to the ECM, but their presence can control IFF within the tissue and thus viscosity because they encapsulate fluid. Moreover, cells modify and determine ECM amount and composition in response to stress.
- If a relationship is unclear, it helps to consider the purpose of the mechanism, to think about evolutionary forces, and to identify favourable set points.
- A causal growth model has elements that can be directly linked to experimental data and biological mechanisms. Even if a parameter cannot be assessed, it must be evaluated whether this parameter is in realistic ranges.
- A valuable growth model requires not only experimental orientation points but might also benefit from parameter range as done for constrained-based models.
- Parameters obtained in unrealistic experimental settings or settings that do not fit the modelled tissue conditions are highly questionable.
- Parameters can be obtained from experiments unrelated to tumour growth as long as the experimental setting represents the element in the growth model.

10.1 Swelling within the interstitial space is meaningful

The novelty of this PhD candidate work lays, *e.g.*, in the consequent distinction between collagen and GaG in the behaviour of tissues, their impact on the mechanical deformation of tissues, and how these deformations feedback to biochemical pathway alterations and

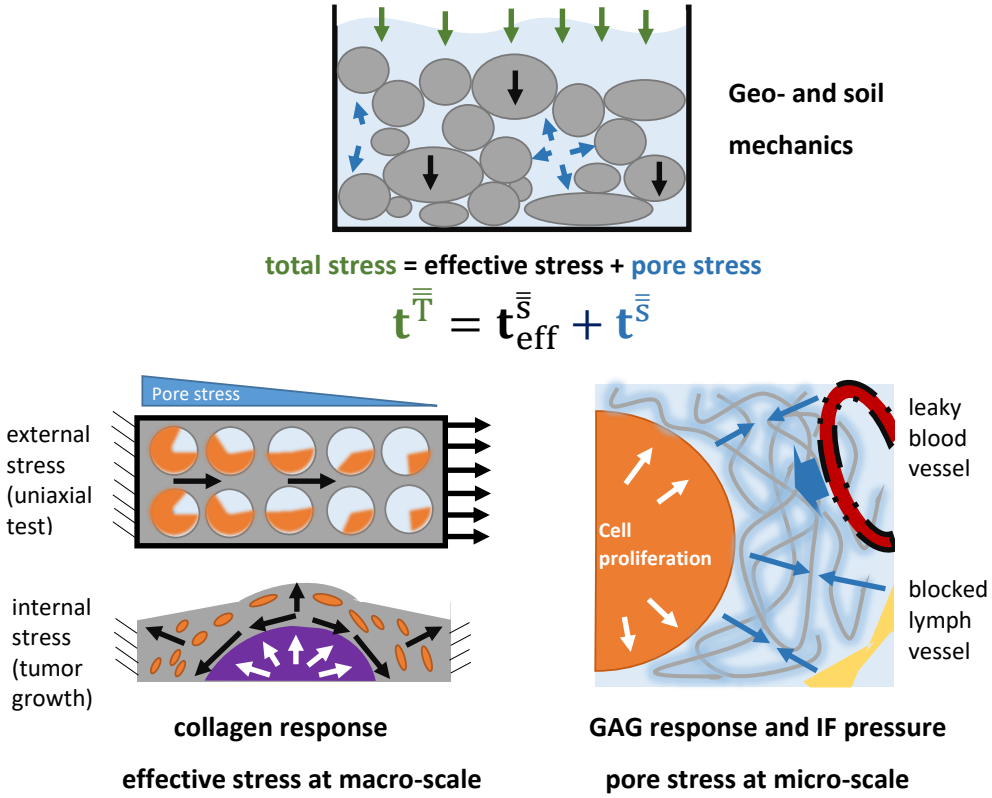

Figure 10.1: Upper picture and then clockwise: the total stress above bulk solids reduces in lower located stones and sand grains to effective stress because of the hydrostatic pressure in the pore space act uniformly and also upwards. In the pore space of organic tissues, increasing cellularity cause pressure on the extracellular matrix and increase solid stress. Moreover, the coincidence of leaky blood vessels and blocked lymph vessels might elevate IFP up to the pressure within microvasculature. At the macroscale, the tumour grows within tissues and makes ECM fibres circumferentially aligned and stretched, which leads to tensile stress at the tumour margin and thus collagen response. The collagen response is also activated if tensile stress acts externally on a tissue. Pore stress increases in consequence of increasing pore saturation with cells.

drug resistance. Both collagen and GaG influence mechanoregulatory signalling pathways but with different mechanisms as described in the review paper presented in Chapter 7. After parameters have been collected in Appendix D, which were needed for the TCAT framework described in Appendix B, it became clear that the ECM-fibres make up a tiny volume fraction far below currently assumed values. Consequently, it was suspected that a part of the IF must be immobilised to the ECM. Thus, papers have been checked to learn more about absorbent polymers [79, 410], the Flory-Rehner theory [411], and its application in food science considering porous media [411, 412]. It turned out that GaGs are polyelectrolytes, which need special modelling efforts [343, 413, 414]. The thesis proposes that the contribution of GaG does not influence the solid ECM phase directly, but that it rather mediates how forces from cells and interstitial fluid transfers to the ECM.

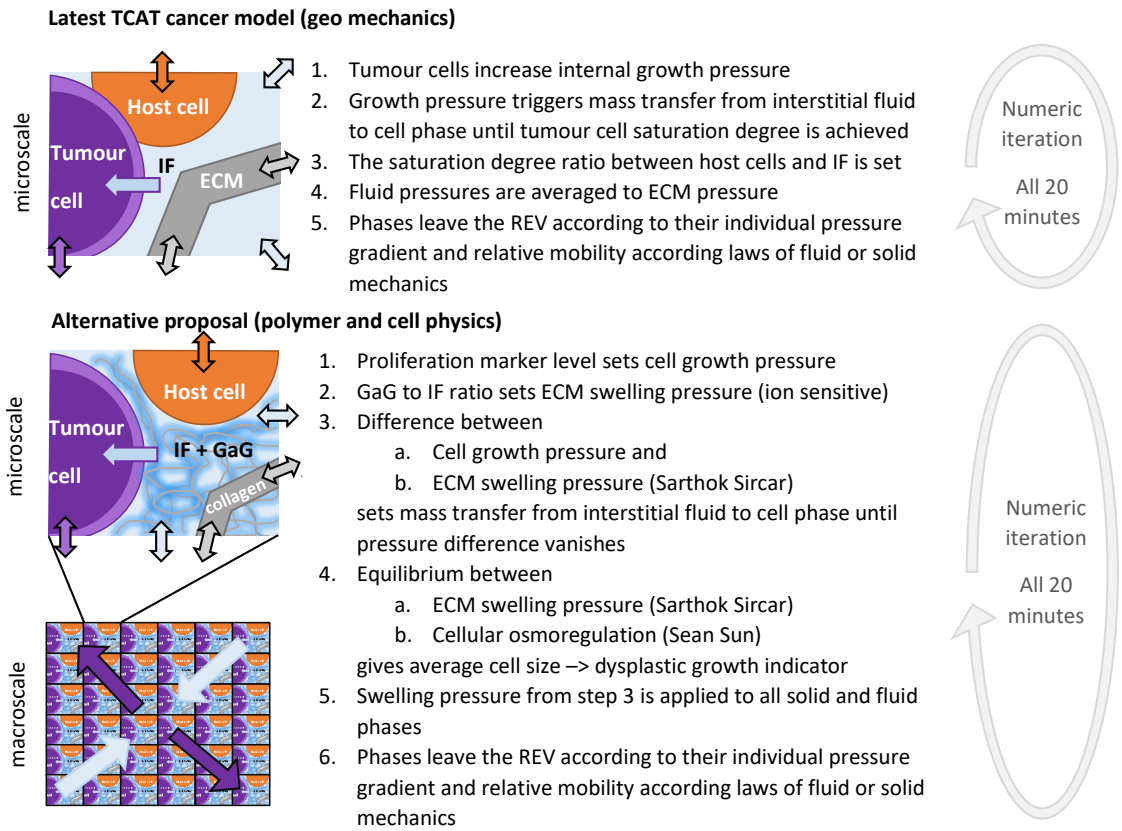

Figure 10.2: Proposed algorithm modification for TCAT cancer growth models. The multiphysics approach might shift from geomechanical rules to polymer physics.

It also motivates that the poly-electrolytic characteristic of GaG, described in Appendix C, modify on the one hand the IFF and thus the viscous response of tissues and on the other hand might facilitate cellular migration as secreted ions could locally open the space. This functional characteristic of GaG seems to rely more on the dynamic swelling behaviour and less on the physical presence of the polymers themselves. Combining both computational frameworks, TCAT and swelling polymer physics, is expected to improve the understanding of IFP and IFF. Moreover, it might help understand cell migration and invasion in tumours, drug delivery, and tissue pathophysiology. Figure 10.1 summarises some of these phenomena and relates pore pressure effects with polymer swelling effects. The polyelectrolyte mucus is a good example to illustrate the importance of the swelling effect. Mucin polymers are crosslinked by Ca^{2+} and in a compact form within intracellular visicles before they are released into the environment. The ion exchange with sodium in the environment leads to an explosive volume increase up to the 600-fold within seconds [343].

Tissues with inner transformations or tissues with impairment of moisture regulation are theoretically well represented by this combination of porous multiphase and soaked polymer network theory. Polymer physics provides information on water binding capacity and the interrelation between IFP, solid pressure, and growth pressure in a physiological

context with parameters, which can be determined with polymer experiments outside of tissues. Experimentally determined ratios between collagen and GaG deliver microscale information about the immobilised water in the interstitium, which has otherwise to be ascertained from macroscale behaviour. The only information needed is the volume fraction of collagen and its ratio to GaG. Interesting might be the case differentiation between IF volume exceeding polymer absorption capacity and absorption capacity exceeding IF volume. The latter case might influence the intracellular fluid holding capacity as the osmotic forces within the cell compete with the osmotic forces within the interstitial polymer.

However, the replacement of the geomechanical terms in the TCAT framework is a far reaching intervention in the implementation and the numeric solution strategy of TCAT cancer growth models. Establishing this modelling environment for cancer-specific simulation studies turned out to be not feasible during the project period. The necessary implementation, falsification, and refinement effort is not performed yet. However, Figure 10.2 might provide a feeling for the potential computational extension work and how this relates to medical and biological phenomena.

An alternative might be the consideration of physically absorbed water and capillary water [415]. However, the extension of additional phases (bound and unbound water) without data inflates only the number of undetermined parameters. To achieve water absorption, neither the ECM nor the IF phase must be technically subdivided into subfluids, which would hamper computational performance. Instead, transportation terms might directly integrate the information on the volume fraction of IF, which is not available for penetration. In addition, it might be helpful to assume that cell types are not in contact with each other and always have a polymer gel separating them. This might enable the definition of limitless numbers of cell type fluids, which mechanically interact with the system solely via one single ECM structure.

10.2 Rheology helps to adjust models across scales

Biological tissues have visco-elastic material properties, which can be measured with a plate rheometer. It has been reported that elastin and collagen fractions determine the elastic response, while the interstitial fluid fraction contributes to the viscous response [68]. Usually, a few parameters for viscosity and elasticity can be easily obtained for phenomenological models. However, because this thesis assumes linear-independent tissue components instead of single homogeneous tissue material and because the physics within the interstitial space was refined, many microscale parameters must be considered and partly identified by macroscale tests. Constructing virtual rheological testing might be an option, and a new parameter identification procedure must be adopted. After a tissue model has been set up with microscale parameters from various literature sources, it must be made consistent with the macroscale rheology. In order to reach the experimentally determined macroscale behaviour, microscale parameters have to

be adjusted until sufficient alignment is achieved at the macroscale. Therefore, the experimental settings for uniaxial-stretching, suction, indentation, and rheometry must be virtually represented.
From the experimental point of view, frequency dependent parameters are not optimal as the biologically relevant strain rate is not known. On the one hand, mechanical parameter values obtained at lower frequencies are relevant because cell proliferation is a relativ slow process. On the other hand, mechanical parameter values obtained at higher frequencies are relevant because the mechanosensor of the second kind such as PTK2 uses the contractility of the cytoskeleton to access the rheological properties of the environment [296]. Moreover, the viscous response might also depend on the time scale. On the fast time scale, IF flows between cells [98] and also through them via aquaporins [416]. The slow viscous behaviour of tissues might be based on cell shift or cell migration and on physical transfer of single polymers depending on the ECM network density [95, 417]. If tissues are exposed to long-lasting loading, cells may contribute to the viscous net ECM shift by pressure-dependent production or degradation of ECM. Thus, the careful determination of how microscale parameters relate to the microscale parameters is challenging.
The observed dextran gel response resembles the viscoelastic behaviour of the mechanical Wiechert model shown in Figure 8.2 [76] and seem suitable to replace the Kelvin-Voigt material describing the mechanical properties of the ECM scaffold in the TCAT model. The Wiechert model is an engineering concept and is composed of idealised springs and dashpots, as shown in Figure 2.6. The springs account for immediate response with maintained elastic energy, while dashpots react slowly and irreversible. The Wiechert model is composed of two parts. One part is the generalised Maxwell model that has a sequence of one spring and one dashpot. This element is repeated in parallel and considers the polymers as viscoelastic material with irreversible deformation. The second part of the Wiechert model is the parallel spring, which accounts for the crosslinking molecules and allows the reversible elastic response of the material. Reducing the effect of the second Wiechert model part is, therefore, suitable to describe the consequence of ECM cleavage. Thus, the Wiechert model can be directly linked to biology and should be used instead of the currently implemented Kelvin-Voigt material.

10.3 Many steps are needed to improve tumour modelling with TCAT

To further develop this topic, this thesis provides material for a series of subsequent papers on healthy tissues. In a first step, the pressure-saturation relationship in TCAT [418] might be replaced by a corrected version of swelling polymer physics by Sarthok Sircar as described in Appendix C. The polymer model does not have to capture all possible changes. Ion concentration alterations but might be restricted to one configuration being accompanied by a statement of which ion and pH setting is meant by the model. Then, the virtual rheometer model can be used to adjust the interstitial fluid

characteristic and the mechanical parameters until the macro-scale behaviour falls in line with experimental observations in rheology. A subsequent paper might investigate the difference between tissue and hydrogel materials in rheological tests. Then, a paper might tackle the oxygen problematic in a way that the model integrates all parameter values, obeys the need for extensive quantities, but also represent more commonly used partial pressures for medical applications. Then a system biologists might set up the equations for the mechanoregulation and a physicist might integrate the osmoregulation. Having the biochemical pathways, a control engineer has to check the controllability and observability of TCAT models and defines the ranges within TCAT models can be steered. The control theory of TCAT tissue models might be studied from the perspective of different cell types but also from the standpoint of potential drug regimens and physical therapies. With sufficient model maturation and increasing computer power, the cell phases might be replaced by computational vertex and agent models which are already very advanced in representing epithelial and embryonic tissues [3–5].

Only after these papers provided more confidence in the correct representation of healthy host tissues and the respective controllability, diseases and malignant contortions of these tissues can be addressed. The provided spheroid growth behaviour might be used to understand cancer growth in different tissues, as shown in Figure 10.3. Given the hydrogel system is mechanically well characterised, many different celllines might be tested to isolate cell-line specific parameters and to understand their growth behaviour within the given hydrogel system. By changing the environmental characteristic from hydrogel to any tissue that has been characterised before, one might get different growth patterns. These patterns can be compared with histological sections of different malignant contortions. This will not explain everything but could explain something. Adjustments and extensions of cellular pathways with connections to mechanoregulation might be studied by a system biologist until the right network configuration shifts the growth patterns realistically. The growth

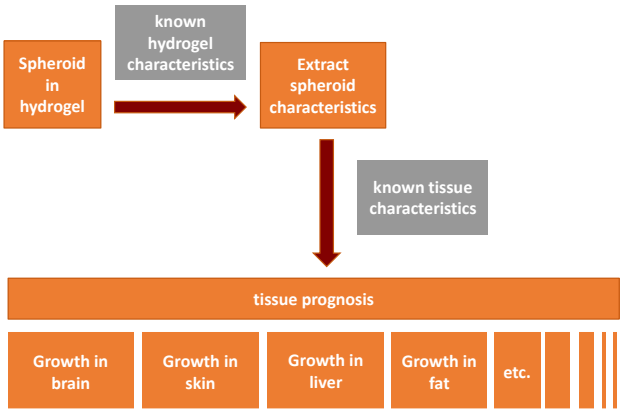

Figure 10.3: To explain a part of tumour heterogeneity and to transfer results across different tissues, a workflow must be established. One strategy might be the following. In a first step, spheroid growth experiments are performed in hydrogels of known mechanical characteristics. Simulating the growth gives the cell-line-specific parameters. With this information, one can change the settings of the environmental host tissue and can then see which clinical observations can be explained and what cannot be explained.

patterns should be approved by a pathologist. Also, studies of immune system actions might follow, such as the penetration of tissues by immune cells during inflammation.
Advanced understanding of the physiology of the dermal tissue might also greatly improve drug delivery models for topical and transdermal applications [419], which are increasingly demanded for clinical purposes, but which are often oversimplified semi-mechanistic compartment or geometric models [420, 421]. The separate modelling of tissue constitutes can thereby mechanistically follow shifts in volume fractions as observed for various diseases.
Physiologically based pharmacokinetic model software, such as PKsim and MoBi [422], contains tumour growth simulations based on agent-based, small nonlinear, or compartment models. TCAT tumour growth models might be a good implemented alternative if mechanical phenomena play a role in a particular cancer type. In this way, the model profits from age and patent-group specific body fluid distribution data and can be faster utilised for clinical research. The proposed approaches presented in this thesis might enable simulations of body fluid distribution alterations upon disturbed ion-balances and systemic shocks or could consider drug-delivery problems in tissues with mechanical contortions or pathologic ECM accumulation.
However, a credible proof-of-concept model, that is directly useful for real-world settings and promises a high return on investment, is not expected within the next five to ten years. This is in conflict with the increasing demand for fast, risk-free, predictable, and straight-forward translational research that results swiftly in products and medical treatment options. It also falls behind the promises of artificial intelligence, which might enable fast solutions without the need to understand causation.

11. Experimental hints

11.1 LU451 spheroids growth faster in stiffer environments

Following observations can be made about spheroid growth in hydrogels. The stiffer the degradable hydrogel is, the higher the growth rate is during the first six days. After seven days, the spheroids in the stiffest gel type reach a plateau, while the spheroids in the slightly weaker gel tend to develop an exponential growth phase. This cannot be said with certainty, as the two curves for the two stiffest gels are too close to each other and the shear modulus is almost similar. The stiffest gel is only $0.6\ \mathrm{kPa}$ stiffer but has 33% more polymer material per volume. The excess of material and crosslinks might not be degraded fast enough. The high amount of ECM degrading enzymes in melanoma is known [423] and must be considered in the modelling procedure. The importance of MMPs is also emphasised by the increased spheroid growth rate within the cell degradable CD gel compared to the lack of growth in the not degradable PEG gel. Consequently, the experiments point to the importance of the right balance between growth rate, polymer strength, and ECM degradation capacity.

The inspection of spheroid sizes alone does not allow conclusions about the activity of proliferation signalling pathways. The more rigid the environment is, the more growth is physically suppressed, and a proliferation signal might not turn into spheroid expansion. Mechanics reveal how far the tumour environment relents upon growth pressure and the compressed environment is then in force balance with the growth pressure. Moreover, it is also known, that the stiffness of 2D surfaces composed of polydimethylsiloxane (PDMS) has already a significant impact on cellular behaviour and morphology of melanoma celllines (WM115, WM266-4) without ECM [424]. The activation of mechanotransduction [40] is likely responsible for the increased growth in stiffer gels, which even surpasses the

additional mechanical constraints by additional polymers. However, the strong positive feedback mechanism is in contradiction to the modelling community, which assumes only increasing physical suppression following compression of the environment. The reason for these different views is fibronectin. The modelling community relies on pure collagen networks [425] whereby the decreasing compliance toward the expanding malignant mass lead to a reduced final volume. However, biological cells adjust *in vivo*, and fibronectin is needed as a mediator between mechanical stroma stiffness and the cells to activate sufficiently the mechano-homeostasis [12, 40]. However, as discussed in this thesis, hydrogels are structurally not tissue what further complicates the transferability of results and parameters.

The observed difference between CD and PEG gel-type might be caused by gel network defects, which might also facilitate the observed escaping of spheroids in the stiffer PEG gel. Compared to the stable CD gel, the frequency sweep revealed a lower elastic modulus of the PEG gel and the shift into the polymer transition phase. The cross-linker length might be an explanation. The degradable CD-linker (12 kDa) is a PEG-linker (10 kDa) conjugated with a degradable group making the CD linker longer. The PEG-linker might be too short to efficiently crosslink the dextran polymers or might lead to polymer crystallisation. Discovered gel defects were reported back to the manufacturer Cellendes, which is ready to invest in researching different crosslinker lengths to improve the gels.

Furthermore, the thesis showed the impact of the mechanical environment on drug sensitivity. As expected, pERK levels in spheroids are significantly reduced when treated for 48 h with 10 uM dabrafenib. However, If dabrafenib is highly dosed, melanoma cells become resistant within a confined and fibronectin supplemented environment.

11.2 Hypothesis network explains experimental results

In order to have an explanation of the experimental findings, an unproven hypothesis network has been created (Figure 11.1). In the context of the tumour modelling approach presented in this thesis, the network starts with the input layer with oxygen level and mechanical cues. The network output layer integrates various proliferation marker and includes a node representing MMPs. If the output layer triggers proliferation, the network feeds back to the mechanical cues in the input layer.

The network can consider a constitutive active BRAF or NRAS mutation but also reflects grow via mutation-independent pathways. The environmental cues might increasingly shift the molecular pathways to drug-resistant and invasive pathways.

In the cellular monolayer, the classical melanoma BRAF-MAP2K-MAPK1 pathway is constitutive active [373], whereby the inhibition of BRAF can intensify the same signalling pathway via paradoxical activation of Raf-1 proto-oncogene, serine/threonine kinase (RAF1) [1] [426]. RAF1, in turn, is known to be activated by SRC via connector enhancer of kinase suppressor of Ras 1 (CNKSR1) [427]. SRC can be activated by hypoxia marker

[1] Also known as RAF proto-oncogene serine/threonine-protein kinase (CRAF)

HIF1A and endothelial PAS domain protein 1 (EPAS1)[2] independently from each other [243].
The hanging-drop spheroids might differ most from cellular monolayer in the presence of hypoxic cores. The SRC/RTK pathway is able to reactivate the BRAF cascade in melanoma in a RAS-dependent manner, which suggests the use of BRAF inhibitors being also concomitantly active against SRC [428].
The SRC pool does trigger not only the PIK3CA and the classical BRAF dependent pathway, but also the mechanosensitive PTK2-PXN pathway [429]. The mechanosensitive PTK2/ SRC complex also activates the PIK3CA/MTOR pathway in fibroblast co-culture [13], whereby the amount of fibronectin is sufficient to enable the same effect in melanoma [12]. MMP are essential for melanoma progression [430]. However, in combination with PIK3CA and PTK2, it is researched more in the context of traditional Chinese medicine and nutrition [431–433]. The lack of research between cancer pathways and MMPs might be explained with the failed clinical trials and the question whether MMPs with their abundant biological functions are drugable albeit new research, *e.g.*, with "degradomics", is motivated [434–436].
A hypothesis network that directly links parameter from a tissue model and feeds back to other parameters of the same tissue is a crucial step to understand cancer. In the presented hypothesis network above, one has the melanoma-specific BRAF pathway, an oxygen-dependent PIK3CA pathway, and a mechanosensitive pathway, with cross-talk. Interestingly, one has a RAS pool that mediates between the BRAF pathway and the oxygen-dependent pathway as well as a SRC pool that mediates between the oxygen-dependent pathway and the mechanosensitive pathway. One could say that with the increasing complexity of the experimental model, the cancer pathway shifts increasingly towards the aggressive pathway that is independent of the initial deregulation. In a systems perspective, the following could happen: by blocking the BRAF pathways, RAS might have an interaction partner less and could automatically strengthen the BRAF independent pathways, and by applying forces, the equilibrium might further shift to the right side.
Albeit, this network is highly speculative and requires an intensive treatment by a system biologist, it is an attempt to explain why higher drug doses increase the proliferation marker to a certain extent. As a consequence of these observations, one can assume that the signals of biochemical networks determine the potential to grow, but that the mechanical properties of the environment and the extracellular matrix determine the translation of this potential into the final tumour/metastasis size and shape. This relationship becomes more complicated as cells respond to the stiffness in a positive feedback loop.

[2] Also known as HIF2α

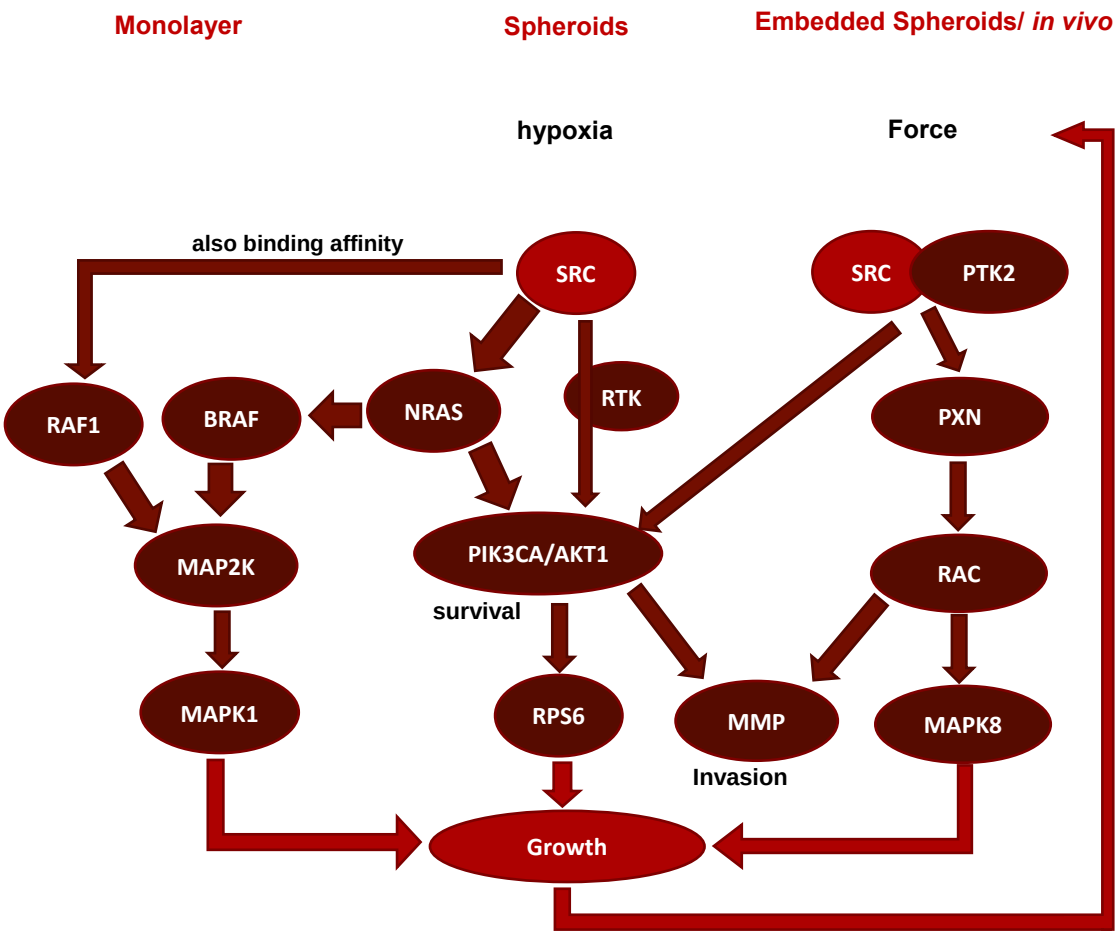

Figure 11.1: Possible biochemical network model as an explanation for the experimental results and as a potential control unit for a mechanical tissue model. Hypoxic and mechanical signals shift the signal flow increasingly toward more invasive and BRAF independent pathways.

12. Quantitative Systems Pharmacology

12.1 PK shows that dabrafenib might overdose

The discovered dabrafenib resistance and the wish to relate tissue drug concentration with the drug regimen inspired a PK-model of melanoma. The model predicts an eight-fold increase in peak concentration of the two dabrafenib metabolites carbo-dabrafenib and desmethyl-dabrafenib. As a result, the prediction supports the relevance of the previously obtained discovery that high dabrafenib doses drive melanoma cells drug-resistant if a mechanical environment encapsulates the melanoma spheroid.
The PK model itself is a rarity as only a few models use the reaction network theory to integrate several context-dependent time courses of blood plasma drug levels. Studies most commonly fit individual PK-profile independent of each other to support statistical models. The proposed model enables a mechanistic implementation of drug-drug interaction while most other approaches are purely statistical. Furthermore, the European Medicines Agency (EMA) states that currently no model sufficiently considers drug-induced changes of CYP450 enzymes, which anon influence the PK-profiles. The proposed workflow enables mechanistic insights in enzyme induction, which might allow more trust into the proposed model than purely descriptive models can expect.

12.2 Mechanistic drug-drug interaction might help physicians

The proposed PK- module is not only useful to extend a tissue model, but it is also helpful in itself. Especially the new approach to mechanistically approach drug-drug interactions is elaborate but promises better predictions beyond the ability of statistical tests. A series of future papers might stepwise add liver enzyme altering drugs to obtain a large mechanistic

network of enzymes and drugs, which can be used to interpolate and even extrapolate optimal therapy ranges for multiple medications. A translational perspective might be software for general practitioners and hospitals.

13. How a useful software might look like

Writing papers on different aspects of the TCAT framework or dedicating a paper to a specific biological problem is a good start. A TCAT model can integrate a large amount of information which can be considered helpful in times where the whole publication count in medical and health sciences double in less than eight years [437]. However, an integrated functional model is not enough. The potential of a working tissue model is larger, and different people might want to apply that framework to a large variety of questions. The traditional way to read papers and to implement these methods themselves for any single question is very time consuming, for tissue models too interdisciplinary, increasingly too comprehensive, and inappropriate for applied research. Especially because many published methods are seen increasingly sceptical [291, 438], and scientists neither know whether these models work in reality nor what is possible to do with them; a transparent, trustworthy, and easily accessible modelling strategy is needed, which is accredited by a regulatory authority such as the EMA. Potential users do not want to spent too much time anymore to figure out whether it works for them and increasingly prefer professional software and apps. It makes sense to perform the research on one tissue model once, update this model regularly at a central place, and make it available to others in a collaborative open platform such as done for physiological based pharmacokinetics [422] or agent-based models [439].

A TCAT software that might be useful for biology and medicine is shown in Figure 13.1. This proposal shows that the user might require a large variety of tissues and cell lines, which are stored in a curated database. System biologists could clamp in potential biochemical networks to achieve a *in vivo* extrapolation. If applied to different tissues, a part of environmental alterations across various tissues might be better understood, and

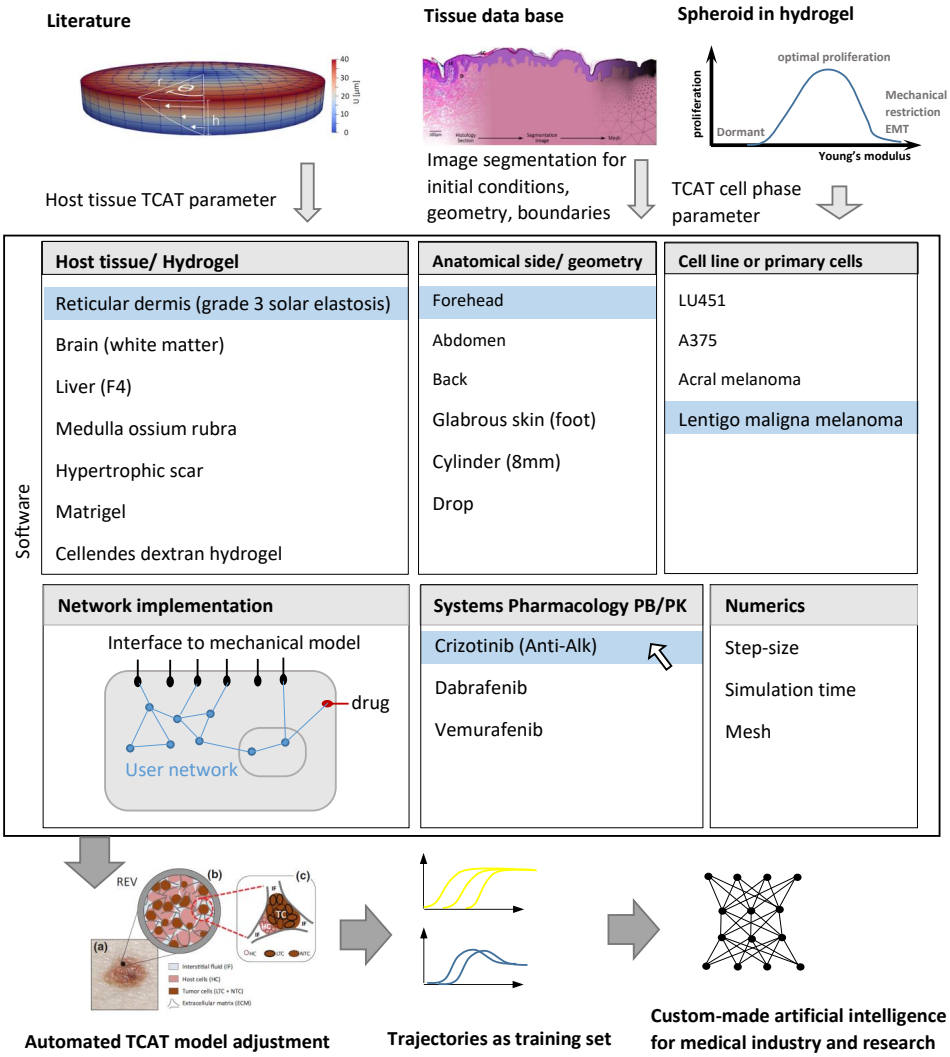

Figure 13.1: Hypothetical software functionality. Available information is saved in a database in three disjunct information areas. The first source includes all geometry independent parameters of the host tissue, including the mechanical parameter. The second source is databases with tissue sections. Segmentation and meshing algorithms can analyse sections to determine boundary conditions and initial conditions. The third source is spheroid growth trajectories depending on hydrogel stiffness. These information sources are necessary to set up a TCAT model. In addition, the user might be allowed to implement their hypothesis networks. Therefore, pathways for mechano-regulation and pathways with direct modification of TCAT associated elements are pre-implemented as well as a drug-receptor for the related pharmacokinetic model. User networks can be linked to these pre-implemented attachment points. The building blocks of the associated TCAT equations might be assembled automatically, or the appropriate TCAT equation set is selected from a pool of pre-implemented raw models. Such a model can be computationally too large and too slow. To accelerate the computation, some reference trajectories might be generated and subsequently used to train an artificial intelligence model. Therefore, nonlinear model order reduction might be performed based on local reduced-order bases as demonstrated by Charbel Farhat [440]. However, this is out of the scope of the thesis and might be a work for theoretical engineers and mathematicians. Figure source of tissue segmentation [441] & of TCAT model adjustment [415].

the diversity of growth patterns can be reflected. Thereby, comparing specific host tissue conditions can be a valuable simulation test. Most common for melanoma-associated host tissue is CSD skin with pericellular excess of elastin [15]. But also rare cases could require a model that specifically predicts the impact of altered ECM condition on melanoma growth and treatment-related pathways. For example, uveal melanoma might metastasise in the liver [444] with advanced fibrosis [445]. Or the host tissue is affected by myxedema, which is an excess of glycosaminoglycans in the extracellular space caused by hypothyroidism [446]. In one case, the melanoma anti-PDCD1-drug Nivolumab caused even a myxedema crisis [447]. Albeit such melanoma-drug associated condition is rare, the independent occurrence of multiple tissue pathologies is not. A separation from the melanocytic tumour information and the affected host tissue information might help to understand a part of the observed histopathological complexity and would reduce the combinatoric number of tumour-host-tissue combinations. Ideally, the software exports a list with all parameters, value conversion, assumptions, and associated references as PDF along with the model simulations.

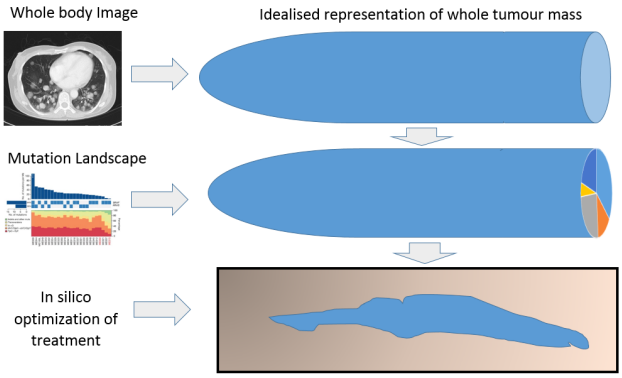

Figure 13.2: A concept of the application. Clinical image analysis gives a distribution of melanocytic lesion sizes. The mutation distribution or more likely the associated host tissue conditions are added. The programme might use this idealised approach to optimise treatment of the whole tumour load in a patient-specific manner. Source of subfigures: [442, 443].

The information of TCAT on physiology and extensions to a collection of pharmacokinetic models might further extend the applicability for the pharma industry. A strategy in this regard might be shown in Figure 13.2. Clinical images might be translated into hypothetical sausages that represent the distribution of diameters of a patient's melanocytic lesions. A circumferential distribution of genetic information, or more likely, different tissue environments further advance the representation. An algorithm might than optimise the best treatment regimen for a particular patient under consideration of biochemical pathways, physiology, and host tissue.

Consequently, the thesis merges concepts of civil and geomechanical engineering with polymer physics to approach phenomena in histology, molecular biology, and pharmacometrics. Such an interdisciplinary overview was necessary to build a better base for further development and to decide which theoretical and experimental work is still required to pursue a translational development providing applicable models.

"Everything will be okay in the end. If it's not okay then it's not the end"

Fernando Tavares Sabino (1991, Brazilian writer)

Bibliography

1. Seip, K. *et al.* Stroma-induced phenotypic plasticity offers phenotype-specific targeting to improve melanoma treatment. *Cancer letters* **439,** 1–13 (2018).
2. Albrecht, M., Sciumè, G., Lucarelli, P. & Sauter, T. Thermodynamically constrained averaging theory for cancer growth modelling. *IFAC-PapersOnLine* **49,** 289–294 (2016).
3. Sütterlin, T., Tsingos, E., Bensaci, J., Stamatas, G. N. & Grabe, N. A 3D self-organizing multicellular epidermis model of barrier formation and hydration with realistic cell morphology based on EPISIM. *Scientific reports* **7,** 43472 (2017).
4. Pietak, A. & Levin, M. Exploring instructive physiological signaling with the bioelectric tissue simulation engine. *Frontiers in bioengineering and biotechnology* **4,** 55 (2016).
5. Delile, J., Herrmann, M., Peyriéras, N. & Doursat, R. A cell-based computational model of early embryogenesis coupling mechanical behaviour and gene regulation. *Nature communications* **8,** 13929 (2017).
6. Sciumè, G., Santagiuliana, R., Ferrari, M., Decuzzi, P. & Schrefler, B. A tumor growth model with deformable ECM. *Physical biology* **11,** 065004 (2014).
7. Weinberg, R. A. Coming full circle–from endless complexity to simplicity and back again. *Cell* **157,** 267–271 (2014).
8. Whittier, L. *Pigmentation* Oregon State University. `http://library.open.oregonstate.edu/aandp/chapter/5-1-layers-of-the-skin/`.

9. Cichorek, M., Wachulska, M., Stasiewicz, A. & Tymińska, A. Skin melanocytes: biology and development. *Advances in Dermatology and Allergology/Postepy Dermatologii I Alergologii* **30,** 30 (2013).

10. Hodis, E. *et al.* A landscape of driver mutations in melanoma. *Cell* **150,** 251–263 (2012).

11. Bastian, B. C. The molecular pathology of melanoma: an integrated taxonomy of melanocytic neoplasia. *Annual Review of Pathology: Mechanisms of Disease* **9,** 239–271 (2014).

12. Hirata, E. *et al.* Intravital imaging reveals how BRAF inhibition generates drug-tolerant microenvironments with high integrin β1/FAK signaling. *Cancer cell* **27,** 574–588 (2015).

13. Seip, K. *et al.* Fibroblast-induced switching to the mesenchymal-like phenotype and PI3K/mTOR signaling protects melanoma cells from BRAF inhibitors. *Oncotarget* **7,** 19997 (2016).

14. Shain, A. H. & Bastian, B. C. From melanocytes to melanomas. *nature reviews Cancer* **16,** 345 (2016).

15. Elder, D. *WHO Cclassification of skin tumours* (Lyon: IARC, 2018).

16. Vena, G. A., Fargnoli, M. C., Cassano, N. & Argenziano, G. Drug-induced eruptive melanocytic nevi. *Expert opinion on drug metabolism & toxicology* **13,** 293–300 (2017).

17. Dadras, S. S., Lu, J., Zembowicz, A., Flotte, T. J. & Mihm, M. C. Histological features and outcome of inverted type-A melanocytic nevi. *Journal of cutaneous pathology* **45,** 254–262 (2018).

18. Rosendahl, C. O., Grant-Kels, J. M. & Que, S. K. T. Dysplastic nevus: Fact and fiction. *Journal of the American Academy of Dermatology* **73,** 507–512 (2015).

19. Behrens, D. T. *et al.* The epidermal basement membrane is a composite of separate laminin-or collagen IV-containing networks connected by aggregated perlecan, but not by nidogens. *Journal of Biological Chemistry,* jbc–M111 (2012).

20. Halfter, W. *et al.* New concepts in basement membrane biology. *The FEBS journal* **282,** 4466–4479 (2015).

21. Hoek, K. S. & Goding, C. R. Cancer stem cells versus phenotype-switching in melanoma. *Pigment cell & melanoma research* **23,** 746–759 (2010).

22. Faries, M. B. *et al.* Completion dissection or observation for sentinel-node metastasis in melanoma. *New England Journal of Medicine* **376,** 2211–2222 (2017).

23. Pickup, M. W., Mouw, J. K. & Weaver, V. M. The extracellular matrix modulates the hallmarks of cancer. *EMBO reports* **15,** 1243–1253 (2014).

24. Jonietz, E. The forces of cancer. *Nature* **491,** S56 (2012).

25. Yap, A. S., Duszyc, K. & Viasnoff, V. Mechanosensing and mechanotransduction at cell–cell junctions. *Cold Spring Harbor perspectives in biology* **10,** a028761 (2018).

26. Kirby, T. J. & Lammerding, J. Emerging views of the nucleus as a cellular mechanosensor. *Nature cell biology,* 1 (2018).

27. Freutel, M., Schmidt, H., Dürselen, L., Ignatius, A. & Galbusera, F. Finite element modeling of soft tissues: material models, tissue interaction and challenges. *Clinical Biomechanics* **29,** 363–372 (2014).

28. Kalyanam, S., Yapp, R. D. & Insana, M. F. Poro-viscoelastic behavior of gelatin hydrogels under compression-implications for bioelasticity imaging. *Journal of biomechanical engineering* **131,** 081005 (2009).

29. Carter, T. J. *et al.* Application of soft tissue modelling to image-guided surgery. *Medical engineering & physics* **27,** 893–909 (2005).

30. Delingette, H. & Ayache, N. Soft tissue modeling for surgery simulation. *Handbook of Numerical Analysis* **12,** 453–550 (2004).

31. Famaey, N. & Sloten, J. V. Soft tissue modelling for applications in virtual surgery and surgical robotics. *Computer methods in biomechanics and biomedical engineering* **11,** 351–366 (2008).

32. Holzapfel, G. A. & Ogden, R. W. On fiber dispersion models: exclusion of compressed fibers and spurious model comparisons. *Journal of Elasticity,* 1–20 (2016).

33. Nisansala, A., Weerasinghe, M., Dias, G., Sandaruwan, D. & Kodikara, N. Soft tissue modeling techniques in surgery simulation. *International Journal of Computer and Information Technology (IJCIT)* **4,** 826–831 (2015).

34. Stylianopoulos, T. & Barocas, V. H. Volume-averaging theory for the study of the mechanics of collagen networks. *Computer methods in applied mechanics and engineering* **196,** 2981–2990 (2007).

35. Chandran, P. L. & Mofrad, M. R. Averaged implicit hydrodynamic model of semiflexible filaments. *Physical Review E* **81,** 031920 (2010).

36. Lanir, Y. Multi-scale structural modeling of soft tissues mechanics and mechanobiology. *Journal of Elasticity* **129,** 7–48 (2017).

37. Xue, S.-L., Lin, S.-Z., Li, B. & Feng, X.-Q. A nonlinear poroelastic theory of solid tumors with glycosaminoglycan swelling. *Journal of theoretical biology* **433,** 49–56 (2017).

38. Lai, V. K., Hadi, M. F., Tranquillo, R. T. & Barocas, V. H. A multiscale approach to modeling the passive mechanical contribution of cells in tissues. *Journal of biomechanical engineering* **135,** 071007 (2013).

39. Barnes, J. M., Przybyla, L. & Weaver, V. M. Tissue mechanics regulate brain development, homeostasis and disease. *J Cell Sci* **130,** 71–82 (2017).

40. Humphrey, J. D., Dufresne, E. R. & Schwartz, M. A. Mechanotransduction and extracellular matrix homeostasis. *Nature reviews Molecular cell biology* **15,** 802–812 (2014).

41. Ateshian, G. A. On the theory of reactive mixtures for modeling biological growth. *Biomechanics and modeling in mechanobiology* **6,** 423–445 (2007).

42. Sciumè, G., Gray, W., Ferrari, M., Decuzzi, P. & Schrefler, B. On computational modeling in tumor growth. *Archives of Computational Methods in Engineering* **20,** 327–352 (2013).

43. Coussy, O., Dormieux, L. & Detournay, E. From mixture theory to Biot's approach for porous media. *International Journal of Solids and Structures* **35,** 4619–4635 (1998).

44. Schrefler, B. Mechanics and thermodynamics of saturated/unsaturated porous materials and quantitative solutions. *Applied Mechanics Reviews* **55,** 351–388 (2002).

45. Jain, R. K., Martin, J. D. & Stylianopoulos, T. The role of mechanical forces in tumor growth and therapy. *Annual review of biomedical engineering* **16,** 321–346 (2014).

46. Amack, J. D. & Manning, M. L. Knowing the boundaries: extending the differential adhesion hypothesis in embryonic cell sorting. *Science* **338,** 212–215 (2012).

47. Van Liedekerke, P., Palm, M., Jagiella, N. & Drasdo, D. Simulating tissue mechanics with agent-based models: concepts, perspectives and some novel results. *Computational Particle Mechanics* **2,** 401–444 (2015).

48. Jamali, Y., Azimi, M. & Mofrad, M. R. A sub-cellular viscoelastic model for cell population mechanics. *PLoS One* **5,** e12097 (2010).

49. Histology, B. *Integumentary System* School of Anatomy and Human Biology - The University of Western Australia. `http://www.lab.anhb.uwa.edu.au/mb140/corepages/integumentary/integum.htm`.

50. Sciumè, G., Boso, D., Gray, W., Cobelli, C. & Schrefler, B. A two-phase model of plantar tissue: a step toward prediction of diabetic foot ulceration. *International journal for numerical methods in biomedical engineering* **30,** 1153–1169 (2014).

51. Gray, W. G. & Miller, C. T. *Introduction to the thermodynamically constrained averaging theory for porous medium systems* (Springer, 2014).

52. Wiig, H. & Swartz, M. A. Interstitial fluid and lymph formation and transport: physiological regulation and roles in inflammation and cancer. *Physiological reviews* **92,** 1005–1060 (2012).

53. Mow, V. C., Wang, C. C. & Hung, C. T. The extracellular matrix, interstitial fluid and ions as a mechanical signal transducer in articular cartilage. *Osteoarthritis and Cartilage* **7,** 41–58 (1999).

54. Prasertsung, I., Kanokpanont, S., Bunaprasert, T., Thanakit, V. & Damrongsakkul, S. Development of acellular dermis from porcine skin using periodic pressurized technique. *Journal of Biomedical Materials Research Part B: Applied Biomaterials* **85,** 210–219 (2008).

55. Anatomy, L. & Physiology. *Dense Connective Tissue* University of Michigan Medical School & William Marsh Rice University. https://courses.lumenlearning.com/nemcc-ap/chapter/connective-tissue-supports-and-protects/.

56. Badylak, S. F., Freytes, D. O. & Gilbert, T. W. Extracellular matrix as a biological scaffold material: structure and function. *Acta biomaterialia* **5,** 1–13 (2009).

57. Crapo, P. M., Gilbert, T. W. & Badylak, S. F. An overview of tissue and whole organ decellularization processes. *Biomaterials* **32,** 3233–3243 (2011).

58. Mayorca-Guiliani, A. E. *et al.* ISDoT: in situ decellularization of tissues for high-resolution imaging and proteomic analysis of native extracellular matrix. *Nature medicine* **23,** 890 (2017).

59. Nia, H. T. *et al.* Solid stress and elastic energy as measures of tumour mechanopathology. *Nature Biomedical Engineering* **1,** 0004 (2016).

60. Stylianopoulos, T. *et al.* Causes, consequences, and remedies for growth-induced solid stress in murine and human tumors. *Proceedings of the National Academy of Sciences* **109,** 15101–15108 (2012).

61. Mitchell, J. Components of pore water pressure and their engineering significance. *Clays and clay minerals* **9,** 162–184 (2013).

62. Petridou, N. I., Spiro, Z. & Heisenberg, C.-P. Multiscale force sensing in development. *Nature cell biology* **19,** 581 (2017).

63. Muiznieks, L. D. & Keeley, F. W. Molecular assembly and mechanical properties of the extracellular matrix: a fibrous protein perspective. *Biochimica et Biophysica Acta (BBA)-Molecular Basis of Disease* **1832,** 866–875 (2013).

64. Hynes, R. O. & Naba, A. Overview of the matrisome-an inventory of extracellular matrix constituents and functions. *Cold Spring Harbor perspectives in biology* **4,** a004903 (2012).

65. Naba, A. *et al.* The extracellular matrix: Tools and insights for the “omics” era. *Matrix Biology* **49,** 10–24 (2016).

66. Hofmann, M. *et al.* Lowering of tumor interstitial fluid pressure reduces tumor cell proliferation in a xenograft tumor model. *Neoplasia* **8,** 89–95 (2006).

67. Pritchard, R. H., Huang, Y. Y. S. & Terentjev, E. M. Mechanics of biological networks: from the cell cytoskeleton to connective tissue. *Soft matter* **10,** 1864–1884 (2014).

68. Derler, S. & Gerhardt, L.-C. Tribology of skin: review and analysis of experimental results for the friction coefficient of human skin. *Tribology Letters* **45,** 1–27 (2012).

69. Gjorevski, N. *et al.* Designer matrices for intestinal stem cell and organoid culture. *Nature* **539,** 560 (2016).

70. Voutouri, C. & Stylianopoulos, T. Accumulation of mechanical forces in tumors is related to hyaluronan content and tissue stiffness. *PloS one* **13,** e0193801 (2018).

71. Waller, J. M. & Maibach, H. I. Age and skin structure and function, a quantitative approach (II): protein, glycosaminoglycan, water, and lipid content and structure. *Skin Research and Technology* **12,** 145–154 (2006).

72. Sircar, S., Aisenbrey, E., Bryant, S. J. & Bortz, D. M. Determining equilibrium osmolarity in poly (ethylene glycol)-chondrotin sulfate gels mimicking articular cartilage. *Journal of theoretical biology* **364,** 397–406 (2015).

73. D'Amore, A., Stella, J. A., Wagner, W. R. & Sacks, M. S. Characterization of the complete fiber network topology of planar fibrous tissues and scaffolds. *Biomaterials* **31,** 5345–5354 (2010).

74. Wolf, M. T. *et al.* A hydrogel derived from decellularized dermal extracellular matrix. *Biomaterials* **33,** 7028–7038 (2012).

75. Medberry, C. J. *et al.* Hydrogels derived from central nervous system extracellular matrix. *Biomaterials* **34,** 1033–1040 (2013).

76. Brinson, H. F. & Brinson, L. C. Polymer engineering science and viscoelasticity. *New York: Springer* **66,** 79 (2015).

77. Chaudhuri, O. *et al.* Hydrogels with tunable stress relaxation regulate stem cell fate and activity. *Nature materials* **15,** 326 (2016).

78. Flory, P. J. Statistical mechanics of swelling of network structures. *The Journal of Chemical Physics* **18,** 108–111 (1950).

79. Doi, M. *Soft matter physics* (Oxford University Press, 2013).

80. Cassereau, L., Miroshnikova, Y. A., Ou, G., Lakins, J. & Weaver, V. M. A 3D tension bioreactor platform to study the interplay between ECM stiffness and tumor phenotype. *Journal of biotechnology* **193,** 66–69 (2015).

81. Soofi, S. S., Last, J. A., Liliensiek, S. J., Nealey, P. F. & Murphy, C. J. The elastic modulus of Matrigel™ as determined by atomic force microscopy. *Journal of structural biology* **167,** 216–219 (2009).

82. Hompland, T., Ellingsen, C., Øvrebø, K. M. & Rofstad, E. K. Interstitial fluid pressure and associated lymph node metastasis revealed in tumors by dynamic contrast-enhanced MRI. *Cancer research* **72,** 4899–4908 (2012).

83. Nieskoski, M. D. *et al.* Separation of solid stress from interstitial fluid pressure in pancreas cancer correlates with collagen area fraction. *Journal of Biomechanical Engineering* **139,** 061002 (2017).

84. Landerer, A. Die Gewebespannung in ihrem Einfluss auf die ortliche Blut and Lymphbewegung, Leipsig, FCW Vogel, 1884. Quoted in McMaster PD. *J. Exp. Med* **84,** 473–494 (1946).

85. Young, J., Llumsden, C. & Stalker, A. The significance of the “tissue pressure” of normal testicular and of neoplastic (Brown-Pearce carcinoma) tissue in the rabbit. *The Journal of pathology and bacteriology* **62,** 313–333 (1950).

86. Boucher, Y., Kirkwood, J. M., Opacic, D., Desantis, M. & Jain, R. K. Interstitial hypertension in superficial metastatic melanomas in humans. *Cancer research* **51,** 6691–6694 (1991).

87. Curti, B. D. *et al.* Interstitial pressure of subcutaneous nodules in melanoma and lymphoma patients: changes during treatment. *Cancer research* **53,** 2204–2207 (1993).

88. Tufto, I. & Rofstad, E. K. Interstitial fluid pressure, fraction of necrotic tumor tissue, and tumor cell density in human melanoma xenografts. *Acta Oncologica* **37,** 291–297 (1998).

89. Tufto, I. & Rofstad, E. K. Interstitial fluid pressure and capillary diameter distribution in human melanoma xenografts. *Microvascular research* **58,** 205–214 (1999).

90. Simonsen, T. G., Gaustad, J.-V., Leinaas, M. N. & Rofstad, E. K. High interstitial fluid pressure is associated with tumor-line specific vascular abnormalities in human melanoma xenografts. *PloS one* **7,** e40006 (2012).

91. Munson, J. M. & Shieh, A. C. Interstitial fluid flow in cancer: implications for disease progression and treatment. *Cancer management and research* **6,** 317 (2014).

92. Shieh, A. C. & Swartz, M. A. Regulation of tumor invasion by interstitial fluid flow. *Physical biology* **8,** 015012 (2011).

93. Tait, M. J., Saadoun, S., Bell, B. A. & Papadopoulos, M. C. Water movements in the brain: role of aquaporins. *TRENDS in Neurosciences* **31,** 37–43 (2008).

94. Happel, J. Viscous flow relative to arrays of cylinders. *AIChE Journal* **5,** 174–177 (1959).

95. Ramanujan, S. *et al.* Diffusion and convection in collagen gels: implications for transport in the tumor interstitium. *Biophysical journal* **83,** 1650–1660 (2002).

96. Pedersen, J. A., Boschetti, F. & Swartz, M. A. Effects of extracellular fiber architecture on cell membrane shear stress in a 3D fibrous matrix. *Journal of biomechanics* **40,** 1484–1492 (2007).

97. McCarty, W. J., Chimento, M. F., Curcio, C. A. & Johnson, M. Effects of particulates and lipids on the hydraulic conductivity of Matrigel. *Journal of Applied Physiology* **105,** 621–628 (2008).

98. Swartz, M. A. & Fleury, M. E. Interstitial flow and its effects in soft tissues. *Annu. Rev. Biomed. Eng.* **9,** 229–256 (2007).

99. Hladky, S. B. & Barrand, M. A. Mechanisms of fluid movement into, through and out of the brain: evaluation of the evidence. *Fluids and Barriers of the CNS* **11,** 26 (2014).

100. Bernabé, Y., Wang, Y., Qi, T. & Li, M. Passive advection-dispersion in networks of pipes: effect of connectivity and relationship to permeability. *Journal of Geophysical Research: Solid Earth* **121,** 713–728 (2016).

101. Tourell, M. C., Powell, S. K. & Momot, K. I. Diffusion tensor of water in partially aligned fibre networks. *Journal of Physics D: Applied Physics* **46,** 455401 (2013).

102. Amsden, B. Solute diffusion within hydrogels. Mechanisms and models. *Macromolecules* **31,** 8382–8395 (1998).

103. Phillips, R. J. A hydrodynamic model for hindered diffusion of proteins and micelles in hydrogels. *Biophysical Journal* **79,** 3350 (2000).

104. Stylianopoulos, T., Diop-Frimpong, B., Munn, L. L. & Jain, R. K. Diffusion anisotropy in collagen gels and tumors: the effect of fiber network orientation. *Biophysical journal* **99,** 3119–3128 (2010).

105. Wiig, H., Reed, R. K. & Tenstad, O. Interstitial fluid pressure, composition of interstitium, and interstitial exclusion of albumin in hypothyroid rats. *American Journal of Physiology-Heart and Circulatory Physiology* **278,** H1627–H1639 (2000).

106. Guthe, H. J. T., Nedrebø, T., Tenstad, O., Wiig, H. & Berg, A. Effect of topical anaesthetics on interstitial colloid osmotic pressure in human subcutaneous tissue sampled by wick technique. *PloS one* **7,** e31332 (2012).

107. Guthe, H. J. T. *et al.* Interstitial fluid colloid osmotic pressure in healthy children. *PloS one* **10,** e0122779 (2015).

108. Noddeland, H. *Influence of body posture on transcapillary pressures in human subcutaneous tissue* 1982.

109. Bates, D., Levick, J. & Mortimer, P. Starling pressures in the human arm and their alteration in postmastectomy oedema. *The Journal of Physiology* **477,** 355–363 (1994).

110. Nikpey, E. *et al.* High-salt diet causes osmotic gradients and hyperosmolality in skin without affecting interstitial fluid and lymph. *Hypertension,* 116 (2017).

111. Stewart, M. P. *et al.* Hydrostatic pressure and the actomyosin cortex drive mitotic cell rounding. *Nature* **469,** 226 (2011).

112. Jiang, H. & Sun, S. X. Cellular pressure and volume regulation and implications for cell mechanics. *Biophysical journal* **105,** 609–619 (2013).

113. Levick, J. R. & Michel, C. C. Microvascular fluid exchange and the revised Starling principle. *Cardiovascular research* **87,** 198–210 (2010).

114. Raghunathan, K. *et al.* Choice of fluid in acute illness: what should be given? An international consensus. *British journal of anaesthesia* **113,** 772–783 (2014).

115. Woodcock, T. Plasma volume, tissue oedema, and the steady-state Starling principle. *Bja Education* **17,** 74–78 (2016).

116. Woodcock, T. & Woodcock, T. M. Revised Starling equation and the glycocalyx model of transvascular fluid exchange: an improved paradigm for prescribing intravenous fluid therapy. *British journal of anaesthesia* **108,** 384–394 (2012).

117. Titze, J. & Machnik, A. Sodium sensing in the interstitium and relationship to hypertension. *Current opinion in nephrology and hypertension* **19,** 385–392 (2010).

118. Loret, B. & Simoes, F. M. F. *Biomechanical aspects of soft tissues* (Crc Press, 2017).

119. Werner, E. Urea as a hygroscopic substance. *Nature* **139,** 512 (1937).

120. Cristini, V. & Lowengrub, J. *Multiscale modeling of cancer: an integrated experimental and mathematical modeling approach* (Cambridge University Press, 2010).

121. Bertout, J. A., Patel, S. A. & Simon, M. C. The impact of O2 availability on human cancer. *Nature Reviews Cancer* **8,** 967 (2008).

122. Macklin, P., Mumenthaler, S. & Lowengrub, J. in *Multiscale computer modeling in biomechanics and biomedical engineering* 349–380 (Springer, 2013).

123. Harrell, M. I., Iritani, B. M. & Ruddell, A. Tumor-induced sentinel lymph node lymphangiogenesis and increased lymph flow precede melanoma metastasis. *The American journal of pathology* **170,** 774–786 (2007).

124. Chauhan, V. P. *et al.* Compression of pancreatic tumor blood vessels by hyaluronan is caused by solid stress and not interstitial fluid pressure. *Cancer cell* **26,** 14 (2014).

125. Jain, R. K. Normalization of tumor vasculature: an emerging concept in antiangiogenic therapy. *Science* **307,** 58–62 (2005).

126. Cristini, V. *et al.* Morphologic instability and cancer invasion. *Clinical Cancer Research* **11,** 6772–6779 (2005).

127. Wu, M. *et al.* The effect of interstitial pressure on therapeutic agent transport: coupling with the tumor blood and lymphatic vascular systems. *Journal of theoretical biology* **355,** 194–207 (2014).

128. Minchinton, A. I. & Tannock, I. F. Drug penetration in solid tumours. *Nature Reviews Cancer* **6,** 583 (2006).

129. Ma, Q., Dieterich, L. C. & Detmar, M. Biology of melanoma metastasis. *Melanoma,* 1–17 (2017).

130. Weder, G. *et al.* Increased plasticity of the stiffness of melanoma cells correlates with their acquisition of metastatic properties. *Nanomedicine: Nanotechnology, Biology and Medicine* **10,** 141–148 (2014).

131. Hoek, K. S. *et al.* In vivo switching of human melanoma cells between proliferative and invasive states. *Cancer research* **68,** 650–656 (2008).

132. Wei, S. C. & Yang, J. Forcing through tumor metastasis: the interplay between tissue rigidity and epithelial–mesenchymal transition. *Trends in cell biology* **26,** 111–120 (2016).

133. Guck, J., Lautenschläger, F., Paschke, S. & Beil, M. Critical review: cellular mechanobiology and amoeboid migration. *Integrative biology* **2,** 575–583 (2010).

134. Widmer, D. S., Eichhoff, O. M., Dummer, R. & Levesque, M. P. Melanoma's next top model, it is in the air. *Experimental dermatology* **24,** 659–660 (2015).

135. Case, L. B. & Waterman, C. M. Integration of actin dynamics and cell adhesion by a three-dimensional, mechanosensitive molecular clutch. *Nature cell biology* **17,** 955 (2015).

136. Te Boekhorst, V., Preziosi, L. & Friedl, P. Plasticity of cell migration in vivo and in silico. *Annual review of cell and developmental biology* **32,** 491–526 (2016).

137. Chan, C. J. *et al.* Myosin II activity softens cells in suspension. *Biophysical journal* **108,** 1856–1869 (2015).

138. Bonakdar, N. *et al.* Mechanical plasticity of cells. *Nature materials* **15,** 1090–1094 (2016).

139. Tozluoğlu, M. *et al.* Matrix geometry determines optimal cancer cell migration strategy and modulates response to interventions. *Nature cell biology* **15,** 751 (2013).

140. Paul, C. D., Mistriotis, P. & Konstantopoulos, K. Cancer cell motility: lessons from migration in confined spaces. *Nature reviews. Cancer* **17,** 131 (2017).

141. Lautscham, L. A. *et al.* Migration in confined 3D environments is determined by a combination of adhesiveness, nuclear volume, contractility, and cell stiffness. *Biophysical journal* **109,** 900–913 (2015).

142. Deakin, N. O. & Turner, C. E. Distinct roles for paxillin and Hic-5 in regulating breast cancer cell morphology, invasion, and metastasis. *Molecular biology of the cell* **22,** 327–341 (2011).

143. Moriyama, K. & Kidoaki, S. Cellular durotaxis revisited: Initial-position-dependent determination of the threshold stiffness gradient to induce durotaxis. *Langmuir* (2018).

144. Harland, B., Walcott, S. & Sun, S. X. Adhesion dynamics and durotaxis in migrating cells. *Physical biology* **8,** 015011 (2011).

145. DuChez, B. J., Doyle, A. D., Dimitriadis, E. K. & Yamada, K. M. Durotaxis by human cancer cells. *Biophysical journal* (2019).

146. Stroka, K. M. *et al.* Water permeation drives tumor cell migration in confined microenvironments. *Cell* **157,** 611–623 (2014).

147. Sciumè, G. *et al.* Three phase flow dynamics in tumor growth. *Computational Mechanics* **53,** 465–484 (2014).

148. Sciumè, G. *et al.* A multiphase model for three-dimensional tumor growth. *New journal of physics* **15,** 015005 (2013).

149. Karimkhani, C. *et al.* The global burden of melanoma: results from the global burden of disease study 2015. *British Journal of Dermatology* **177,** 134–140 (2017).

150. Kunz, M. Oncogenes in melanoma: an update. *European journal of cell biology* **93,** 1–10 (2014).

151. Omholt, K., Platz, A., Kanter, L., Ringborg, U. & Hansson, J. NRAS and BRAF mutations arise early during melanoma pathogenesis and are preserved throughout tumor progression. *Clinical Cancer Research* **9,** 6483–6488 (2003).

152. Aris, M. & Barrio, M. M. Combining immunotherapy with oncogene-targeted therapy: a new road for melanoma treatment. *Frontiers in immunology* **6,** 46 (2015).

153. Ugurel, S. *et al.* Survival of patients with advanced metastatic melanoma: the impact of novel therapies–update 2017. *European Journal of Cancer* **83,** 247–257 (2017).

154. Amaral, T. *et al.* MAPK pathway in melanoma part II—secondary and adaptive resistance mechanisms to BRAF inhibition. *European journal of cancer* **73,** 93–101 (2017).

155. Amaral, T. *et al.* The mitogen-activated protein kinase pathway in melanoma part I–activation and primary resistance mechanisms to BRAF inhibition. *European journal of cancer* **73,** 85–92 (2017).

156. Sharma, P., Hu-Lieskovan, S., Wargo, J. A. & Ribas, A. Primary, adaptive, and acquired resistance to cancer immunotherapy. *Cell* **168,** 707–723 (2017).

157. Levesque, M. P., Cheng, P. F., Raaijmakers, M. I., Saltari, A. & Dummer, R. Metastatic melanoma moves on: translational science in the era of personalized medicine. *Cancer and Metastasis Reviews* **36,** 7–21 (2017).

158. Hutchenreuther, J. & Leask, A. Why target the tumor stroma in melanoma? *Journal of cell communication and signaling* **12,** 113–118 (2018).

159. Izar, B. *et al.* Bidirectional cross talk between patient-derived melanoma and cancer-associated fibroblasts promotes invasion and proliferation. *Pigment cell & melanoma research* **29,** 656–668 (2016).

160. Werner, H. M., Mills, G. B. & Ram, P. T. Cancer Systems Biology: a peek into the future of patient care? *Nature reviews Clinical oncology* **11,** 167 (2014).

161. Mocellin, S. & Rossi, C. R. *The melanoma molecular map project* 2008.

162. Antonopoulou, K. *et al.* Updated field synopsis and systematic meta-analyses of genetic association studies in cutaneous melanoma: the MelGene database. *Journal of Investigative Dermatology* **135,** 1074–1079 (2015).

163. Trevarton, A. J. *et al.* MelanomaDB: a web tool for integrative analysis of melanoma genomic information to identify disease-associated molecular pathways. *Frontiers in oncology* **3,** 184 (2013).

164. Reinhold, W. C. Commentary on "MelanomaDB: a web tool for integrative analysis of melanoma genomic information to identify disease-associated molecular pathways". *Frontiers in genetics* **4,** 156 (2013).

165. Chatzinasiou, F. *et al.* Comprehensive field synopsis and systematic meta-analyses of genetic association studies in cutaneous melanoma. *Journal of the National Cancer Institute* **103,** 1227–1235 (2011).

166. Zhang, D., Zhu, R., Zhang, H., Zheng, C.-H. & Xia, J. MGDB: a comprehensive database of genes involved in melanoma. *Database* **2015** (2015).

167. Subramanian, A. *et al.* Gene set enrichment analysis: a knowledge-based approach for interpreting genome-wide expression profiles. *Proceedings of the National Academy of Sciences* **102,** 15545–15550 (2005).

168. Wolkenhauer, O. Why model? *Frontiers in physiology* **5,** 21 (2014).

169. Akbani, R. *et al.* Genomic classification of cutaneous melanoma. *Cell* **161,** 1681–1696 (2015).

170. Loftus, S. K. The next generation of melanocyte data: Genetic, epigenetic, and transcriptional resource datasets and analysis tools. *Pigment cell & melanoma research* **31,** 442–447 (2018).

171. Mittal, P. & Jain, M. Proteomics: An indispensable tool for novel biomarker identification in melanoma. *J Data Mining Genomics Proteomics* **7,** 2153–0602 (2016).

172. Liberato, T. *et al.* Signatures of protein expression revealed by secretome analyses of cancer associated fibroblasts and melanoma cell lines. *Journal of proteomics* **174,** 1–8 (2018).

173. Fischer, G. M. *et al.* Metabolic strategies of melanoma cells: Mechanisms, interactions with the tumor microenvironment, and therapeutic implications. *Pigment cell & melanoma research* **31,** 11–30 (2018).

174. Ratnikov, B. I., Scott, D. A., Osterman, A. L., Smith, J. W. & Ronai, Z. A. Metabolic rewiring in melanoma. *Oncogene* **36,** 147 (2017).

175. Emmert-Streib, F., Glazko, G., De Matos Simoes, R., *et al.* Statistical inference and reverse engineering of gene regulatory networks from observational expression data. *Frontiers in genetics* **3,** 8 (2012).

176. Ciriello, G., Cerami, E., Sander, C. & Schultz, N. Mutual exclusivity analysis identifies oncogenic network modules. *Genome research* **22,** 398–406 (2012).

177. Guan, J., Gupta, R. & Filipp, F. V. Cancer systems biology of TCGA SKCM: efficient detection of genomic drivers in melanoma. *Scientific reports* **5,** 7857 (2015).

178. Marzese, D. M. *et al.* DNA methylation and gene deletion analysis of brain metastases in melanoma patients identifies mutually exclusive molecular alterations. *Neuro-oncology* **16,** 1499–1509 (2014).

179. Barter, R. L., Schramm, S.-J., Mann, G. J. & Yang, Y. H. Network-based biomarkers enhance classical approaches to prognostic gene expression signatures. *BMC systems biology* **8,** S5 (2014).

180. Wang, L. *et al.* Cell cycle gene networks are associated with melanoma prognosis. *PloS one* **7,** e34247 (2012).

181. Kaushik, A., Bhatia, Y., Ali, S. & Gupta, D. Gene network rewiring to study melanoma stage progression and elements essential for driving melanoma. *PloS one* **10,** e0142443 (2015).

182. Saez-Rodriguez, J., MacNamara, A. & Cook, S. Modeling signaling networks to advance new cancer therapies. *Annual review of biomedical engineering* **17,** 143–163 (2015).

183. Passante, E., Würstle, M. L., Hellwig, C. T., Leverkus, M. & Rehm, M. Systems analysis of apoptosis protein expression allows the case-specific prediction of cell death responsiveness of melanoma cells. *Cell death and differentiation* **20,** 1521 (2013).

184. Fallahi-Sichani, M. *et al.* Systematic analysis of BRAFV600E melanomas reveals a role for JNK/c-Jun pathway in adaptive resistance to drug-induced apoptosis. *Molecular systems biology* **11,** 797 (2015).

185. Fallahi-Sichani, M. *et al.* Adaptive resistance of melanoma cells to RAF inhibition via reversible induction of a slowly dividing de-differentiated state. *Molecular systems biology* **13,** 905 (2017).

186. Bernardo-Faura, M., Massen, S., Falk, C. S., Brady, N. R. & Eils, R. Data-derived modeling characterizes plasticity of MAPK signaling in melanoma. *PLoS computational biology* **10,** e1003795 (2014).

187. Korkut, A. *et al.* Perturbation biology nominates upstream–downstream drug combinations in RAF inhibitor resistant melanoma cells. *Elife* **4,** e04640 (2015).

188. Levesque, M. P., Dummer, R. & Beerenwinkel, N. Perturbing resistance: a network perspective. *Pigment cell & melanoma research* **1,** 5–7 (2015).

189. Scott, D. A. *et al.* Comparative metabolic flux profiling of melanoma cell lines beyond the warburg effect. *Journal of Biological Chemistry* **286,** 42626–42634 (2011).

190. Lee, H.-S. *et al.* A systems-biological study on the identification of safe and effective molecular targets for the reduction of ultraviolet B-induced skin pigmentation. *Scientific reports* **5,** 10305 (2015).

191. Pappalardo, F. *et al.* Computational modeling of PI3K/AKT and MAPK signaling pathways in melanoma cancer. *PLoS One* **11,** e0152104 (2016).

192. Brown, K. S. *et al.* The statistical mechanics of complex signaling networks: nerve growth factor signaling. *Physical biology* **1,** 184 (2004).

193. Flach, E. H., Rebecca, V. W., Herlyn, M., Smalley, K. S. & Anderson, A. R. Fibroblasts contribute to melanoma tumor growth and drug resistance. *Molecular pharmaceutics* **8,** 2039–2049 (2011).

194. Fedorenko, I. V. *et al.* Fibronectin induction abrogates the BRAF inhibitor response of BRAF V600E/PTEN-null melanoma cells. *Oncogene* **35,** 1225 (2016).

195. Picco, N., Sahai, E., Maini, P. K. & Anderson, A. R. Integrating models to quantify environment-mediated drug resistance. *Cancer research* **77,** 5409–5418 (2017).

196. Kim, E., Rebecca, V. W., Smalley, K. S. & Anderson, A. R. Phase i trials in melanoma: A framework to translate preclinical findings to the clinic. *European Journal of Cancer* **67,** 213–222 (2016).

197. Sun, X., Bao, J. & Shao, Y. Mathematical modeling of therapy-induced cancer drug resistance: connecting cancer mechanisms to population survival rates. *Scientific reports* **6,** 22498 (2016).

198. Ouellet, D. *et al.* Population pharmacokinetics of dabrafenib, a BRAF inhibitor: effect of dose, time, covariates, and relationship with its metabolites. *The Journal of Clinical Pharmacology* **54,** 696–706 (2014).

199. Herzberg, B. & Fisher, D. E. Metastatic melanoma and immunotherapy. *Clinical Immunology* **172,** 105–110 (2016).

200. Hodi, F. S. *et al.* Improved survival with ipilimumab in patients with metastatic melanoma. *New England Journal of Medicine* **363,** 711–723 (2010).

201. Andtbacka, R. *et al.* Talimogene laherparepvec improves durable response rate in patients with advanced melanoma. *J clin Oncol* **33,** 2780–2788 (2015).

202. Kogan, Y., Agur, Z. & Elishmereni, M. A mathematical model for the immunotherapeutic control of the Th1/Th2 imbalance in melanoma. *Discrete & Continuous Dynamical Systems-Series B* **18** (2013).

203. Cappuccio, A., Elishmereni, M. & Agur, Z. Cancer immunotherapy by interleukin-21: potential treatment strategies evaluated in a mathematical model. *Cancer Research* **66,** 7293–7300 (2006).

204. Den Breems, N. Y. & Eftimie, R. The re-polarisation of M2 and M1 macrophages and its role on cancer outcomes. *Journal of theoretical biology* **390,** 23–39 (2016).

205. Eftimie, R. & Hamam, H. Modelling and investigation of the CD4+ T cells–Macrophages paradox in melanoma immunotherapies. *Journal of theoretical biology* **420,** 82–104 (2017).

206. DePillis, L., Gallegos, A. & Radunskaya, A. A model of dendritic cell therapy for melanoma. *Frontiers in oncology* **3** (2013).

207. Pizzurro, G. A. & Barrio, M. M. Dendritic cell-based vaccine efficacy: aiming for hot spots. *Frontiers in immunology* **6,** 91 (2015).

208. Santos, G. *et al.* Model-based genotype-phenotype mapping used to investigate gene signatures of immune sensitivity and resistance in melanoma micrometastasis. *Scientific reports* **6,** 24967 (2016).

209. Pappalardo, F. *et al.* SimB16: modeling induced immune system response against B16-melanoma. *PloS one* **6,** e26523 (2011).

210. Altrock, P. M., Liu, L. L. & Michor, F. The mathematics of cancer: integrating quantitative models. *Nature Reviews Cancer* **15,** 730 (2015).

211. Treloar, K. K., Simpson, M. J., Binder, B. J., McElwain, D. S. & Baker, R. E. Assessing the role of spatial correlations during collective cell spreading. *Scientific reports* **4,** 5713 (2014).

212. Treloar, K. K. *et al.* Multiple types of data are required to identify the mechanisms influencing the spatial expansion of melanoma cell colonies. *BMC systems biology* **7,** 137 (2013).

213. Vo, B. N., Drovandi, C. C., Pettitt, A. N. & Pettet, G. J. Melanoma cell colony expansion parameters revealed by approximate Bayesian computation. *PLoS computational biology* **11,** e1004635 (2015).

214. Haridas, P., Penington, C. J., McGovern, J. A., McElwain, D. S. & Simpson, M. J. Quantifying rates of cell migration and cell proliferation in co-culture barrier assays reveals how skin and melanoma cells interact during melanoma spreading and invasion. *Journal of theoretical biology* **423,** 13–25 (2017).

215. La Porta, C. A. *et al.* Osmotic stress affects functional properties of human melanoma cell lines. *The European Physical Journal Plus* **130,** 64 (2015).

216. Barton, D. L., Henkes, S., Weijer, C. J. & Sknepnek, R. Active vertex model for cell-resolution description of epithelial tissue mechanics. *PLoS computational biology* **13,** e1005569 (2017).

217. Stichel, D. *et al.* An individual-based model for collective cancer cell migration explains speed dynamics and phenotype variability in response to growth factors. *NPJ systems biology and applications* **3,** 5 (2017).

218. Breitkreutz, D., Koxholt, I., Thiemann, K. & Nischt, R. Skin basement membrane: the foundation of epidermal integrity—BM functions and diverse roles of bridging molecules nidogen and perlecan. *BioMed research international* **2013** (2013).

219. Evans, N. D., Oreffo, R. O., Healy, E., Thurner, P. J. & Man, Y. H. Epithelial mechanobiology, skin wound healing, and the stem cell niche. *Journal of the mechanical behavior of biomedical materials* **28,** 397–409 (2013).

220. Leight, J. L., Tokuda, E. Y., Jones, C. E., Lin, A. J. & Anseth, K. S. Multifunctional bioscaffolds for 3D culture of melanoma cells reveal increased MMP activity and migration with BRAF kinase inhibition. *Proceedings of the National Academy of Sciences* **112,** 5366–5371 (2015).

221. Shao, Y. & Aplin, A. E. Akt3-mediated resistance to apoptosis in B-RAF–targeted melanoma cells. *Cancer research,* 0008–5472 (2010).

222. Ambrosi, D., Pezzuto, S., Riccobelli, D., Stylianopoulos, T. & Ciarletta, P. Solid tumors are poroelastic solids with a chemo-mechanical feedback on growth. *Journal of Elasticity* **129,** 107–124 (2017).

223. Paszek, M. J. *et al.* Tensional homeostasis and the malignant phenotype. *Cancer cell* **8,** 241–254 (2005).

224. Halder, G., Dupont, S. & Piccolo, S. Transduction of mechanical and cytoskeletal cues by YAP and TAZ. *Nature reviews Molecular cell biology* **13,** 591 (2012).

225. Kim, M. H. *et al.* Actin remodeling confers BRAF inhibitor resistance to melanoma cells through YAP/TAZ activation. *The EMBO journal* **35,** 462–478 (2016).

226. Feng, X. *et al.* Hippo-independent activation of YAP by the GNAQ uveal melanoma oncogene through a trio-regulated rho GTPase signaling circuitry. *Cancer cell* **25,** 831–845 (2014).

227. Sanchez, I. M. & Aplin, A. E. Hippo: hungry, hungry for melanoma invasion. *Journal of Investigative Dermatology* **134,** 14–16 (2014).

228. Nallet-Staub, F. *et al.* Pro-invasive activity of the Hippo pathway effectors YAP and TAZ in cutaneous melanoma. *Journal of Investigative Dermatology* **134,** 123–132 (2014).

229. Querleux, B. *Computational biophysics of the skin* (2014).

230. Balois, T. & Amar, M. B. Morphology of melanocytic lesions in situ. *Scientific reports* **4,** 3622 (2014).

231. Ciarletta, P., Foret, L. & Ben Amar, M. The radial growth phase of malignant melanoma: multi-phase modelling, numerical simulations and linear stability analysis. *Journal of the Royal Society Interface* **8,** 345–368 (2010).

232. Taloni, A. *et al.* Mechanical properties of growing melanocytic nevi and the progression to melanoma. *PloS one* **9,** e94229 (2014).

233. Grashoff, C. *et al.* Measuring mechanical tension across vinculin reveals regulation of focal adhesion dynamics. *Nature* **466,** 263 (2010).

234. Campàs, O. *et al.* Quantifying cell-generated mechanical forces within living embryonic tissues. *Nature methods* **11,** 183 (2014).

235. Alessandri, K. *et al.* Cellular capsules as a tool for multicellular spheroid production and for investigating the mechanics of tumor progression in vitro. *Proceedings of the National Academy of Sciences* **110,** 14843–14848 (2013).

236. Otto, O. *et al.* Real-time deformability cytometry: on-the-fly cell mechanical phenotyping. *Nature methods* **12,** 199 (2015).

237. Swift, J. *et al.* Nuclear lamin-A scales with tissue stiffness and enhances matrix-directed differentiation. *Science* **341,** 1240104 (2013).

238. Kim, W., Ferguson, V. L., Borden, M. & Neu, C. P. Application of elastography for the noninvasive assessment of biomechanics in engineered biomaterials and tissues. *Annals of biomedical engineering* **44,** 705–724 (2016).

239. Jid, C. B. *et al.* Doppler ultrasound and strain elastography in the assessment of cutaneous melanoma: preliminary results. *Medical ultrasonography* **17,** 509–514 (2015).

240. Stücker, M. *et al.* The cutaneous uptake of atmospheric oxygen contributes significantly to the oxygen supply of human dermis and epidermis. *The Journal of physiology* **538,** 985–994 (2002).

241. Wang, W., Winlove, C. & Michel, C. Oxygen partial pressure in outer layers of skin of human finger nail folds. *The Journal of physiology* **549,** 855–863 (2003).

242. Horikoshi, T., Balin, A. K. & Carter, D. M. Effects of oxygen tension on the growth and pigmentation of normal human melanocytes. *Journal of investigative dermatology* **96,** 841–844 (1990).

243. Hanna, S. C. *et al.* HIF1α and HIF2α independently activate SRC to promote melanoma metastases. *The Journal of clinical investigation* **123,** 2078–2093 (2013).

244. Carreau, A., Hafny-Rahbi, B. E., Matejuk, A., Grillon, C. & Kieda, C. Why is the partial oxygen pressure of human tissues a crucial parameter? Small molecules and hypoxia. *Journal of cellular and molecular medicine* **15,** 1239–1253 (2011).

245. Dmitriev, R. I. *et al.* Versatile conjugated polymer nanoparticles for high-resolution O2 imaging in cells and 3D tissue models. *ACS nano* **9,** 5275–5288 (2015).

246. Erapaneedi, R., Belousov, V. V., Schäfers, M. & Kiefer, F. A novel family of fluorescent hypoxia sensors reveal strong heterogeneity in tumor hypoxia at the cellular level. *The EMBO journal* **35,** 102–113 (2016).

247. Brand, M. D. & Nicholls, D. G. Assessing mitochondrial dysfunction in cells. *Biochemical Journal* **435,** 297–312 (2011).

248. Hall, A. *et al.* Dysfunctional oxidative phosphorylation makes malignant melanoma cells addicted to glycolysis driven by the V600EBRAF oncogene. *Oncotarget* **4,** 584 (2013).

249. Chwalek, K., Tsurkan, M. V., Freudenberg, U. & Werner, C. Glycosaminoglycan-based hydrogels to modulate heterocellular communication in in vitro angiogenesis models. *Scientific reports* **4,** 4414 (2014).

250. Balcioglu, H. E., Van De Water, B. & Danen, E. H. Tumor-induced remote ECM network orientation steers angiogenesis. *Scientific reports* **6,** 22580 (2016).

251. Scianna, M., Bell, C. & Preziosi, L. A review of mathematical models for the formation of vascular networks. *Journal of theoretical biology* **333,** 174–209 (2013).

252. Welter, M. & Rieger, H. Physical determinants of vascular network remodeling during tumor growth. *The European Physical Journal E* **33,** 149–163 (2010).

253. Döme, B., Paku, S., Somlai, B. & Tıémár, J. Vascularization of cutaneous melanoma involves vessel co-option and has clinical significance. *The Journal of pathology* **197,** 355–362 (2002).

254. Wang, J. *et al.* Multi-scale agent-based modeling on melanoma and its related angiogenesis analysis. *Theoretical Biology and Medical Modelling* **10,** 41 (2013).

255. Dzwinel, W., Kłusek, A. & Vasilyev, O. V. Supermodeling in simulation of melanoma progression. *Procedia Computer Science* **80,** 999–1010 (2016).

256. Łoś, M., Paszyński, M., Kłusek, A. & Dzwinel, W. Application of fast isogeometric L2 projection solver for tumor growth simulations. *Computer Methods in Applied Mechanics and Engineering* **316,** 1257–1269 (2017).

257. Duane, G. S., Grabow, C., Selten, F. & Ghil, M. *Introduction to focus issue: Synchronization in large networks and continuous media—data, models, and supermodels* 2017.

258. Gaustad, J.-V., Simonsen, T. G., Leinaas, M. N. & Rofstad, E. K. Sunitinib treatment does not improve blood supply but induces hypoxia in human melanoma xenografts. *BMC cancer* **12,** 388 (2012).

259. Schweitzer, A. D. *et al.* Computational model predicts effective delivery of 188-Re-labeled melanin-binding antibody to metastatic melanoma tumors with wide range of melanin concentrations. *Melanoma research* **17,** 291–303 (2007).

260. Liu, J. *et al.* A theoretical study on inhibition of melanoma with controlled and targeted delivery of siRNA via skin using SPACE-EGF. *Annals of biomedical engineering* **45,** 1407–1419 (2017).

261. Ramıérez-Torres, A. *et al.* The influence of anisotropic growth and geometry on the stress of solid tumors. *International Journal of Engineering Science* **119,** 40–49 (2017).

262. Mendes, A. I., Nogueira, C., Pereira, J. & Fonseca-Pinto, R. On the geometric modulation of skin lesion growth: a mathematical model for melanoma. *Research on Biomedical Engineering* **32,** 44–54 (2016).

263. Lee, H. & Kwon, K. A mathematical analysis of the ABCD criteria for diagnosing malignant melanoma. *Physics in Medicine & Biology* **62,** 1865 (2017).

264. Esteva, A. *et al.* Dermatologist-level classification of skin cancer with deep neural networks. *Nature* **542,** 115 (2017).

265. Haenssle, H. *et al.* Man against machine: diagnostic performance of a deep learning convolutional neural network for dermoscopic melanoma recognition in comparison to 58 dermatologists. *Annals of Oncology* **29,** 1836–1842 (2018).

266. Marchetti, M. A. *et al.* Results of the 2016 international skin imaging collaboration international symposium on biomedical imaging challenge: comparison of the accuracy of computer algorithms to dermatologists for the diagnosis of melanoma from dermoscopic images. *Journal of the American Academy of Dermatology* **78,** 270–277 (2018).

267. Satheesha, T., Satyanarayana, D., Prasad, M. G. & Dhruve, K. D. Melanoma is skin deep: a 3D reconstruction technique for computerized dermoscopic skin lesion classification. *IEEE journal of translational engineering in health and medicine* **5,** 1–17 (2017).

268. Xu, H., Wang, H., Berendt, R., Jha, N. & Mandal, M. *Computerized measurement of melanoma depth of invasion in skin biopsy images* in *2017 IEEE EMBS International Conference on Biomedical & Health Informatics (BHI)* (2017), 17–20.

269. Eikenberry, S., Thalhauser, C. & Kuang, Y. Tumor-immune interaction, surgical treatment, and cancer recurrence in a mathematical model of melanoma. *PLoS computational biology* **5,** e1000362 (2009).

270. Payan, Y. *Soft tissue biomechanical modeling for computer assisted surgery* (Springer, 2012).

271. Holle, A. W., Young, J. L. & Spatz, J. P. In vitro cancer cell–ECM interactions inform in vivo cancer treatment. *Advanced drug delivery reviews* **97,** 270–279 (2016).

272. Silk, D., Kirk, P. D., Barnes, C. P., Toni, T. & Stumpf, M. P. Model selection in systems biology depends on experimental design. *PLoS computational biology* **10,** e1003650 (2014).

273. Stanford, N. J. *et al.* The evolution of standards and data management practices in systems biology. *Molecular systems biology* **11,** 851 (2015).

274. Weiswald, L.-B., Bellet, D. & Dangles-Marie, V. Spherical cancer models in tumor biology. *Neoplasia* **17,** 1–15 (2015).

275. Kulms, D. & Meier, F. in *Skin Tissue Models* 57–75 (Elsevier, 2018).

276. Vörsmann, H. *et al.* Development of a human three-dimensional organotypic skin-melanoma spheroid model for in vitro drug testing. *Cell death & disease* **4,** e719 (2013).

277. Northey, J. J., Przybyla, L. & Weaver, V. M. Tissue force programs cell fate and tumor aggression. *Cancer discovery* (2017).

278. Caliari, S. R. & Burdick, J. A. A practical guide to hydrogels for cell culture. *Nature methods* **13,** 405–414 (2016).

279. Rimann, M., Angres, B., Patocchi-Tenzer, I., Braum, S. & Graf-Hausner, U. Automation of 3D cell culture using chemically defined hydrogels. *Journal of laboratory automation* **19,** 191–197 (2014).

280. Verjans, E.-T., Doijen, J., Luyten, W., Landuyt, B. & Schoofs, L. Three-dimensional cell culture models for anticancer drug screening: Worth the effort? *Journal of cellular physiology* **233,** 2993–3003 (2018).

281. Peela, N. *et al.* Advanced biomaterials and microengineering technologies to recapitulate the stepwise process of cancer metastasis. *Biomaterials* **133,** 176–207 (2017).

282. Hanahan, D. & Weinberg, R. A. Hallmarks of cancer: the next generation. *cell* **144,** 646–674 (2011).

283. Shain, A. H. *et al.* The genetic evolution of melanoma from precursor lesions. *New England Journal of Medicine* **373,** 1926–1936 (2015).

284. Antoniewicz, M. R. Methods and advances in metabolic flux analysis: a mini-review. *Journal of industrial microbiology & biotechnology* **42,** 317–325 (2015).

285. Pacheco, M. P. & Sauter, T. in *Metabolic Network Reconstruction and Modeling* 101–110 (Springer, 2018).

286. Brodland, G. W. *How computational models can help unlock biological systems* in *Seminars in cell & developmental biology* **47** (2015), 62–73.

287. Cristini, V., Koay, E. & Wang, Z. *An Introduction to physical oncology: how mechanistic mathematical modeling can improve cancer therapy outcomes* (CRC Press, 2017).

288. Konstorum, A., Vella, A. T., Adler, A. J. & Laubenbacher, R. C. Addressing current challenges in cancer immunotherapy with mathematical and computational modelling. *Journal of The Royal Society Interface* **14,** 20170150 (2017).

289. Howard, J. Quantitative cell biology: the essential role of theory. *Molecular biology of the cell* **25,** 3438–3440 (2014).

290. Begley, C. G. & Ioannidis, J. P. Reproducibility in science: improving the standard for basic and preclinical research. *Circulation research* **116,** 116–126 (2015).

291. Waltemath, D. & Wolkenhauer, O. How modeling standards, software, and initiatives support reproducibility in systems biology and systems medicine. *IEEE Transactions on Biomedical Engineering* **63,** 1999–2006 (2016).

292. Ringer, P., Colo, G., Faessler, R. & Grashoff, C. Sensing the mechano-chemical properties of the extracellular matrix. *Matrix Biology* **64,** 6–16 (2017).

293. Charras, G. & Yap, A. S. Tensile forces and mechanotransduction at cell–cell junctions. *Current Biology* **28,** R445–R457 (2018).

294. Frieboes, H. B. *et al.* Physical oncology: a bench-to-bedside quantitative and predictive approach. *Cancer research* **71,** 298–302 (2011).

295. Hatzikirou, H. *et al.* Integrative physical oncology. *Wiley Interdisciplinary Reviews: Systems Biology and Medicine* **4,** 1–14 (2012).

296. Bell, S. & Terentjev, E. M. Focal adhesion kinase: the reversible molecular mechanosensor. *Biophysical journal* **112,** 2439–2450 (2017).

297. Baird, M. A. *et al.* Local pulsatile contractions are an intrinsic property of the myosin 2A motor in the cortical cytoskeleton of adherent cells. *Molecular biology of the cell* **28,** 240–251 (2017).

298. Butcher, D. T., Alliston, T. & Weaver, V. M. A tense situation: forcing tumour progression. *Nature Reviews Cancer* **9,** 108–122 (2009).

299. Guck, J. *et al.* Optical deformability as an inherent cell marker for testing malignant transformation and metastatic competence. *Biophysical journal* **88,** 3689–3698 (2005).

300. Greaves, M. & Maley, C. C. Clonal evolution in cancer. *Nature* **481,** 306–313 (2012).

301. Achilli, M. & Mantovani, D. Tailoring mechanical properties of collagen-based scaffolds for vascular tissue engineering: the effects of pH, temperature and ionic strength on gelation. *Polymers* **2,** 664–680 (2010).

302. Heldin, C.-H., Rubin, K., Pietras, K. & Östman, A. High interstitial fluid pressure–an obstacle in cancer therapy. *Nature reviews. Cancer* **4,** 806 (2004).

303. Levental, K. R. *et al.* Matrix crosslinking forces tumor progression by enhancing integrin signaling. *Cell* **139,** 891–906 (2009).

304. Avizienyte, E. & Frame, M. C. Src and FAK signalling controls adhesion fate and the epithelial-to-mesenchymal transition. *Current opinion in cell biology* **17,** 542–547 (2005).

305. Iskratsch, T., Wolfenson, H. & Sheetz, M. P. Appreciating force and shape—the rise of mechanotransduction in cell biology. *Nature Reviews Molecular Cell Biology* **15,** 825 (2014).

306. Pinheiro, D. & Bellaiche, Y. Mechanical force-driven adherens junction remodeling and epithelial dynamics. *Developmental cell* **47,** 3–19 (2018).

307. Roca-Cusachs, P., Conte, V. & Trepat, X. Quantifying forces in cell biology. *Nature cell biology* **19,** 742 (2017).

308. Tao, J., Li, Y., Vig, D. K. & Sun, S. X. Cell mechanics: a dialogue. *Reports on Progress in Physics* **80,** 036601 (2017).

309. Hoffmann, E. K., Lambert, I. H. & Pedersen, S. F. Physiology of cell volume regulation in vertebrates. *Physiological reviews* **89,** 193–277 (2009).

310. Greiner, A. M. *et al.* Cell type-specific adaptation of cellular and nuclear volume in micro-engineered 3D environments. *Biomaterials* **69,** 121–132 (2015).

311. Hui, T. *et al.* Volumetric deformation of live cells induced by pressure-activated cross-membrane ion transport. *Physical review letters* **113,** 118101 (2014).

312. Xie, K., Yang, Y. & Jiang, H. Controlling cellular volume via mechanical and physical properties of substrate. *Biophysical Journal* **114,** 675–687 (2018).

313. McGrail, D. J. *et al.* Osmotic regulation is required for cancer cell survival under solid stress. *Biophysical journal* **109,** 1334–1337 (2015).

314. Stock, C. & Pedersen, S. F. *Roles of pH and the Na+/H+ exchanger NHE1 in cancer: From cell biology and animal models to an emerging translational perspective?* in *Seminars in cancer biology* **43** (2017), 5–16.

315. Melli, L. *et al.* Bipolar filaments of human nonmuscle myosin 2-A and 2-B have distinct motile and mechanical properties. *eLife* **7,** e32871 (2018).

316. Martin, A. C., Kaschube, M. & Wieschaus, E. F. Pulsed contractions of an actin-myosin network drive apical constriction. *Nature* **457,** 495 (2009).

317. Hao, L., Ha, J., Kuzel, P., Garcia, E. & Persad, S. Cadherin switch from E-to N-cadherin in melanoma progression is regulated by the PI3K/PTEN pathway through Twist and Snail. *British Journal of Dermatology* **166,** 1184–1197 (2012).

318. Massoumi, R. *et al.* Down-regulation of CYLD expression by Snail promotes tumor progression in malignant melanoma. *Journal of Experimental Medicine* **206,** 221–232 (2009).

319. Dupont, S. Role of YAP/TAZ in cell-matrix adhesion-mediated signalling and mechanotransduction. *Experimental cell research* **343,** 42–53 (2016).

320. Martino, F., Perestrelo, A. R., Vinarsky, V., Pagliari, S. & Forte, G. Cellular Mechanotransduction: from tension to function. *Frontiers in physiology* **9** (2018).

321. Gupta, M. *et al.* Adaptive rheology and ordering of cell cytoskeleton govern matrix rigidity sensing. *Nature communications* **6,** 7525 (2015).

322. Alt, S., Ganguly, P. & Salbreux, G. Vertex models: from cell mechanics to tissue morphogenesis. *Phil. Trans. R. Soc. B* **372,** 20150520 (2017).

323. Brasch, J., Harrison, O. J., Honig, B. & Shapiro, L. Thinking outside the cell: how cadherins drive adhesion. *Trends in cell biology* **22,** 299–310 (2012).

324. Kim, S. A., Tai, C.-Y., Mok, L.-P., Mosser, E. A. & Schuman, E. M. Calcium-dependent dynamics of cadherin interactions at cell–cell junctions. *Proceedings of the National Academy of Sciences* **108,** 9857–9862 (2011).

325. Brasch, J. *et al.* Homophilic and heterophilic interactions of type II cadherins identify specificity groups underlying cell-adhesive behavior. *Cell reports* **23,** 1840–1852 (2018).

326. Labernadie, A. *et al.* A mechanically active heterotypic E-cadherin/N-cadherin adhesion enables fibroblasts to drive cancer cell invasion. *Nature cell biology* **19,** 224 (2017).

327. Hoffman, B. D. & Yap, A. S. Towards a dynamic understanding of cadherin-based mechanobiology. *Trends in cell biology* **25,** 803–814 (2015).

328. Canel, M., Serrels, A., Frame, M. C. & Brunton, V. G. E-cadherin–integrin crosstalk in cancer invasion and metastasis. *J Cell Sci,* jcs–100115 (2013).

329. Lecuit, T. & Yap, A. S. E-cadherin junctions as active mechanical integrators in tissue dynamics. *Nature cell biology* **17,** 533 (2015).

330. Bazellières, E. *et al.* Control of cell–cell forces and collective cell dynamics by the intercellular adhesome. *Nature cell biology* **17,** 409 (2015).

331. Benham-Pyle, B. W., Pruitt, B. L. & Nelson, W. J. Mechanical strain induces E-cadherin–dependent Yap1 and β-catenin activation to drive cell cycle entry. *Science* **348,** 1024–1027 (2015).

332. Totaro, A., Panciera, T. & Piccolo, S. YAP/TAZ upstream signals and downstream responses. *Nature cell biology* **20,** 888 (2018).

333. Cosgrove, B. D. *et al.* N-cadherin adhesive interactions modulate matrix mechanosensing and fate commitment of mesenchymal stem cells. *Nature materials* **15,** 1297 (2016).

334. Chung, H. *et al.* Keratinocytes negatively regulate the N-cadherin levels of melanoma cells via contact-mediated calcium regulation. *Biochemical and biophysical research communications* (2018).

335. Turley, R. S. *et al.* Targeting N-cadherin increases vascular permeability and differentially activates AKT in melanoma. *Annals of surgery* **261,** 368 (2015).

336. Barua, D., Parent, S. E. & Winklbauer, R. Mechanics of fluid-filled interstitial gaps. II. gap characteristics in xenopus embryonic ectoderm. *Biophysical Journal* **113,** 923–936 (2017).

337. Parent, S. E., Barua, D. & Winklbauer, R. Mechanics of fluid-filled interstitial gaps. I. Modeling gaps in a compact tissue. *Biophysical Journal* **113,** 913–922 (2017).

338. Kalluri, R. The biology and function of fibroblasts in cancer. *Nature Reviews Cancer* **16,** 582 (2016).

339. Hastings, J. F., Skhinas, J. N., Fey, D., Croucher, D. R. & Cox, T. R. The extracellular matrix as a key regulator of intracellular signalling networks. *British journal of pharmacology* **176,** 82–92 (2019).

340. Byfield, F. J. *et al.* Absence of filamin A prevents cells from responding to stiffness gradients on gels coated with collagen but not fibronectin. *Biophysical journal* **96,** 5095–5102 (2009).

341. Gaggioli, C. *et al.* Tumor-derived fibronectin is involved in melanoma cell invasion and regulated by V600E B-Raf signaling pathway. *Journal of Investigative Dermatology* **127,** 400–410 (2007).

342. Pei, G., Lan, Y., Chen, D., Ji, L. & Hua, Z.-c. FAK regulates E-cadherin expression via p-SrcY416/p-ERK1/2/p-Stat3Y705 and PPARγ/miR-125b/Stat3 signaling pathway in B16F10 melanoma cells. *Oncotarget* **8,** 13898 (2017).

343. Sircar, S., Keener, J. P. & Fogelson, A. L. The effect of divalent vs. monovalent ions on the swelling of Mucin-like polyelectrolyte gels: Governing equations and equilibrium analysis. *The Journal of chemical physics* **138,** 014901 (2013).

344. Roberts, D. R. *et al.* Effects of spaceflight on astronaut brain structure as indicated on MRI. *New England Journal of Medicine* **377,** 1746–1753 (2017).

345. Goyal, S. *et al.* Clinical management of multiple melanoma brain metastases: a systematic review. *JAMA oncology* **1,** 668–676 (2015).

346. Xue, G., Romano, E., Massi, D. & Mandalà, M. Wnt/β-catenin signaling in melanoma: Preclinical rationale and novel therapeutic insights. *Cancer treatment reviews* **49,** 1–12 (2016).

347. Boespflug, A., Caramel, J., Dalle, S. & Thomas, L. Treatment of NRAS-mutated advanced or metastatic melanoma: rationale, current trials and evidence to date. *Therapeutic advances in medical oncology* **9,** 481–492 (2017).

348. Huang, J., Wang, L., Xiong, C. & Yuan, F. Elastic hydrogel as a sensor for detection of mechanical stress generated by single cells grown in three-dimensional environment. *Biomaterials* **98,** 103–112 (2016).

349. Hynes, R. O. The extracellular matrix: not just pretty fibrils. *Science* **326,** 1216–1219 (2009).

350. Doyle, J. J., Gerber, E. E. & Dietz, H. C. Matrix-dependent perturbation of TGFβ signaling and disease. *FEBS letters* **586,** 2003–2015 (2012).

351. Chakraborty, S. *et al.* Agrin as a mechanotransduction signal regulating YAP through the Hippo pathway. *Cell reports* **18,** 2464–2479 (2017).

352. Andrlová, H. *et al.* Biglycan expression in the melanoma microenvironment promotes invasiveness via increased tissue stiffness inducing integrin-β1 expression. *Oncotarget* **8,** 42901 (2017).

353. Miroshnikova, Y. A. *et al.* Tissue mechanics promote IDH1-dependent HIF1α–tenascin C feedback to regulate glioblastoma aggression. *Nature cell biology* **18,** 1336 (2016).

354. Saotome, K. *et al.* Structure of the mechanically activated ion channel Piezo1. *Nature* **554,** 481 (2018).

355. Murthy, S. E., Dubin, A. E. & Patapoutian, A. Piezos thrive under pressure: mechanically activated ion channels in health and disease. *Nature Reviews Molecular Cell Biology* **18,** 771 (2017).

356. Hung, W.-C. *et al.* Confinement sensing and signal optimization via Piezo1/PKA and myosin II pathways. *Cell reports* **15,** 1430–1441 (2016).

357. Chen, X. *et al.* A feedforward mechanism mediated by mechanosensitive ion channel PIEZO1 and tissue mechanics promotes glioma aggression. *Neuron* **100,** 799–815 (2018).

358. Hofschröer, V. *et al.* Extracellular protonation modulates cell-cell interaction mechanics and tissue invasion in human melanoma cells. *Scientific reports* **7,** 42369 (2017).

359. Ishibashi, K., Hara, S. & Kondo, S. Aquaporin water channels in mammals. *Clinical and experimental nephrology* **13,** 107–117 (2009).

360. Hara-Chikuma, M. & Verkman, A. Prevention of skin tumorigenesis and impairment of epidermal cell proliferation by targeted aquaporin-3 gene disruption. *Molecular and cellular biology* **28,** 326–332 (2008).

361. Nicchia, G. P. *et al.* Inhibition of aquaporin-1 dependent angiogenesis impairs tumour growth in a mouse model of melanoma. *Journal of Molecular Medicine* **91,** 613–623 (2013).

362. Rosińczuk, J., Taradaj, J., Dymarek, R. & Sopel, M. Mechanoregulation of wound healing and skin homeostasis (2018).

363. Rübsam, M. *et al.* E-cadherin integrates mechanotransduction and EGFR signaling to control junctional tissue polarization and tight junction positioning. *Nature Communications* **8,** 1250 (2017).

364. Zihni, C., Mills, C., Matter, K. & Balda, M. S. Tight junctions: from simple barriers to multifunctional molecular gates. *Nature reviews Molecular cell biology* **17,** 564 (2016).

365. Elbediwy, A. *et al.* Integrin signalling regulates YAP and TAZ to control skin homeostasis. *Development* **143,** 1674–1687 (2016).

366. Golan, T. *et al.* Interactions of melanoma cells with distal keratinocytes trigger metastasis via notch signaling inhibition of MITF. *Molecular cell* **59,** 664–676 (2015).

367. Mack, J. J. *et al.* NOTCH1 is a mechanosensor in adult arteries. *Nature communications* **8,** 1620 (2017).

368. Meloty-Kapella, L., Shergill, B., Kuon, J., Botvinick, E. & Weinmaster, G. Notch ligand endocytosis generates mechanical pulling force dependent on dynamin, epsins, and actin. *Developmental cell* **22,** 1299–1312 (2012).

369. Langridge, P. D. & Struhl, G. Epsin-dependent ligand endocytosis activates Notch by force. *Cell* **171,** 1383–1396 (2017).

370. Beedle, A. E., Williams, A., Relat-Goberna, J. & Garcia-Manyes, S. Mechanobiology—chemical origin of membrane mechanical resistance and force-dependent signaling. *Current opinion in chemical biology* **29,** 87–93 (2015).

371. Davies, H. *et al.* Mutations of the BRAF gene in human cancer. *Nature* **417,** 949 (2002).

372. Chapman, P. B. *et al.* Improved survival with vemurafenib in melanoma with BRAF V600E mutation. *New England Journal of Medicine* **364,** 2507–2516 (2011).

373. Flaherty, K. T. *et al.* Inhibition of mutated, activated BRAF in metastatic melanoma. *New England Journal of Medicine* **363,** 809–819 (2010).

374. Falchook, G. S. *et al.* Dose selection, pharmacokinetics, and pharmacodynamics of BRAF-inhibitor Dabrafenib (GSK2118436). *Clinical Cancer Research,* clincanres–0887 (2014).

375. Lawrence, S. K., Nguyen, D., Bowen, C., Richards-Peterson, L. & Skordos, K. W. The metabolic drug-drug interaction profile of dabrafenib: in vitro investigations and quantitative extrapolation of the P450-mediated DDI risk. *Drug Metabolism and Disposition* **42,** 1180–1190 (2014).

376. Zanger, U. M. & Schwab, M. Cytochrome P450 enzymes in drug metabolism: regulation of gene expression, enzyme activities, and impact of genetic variation. *Pharmacology & therapeutics* **138,** 103–141 (2013).

377. Arakawa, H. *et al.* Preliminary evaluation of three-dimensional primary human hepatocyte culture system for assay of drug-metabolizing enzyme-inducing potential. *Biological and Pharmaceutical Bulletin* **40,** 967–974 (2017).

378. Polasek, T. M., Lin, F. P., Miners, J. O. & Doogue, M. P. Perpetrators of pharmacokinetic drug–drug interactions arising from altered cytochrome P450 activity: a criteria-based assessment. *British journal of clinical pharmacology* **71,** 727–736 (2011).

379. Yadav, J., Korzekwa, K. & Nagar, S. Improved predictions of drug–drug interactions mediated by time-dependent inhibition of CYP3A. *Molecular pharmaceutics* **15,** 1979–1995 (2018).

380. Prueksaritanont, T. *et al.* Drug–drug interaction studies: regulatory guidance and an industry perspective. *The AAPS journal* **15,** 629–645 (2013).

381. Chou, T.-C. & Talaly, P. A simple generalized equation for the analysis of multiple inhibitions of Michaelis-Menten kinetic systems. *Journal of Biological Chemistry* **252,** 6438–6442 (1977).

382. Cornish-Bowden, A. & Cornish-Bowden, A. *Fundamentals of enzyme kinetics* (Wiley-Blackwell Weinheim, Germany, 2012).

383. Yeo, K. R., Jamei, M., Yang, J., Tucker, G. T. & Rostami-Hodjegan, A. Physiologically based mechanistic modelling to predict complex drug–drug interactions involving simultaneous competitive and time-dependent enzyme inhibition by parent compound and its metabolite in both liver and gut - the effect of diltiazem on the time-course of exposure to triazolam. *European Journal of Pharmaceutical Sciences* **39,** 298–309 (2010).

384. Wicha, S. G., Chen, C., Clewe, O. & Simonsson, U. S. A general pharmacodynamic interaction model identifies perpetrators and victims in drug interactions. *Nature communications* **8,** 2129 (2017).

385. Bershas, D. A. *et al.* Metabolism and disposition of oral dabrafenib in cancer patients: proposed participation of aryl nitrogen in carbon-carbon bond cleavage via decarboxylation following enzymatic oxidation. *Drug Metabolism and Disposition* **41,** 2215–2224 (2013).

386. Heel, R. *et al.* Ketoconazole: a review of its therapeutic efficacy in superficial and systemic fungal infections. *Drugs* **23,** 1–36 (1982).

387. Suttle, A. B. *et al.* Assessment of the drug interaction potential and single-and repeat-dose pharmacokinetics of the BRAF inhibitor dabrafenib. *The Journal of Clinical Pharmacology* **55,** 392–400 (2015).

388. Schäuble, S., Stavrum, A. K., Puntervoll, P., Schuster, S. & Heiland, I. Effect of substrate competition in kinetic models of metabolic networks. *FEBS letters* **587,** 2818–2824 (2013).

389. Kim, J.-H., Choi, W.-G., Lee, S. & Lee, H. S. Revisiting the Metabolism and Bioactivation of Ketoconazole in Human and Mouse Using Liquid Chromatography–Mass Spectrometry-Based Metabolomics. *International journal of molecular sciences* **18,** 621 (2017).

390. Daneshmend, T. K. *et al.* Influence of food on the pharmacokinetics of ketoconazole. *Antimicrobial agents and chemotherapy* **25,** 1–3 (1984).

391. Van der Graaf, P. H. & Benson, N. Systems pharmacology: bridging systems biology and pharmacokinetics-pharmacodynamics (PKPD) in drug discovery and development. *Pharmaceutical research* **28,** 1460–1464 (2011).

392. Köhler, G. *et al.* Drug-drug interactions in medical patients: effects of in-hospital treatment and relation to multiple drug use. *International journal of clinical pharmacology and therapeutics* **38,** 504–513 (2000).

393. Bruyere, A. *et al.* Effect of variations in the amounts of P-glycoprotein (ABCB1), BCRP (ABCG2) and CYP3A4 along the human small intestine on PBPK models for predicting intestinal first pass. *Molecular pharmaceutics* **7,** 1596–1607 (2010).

394. Novotna, A. *et al.* Dual effects of ketoconazole cis-enantiomers on CYP3A4 in human hepatocytes and HepG2 Cells. *PloS one* **9,** e111286 (2014).

395. Wei, Y. *et al.* A molecular aspect in the regulation of drug metabolism: does PXR-induced enzyme expression always lead to functional changes in drug metabolism? *Current pharmacology reports* **2,** 187–192 (2016).

396. Huang, H. *et al.* Inhibition of drug metabolism by blocking the activation of nuclear receptors by ketoconazole. *Oncogene* **26,** 258 (2007).

397. Fuchs, I. *et al.* Effect of the CYP3A inhibitor ketoconazole on the PXR-mediated induction of CYP3A activity. *European journal of clinical pharmacology* **69,** 507–513 (2013).

398. Stubbs, M., McSheehy, P. M., Griffiths, J. R. & Bashford, C. L. Causes and consequences of tumour acidity and implications for treatment. *Molecular medicine today* **6,** 15–19 (2000).

399. Mouton, J. W. *et al.* Tissue concentrations: do we ever learn? *Journal of Antimicrobial Chemotherapy* **61,** 235–237 (2007).

400. Gentilcore, G. *et al.* Effect of dabrafenib on melanoma cell lines harbouring the BRAF V600D/R mutations. *BMC cancer* **13,** 17 (2013).

401. Adelmann, C. H. *et al.* Comparative profiles of BRAF inhibitors: the paradox index as a predictor of clinical toxicity. *Oncotarget* **7,** 30453 (2016).

402. Dupont, S. *et al.* Role of YAP/TAZ in mechanotransduction. *Nature* **474,** 179 (2011).

403. Hutchenreuther, J. & Leask, A. Why target the tumor stroma in melanoma? *Journal of cell communication and signaling,* 1–6 (2017).

404. Astashkina, A., Mann, B. & Grainger, D. W. A critical evaluation of in vitro cell culture models for high-throughput drug screening and toxicity. *Pharmacology & therapeutics* **134,** 82–106 (2012).

405. Bucher, J. Dynamische Modellierung und Simulation des Arzneimittelmetabolismus in humanen Leberzellen: Identifizierbarkeit, Robustheit und inter-individuelle Variabilität. *Dissertation at the University of Stuttgart* (Dec. 2011).

406. Wei, Z. *et al.* The effect of microRNAs in the regulation of human CYP3A4: a systematic study using a mathematical model. *Scientific reports* **4,** 4283 (2014).

407. Giagkiozis, I., Purshouse, R. C. & Fleming, P. J. An overview of population-based algorithms for multi-objective optimisation. *International Journal of Systems Science* **46,** 1572–1599 (2015).

408. Gábor, A. & Banga, J. R. Robust and efficient parameter estimation in dynamic models of biological systems. *BMC systems biology* **9,** 74 (2015).

409. Villaverde, A. F. *et al.* BioPreDyn-bench: a suite of benchmark problems for dynamic modelling in systems biology. *BMC systems biology* **9,** 8 (2015).

410. Canal, T. & Peppas, N. A. Correlation between mesh size and equilibrium degree of swelling of polymeric networks. *Journal of Biomedical Materials Research Part A* **23,** 1183–1193 (1989).

411. Quesada-Pérez, M., Maroto-Centeno, J. A., Forcada, J. & Hidalgo-Alvarez, R. Gel swelling theories: the classical formalism and recent approaches. *Soft Matter* **7,** 10536–10547 (2011).

412. Van der Sman, R. Biopolymer gel swelling analysed with scaling laws and flory–rehner theory. *Food Hydrocolloids* **48,** 94–101 (2015).

413. Sing, C. E. & Olvera de la Cruz, M. Polyelectrolyte Blends and Nontrivial Behavior in Effective Flory–Huggins Parameters. *ACS Macro Letters* **3,** 698–702 (2014).

414. Baeurle, S., Kiselev, M., Makarova, E. & Nogovitsin, E. Effect of the counterion behavior on the frictional–compressive properties of chondroitin sulfate solutions. *Polymer* **50,** 1805–1813 (2009).

415. Pesavento, F., Schrefler, B. A. & Sciumè, G. Multiphase flow in deforming porous media: A review. *Archives of Computational Methods in Engineering* **24,** 423–448 (2017).

416. Day, R. E. *et al.* Human aquaporins: regulators of transcellular water flow. *Biochimica et Biophysica Acta (BBA)-General Subjects* **1840,** 1492–1506 (2014).

417. Magzoub, M., Jin, S. & Verkman, A. Enhanced macromolecule diffusion deep in tumors after enzymatic digestion of extracellular matrix collagen and its associated proteoglycan decorin. *The FASEB Journal* **22,** 276–284 (2008).

418. Sciumè, G., Ferrari, M. & Schrefler, B. A. Saturation–pressure relationships for two-and three-phase flow analogies for soft matter. *Mechanics Research Communications* **62,** 132–137 (2014).

419. Jepps, O. G., Dancik, Y., Anissimov, Y. G. & Roberts, M. S. Modeling the human skin barrier—Towards a better understanding of dermal absorption. *Advanced drug delivery reviews* **65,** 152–168 (2013).

420. Dancik, Y., Jepps, O. G. & Roberts, M. S. 11 Physiologically Based Pharmacokinetics and Pharmacodynamics of Skin. *Dermal absorption and toxicity assessment* **177,** 179 (2007).

421. Mitragotri, S. *et al.* Mathematical models of skin permeability: an overview. *International journal of pharmaceutics* **418,** 115–129 (2011).

422. Eissing, T. *et al.* A computational systems biology software platform for multiscale modeling and simulation: integrating whole-body physiology, disease biology, and molecular reaction networks. *Frontiers in physiology* **2,** 4 (2011).

423. Bogenrieder, T. & Herlyn, M. Cell-surface proteolysis, growth factor activation and intercellular communication in the progression of melanoma. *Critical reviews in oncology/hematology* **44,** 1–15 (2002).

424. Prauzner-Bechcicki, S. *et al.* PDMS substrate stiffness affects the morphology and growth profiles of cancerous prostate and melanoma cells. *Journal of the mechanical behavior of biomedical materials* **41,** 13–22 (2015).

425. Liang, Y. *et al.* A cell-instructive hydrogel to regulate malignancy of 3D tumor spheroids with matrix rigidity. *Biomaterials* **32,** 9308–9315 (2011).

426. Heidorn, S. J. *et al.* Kinase-dead BRAF and oncogenic RAS cooperate to drive tumor progression through CRAF. *Cell* **140,** 209–221 (2010).

427. Ziogas, A., Moelling, K. & Radziwill, G. CNK1 is a scaffold protein that regulates Src-mediated Raf-1 activation. *Journal of Biological Chemistry* **280,** 24205–24211 (2005).

428. Girotti, M. R. *et al.* Paradox-breaking RAF inhibitors that also target SRC are effective in drug-resistant BRAF mutant melanoma. *Cancer cell* **27,** 85–96 (2015).

429. Mayer, E. L. & Krop, I. E. Advances in targeting SRC in the treatment of breast cancer and other solid malignancies. *Clinical Cancer Research* **16,** 3526–3532 (2010).

430. Hofmann, U. B., Houben, R., Bröcker, E.-B. & Becker, J. C. Role of matrix metalloproteinases in melanoma cell invasion. *Biochimie* **87,** 307–314 (2005).

431. Yang, T.-Y. *et al.* Bornyl cis-4-Hydroxycinnamate Suppresses Cell Metastasis of Melanoma through FAK/PI3K/Akt/mTOR and MAPK Signaling Pathways and Inhibition of the Epithelial-to-Mesenchymal Transition. *International journal of molecular sciences* **19,** 2152 (2018).

432. Chen, Y.-Y. *et al.* Ethanol extracts of fruiting bodies of Antrodia cinnamomea exhibit anti-migration action in human adenocarcinoma CL1-0 cells through the MAPK and PI3K/AKT signaling pathways. *Phytomedicine* **19,** 768–778 (2012).

433. Hwang, Y. P. *et al.* Suppression of EGF-induced tumor cell migration and matrix metalloproteinase-9 expression by capsaicin via the inhibition of EGFR-mediated FAK/Akt, PKC/Raf/ERK, p38 MAPK, and AP-1 signaling. *Molecular nutrition & food research* **55,** 594–605 (2011).

434. Rodrıéguez, D., Morrison, C. J. & Overall, C. M. Matrix metalloproteinases: what do they not do? New substrates and biological roles identified by murine models and proteomics. *Biochimica et Biophysica Acta (BBA)-Molecular Cell Research* **1803,** 39–54 (2010).

435. Cathcart, J., Pulkoski-Gross, A. & Cao, J. Targeting matrix metalloproteinases in cancer: bringing new life to old ideas. *Genes & diseases* **2,** 26–34 (2015).

436. López-Otıén, C. & Overall, C. M. Protease degradomics: a new challenge for proteomics. *Nature reviews Molecular cell biology* **3,** 509 (2002).

437. Bornmann, L. & Mutz, R. Growth rates of modern science: A bibliometric analysis based on the number of publications and cited references. *Journal of the Association for Information Science and Technology* **66,** 2215–2222 (2015).

438. Grimes, D. R., Bauch, C. T. & Ioannidis, J. P. Modelling science trustworthiness under publish or perish pressure. *Royal Society open science* **5,** 171511 (2018).

439. Sütterlin, T., Kolb, C., Dickhaus, H., Jäger, D. & Grabe, N. Bridging the scales: semantic integration of quantitative SBML in graphical multi-cellular models and simulations with EPISIM and COPASI. *Bioinformatics* **29,** 223–229 (2012).

440. Amsallem, D., Zahr, M. J. & Farhat, C. Nonlinear model order reduction based on local reduced-order bases. *International Journal for Numerical Methods in Engineering* **92,** 891–916 (2012).

441. Leyva-Mendivil, M. F., Page, A., Bressloff, N. W. & Limbert, G. A mechanistic insight into the mechanical role of the stratum corneum during stretching and compression of the skin. *Journal of the mechanical behavior of biomedical materials* **49,** 197–219 (2015).

442. Marques, S., Silva, R., Bispo, M., Silva, F. & Matos, L. An aggressive case of anorectal melanoma. *GE Jornal Português de Gastrenterologia* **21,** 169–171 (2014).

443. Berger, M. F. *et al.* Melanoma genome sequencing reveals frequent PREX2 mutations. *Nature* **485,** 502 (2012).

444. Bakalian, S. *et al.* Molecular pathways mediating liver metastasis in patients with uveal melanoma. *Clinical Cancer Research* **14,** 951–956 (2008).

445. Lee, Y. A., Wallace, M. C. & Friedman, S. L. Pathobiology of liver fibrosis: a translational success story. *Gut* **64,** 830–841 (2015).

446. Kriss, J. P. Pathogenesis and treatment of pretibial myxedema. *Endocrinology and metabolism clinics of North America* **16,** 409–415 (1987).

447. Khan, U., Rizvi, H., Sano, D., Chiu, J. & Hadid, T. Nivolumab induced myxedema crisis. *Journal for immunotherapy of cancer* **5,** 13 (2017).

448. Ferry, J. D. & Myers, H. S. Viscoelastic properties of polymers. *Journal of The Electrochemical Society* **108,** 142C–143C (1961).

449. Gray, W. G., Miller, C. T. & Schrefler, B. A. Averaging theory for description of environmental problems: What have we learned? *Advances in water resources* **51,** 123–138 (2013).

450. Gray, W. G., Leijnse, A., Kolar, R. L. & Blain, C. A. *Mathematical tools for changing scale in the analysis of physical systems* (CRC Press, 1993).

451. Mannaerts, S. H. Extensive quantities in thermodynamics. *European Journal of Physics* **35,** 035017 (2014).

452. De Groot, S. R. & Mazur, P. *Non-equilibrium thermodynamics* (Courier Corporation, 2013).

453. Gelfand, I. M., Silverman, R. A., *et al. Calculus of variations* (Courier Corporation, 2000).

454. Gershenfeld, N. A. & Gershenfeld, N. *The nature of mathematical modeling* (Cambridge university press, 1999).

455. Liu, I.-S. Method of Lagrange multipliers for exploitation of the entropy principle. *Archive for Rational Mechanics and Analysis* **46,** 131–148 (1972).

456. `todayifoundout.com/wp-content/uploads/2015/08/olive-oil-in-water.png`.

457. `engineering . com / DesignSoftware / DesignSoftwareArticles / ArticleID/7241/APA-welcomes-MATELYS-AlphaCell.aspx`.

458. Parker, J. & Lenhard, R. A model for hysteretic constitutive relations governing multiphase flow: 1. Saturation-pressure relations. *Water Resources Research* **23,** 2187–2196 (1987).

459. Parker, J. & Lenhard, R. Determining three-phase permeability—saturation—pressure relations from two-phase system measurements. *Journal of Petroleum Science and Engineering* **4,** 57–65 (1990).

460. Diz-Muñoz, A., Fletcher, D. A. & Weiner, O. D. Use the force: membrane tension as an organizer of cell shape and motility. *Trends in cell biology* **23,** 47–53 (2013).

461. Ambrosi, D., Preziosi, L. & Vitale, G. The interplay between stress and growth in solid tumors. *Mechanics Research Communications* **42,** 87–91 (2012).

462. Dunlop, J. *et al.* The modeling of tissue growth in confined geometries, effect of surface tension. *Proc CMM-2011 (Warsaw) computer methods in mechanics* (2011).

463. Bidan, C. M. *et al.* How linear tension converts to curvature: geometric control of bone tissue growth. *PloS one* **7,** e36336 (2012).

464. Jackson, A. S., Miller, C. T. & Gray, W. G. Thermodynamically constrained averaging theory approach for modeling flow and transport phenomena in porous medium systems: 6. Two-fluid-phase flow. *Advances in Water Resources* **32,** 779–795 (2009).

465. Zienkiewicz, O. C. & Taylor, R. L. *The finite element method for solid and structural mechanics* (Elsevier, 2005).

466. Eliassi, A., Modarress, H. & Mansoori, G. A. Measurement of activity of water in aqueous poly (ethylene glycol) solutions (effect of excess volume on the Flory-Huggins χ-parameter). *Journal of Chemical & Engineering Data* **44,** 52–55 (1999).

467. Akalp, U. *et al.* Determination of the polymer-solvent interaction parameter for PEG hydrogels in water: Application of a self learning algorithm. *Polymer* **66,** 135–147 (2015).

468. Keener, J. P., Sircar, S. & Fogelson, A. L. Influence of the standard free energy on swelling kinetics of gels. *Physical Review E* **83,** 041802 (2011).

469. Van Oss, C., Arnold, K., Good, R., Gawrisch, K. & Ohki, S. Interfacial tension and the osmotic pressure of solutions of polar polymers. *Journal of Macromolecular Science-Chemistry* **27,** 563–580 (1990).

470. Pietuch, A., Brückner, B. R. & Janshoff, A. Membrane tension homeostasis of epithelial cells through surface area regulation in response to osmotic stress. *Biochimica et Biophysica Acta (BBA)-Molecular Cell Research* **1833,** 712–722 (2013).

471. Morales, M. F., Rathbuk, E., Smith, R. E., Pace, N., *et al.* Studies on body composition. 2. Theoretical considerations regarding the major body tissue components, with suggestions for application to man. *Journal of Biological Chemistry* **158,** 677–684 (1945).

472. Levick, J. Flow through interstitium and other fibrous matrices. *Quarterly journal of experimental physiology* **72,** 409–437 (1987).

473. Basser, P. J., Schneiderman, R., Bank, R. A., Wachtel, E. & Maroudas, A. Mechanical properties of the collagen network in human articular cartilage as measured by osmotic stress technique. *Archives of biochemistry and biophysics* **351,** 207–219 (1998).

474. Bert, J. L., Mathieson, J. M. & Pearce, R. H. The exclusion of human serum albumin by human dermal collagenous fibres and within human dermis. *Biochemical Journal* **201,** 395–403 (1982).

475. Ellis, R. J. Macromolecular crowding: obvious but underappreciated. *Trends in biochemical sciences* **26,** 597–604 (2001).

476. Fischer, H., Polikarpov, I. & Craievich, A. F. Average protein density is a molecular-weight-dependent function. *Protein Science* **13,** 2825–2828 (2004).

477. Wei, Q., Reidler, D., Shen, M. Y. & Huang, H. Keratinocyte cytoskeletal roles in cell sheet engineering. *BMC biotechnology* **13,** 17 (2013).

478. Ngo, M. A., Sinitsyna, N. N., Qin, Q. & Rice, R. H. Oxygen-dependent differentiation of human keratinocytes. *Journal of Investigative Dermatology* **127,** 354–361 (2007).

479. Imaizumi, T. *et al.* Effect of human basic fibroblast growth factor on fibroblast proliferation, cell volume, collagen lattice contraction: in comparison with acidic type. *Journal of dermatological science* **11,** 134–141 (1996).

480. Ekpenyong, A. E. *et al. Study of 3D cell morphology and effect on light scattering distribution* in *European Conference on Biomedical Optics* (2009), 7367_1J.

481. Hevia, D. *et al.* Cell volume and geometric parameters determination in living cells using confocal microscopy and 3D reconstruction. *Protocol Exchange* (2011).

482. Rossi, A. *et al.* Lymphatic and blood vessels in scleroderma skin, a morphometric analysis. *Human pathology* **41,** 366–374 (2010).

483. Yudovsky, D. & Pilon, L. Retrieving skin properties from in vivo spectral reflectance measurements. *Journal of biophotonics* **4,** 305–314 (2011).

484. Pittman, R. N. Oxygen transport in the microcirculation and its regulation. *Microcirculation* **20,** 117–137 (2013).

485. Dubin, A. & Silva, E. in *Monitoring Tissue Perfusion in Shock* 77–92 (Springer, 2018).

486. Castro, R., Hernández, G. & Bakker, J. in *Monitoring Tissue Perfusion in Shock* 15–23 (Springer, 2018).

487. Dmitriev, R. I. & Papkovsky, D. B. *Quenched-phosphorescence Detection of Molecular Oxygen: Applications in Life Sciences* (Royal Society of Chemistry, 2018).

488. Valabrègue, R., Aubert, A., Burger, J., Bittoun, J. & Costalat, R. Relation between cerebral blood flow and metabolism explained by a model of oxygen exchange. *Journal of Cerebral Blood Flow & Metabolism* **23,** 536–545 (2003).

489. Carpenter, J. H. New measurements of oxygen solubility in pure and natural water. *Limnology and oceanography* **11,** 264–277 (1966).

490. Evans, N. & Naylor, P. The oxygen tension gradient across human epidermis. *Respiration physiology* **3,** 38–42 (1967).

491. Evans, N. & Naylor, P. The dynamics of changes in dermal oxygen tension. *Respiration physiology* **2,** 61–72 (1966).

492. Jain, V., Langham, M. C. & Wehrli, F. W. MRI estimation of global brain oxygen consumption rate. *Journal of Cerebral Blood Flow & Metabolism* **30,** 1598–1607 (2010).

493. Warburg, O. Über den stoffwechsel der carcinomzelle. *Naturwissenschaften* **12,** 1131–1137 (1924).

494. Koppenol, W. H., Bounds, P. L. & Dang, C. V. Otto Warburg's contributions to current concepts of cancer metabolism. *Nature Reviews Cancer* **11,** 325 (2011).

495. Bensinger, S. J. & Christofk, H. R. *New aspects of the Warburg effect in cancer cell biology* in *Seminars in cell & developmental biology* **23** (2012), 352–361.

496. Tung, J. C. *et al.* Tumor mechanics and metabolic dysfunction. *Free Radical Biology and Medicine* **79,** 269–280 (2015).

497. Wahl, M. L. *et al.* Regulation of Intracellular pH in Human Melanoma: Potential Therapeutic Implications 1 Supported by NIH Grant P01 CA56690 (to MLW, RB, CSO, DBL); Grant R25CA48010 from National Cancer Institute, NIH, and Department of Health and Human Services, National Science Foundation MCB RUI Grant 9057010 (to JAO, SSN, RAH); and NIH Grant CA39248 (to DB). 1. *Molecular Cancer Therapeutics* **1,** 617–628 (2002).

498. Papandreou, I., Cairns, R. A., Fontana, L., Lim, A. L. & Denko, N. C. HIF-1 mediates adaptation to hypoxia by actively downregulating mitochondrial oxygen consumption. *Cell metabolism* **3,** 187–197 (2006).

499. Streeter, I. & Cheema, U. Oxygen consumption rate of cells in 3D culture: the use of experiment and simulation to measure kinetic parameters and optimise culture conditions. *Analyst* **136,** 4013–4019 (2011).

500. Balu, M. *et al.* In vivo multiphoton NADH fluorescence reveals depth-dependent keratinocyte metabolism in human skin. *Biophysical journal* **104,** 258–267 (2013).

501. Androjna, C., Gatica, J. E., Belovich, J. M. & Derwin, K. A. Oxygen diffusion through natural extracellular matrices: implications for estimating "critical thickness" values in tendon tissue engineering. *Tissue Engineering Part A* **14,** 559–569 (2008).

502. Mookerjee, S. A. & Brand, M. D. Measurement and analysis of extracellular acid production to determine glycolytic rate. *Journal of visualized experiments: JoVE* (2015).

503. Balin, A. K., Fisher, A. J. & Carter, D. M. Oxygen modulates growth of human cells at physiologic partial pressures. *Journal of Experimental Medicine* **160,** 152–166 (1984).

504. Horikoshi, T., Balin, A. K. & Carter, D. M. Effect of oxygen on the growth of human epidermal keratinocytes. *Journal of investigative dermatology* **86** (1986).

505. Sander, R. Compilation of Henry's law constants (version 4.0) for water as solvent. *Atmospheric Chemistry & Physics* **15** (2015).

506. Baumgärtl, H., Ehrly, A., Saeger-Lorenz, K. & Lübbers, D. in *Clinical oxygen pressure measurement* 121–128 (Springer, 1987).

507. Höckel, M., Schlenger, K., Knoop, C. & Vaupel, P. Oxygenation of carcinomas of the uterine cervix: evaluation by computerized O2 tension measurements. *Cancer Research* **51,** 6098–6102 (1991).

508. Chaix, E., Guillaume, C. & Guillard, V. Oxygen and carbon dioxide solubility and diffusivity in solid food matrices: a review of past and current knowledge. *Comprehensive Reviews in Food Science and Food Safety* **13,** 261–286 (2014).

509. Zacharia, I. G. & Deen, W. M. Diffusivity and solubility of nitric oxide in water and saline. *Annals of biomedical engineering* **33,** 214–222 (2005).

510. Zurovsky, Y., Mitchell, G. & Hattingh, J. Composition and viscosity of interstitial fluid of rabbits. *Experimental physiology* **80,** 203–207 (1995).

511. Dietrich, N. *et al.* Fast Measurements of the Gas-Liquid Diffusion Coefficient in the Gaussian Wake of a Spherical Bubble. *Chemical Engineering & Technology* **38,** 941–946 (2015).

512. Peng, C.-A. & Palsson, B. O. Determination of specific oxygen uptake rates in human hematopoietic cultures and implications for bioreactor design. *Annals of biomedical engineering* **24,** 373–381 (1996).

513. Silver, F. H., Freeman, J. W. & DeVore, D. Viscoelastic properties of human skin and processed dermis. *Skin research and technology* **7,** 18–23 (2001).

514. Cheema, U. *et al.* Oxygen diffusion through collagen scaffolds at defined densities: implications for cell survival in tissue models. *Journal of tissue engineering and regenerative medicine* **6,** 77–84 (2012).

515. Vaupel, P. Effect of percentual water content in tissues and liquids on the diffusion coefficients of O2, CO2, N2, and H2. *Pflügers Archiv* **361,** 201–204 (1976).

516. Schaefer, H., Schalla, W., Zesch, A. & Stüttgen, G. *Skin permeability* (Springer Science & Business Media, 2013).

517. Mitragotri, S. Modeling skin permeability to hydrophilic and hydrophobic solutes based on four permeation pathways. *Journal of Controlled Release* **86,** 69–92 (2003).

518. Kuimova, M. K. *et al.* Imaging intracellular viscosity of a single cell during photoinduced cell death. *Nature Chemistry* **1,** 69 (2009).

519. Peng, X. *et al.* Fluorescence ratiometry and fluorescence lifetime imaging: using a single molecular sensor for dual mode imaging of cellular viscosity. *Journal of the American Chemical Society* **133,** 6626–6635 (2011).

520. Liu, T. *et al.* Quantitatively mapping cellular viscosity with detailed organelle information via a designed PET fluorescent probe. *Scientific reports* **4,** 5418 (2014).

521. Bates, D., Levick, J. & Mortimer, P. Change in Macro Molecular Composition of Interstitial Fluid from Swollen Arms after Breast Cancer Treatment, and Its Implications. *Clinical Science* **85,** 737–746 (1993).

522. Bambardekar, K., Clément, R., Blanc, O., Chardès, C. & Lenne, P.-F. Direct laser manipulation reveals the mechanics of cell contacts in vivo. *Proceedings of the National Academy of Sciences* **112,** 1416–1421 (2015).

523. DiResta, G. R. *et al.* Cell proliferation of cultured human cancer cells are affected by the elevated tumor pressures that exist in vivo. *Annals of biomedical engineering* **33,** 1270–1280 (2005).

524. Ju, W.-K. *et al.* Elevated hydrostatic pressure triggers release of OPA1 and cytochrome C, and induces apoptotic cell death in differentiated RGC-5 cells. *Molecular vision* **15,** 120 (2009).

525. Diehl, P. *et al.* Induction of tumor cell death by high hydrostatic pressure as a novel supporting technique in orthopedic surgery. *Oncology reports* **10,** 1851–1855 (2003).

526. Fucikova, J. *et al.* High hydrostatic pressure induces immunogenic cell death in human tumor cells. *International journal of cancer* **135,** 1165–1177 (2014).

527. Rimann, M. & Graf-Hausner, U. Synthetic 3D multicellular systems for drug development. *Current opinion in biotechnology* **23,** 803–809 (2012).

528. Tibbitt, M. W. & Anseth, K. S. Hydrogels as extracellular matrix mimics for 3D cell culture. *Biotechnology and bioengineering* **103,** 655–663 (2009).

529. Shu, X. Z., Ahmad, S., Liu, Y. & Prestwich, G. D. Synthesis and evaluation of injectable, in situ crosslinkable synthetic extracellular matrices for tissue engineering. *Journal of Biomedical Materials Research Part A* **79,** 902–912 (2006).

530. Chen, F., Kang, D.-J. & Park, J.-H. New measurement method of Poisson's ratio of PVA hydrogels using an optical flow analysis for a digital imaging system. *Measurement Science and Technology* **24,** 055602 (2013).

531. Rizzi, S. & Lutolf, M. *Hydrogel precursor formulation and production process thereof* US Patent App. 14/684,490. 2015. `https://www.google.com/patents/US20150247119`.

532. Angres, B. M. & Wurst, H. 3-D Life biomimetic hydrogels: A modular system for cell environment design. *Technology Platforms for 3D Cell Culture: A User's Guide,* 197 (2017).

533. Geerligs, M. Skin layer mechanics. *TU Eindhoven* (2010).

534. Agache, P. & Humbert, P. *Measuring the skin* (Springer Science and Business Media, 2004).

535. Gefen, A. & Haberman, E. Viscoelastic properties of ovine adipose tissue covering the gluteus muscles. *Journal of biomechanical engineering* **129,** 924–930 (2007).

536. Pailler-Mattei, C. & Zahouani, H. Study of adhesion forces and mechanical properties of human skin in vivo. *Journal of Adhesion Science and Technology* **18,** 1739–1758 (2004).

537. Bader, D. & Bowker, P. Mechanical characteristics of skin and underlying tissues in vivo. *Biomaterials* **4,** 305–308 (1983).

538. Wong, R., Geyer, S., Weninger, W., Guimberteau, J.-C. & Wong, J. K. The dynamic anatomy and patterning of skin. *Experimental dermatology* **25,** 92–98 (2016).

539. Wu, K. S., van Osdol, W. W. & Dauskardt, R. H. Mechanical properties of human stratum corneum: effects of temperature, hydration, and chemical treatment. *Biomaterials* **27,** 785–795 (2006).

540. Pailler-Mattei, C., Bec, S. & Zahouani, H. In vivo measurements of the elastic mechanical properties of human skin by indentation tests. *Medical engineering and physics* **30,** 599–606 (2008).

541. Diridollou, S. *et al.* In vivo model of the mechanical properties of the human skin under suction. *Skin Research and technology* **6,** 214–221 (2000).

542. Annaidh, A. N., Bruyère, K., Destrade, M., Gilchrist, M. D. & Otténio, M. Characterization of the anisotropic mechanical properties of excised human skin. *Journal of the mechanical behavior of biomedical materials* **5,** 139–148 (2012).

543. Gallagher, A., NI Annaidh, A., Bruyere, K., *et al. Dynamic tensile properties of human skin* in *IRCOBI Conference 2012, 12-14 September 2012, Dublin (Ireland)* (2012).

V

Appendix

A. Rheology theory

Setting the plate rheometer

The material is placed between two circular plates in cylindrical shape[1]. With a given shear strain γ_0, radius of the plate r $[m]$ and the hight of the gel h $[m]$, one obtains the angular deflection $\Theta = \frac{\gamma_0 \cdot h}{r}$ $[rad]$, which represents the angle of rotation of the upper plate, while the lower plate is fixed. To set the desired strain, one has to apply the torque M $[\mu N \cdot m]$, which results in the anticipated stress $\sigma_0 = \frac{2}{\pi \cdot r^3} \cdot M$ $[Pa]$. The upper plate moves between Θ and $-\Theta$ with the motor angular velocity ω_{rad} $[rad/s]$ resulting in a sinusoidal oscillation of the strain $\gamma(t) = \gamma_0 \cdot \sin(\omega_{rad} \cdot t)$ with strain amplitude γ_0.

The phase shift in stress indicates the elastic and the viscous contribution

The sinusoidal oscillation of stress $\sigma(t) = \sigma_0 \cdot \sin(\omega_{rad} \cdot t + \Delta\varphi)$ with stress amplitude σ_0 follows with a phase shift angle $\Delta\varphi$ as shown in Figure 3.1. In ideal elastic materials, the stress is in-phase and proportional to strain $\sigma(t) = E \cdot \gamma(t)$. One obtains the equation $\sigma_0 \cdot \sin(\omega_{rad} \cdot t + \Delta\varphi) = E \cdot \gamma_0 \cdot \sin(\omega_{rad} \cdot t)$. In-phase behaviour can only be satisfied without phase lag $\Delta\varphi = 0$. However, the ideal elastic characteristic is rare in bio-polymers and a viscous characteristic must be considered. Ideal viscous Newtonian fluids are not time and not shear strain dependent. Instead, the shear stress is proportional to the shear strain rate $\sigma(t) = K \cdot \frac{d\gamma(t)}{dt}$. The following equation $\sigma_0 \cdot \sin(\omega_{rad} \cdot t + \Delta\varphi) = K \cdot \gamma_0 \cdot \omega_{rad} \cdot \cos(\omega_{rad} \cdot t)$ can only be solved if the phase lag is $\Delta\varphi = \frac{\pi}{2}$, which is out-phase.

Shear modulus and where it comes from

The shear modulus $G = \sqrt{G'^2 + G''^2}$ encompasses the storage modulus $G' = \frac{\sigma^0}{\gamma_0} \cos(\Delta\varphi)$ for the elastic response and the loss modulus $G'' = \frac{\sigma^0}{\gamma_0} \sin(\Delta\varphi)$ for the viscous response.

[1] Parts of this text have been published on Wikipedia by the author of this thesis

The origin of these equations will be explained in the following [448]. The shear stress $\sigma(t) = \int_{-\infty}^{t} G(t-t')\dot{\gamma}(t')dt'$ of a finite element in one direction can be expressed with the relaxation modulus G(t-t') and the strain rate $\dot{\gamma}$. The integration is made over all past times t' up to the current time t. With the strain rate $\dot{\gamma}(t) = \omega \cdot \gamma_0 \cdot \cos(\omega t)$ and substitution $\xi(t') = t - t' = s$, one obtains $\sigma(t) = \int_{\xi(-\infty)=t-(-\infty)}^{\xi(t)=t-t} G(s)\omega\gamma_0 \cdot \cos(\omega(t-s))(-ds) = \gamma_0 \int_0^{\infty} \omega G(s)\cos(\omega(t-s))ds$. Application of the trigonometric addition theorem $\cos(x \pm y) = \cos(x)\cos(y) \pm \sin(x)\sin(y)$ lead to the expression

$$\frac{\sigma(t)}{\gamma(t)} = \underbrace{[\omega \int_o^{\infty} G(s)\sin(\omega s)ds]}_{\text{shear storage modulus } G'} \sin(\omega t) + \underbrace{[\omega \int_o^{\infty} G(s)\cos(\omega s)ds]}_{\text{shear loss modulus } G''} \cos(\omega t). \tag{A.1}$$

with converging integrals, if $G(s) \to 0$ for $s \to \infty$, which depends on frequency and not time. Extension of $\sigma(t) = \sigma_0 \cdot \sin(\omega \cdot t + \Delta\varphi)$ with the trigonometric identity $\sin(x \pm y) = \sin(x) \cdot \cos(y) \pm \cos(x) \cdot \sin(y)$ leads to

$$\frac{\sigma(t)}{\gamma(t)} = \underbrace{\frac{\sigma_0}{\gamma_0} \cdot \cos(\Delta\varphi)}_{G'} \cdot \sin(\omega \cdot t) + \underbrace{\frac{\sigma_0}{\gamma_0} \cdot \sin(\Delta\varphi)}_{G''} \cdot \cos(\omega \cdot t) \tag{A.2}$$

Comparison of equation A.1 with A.1 leads to the definition of G' and G'' [448].

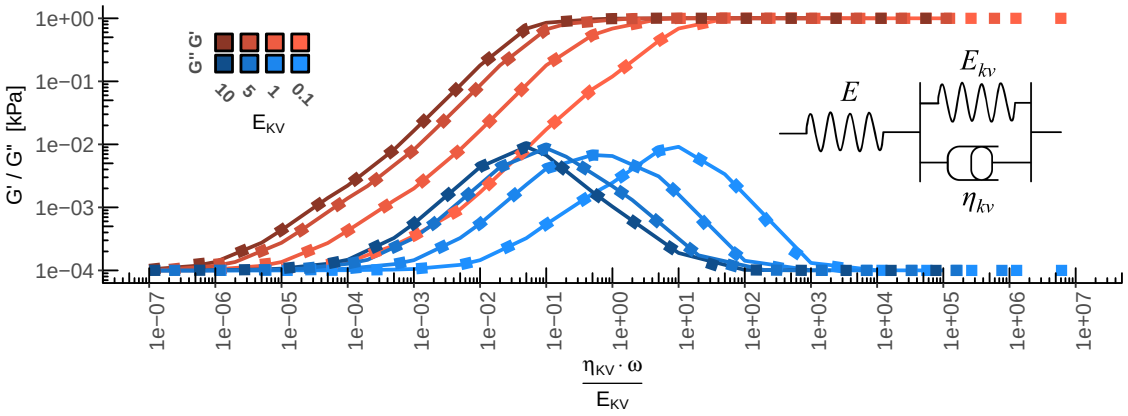

Figure A.1: The virtual rheometer reproduced a pattern of a Kelvin-Voigt material.

Other indicators of the frequency sweep test

The ratio of booth moduli gives $\tan(\Delta\varphi) = \frac{G''}{G'}$. The applied stress for a given strain is $\sigma_0 = \frac{\gamma_0 \cdot G'}{\cos(\Delta\varphi)} = \frac{\gamma_0 \cdot G''}{\sin(\Delta\varphi)}$ and the torque $M = \frac{\sigma_0 \pi r^3}{2}$ can be subsequently derived from the stress σ_0. The complex viscosity effect $\eta^* = \sqrt{\eta' 2 + \eta'' 2} = \sqrt{(\frac{G''}{\omega_{rad}})^2 + (\frac{G'}{\omega_{rad}})^2} = \frac{G^*}{\omega_{rad}}$ $[Pa \cdot s]$ is based on $\eta' = \frac{G''}{\omega_{rad}}$ and $\eta'' = \frac{G'}{\omega_{rad}}$. The oscillatory complex viscosity $|\eta^*|$ relates to steady shear rate viscosity $\eta = \frac{\sigma(t)}{\dot{\gamma}(t)}$ with $\dot{\gamma} = \frac{r}{h} \cdot \omega_{rad}$ via the Cox-Merz rule for linear polymers $\eta(\dot{\gamma}) \equiv \eta(\omega_{rad})$ if shear rate $\dot{\gamma}$ equals the angular velocity ω_{rad}.

Young's and bulk modulus

The relationships between Young's modulus $E = |E^*|$, shear modulus G, bulk modulus K, and Poisson's ratio ν are: $E = 2G(1+\nu) = 3K(1-2\nu) = \frac{9KG}{3K+G}$. The Young's modulus can also be obtained with $E = \frac{\sigma_0 \cdot \sin(\omega_{rad} \cdot t + \Delta\varphi)}{\gamma_0 \cdot \sin(\omega_{rad} \cdot t)}$. In the complex notation, the modulus is assumed to be complex with real part E' and imaginary part E". The ratio of strain ϵ and stress σ is

$$\frac{\sigma}{\epsilon} = E^* = \frac{\sigma_0}{\epsilon_0} e^{i\Delta\varphi} = \frac{\sigma_0}{\epsilon_0}(\cos(\Delta\varphi) + i\sin(\Delta\varphi)) = \underbrace{\frac{\sigma_0}{\epsilon_0}(\cos(\Delta\varphi)))}_{E'(\text{storage})} + i\underbrace{\frac{\sigma_0}{\epsilon_0}(\sin(\Delta\varphi))}_{E''(\text{loss})}$$

Analogy to shear modulus delivers $|G^*| = |G' + i \cdot G''| = \sqrt{G'^2 + G''^2} = G$.

This summarised theory supports the calculation of parameters, which are usually experimentally determined with a plate rheometer. The functionality of the virtual rheometer shown in Figure 3.1 is shown in Figure A.1 for an assumed Kelvin-Voigt material. The temporal behaviour of the simulation in Figure 3.1 right will be shown in the thesis defence presentation.

B. Modelling irregular fibrous tissues

B.1 Thermodynamically constrained averaging theory

The TCAT framework were developed to represent porous media problems in geology such as the groundwater flow in aquifier and sediments [449].
The TCAT framework can bridge several length scales as shown in Figure B.1 left and provides a series of averaging theorems to interconnect these scales [450]. The setting of a TCAT model follows a workflow, which is illustrated in Figure B.1 right [51]. The parts of the workflow will be explained in the following.

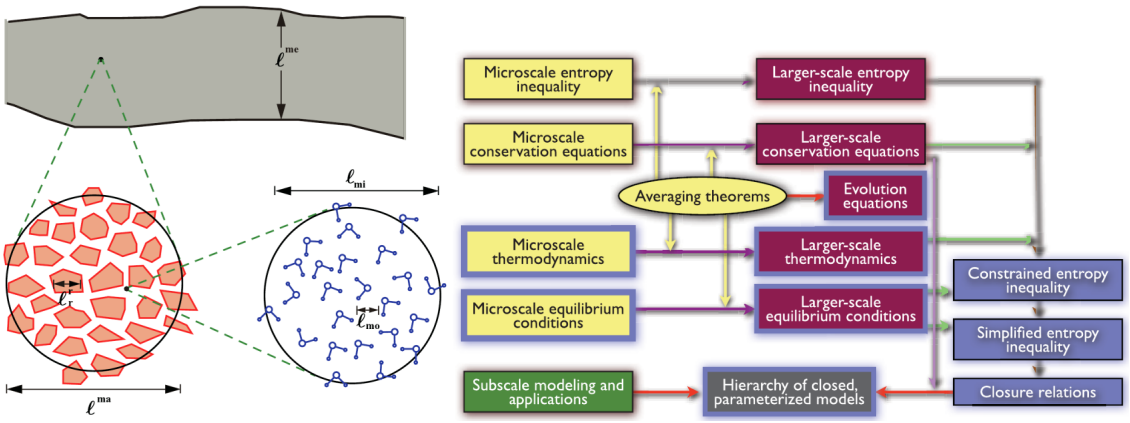

Figure B.1: **Left:** Length scales of a porous medium system. The megascale (ℓ^{me}) on the top in gray has smaller segments on the macroscale (ℓ^{ma}) containing solid grains with resolution scale size (ℓ_r^r) indicated in red. The fluid between them is shown on the bottem right side. The fluid in a representative volume element on the microscale (ℓ_{mi}) contains molecules with an average distance between two molecules in the level of the molecular scale (ℓ_{mo}). **Right:** Workflow of TCAT [51, 449].

B.1.1 A model should not be more flexible than reality: conservation equation

Conservation equations ensure that a quantity neither comes from nowhere nor disappears suddenly in the mathematical space in disagreement to the physical laws. The total amount of mass, energy, and momentum is always constant in a closed system. Simply put, any extensive quantity[1] $\mathbb{F}$ represents the density distribution F in a domain Ω: $\mathbb{F} = \int_\Omega F d\mathfrak{r}$. As general integration variable over a region, $\mathfrak{r}$ is used. The conservation equation is formulated on the microscale and describes the balance between body sources. The equation contains the rate of accumulation, the generation of the quantity, the non-advective boundary source and the advective transport[2] over the boundary. Advective transport occurs as long the transport velocity $\mathbf{v}$ of a quantity is different to the velocity of the domain $\mathbf{w}$ itself [51, (eq: 2.7)]:

$$\underbrace{\frac{d}{dt}\int_\Omega F d\mathfrak{r}}_{\substack{\text{rate of}\\ \text{accumulation}}} = \underbrace{\int_\Omega S_{\Omega T} d\mathfrak{r}}_{\substack{\text{body source}}} + \underbrace{\int_\Omega G_\Omega d\mathfrak{r}}_{\substack{\text{rate of generation}}} + \underbrace{\int_\Gamma \boldsymbol{S}_\Gamma \cdot \mathbf{n} d\mathfrak{r}}_{\substack{\text{Non-advective}\\ \text{boundary sources}}} - \underbrace{\int_\Gamma F(\mathbf{v}-\mathbf{w})\cdot\mathbf{n} d\mathfrak{r}}_{\substack{\text{net outward advective flux}}} . \tag{B.1}$$

The outwardly directed normal unit vector $\mathbf{n}$ stands perpendicular on the boundary Γ of the domain Ω_α. The Equation B.1 can also represent different chemical species $i \in \mathcal{I}_s$, such as oxygen, and different entities $\alpha \in \mathcal{I}$, such as interphase or volume. Such equation is written as [51, (eq: 2.8)]:

$$\frac{d}{dt}\int_{\Omega_\alpha} F_{i\alpha} d\mathfrak{r} = \int_{\Omega_\alpha} S_{\Omega T i\alpha} d\mathfrak{r} + \int_{\Omega_\alpha} G_{\Omega i\alpha} d\mathfrak{r} + \int_{\Gamma_\alpha} \boldsymbol{S}_{\Gamma_{i\alpha}}\cdot\mathbf{n}_\alpha d\mathfrak{r} - \int_{\Gamma_\alpha} F_{i\alpha}(\mathbf{v}_{i\alpha}-\mathbf{w}_\alpha)\cdot\mathbf{n}_\alpha d\mathfrak{r}. \tag{B.2}$$

This equation has to be derived separately for the entity of a phase ($\mathcal{I}_P$); an interface ($\mathcal{I}_I$), appearing between two phases; a common curve ($\mathcal{I}_C$), appearing between three phases, and for the entity called common point ($\mathcal{I}_{Pt}$), appearing between four phases: $\mathcal{I} = \mathcal{I}_P \cup \mathcal{I}_I \cup \mathcal{I}_C \cup \mathcal{I}_{Pt}$. With the important transport theorem T[3,(0,0),3] and the divergence theorem D[3,(0,0),3] the equation B.2 can be rewritten so that the implicit form is solely within the domain integral $\int_{\Omega_\alpha}(\ldots)d\mathfrak{r} = 0$, with the benefit that the integral can be neglected.

Theorem B.1.1 — T[3,(0,0),3]. For a smooth continuous and differentiable function f defined over a domain $\Omega_\alpha \subset \mathbb{R}^3$ that may deform with time t due to velocity $\mathbf{w}_\alpha$ of closed boundary Γ_α with outward normal form the boundary $\mathbf{n}_\alpha$,

$$\frac{d}{dt}\int_{\Omega_\alpha(t)} f d\mathfrak{r} = \int_{\Omega_\alpha(t)} \frac{\partial f}{\partial t} d\mathfrak{r} + \int_{\Gamma_\alpha(t)} f\mathbf{w}_\alpha\cdot\mathbf{n}_\alpha d\mathfrak{r}$$

[1] An **extensive quantity**, like mass or volume, has a doubled value if the system size is doubled; an **intensive quantity**, like temperature and density, remains unaffected by systems size changes. A deep and structured discussion of extensive and intensive quantities is provided by Sebastiaan H. Mannaerts [451].

[2] **Advective transport** is related to the velocity of the fluid, whereby **non-advective transport**, like diffusion, is not. Both together represent **convection**.

Thereby, f can be replaced by the property $F_{i\alpha}$ and tensor function $\mathbf{f}$ can be replaced by $F_{i\alpha}\mathbf{v}_{i\alpha}$. Both theorems are a selection of theorems for gradient (G), divergence (D), curl (C) and transport (T) phenomena across scales [450]. The theorem identifier <letter>[i,(j,k),l] ensures the overview. The letter i indicates the dimensionality of the microscale domain and letter l of the megascale. In the middle are indexes indicating the macroscale. While letter j is the number of dimensions using differential operators, letter k indicates the number of integrated dimensions.

Theorem B.1.2 — D[3,(0,0),3]. For a smooth continuous and differentiable tensor function $\mathbf{f}$ defined over a domain $\Omega_\alpha \subset \mathbb{R}^3$ that may deform with time t due to velocity $\mathbf{w}_\alpha$ of closed boundary Γ_α with outward normal form the boundary $\mathbf{n}_\alpha$,

$$\int_{\Omega_\alpha(t)} \text{div } \mathbf{f}\, d\mathfrak{r} = \int_{\Gamma_\alpha(t)} \mathbf{f}\cdot\mathbf{n}_\alpha d\mathfrak{r}$$

where div is a divergence operator that contracts the last index of $\mathbf{f}$.

The general equations are then [51, (eq: 2.13)]

$$\mathcal{F}_{i\alpha} = \frac{\partial F_{i\alpha}}{\partial t} + \nabla\cdot(\mathbf{v}_{i\alpha}F_{i\alpha}) - S_{\Omega Ti\alpha} - \text{div}\boldsymbol{S}_{\Gamma_{i\alpha}} - G_{\Omega i\alpha} = 0 \quad \text{for} \quad i\in\mathfrak{I}_s, \alpha\in\mathfrak{I} \tag{B.3}$$

and [51, (eq: 2.14)]

$$\mathcal{F}_{*i\alpha} = \frac{\mathrm{D}F_{i\alpha}}{\mathrm{D}t} + F_{i\alpha}\mathbf{I}{:}\mathbf{d}_{ia} - S_{\Omega Ti\alpha} - \text{div}\boldsymbol{S}_{\Gamma_{i\alpha}} - G_{\Omega i\alpha} = 0 \quad \text{for} \quad i\in\mathfrak{I}_s, \alpha\in\mathfrak{I}$$

when using the material derivative operator [51, (eq: 2.15)]

$$\frac{\mathrm{D}_{i\alpha}}{\mathrm{D}t} = \frac{\partial}{\partial t} + \mathbf{v}_{i\alpha}\cdot\nabla, \tag{B.4}$$

and the double dot product[3] of the unit tensor $\mathbf{I}$ and symetric rate of strain tensor [51, (eq: 2.16)]:

$$\mathbf{d}_{i\alpha} = \frac{1}{2}[\nabla\mathbf{v}_{i\alpha} + (\nabla\mathbf{v}_{i\alpha})^{\mathrm{T}}]. \tag{B.5}$$

The general equation B.3 for $\mathcal{F}$ can be tailored to the specific conservation of mass $\mathcal{M}$, momentum $\mathcal{P}$, energy $\mathcal{E}$, gravitational potential $\mathcal{G}$ and to the balance equation for entropy $\mathcal{S}$ in the partial time derivative form or in the material derivative form with $\mathcal{M}_*$, $\mathcal{P}_*$, $\mathcal{E}_*$, $\mathcal{G}_*$ and $\mathcal{S}_*$. The mass conservation

$$\mathcal{M}_{i\alpha} = \frac{\partial(\rho_\alpha\omega_{i\alpha})}{\partial t} + \nabla\cdot(\rho_\alpha\omega_{i\alpha}\mathbf{v}_{i\alpha}) - r_{i\alpha} = 0 \quad \text{for} \quad i\in\mathfrak{I}_s, \alpha\in\mathfrak{I}_P \tag{B.6}$$

depending on the mass density ρ, the mass fraction ω and the generation rate r_{ia} of a

[3] The double dot product of two matrices A and B indicates point-wise multiplication $\mathrm{A}:\mathrm{B} := \sum_{\mathrm{ij}} \mathrm{A_{ij}B_{ij}} = \mathrm{tr}(\mathrm{A^T B})$

species i [51, (eq: 2.17)].

B.1.2 Equations to parameters balance enables unique solutions: closure relations

The derived conservation equations encompass more unknowns than equations. To reduce the number of variables, closure relations are used. Closure relations provide linkages between the variables of the system. In TCAT, famous equations like the Euler-equation and the Gibbs-Duhem equation are applied, and concepts of the Gibbs or Helmholtz free energy and enthalpy are used to put volume, temperature, pressure and chemical potential in relation to each other. Furthermore, some approximative closure relations can link the system's variables to measurable material specific coefficients and may originate from experimental, theoretical, and computational sources. Besides conservation, balance, and closure equations, each model needs an appropriate set of initial and boundary conditions.

B.1.3 Where the model will go: equilibrium and entropy inequality

The conservation and closure relations are defined for systems in steady state; however, such systems are rarely in steady state, and the theory requires extensions to make it work. The theory of classical irreversible thermodynamics (CIT), established by Groot and Mazur [452], is the simplest extension of classical thermodynamics and assumes that an equilibrium can be assumed in sufficient small subsystems. Such equilibrium state and the allocated underlying conditions can be found with variational methods [453], which are often used for optimisation problems. With variational principles, local rules can be replaced with global conditions to obtain local conditions [454], which makes this approach important for porous media systems modelled on different scales. In TCAT, the variational problem searches an equilibrium with minimum internal energy and maximum entropy on the microscale and the macroscale. Moreover, the variational analysis identifies variations of elements that are truly independent from each other, so that dependent variations can be merged. Exemplary dependent variables are phase density, gravitational potential and the Green's deformation tensor, characterised mostly by variations in position.

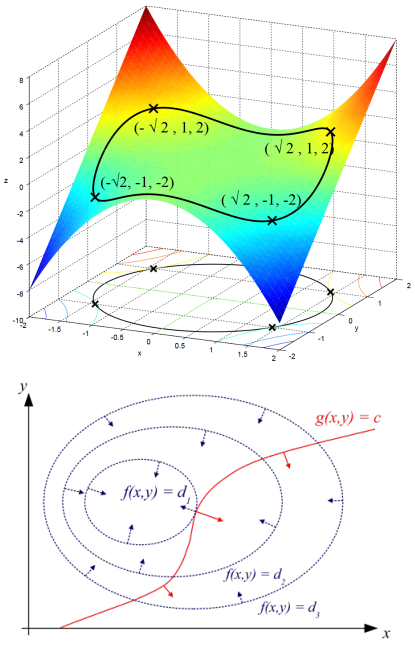

Figure B.2: **Top:** Function to optimize $f(x, y)$ is coloured. The equality constraint $g(x, y) = c$ is the black cycle which is projected to the function of interest with indicated constrained minima and maxima. **Bottom:** Contour lines with their perpendicular vectors. Figure Source: en.wikipedia.org.

Besides CIT and variational analysis, Lagrange multiplier are used in TCAT to formulate the constrained entropy inequality (CEI) equation and their geometrical representation is shown in Figure B.2. Lagrange multiplier are used to optimize a certain problem $f(x, y)$ under satisfaction of restrictive auxiliary conditions $g(x, y) = c$. The multiplier λ ensure that the vectors, being perpendicular on the function contour lines, are parallel and have the same length. The vectors are the gradient of the considered both functions. The Lagrangian[4] is formulated as: $\Lambda(x, y, \lambda) = f(x, y) + \lambda \cdot (g(x, y) - c)$. In TCAT, the variables $x_j \subseteq \mathcal{V}$ are the material derivatives $\mathrm{D}x_j/\mathrm{D}t = \mathcal{D}_j$ for $\mathcal{D}_j \subseteq \mathcal{D}$. The start of the CEI is the second law of thermodynamics. The second law postulates that entropy is produced during irreversible processes and is always positive: $\mathcal{S}_{*w} \geq 0$. This entropy production shall be maximized with the Lagrangian and should be constrained by the conservation equations ($\mathcal{M}_{*w}$, $\mathcal{E}_{*w}$, $\mathcal{P}_{*w}$, $\mathcal{G}_{*w}$), the relation of body force changes per volume to body

[4]The Lagrangian is also called the Lagrange function in honour of Joseph Louis Lagrange (1736-1813).

force changes per mass $\mathcal{T}_{\mathcal{G}*w}$, and the material derivative of thermodynamic Euler equation for the CIT formulation $\mathcal{T}_{*w}$. The CEI is obtained:

$$\mathcal{S}_{*w}(\mathcal{D}) + \lambda_{\mathcal{E}_w}\mathcal{E}_{*w}(\mathcal{D}) + \lambda_{\mathcal{P}_w}\mathcal{P}_{*w}(\mathcal{D}) + \sum_{i\in\mathcal{I}_s}\lambda_{\mathcal{M}_{iw}}\mathcal{M}_{*iw}(\mathcal{D}) \\ +\lambda_{\mathcal{G}_w}\mathcal{G}_{*w}(\mathcal{D}) + \lambda_{\mathcal{T}_w}\mathcal{T}_{*w}(\mathcal{D}) + \lambda_{\mathcal{TG}_w}\mathcal{T}_{\mathcal{G}*w}(\mathcal{D}) = \Lambda_w(\mathcal{D},\lambda) \geq 0.$$

With the concept of I-Shih Liu [455], the augmented entropy inequality (AEI) is obtained:

$$\mathcal{S}_{*w} - \frac{1}{\theta_w}\mathcal{E}_{*w} + \frac{\mathbf{v}_w}{\theta_w}\mathcal{P}_{*w} + \frac{1}{\theta}\sum_{i\in\mathcal{I}_s}(\mu_{iw} + \psi_{iw} - \frac{\mathbf{v}_w\cdot\mathbf{v}_w}{2} + \frac{\mathbf{u}_{iw}\cdot\mathbf{u}_{iw}}{2})\mathcal{M}_{*iw} \\ -\frac{1}{\theta_w}\mathcal{G}_{*w} + \frac{1}{\theta_w}\mathcal{T}_{*w} + \frac{1}{\theta_w}\mathcal{T}_{\mathcal{G}*w} = \Lambda_w \geq 0$$

with temperature θ, chemical potential μ, body force potential per unit mass ψ and diffusion/dispersion vector $\mathbf{u}$ in the coefficients. Several simplifications can be made to obtain the simplified entropy inequality (SEI). A frequently obtained simplification is obtained with closure relations that replace unknown variables to known material properties.

B.1.4 Averaging micro-scale effects to the macroscale

The relationships between scales can be very helpful to build, analyse and interpret models on different levels. TCAT has included several averaging tools to link different length scales. The averaging operator can be applied on a microscale property $\mathcal{P}_\alpha$

$$\langle\mathcal{P}_\alpha\rangle_{\Omega_\beta,\Omega_\gamma,W} := \frac{\int_{\Omega_\beta} W\mathcal{P}_\alpha d\mathfrak{r}}{\int_{\Omega_\gamma} W d\mathfrak{r}}$$

and thereby weighted $W \neq 1$ to obtain mass averages. Here, the domain of integration is of either the function Ω_β or of all components Ω_γ. The averaging theorems are represented by theorem identifiers <letter>[i,(3,0),0]. The operator identifier <letter> = D∪G∪T stands for a gradient, a divergence, or a transport theorem. The dimension identifier stands for an entity $i = 0,\ldots,3$ with $i = 0$ indicating a common point and $i = 3$ indicating a volume [51, p. 213]. The exemplary mass conservation B.6 can be averaged $\langle\mathcal{M}_{i\alpha}\rangle_{\Omega_\alpha,\Omega} := \mathcal{M}^{\overline{\overline{i\alpha}}}$ with theorem T[3,(3,0),0] and D[3,(3,0),0] to the mass conservation equation on a higher length scale [51, (eq: 6.48)]

$$\mathcal{M}^{\overline{\overline{i\alpha}}} := \frac{\partial(\epsilon^{\overline{\alpha}}\rho^\alpha\omega^{i\overline{\alpha}})}{\partial t} + \nabla\cdot(\epsilon^{\overline{\alpha}}\rho^\alpha\omega^{i\overline{\alpha}}\mathbf{v}^{\overline{i\alpha}}) - \epsilon^{\overline{\alpha}}r^{i\alpha} - \sum_{\kappa\in\mathcal{I}_{C\alpha}}\overset{i\kappa\to i\alpha}{\mathrm{M}} = 0 \quad \text{for} \quad \alpha\in\mathcal{I}_P \quad \text{(B.7)}$$

with the volume fraction $\epsilon^{\overline{\alpha}} = \langle 1\rangle_{\Omega_\alpha,\Omega}$ and allocated phase $\alpha\in\mathcal{I}_p$. The porosity is defined as $\epsilon = \sum_{\alpha\in\mathcal{I}_f}\epsilon^{\overline{\alpha}} = 1-\epsilon^{\overline{s}}$ without the solid phase proportion $\epsilon^{\overline{s}}$. The mass exchange

$$\overset{i\kappa\to i\alpha}{\mathrm{M}} = -\langle\rho_\alpha\omega_{i\alpha}(\mathbf{v}_\kappa - \mathbf{v}_{i\alpha})\cdot\mathbf{n}_\alpha\rangle_{\Omega_\kappa,\Omega} \quad \text{for} \quad \kappa\in\mathcal{I}^-_{c\alpha}$$

of species i from interface κ to phase α is a linkage between the entity specific balance equations, where $\mathfrak{I}_{c\alpha}^{-}$ indicates an entity of one dimension lower than entity α. The macroscale velocity of a species $\mathbf{v}^{\overline{i\alpha}}$ minus the convective movement of the phase $\mathbf{v}^{\overline{\alpha}}$ is called diffusion $\mathbf{u}^{\overline{\overline{i\alpha}}} = \mathbf{v}^{\overline{i\alpha}} - \mathbf{v}^{\overline{\alpha}}$. With diffusion, the Equation B.7 becomes [51, (eq: 6.65-6.73)]

$$\frac{\partial(\epsilon^{\overline{\overline{\alpha}}}\rho^{\alpha}\omega^{i\overline{\alpha}})}{\partial t} + \nabla\cdot(\epsilon^{\overline{\overline{\alpha}}}\rho^{\alpha}\omega^{i\overline{\alpha}}\mathbf{v}^{\overline{\alpha}}) + \nabla\cdot(\epsilon^{\overline{\overline{\alpha}}}\rho^{\alpha}\omega^{i\overline{\alpha}}\mathbf{u}^{\overline{\overline{i\alpha}}}) - \epsilon^{\overline{\overline{\alpha}}}r^{i\alpha} - \sum_{\kappa\in\mathfrak{I}_{C\alpha}} \overset{i\kappa\to i\alpha}{\mathrm{M}} = 0 \quad \text{for} \quad \alpha\in\mathfrak{I}_P, \tag{B.8}$$

which describes soluble species in section B.2.11. Another macroscale conservation equation is the momentum balance equation

$$\mathcal{P}^{\overline{\overline{\alpha}}} := \frac{\partial(\epsilon^{\overline{\overline{\alpha}}}\rho^{\alpha}\,\mathbf{v}^{\overline{i\alpha}})}{\partial t} + \nabla\cdot(\epsilon^{\overline{\overline{\alpha}}}\rho^{\alpha}\mathbf{v}^{\overline{i\alpha}}\mathbf{v}^{\overline{i\alpha}}) - \epsilon^{\overline{\overline{\alpha}}}\rho^{\alpha}\mathbf{g}^{\overline{\alpha}} - \sum_{\kappa\in\mathfrak{I}_{C\alpha}} \overset{\kappa\to\alpha}{\mathrm{T}} - \nabla\cdot(\epsilon^{\overline{\overline{\alpha}}}\mathbf{t}^{\overline{\overline{\alpha}}}) = \mathbf{0} \quad \text{for} \quad \alpha\in\mathfrak{I}_P, \tag{B.9}$$

which is averaged over all species in an arbitrary volume. Equation B.9 neglects the momentum from the interphases and common curves [51, (eq: 6.92)] and will play a role in section B.2.2.

B.1.5 How the interfaces between phases move: evolution equations

The geometric properties on the microscale are averaged to the macroscale. The geometric properties at the macroscale are less precise and present a more simplified measure of phase morphology. As a consequence, the interphase geometry cannot be maintained for multi-phase flow in porous material. Instead, evolution equations based on kinematics rather than conservation equations deliver useful approximations. In general, TCAT works with volume fractions so that interface area per volume or common curve length per volume is the used quantity during simulations. All phases and entities are present in each REV in contrast to mixture theory where phases are rather present besides each other at the macroscale.

In this section, the different parts of TCAT, shown in Figure B.1, were briefly described. Thermodynamic laws and relations between the changes of variables are used as closure relations. The conservation, balance, and closure equations were integrated into the entropy inequality equation with the help of Lagrange multiplier. This is done on the microscale and macroscale. Averaging theorems interconnect these different scales and evolution equations help to preserve the geometric systems properties during simulations. All together, the simplified entropy inequality equations are obtained, which can, together with application specific closure relations and initial conditions, provide a useful model of a porous system.

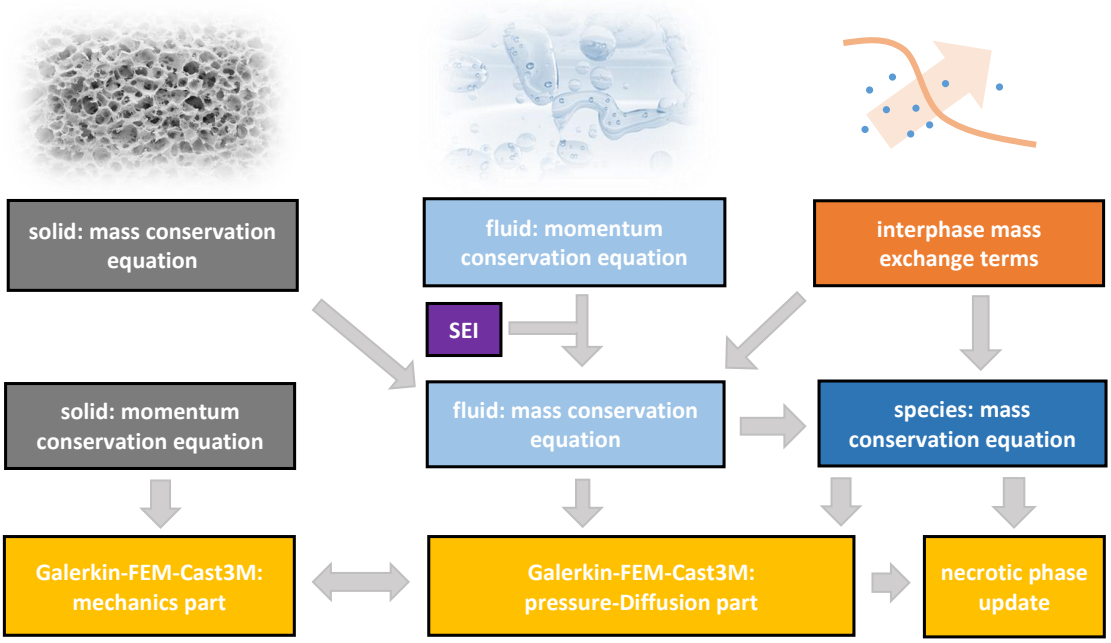

Figure B.3: Principle workflow to use TCAT equations for a cancer growth model. The solid phase can be described with a momentum conservation equation, and the deformation of the solid and sponge-like phase is numerically solved in a separate block. This phase is also represented by a mass conservation equation, which interacts with the fluid phases (cells, IF). The fluid momentum conservation equation is integrated into the mass conservation together with the SEI. Necrotic cells can be seen as a species within the TC, and oxygen can be seen as a species within the IF phase. Therefore, a mass conservation equation of each species is formulated. After setting the tissue and the malignant lesion, the biological rules of growth are implemented with interphase mass exchange terms. The three yellow boxes are equation blocks, which must be made iteratively within and among each other consistent. Source of modified images [456, 457].

B.2 Setting up generic tissues with TCAT

Among the continuous modelling approaches to mimic tissue, TCAT models are exceptionally detailed in physiological processes and stroma representation, but in contrast to pure polymer models [36], TCAT models also let space for a cell phase and the physical interaction between cells and ECM.

The TCAT can be used to describe the growth of tumour mass in a tissue, whereby HC, free moveable IF with soluble factors and a solid deformable ECM as tissue scaffold are represented linear-independent of each other.

This section summarises the work of Giuseppe Sciumé *et al.* [6, 50, 147, 148] with comprehensive derivation of all equations. A high-level orientation is given with Figure B.3, which also shows how TCAT equations feed the development of a generic cancer growth model.

The section starts with the pores within the ECM, which are saturated with IF and cell populations. The fluid saturation within the ECM pores depends on the pressure balance

between the liquids. The movement of fluids trough the ECM matrix involves the fluid momentum conservation equation.
The momentum conservation delivers force-flux closure relations, which describe the movement of fluids trough the ECM network but also describe the deformation of the solid ECM scaffold. The movement of cells depends in addition on the ECM permeability, the cell-cell adhesion, and cell-ECM interactions.
The mass conservation is treated in the following short sections, which tackle the description of the governing mass conservation equations of IF, HC, and TC. The subsequent following three sections explain how the TC develops a necrotic core; how the tumour sustaining oxygen gradient changes over the whole modelled tissue; and how mass exchange between the phases steers tumour growth, oxygen consumption, and TC death.

B.2.1 Cells and IF interact with the ECM scaffold

The tumour growth model assumes a solid network of ECM proteins, which occupies the proportion ϵ^s of a tissue REV with size 1. Between the ECM fibres is space, called porosity $\epsilon = 1 - \epsilon^s$, which is filled with IF and the cytoplasm of two cell populations belonging either to HC or to TC. The IF carries the soluble biochemical molecules and nutrients to maintain tumour cell viability. The IF occupies the fraction ϵ^l of a tissue REV as the HC and TC occupies the fraction ϵ^h and ϵ^t, respectively. Both cell fluid volume fractions define the space for intracellular signalling events. All solid and fluid phases together represent the tissue

$$\epsilon^s + \epsilon^h + \epsilon^t + \epsilon^l = 1$$

and each liquid phase α fills the pore space with its saturation degree

$$S^\alpha = \epsilon^\alpha / \epsilon \tag{B.10}$$

so that the multi-liquid phase describes an own subspace

$$S^h + S^t + S^l = 1$$

Each fluid has an internal pressure that determines the relative occupation within the pore space. Pressure-saturation relationships mediate the fluid balance in dependence of the different fluid pressures. The pressure-saturation relationships are inspired by Parker *et al.* [458, 459]. However, the relationships are presented in the inverse form and were modified to make them differentiable:

$$\begin{aligned} S^l &= 1 - [\frac{2}{\pi} \arctan(\frac{p^{hl}}{a})] \\ S^t &= [\frac{2}{\pi} \arctan(\frac{\sigma_{hl}}{\sigma_{th}} \frac{p^{th}}{a})] \end{aligned} \tag{B.11}$$

$$S^h = 1 - S^l - S^t.$$

The constant parameter a is related to ECM porosity.
The interfacial tension σ_{ij} between fluid phase i and j is similar to the pressure difference $p^{ij} = p^i - p^j$ being divided by the interfacial curvature at the microscale. At the macroscale, the interfacial curvature is not available and Parker's equations serve as a surrogate. The membrane tension interacts with cellular processes, and in turn, cells can sense the membrane surface tension [460]. Several theoretical and biophysical studies investigated surface tension regarding cellular growth and adhesion behaviour [461–463]. The surface tension of water is $72 \cdot 10^{-3} \frac{N}{m}$ and of cell aggregates is $1 - 22 \cdot 10^{-3} \frac{N}{m}$ [461], albeit it is rather tissue surface tension [46], which fits better to mixture theory and thus macroscale boundaries between tumour and environment.
The phase pressures act not only within the pore space but also change the pressure of the deformable solid ECM phase:

$$p^s = \chi^h p^h + \chi^t p^t + \chi^l p^l.$$

The Bishop parameter χ^α represents the contact area of solid material with the liquid phase α. With the assumption that the Bishop parameter is equal to the saturation degree $\chi^\alpha = S^\alpha$, the following relationships can be formulated with their derivatives:

$$\begin{aligned} p^s &= S^h p^h + S^t p^t + S^l p^l \\ p^s &= (1 - S^l - S^t) p^h + S^t p^t + S^l p^l + p^l - p^l \\ p^s &= p^l + p^h - p^l - S^l (p^h - p^l) + S^t (p^t - p^h) \\ p^s &= p^l + (1 - S^l) p^{hl} + S^t p^{th} \end{aligned} \tag{B.12}$$

$$\frac{\partial p^s}{\partial t} = \frac{\partial p^l}{\partial t} - p^{hl} \frac{\partial S^l}{\partial p^{hl}} \frac{\partial p^{hl}}{\partial t} + \frac{\partial p^{hl}}{\partial t} - S^l \frac{\partial p^{hl}}{\partial t} + p^{th} \frac{\partial S^t}{\partial p^{th}} \frac{\partial p^{th}}{\partial t} + S^t \frac{\partial p^{th}}{\partial t} \tag{B.13}$$

Within the TC-HC-IF system, the TC-IF pressure difference is equal to the sum of the TC-HC and HC-IF pressure difference

$$\begin{aligned} p^{th} + p^{hl} = (p^t - p^h) + (p^h - p^l) = p^t - p^l = p^{tl} \\ p^t = p^l + p^{hl} + p^{th}, \end{aligned}$$

what is maintained in the time derivative:

$$\frac{\partial p^t}{\partial t} = \frac{\partial p^l}{\partial t} + \frac{\partial p^{hl}}{\partial t} + \frac{\partial p^{th}}{\partial t} \tag{B.14}$$

B.2.2 Adhesion and migration: momentum balance and force-flux pair closure

The delicate balance of phase pressures determine forces within a tissue. In order to minimise these forces, fluids tend to leave a REV of higher pressure and move to a REV

of lower pressure. However, IF is easier to displace than the fluid that represent well differentiated host cells. However, the current model does not consider that cells tend to move toward stiffer areas; a process known as durotaxis [143].
To understand the movement of fluid phases, the momentum conservation equation of fluids is used. The general momentum balance equation is integrated into the CEI to obtain the AEI. This inequality becomes simpler with the assumption, that the system is composed of two immiscible fluids within an isothermal porous media with massless interfaces. With the additional assumption that the system has low isotropic velocities and low density gradients, the SEI can be derived [464, (eq:108)][51, (eq: 11.79-11.85)]

$$
\begin{aligned}
&-\frac{1}{\Theta^{\overline{\overline{\alpha}}}}\left[\epsilon S^{\alpha}\rho^{\alpha}\mathbf{g}^{\overline{\alpha}}+\epsilon S^{\alpha}\rho^{\alpha}\nabla(\varsigma^{\overline{\alpha}}+\psi^{\overline{\alpha}})-\nabla(\epsilon S^{\alpha}p^{\alpha})+\sum_{\kappa\in\mathfrak{I}_f}{}^{\kappa\to\alpha}\mathrm{T}\right]\cdot(\mathbf{v}^{\alpha}-\mathbf{v}^{s})\\
&+\frac{\epsilon S^{\alpha}}{\Theta^{\overline{\overline{\alpha}}}}(\mathbf{t}^{\overline{\overline{\alpha}}}+p^{\alpha}\mathbf{1}):\mathbf{d}^{\overline{\overline{\alpha}}}\geq 0
\end{aligned}
$$

This SEI ignores all properties from interfaces, common curves, and common points. Changes in fluid volume fraction are minor $\nabla\psi^{\overline{\alpha}}+\mathbf{g}=0$. In isothermal conditions, the Gibbs-Duhem equation $\rho^{\alpha}\nabla\varsigma^{\overline{f}}-\nabla\rho^{\alpha}=0$ can be used to further simplify the SEI

$$
-\frac{1}{\Theta^{\overline{\overline{\alpha}}}}\left[-p^{\alpha}\nabla(\epsilon S^{\alpha})+\sum_{\kappa\in\mathfrak{I}_f}{}^{\kappa\to\alpha}\mathrm{T}\right]\cdot(\mathbf{v}^{\alpha}-\mathbf{v}^{s})+\frac{\epsilon S^{\alpha}}{\Theta^{\overline{\overline{\alpha}}}}(\mathbf{t}^{\overline{\overline{\alpha}}}+p^{\alpha}\mathbf{1}):\mathbf{d}^{\overline{\overline{\alpha}}}\geq 0, \tag{B.15}
$$

which has only two terms. In TCAT, the SEI is minimised to zero and because each physical process produce entropy, each of both terms need to be zero. These two force-flux pairs [51, (page 187, 451)] contain a factor representing the force (e.g.$(\mathbf{v}^{\alpha}-\mathbf{v}^{s})$, $\mathbf{d}^{\overline{\overline{\alpha}}}=\frac{1}{2}[\nabla\mathbf{v}^{\overline{\alpha}}+(\nabla\mathbf{v}^{\overline{\alpha}})^{\mathrm{T}}]$) and a factor for the flux (e.g. $\mathrm{T}^{\kappa\to\alpha}$).

Relationships between pressure and stress

At equilibrium, either the force must be zero $\mathbf{d}^{\overline{\overline{\alpha}}}=0$ or the multiplier need to be zero in the right term of Equation B.15

$$
\mathbf{t}^{\overline{\overline{\alpha}}}+p^{\alpha}\mathbf{1}=0 \tag{B.16}
$$

However, this is an equilibrium that cannot be reached in reality according to CIT. Thus the variations around this equilibrium point are investigated. Small variations around a certain equilibrium $\mathbf{t}^{\overline{\overline{\alpha}}}=-p^{\alpha}\mathbf{1}+\tau$, with $\tau(\mathbf{0})=\mathbf{0}$ at equilibrium, the Taylor series expansion [51, (page 189)]

$$
\begin{aligned}
\mathbf{t}^{\overline{\overline{\alpha}}}+p^{\alpha}\mathbf{1}=\tau(\mathbf{d}^{\overline{\overline{\alpha}}})&=\tau(\mathbf{0})+\left.\frac{\partial\tau}{\partial\mathbf{d}^{\overline{\overline{\alpha}}}}\right|_{\mathbf{d}^{\overline{\overline{\alpha}}}=\mathbf{d}^{\overline{\overline{\alpha}}*}}:\mathbf{d}^{\overline{\overline{\alpha}}}\\
&=\mathbf{A}^{\alpha}:\mathbf{d}^{\overline{\overline{\alpha}}}
\end{aligned} \tag{B.17}
$$

shows the validity of the relation for small velocities with negligible fourth-order tensor $\mathbf{A}^{\alpha}=0$ in case of isotropic flow. Isotropic flow is considered because cancer growth rates

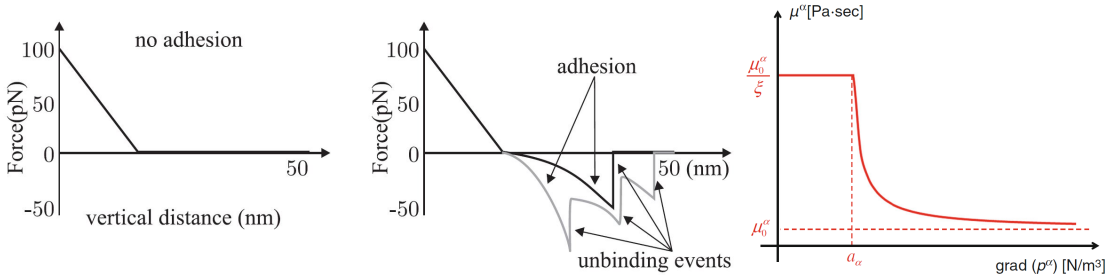

Figure B.4: Adhesion. **Left:** An adhesive bead is attached to the surface of the membrane and is moved from the inward to the outward direction. Positive force indicates cell compression. Beyond a certain tensile stress, adhesion start to fail in several unbinding events [461]. **Right:** Modelling of adhesion in TCAT [147].

are thermodynamically slow with recognisable changes in the magnitude of hours, days, and even years.

Equations for fluid flow through the ECM

The left term of Equation B.15 is treated similar. At equilibrium, the force, describing velocity difference $v^{\alpha s} = \mathbf{v}^\alpha - \mathbf{v}^s = 0$, is zero and at small variations around this equilibrium the other term

$$-p^\alpha \nabla(\epsilon S^\alpha) + \sum_{\kappa \in \mathfrak{I}_f} \overset{\kappa \to \alpha}{\mathrm{T}} = 0 \tag{B.18}$$

has to be zero as well. Taylor series expansion delivers

$$\begin{aligned} -p^\alpha \nabla(\epsilon S^\alpha) + \sum_{\kappa \in \mathfrak{I}_f} \overset{\kappa \to \alpha}{\mathrm{T}} &= \tau(v^{\alpha s}) = \tau(\mathbf{0}) + \left.\frac{\partial \tau}{\partial v^{\alpha s}}\right|_{v^{\alpha s} = v^{\alpha s *}} \cdot (\mathbf{v}^\alpha - \mathbf{v}^s) \\ &= -\sum_{\kappa \in \mathfrak{I}_f} \mathbf{R}_\kappa^\alpha \cdot (\mathbf{v}^\alpha - \mathbf{v}^s) \\ &= -\mathbf{R}^\alpha \cdot (\mathbf{v}^\alpha - \mathbf{v}^s). \end{aligned} \tag{B.19}$$

The flow is slowed down by the symmetric, positive, and semi-definite resistance tensor $\mathbf{R}^\alpha$ [464, (eq:109)]. The Equation B.9 for the original momentum balance of a cell phase reduces if velocity changes are assumed low in respect to time and space. The first two terms are cancelled out and Equation B.9 become

$$-\epsilon S^\alpha \rho^\alpha \mathbf{g}^{\overline{\alpha}} - \sum_{\kappa \in \mathfrak{I}_f} \overset{\kappa \to \alpha}{\mathrm{T}} - \nabla \cdot (\epsilon S^\alpha \mathbf{t}^{\overline{\overline{\alpha}}}) = \mathbf{0} \quad \text{for} \quad \alpha \in \mathfrak{I}_P \tag{B.20}$$

With the Equations B.16 and B.19, Equation B.20 delivers

$$\begin{aligned}
\mathbf{0} &= -p^{\alpha}\nabla(\epsilon S^{\alpha}) + \mathbf{R}^{\alpha}\cdot(\mathbf{v}^{\alpha}-\mathbf{v}^{s}) + \nabla\cdot(\epsilon S^{\alpha}p^{\alpha}\mathbf{1}) \\
\mathbf{0} &= -p^{\alpha}\nabla(\epsilon S^{\alpha}) + \mathbf{R}^{\alpha}\cdot(\mathbf{v}^{\alpha}-\mathbf{v}^{s}) + \mathbf{1}\nabla(\epsilon S^{\alpha}p^{\alpha}) + \epsilon S^{\alpha}p^{\alpha}\nabla\cdot(\mathbf{1}) \\
\mathbf{0} &= -p^{\alpha}\nabla(\epsilon S^{\alpha}) + \mathbf{R}^{\alpha}\cdot(\mathbf{v}^{\alpha}-\mathbf{v}^{s}) + \epsilon S^{\alpha}\nabla(p^{\alpha}) + p^{\alpha}\nabla(\epsilon S^{\alpha}) \\
\mathbf{0} &= \mathbf{R}^{\alpha}\cdot(\mathbf{v}^{\alpha}-\mathbf{v}^{s}) + \epsilon S^{\alpha}\nabla(p^{\alpha}),
\end{aligned} \tag{B.21}$$

whereby the body force $\mathbf{g}^{\overline{\alpha}}$ disappears with the neglected gravity. With the equation for hydraulic conductivity

$$\mathbf{K}^{\alpha} = (\epsilon S^{\alpha})^{2}(\mathbf{R})^{-1} = K^{\alpha}\mathbf{1} = \frac{k_{\mathsf{rel}}^{\alpha}\mathbf{k}}{\mu^{\alpha}}, \tag{B.22}$$

the permeability of the system is described. Low viscosity μ^{α} of the liquid, high permeability of the porous solid ECM $\mathbf{k}$, and a high relative permeability in comparison to the other liquids eases flow. Equation B.21 and Equation B.22 build up the final equation

$$\mathbf{v}^{\overline{\alpha}} - \mathbf{v}^{\overline{s}} = \frac{k_{rel}^{\alpha}\mathbf{k}}{\mu^{\alpha}\epsilon^{\alpha}}\cdot(-\nabla p^{\alpha}) \qquad (\alpha = h,t,l) \tag{B.23}$$

The pressure gradient $-\nabla p^{\alpha}$ is the driving force that directs cells and IF in the direction of lower pressure. The minus ensures the positive contribution of the term, as the gradient is negative in direction of decreasing pressure. The higher the porosity ϵ^{α} for the liquid and the higher the proportion of the liquid, the smaller the velocity of the fluid to reach the same pressure compensation.
The intrinsic permeability tensor **k** facilitates the movement and account for the general permeability in the tissue layer. The factor

$$k_{rel}^{\alpha} = (S^{\alpha})^{A_{\alpha}} \qquad \sum_{\alpha=h,t,l} k_{rel}^{\alpha} < 1, \qquad \text{[147, (eq. 22)]}$$

determines the relative permeability of the ECM for each single fluid and determines which fluid moves first if the multi-phase system is set under pressure. The parameters are set to $A_l := 8$, $A_h := 1.99$ and $A_t := 2$. The parameter A_{α} describes the microscale property wettability in porous media mechanics and determines the relative affinity of a liquid to the solid phase. In this case, IF is attached to the ECM and moves last.
Several cell-cell contacts prevent the movement of the cells. Increased tensile stress can lead to multiple unbinding events, as shown in Figure B.4 left and middle. The pressure gradient has first to exceed the adhesion threshold ψ_{α}. If the threshold is trespassed, cell-cell contacts break and the viscosity of a cell population decreases abruptly according to

$$\mu^{\alpha} = \frac{\mu_0^{\alpha}}{(1-\xi)\left\langle 1 - \frac{\psi_{\alpha}}{|\nabla p^{\alpha}|}\right\rangle_{+} + \xi} \qquad ,\xi = 0.1 \qquad \text{[147, (eq. 21)]}$$

and as shown in Figure B.4 right. The parameter ψ_α represents the viscosity for sufficient large pressure gradients $|\nabla p^\alpha| \to \infty$. The parameter $\xi = 0.1$ means that the viscosity is up to ten times lower, after the threshold is exceeded. This is shown in Figure B.4 right.

B.2.3 Without solar elastosis or fibroses: keeping the ECM mass constant

According to the Equation B.6 of general mass conservation, the adjusted mass conservation equation for the solid phase $\epsilon^s = 1 - \epsilon$ is

$$\frac{\partial[\rho^s(1-\epsilon)]}{\partial t} + \nabla \cdot [\rho^s(1-\epsilon)\mathbf{v}^s] = 0.$$

This equation becomes

$$\frac{(1-\epsilon)}{\rho^s}\frac{\partial \rho^s}{\partial t} - \frac{\partial \epsilon}{\partial t} = -\frac{(1-\epsilon)}{\rho^s}\mathbf{v}^{\bar{s}} \cdot \nabla \rho^s - \nabla \cdot \mathbf{v}^{\bar{s}} + \nabla \cdot (\epsilon \mathbf{v}^{\bar{s}})$$

after the application of the product rule. The spatial derivative of the density $\nabla \rho^s$ has a small impact and will be neglected. The time derivative of porosity is then:

$$\frac{\partial \epsilon}{\partial t} = \nabla \cdot \mathbf{v}^{\bar{s}} + \frac{(1-\epsilon)}{\rho^s}\frac{\partial \rho^s}{\partial t} - \nabla \cdot (\epsilon \mathbf{v}^{\bar{s}}). \tag{B.24}$$

This equation will be merged into the mass balance equations of the fluid phases and is not a governing equation.

B.2.4 Interstitial fluid moves but neither get lost nor suddenly appears

According to the Equation B.6 of the general mass conservation, the adjusted mass conservation equation for the IF is

$$\begin{aligned}
&\left[\frac{1}{K}(S^t + p^{th}\frac{\partial S^t}{\partial p^{th}})\right]\frac{\partial p^{th}}{\partial t} \\
&+ \left[\frac{1}{K}(1 - S^l - p^{hl}\frac{S^l}{p^{hl}})\right]\frac{\partial p^{hl}}{\partial t} + \left[\frac{1}{K}\right]\frac{\partial p^l}{\partial t} \\
&= \nabla \cdot \left[\frac{k^t_{rel}\mathbf{k}}{\mu^t} \cdot \nabla p^{th}\right] + \nabla \cdot \left[\left(\frac{k^t_{rel}\mathbf{k}}{\mu^t} + \frac{k^h_{rel}\mathbf{k}}{\mu^h}\right) \cdot \nabla p^{hl}\right] \\
&+ \nabla \cdot \left[\left(\frac{k^t_{rel}\mathbf{k}}{\mu^t} + \frac{k^h_{rel}\mathbf{k}}{\mu^h} + \frac{k^l_{rel}\mathbf{k}}{\mu^l}\right) \cdot \nabla p^l\right] \\
&- \left[\mathbf{1} : (\dot{\mathbf{e}}^{\bar{\bar{s}}} - \dot{\mathbf{e}}^{\bar{\bar{s}}}_{sp})\right] + \frac{\rho^l - \rho^t}{\rho^t \rho^l}\overset{l \to t}{\mathrm{M}}.
\end{aligned} \tag{B.25}$$

B.2.5 Without proliferation or cell death: host cells keep a constant biomass

According to the Equation B.6 of the general mass conservation, the adjusted mass conservation equation for the HC is

$$\begin{aligned}&\left[\frac{S^h}{K}(S^t + p^{th}\frac{\partial S^t}{\partial p^{th}}) - \epsilon\frac{\partial S^t}{\partial p^{th}}\right]\frac{\partial p^{th}}{\partial t}\\ &+\left[\frac{S^h}{K}(1 - S^l - p^{hl}\frac{S^l}{p^{hl}}) - \epsilon\frac{\partial S^l}{\partial p^{hl}}\right]\frac{\partial p^{hl}}{\partial t} + \left[\frac{S^h}{K}\right]\frac{\partial p^l}{\partial t}\\ =&\nabla\cdot\left[\frac{k^h_{rel}\mathbf{k}}{\mu^h}\cdot\nabla(p^l + p^{hl})\right] - S^h\left[\mathbf{1}:(\dot{\mathbf{e}}^{\bar{s}} - \dot{\mathbf{e}}^{\bar{s}}_{sp})\right] - \epsilon\mathbf{v}^{\bar{s}}\nabla S^h,\end{aligned} \tag{B.26}$$

B.2.6 Dormant melanocytic tumours: cancer cells keep a constant biomass

According to the Equation B.6 of general mass conservation, the adjusted mass conservation equation for the TC is

$$\frac{\partial(\rho^t\epsilon^t)}{\partial t} + \nabla\cdot(\rho^t\epsilon^t\mathbf{v}^t) = \overset{l\to t}{\mathrm{M}}. \tag{B.27}$$

The mass transfer term $\mathrm{M}^{l\to t}$ indicates growth due to transfer of mass from IF to TC as explained on page 230. With Equation B.10 and the product rule, the equation becomes

$$\frac{\epsilon S^t}{\rho^t}\frac{\partial\rho^t}{\partial t} + \epsilon\frac{\partial S^t}{\partial t} + S^t\frac{\partial\epsilon}{\partial t} = -\nabla\cdot(\epsilon S^t\mathbf{v}^{\bar{t}}) - \frac{\epsilon S^t}{\rho^t}\mathbf{v}^{\bar{t}}\cdot\nabla\rho^t + \frac{1}{\rho^t}\overset{l\to t}{\mathrm{M}} \tag{B.28}$$

and after neglecting the density change $\nabla\rho^t$ and fusion with Equation B.24, the equation has the following form:

$$\frac{\epsilon S^t}{\rho^t}\frac{\partial\rho^t}{\partial t} + \epsilon\frac{\partial S^t}{\partial t} + S^t\nabla\cdot\mathbf{v}^{\bar{s}} + S^t\frac{(1-\epsilon)}{\rho^s}\frac{\partial\rho^s}{\partial t} - S^t\nabla\cdot(\epsilon\mathbf{v}^{\bar{s}}) = -\nabla\cdot(\epsilon S^t\mathbf{v}^{\bar{t}}) + \frac{1}{\rho^t}\overset{l\to t}{\mathrm{M}}. \tag{B.29}$$

With $\nabla(\epsilon S^t\cdot\mathbf{v}^{\bar{s}}) = S^t\cdot\nabla(\epsilon\mathbf{v}^{\bar{s}}) + \epsilon\mathbf{v}^{\bar{s}}\nabla S^t$, the reordered equation

$$\begin{aligned}\frac{\epsilon S^t}{\rho^t}\frac{\partial\rho^t}{\partial t} + \epsilon\frac{\partial S^t}{\partial t} + S^t\frac{(1-\epsilon)}{\rho^s}\frac{\partial\rho^s}{\partial t} &= -S^t\nabla\cdot\mathbf{v}^{\bar{s}} + \nabla(\epsilon S^t\cdot\mathbf{v}^{\bar{s}}) - \epsilon\mathbf{v}^{\bar{s}}\nabla S^t - \nabla\cdot(\epsilon S^t\mathbf{v}^{\bar{t}}) + \frac{1}{\rho^t}\overset{l\to t}{\mathrm{M}}\\ &= \nabla\cdot[(\epsilon S^t(\mathbf{v}^{\bar{s}} - \mathbf{v}^{\bar{t}})] - S^t\nabla\cdot\mathbf{v}^{\bar{s}} - \epsilon\mathbf{v}^{\bar{s}}\nabla S^t + \frac{1}{\rho^t}\overset{l\to t}{\mathrm{M}}\end{aligned} \tag{B.30}$$

is obtained. The density of the TC is assumed to only depend on the TC pressure $\frac{\partial\rho^t}{\partial p^t}$, which can be described by a bulk modulus K_T. A bulk modulus quantifies the force, which is necessary to compress a material of interest. Assuming a high effort to compress the tumour, the following terms become zero:

$$\frac{1}{\rho^t}\frac{\partial\rho^t}{\partial p^t} = \frac{1}{K_T} = 0 \quad \text{and} \quad \frac{1}{\rho^t}\frac{\partial\rho^t}{\partial t} = \frac{1}{K_T}\frac{\partial p^t}{\partial t} = 0. \tag{B.31}$$

The density of the solid is assumed to depend on pressure only

$$\frac{1}{\rho^s}\frac{\partial \rho^s}{\partial p^s} = \frac{1}{K_S} = 0, \tag{B.32}$$

The Equations B.31 and B.32 are used to modify the Equation B.30 to

$$\frac{\epsilon S^t}{K_T}\frac{\partial p^t}{\partial t} + \epsilon\frac{\partial S^t}{\partial t} + S^t\frac{(1-\epsilon)}{K_S}\frac{\partial p^s}{\partial t} = \nabla\cdot[(\epsilon S^t(\mathbf{v}^{\bar{s}} - \mathbf{v}^{\bar{t}})] - S^t\nabla\cdot\mathbf{v}^{\bar{s}} - \epsilon\mathbf{v}^{\bar{s}}\nabla S^t + \frac{1}{\rho^t}\overset{l\to t}{\mathrm{M}} \tag{B.33}$$

$$\epsilon\frac{\partial S^t}{\partial t} = \nabla\cdot[(\epsilon S^t(\mathbf{v}^{\bar{s}} - \mathbf{v}^{\bar{t}})] - S^t\nabla\cdot\mathbf{v}^{\bar{s}} - \epsilon\mathbf{v}^{\bar{s}}\nabla S^t + \frac{1}{\rho^t}\overset{l\to t}{\mathrm{M}} \tag{B.34}$$

With the chain rule, Equation B.11 can be written as

$$\frac{\partial S^t(p^{th})}{\partial t} = \frac{\partial S^t}{\partial p^{th}}\frac{\partial p^{th}}{\partial t} = \frac{\partial\left[\frac{2}{\pi}\arctan(\frac{\sigma_{hl}}{\sigma_{th}}\frac{p^{th}}{a})\right]}{\partial p^{th}}\frac{\partial p^{th}}{\partial t} = \frac{2\sigma_{hl}}{a\pi\sigma_{th}}\left(\frac{1}{1+(\frac{\sigma_{hl}}{a\sigma_{th}}p^{th})^2}\right)\frac{\partial p^{th}}{\partial t},$$

where the derivative of the pressure-saturation degree became relevant. This equation is used to change Equation B.34 to

$$\epsilon\frac{\partial S^t}{\partial p^{th}}\frac{\partial p^{th}}{\partial t} = \nabla\cdot[(\epsilon S^t(\mathbf{v}^{\bar{s}} - \mathbf{v}^{\bar{t}})] - S^t\nabla\cdot\mathbf{v}^{\bar{s}} - \epsilon\mathbf{v}^{\bar{s}}\nabla S^t + \frac{1}{\rho^t}\overset{l\to t}{\mathrm{M}} \tag{B.35}$$

The velocity of a fluid $\mathbf{v}^\alpha$, relative to the velocity of the solid ECM scaffold $\mathbf{v}^s$, is exactly the result of the closure relationship in Equation B.23. The relative velocity depends on the pressure field $-\nabla p^\alpha$ being modified by the permeability of the porous medium $k^\alpha_{rel}\mathbf{k}$, the porosity ϵ^α, and the liquid viscosity μ^α.

B.2.7 Tumours deform the sponge-like ECM scaffold

The Equation B.35 becomes with the help of Equation B.14

$$\epsilon\frac{\partial S^t}{\partial p^{th}}\frac{\partial p^{th}}{\partial t} = \nabla\cdot\left[\frac{k^t_{rel}\mathbf{k}}{\mu^t}\cdot\nabla(p^l + p^{hl} + p^{th})\right] - S^t(\mathbf{1}:\mathbf{d}^{\bar{\bar{s}}}) - \epsilon\mathbf{v}^{\bar{s}}\nabla S^t + \frac{1}{\rho^t}\overset{l\to t}{\mathrm{M}}, \tag{B.36}$$

where the divergence of the velocity vector field of the solid $\nabla\cdot\mathbf{v}^{\bar{s}}$ is replaced by the similar expression with the Eulerian strain tensor $\mathbf{d}^{\bar{\bar{s}}}$ of the ECM phase. The Eulerian strain tensor occurs in the equation $\nabla\cdot\mathbf{v}^{\bar{s}} = \mathbf{1}:\mathbf{d}^{\bar{\bar{s}}}$ with a double dot product[5]. The difference between deformation of a liquid system and a solid system is the preserved connection between the molecules in solid materials. The strain e is the deformation of a solid, that relates the absolute displacement u, defined between the new state x and the reference state X, to

[5]The double dot product of two matrices $\mathbf{A}$ and $\mathbf{B}$ indicates point-wise multiplication $\mathbf{A}:\mathbf{B} := \sum_{ij}\mathbf{A}_{ij}\mathbf{B}_{ij} = tr(\mathbf{A}^T\mathbf{B})$

the reference length X, as shown in the following equation:

$$e = \frac{\partial(x - X)}{\partial X} = \frac{\partial u}{\partial X}.$$

This equation in one dimension becomes within a multi-dimensional space a tensor $\mathbf{e}^s = \frac{1}{2}[\nabla \mathbf{u}^{\overline{s}} + (\nabla \mathbf{u}^{\overline{s}})^{\mathrm{T}}]$ [51, (eq: 9.95)]. The rate of the strain tensor

$$d^{\overline{\overline{\alpha}}} = \frac{\partial e}{\partial t} = \frac{\partial^2 u}{\partial t \partial X} = \frac{\partial \mathrm{v}}{\partial X},$$

is similar to the Equation B.5, which can be directly linked to the velocity and describes the displacement per time. A further relationship between deformation and velocity is given with the velocity gradient tensor $\mathbf{L}^{\overline{\overline{s}}} = \nabla \mathbf{v}^{\overline{\overline{s}}} = \mathbf{d}^{\overline{\overline{s}}} + \mathbf{w}^{\overline{\overline{s}}}$ with the symmetric part $\mathbf{d}^{\overline{\overline{s}}}$, which is called the Eulerian strain rate tensor

$$d_{ij}^s = \frac{1}{2}\left(\frac{\partial v_i}{\partial x_j} + \frac{\partial v_j}{\partial x_i}\right)$$

and the skew-symmetric part $\mathbf{w}^{\overline{\overline{s}}}$, which is called the spin tensor

$$w_{ij}^s = \frac{1}{2}\left(\frac{\partial v_i}{\partial x_j} - \frac{\partial v_j}{\partial x_i}\right).$$

The Einstein summation convention is used. With small strain increments and without high compressibility or large rotations, the Jaumann stress rate

$$\frac{\partial^J t_{ij}^{\overline{\overline{s}}}}{\partial t} = \frac{\partial t_{ij}^{\overline{\overline{s}}}}{\partial t} - t_{kj}^{\overline{\overline{s}}} w_{ik}^{\overline{\overline{s}}} + t_{ik}^{\overline{\overline{s}}} w_{jk}^{\overline{\overline{s}}}.$$

is given. The Equation B.36 can be improved in its numerical convergence behaviour if it is directly related to the pressure strain of the solid phase. The rate of the Eulerian strain tensor

$$\mathbf{d}^{\overline{\overline{s}}} = \dot{\mathbf{e}}^{\overline{\overline{s}}} = \dot{\mathbf{e}}_{ts}^{\overline{\overline{s}}} + \dot{\mathbf{e}}_{sp}^{\overline{\overline{s}}} = \mathbf{d}_{ts}^{\overline{\overline{s}}} + \mathbf{d}_{sp}^{\overline{\overline{s}}}$$

is related to the effective stress and can be partitioned into the solid total strain part $\mathbf{e}_{ts}^{\overline{\overline{s}}}$ and the strain part that integrates the ECM solid pressure, which is caused by the fluid phase pressures via Equation B.14. The solid total strain and the solid pressure are related in the equation

$$\mathbf{d}_{sp}^{\overline{\overline{s}}} = \frac{\tilde{\alpha}}{3K}\frac{\partial p^s}{\partial t}\mathbf{1} = \begin{pmatrix} \frac{\tilde{\alpha}}{3K}\frac{\partial p^s}{\partial t} & & \\ & \frac{\tilde{\alpha}}{3K}\frac{\partial p^s}{\partial t} & \\ & & \frac{\tilde{\alpha}}{3K}\frac{\partial p^s}{\partial t} \end{pmatrix}$$

and the equation

$$\mathbf{1} : \mathbf{d}_{sp}^{\bar{\bar{s}}} = \frac{\tilde{\alpha}}{3K}\frac{\partial p^s}{\partial t} + \frac{\tilde{\alpha}}{3K}\frac{\partial p^s}{\partial t} + \frac{\tilde{\alpha}}{3K}\frac{\partial p^s}{\partial t} = \frac{\tilde{\alpha}}{K}\frac{\partial p^s}{\partial t}. \tag{B.37}$$

The compression of the unsaturated ECM scaffold is described by the bulk modulus K. The Biot coefficient $\tilde{\alpha}$ is simplified with the assumption of an incompressible but deformable ECM material with $K_S \to \infty$ to $\tilde{\alpha} = 1 - \mathrm{K}/\mathrm{K_S} = 1$.
The pressure of the solid

$$p^s = \langle \mathbf{n}_s \cdot \mathbf{t}_s \cdot \mathbf{n}_s \rangle_{\Omega_{ls},\Omega_{ls}}$$

is a macroscale variable. The macroscale variable is an averaged product over the interface $\langle\rangle_{\Omega_{ls},\Omega_{ls}}$ between liquid and solid phase [51, p. 359], while Equation B.12 accounts for the relationship between fluid and solid stress at the microscale. The microscale normal vector of the solid $\mathbf{n}_s$ acts together with the microscale solid phase stress tensor

$$\mathbf{t}_s = \frac{2}{j_s}(\nabla_X \mathbf{x}_s)^{\mathrm{T}} \cdot \sigma_s \cdot \nabla_X \mathbf{x}_s, \qquad \text{[51, p. 145]} \tag{B.38}$$

the Jacobian j_s, and the thermodynamic representation of the solid stress tensor σ_s [51, p. 113]. The Equation B.38 can be simplified with Green's deformation tensor $\mathbf{C}_s = \nabla_X \mathbf{x}_s \cdot (\nabla_X \mathbf{x}_s)^{\mathrm{T}}$ [51, p. 138] to $\mathbf{n}_s \cdot \mathbf{t}_s \cdot \mathbf{n}_s = \frac{2\sigma_s : \mathbf{C}_s}{3j_s}$ [51, p. 152]. The related Equation B.23 is obtained from the TCAT macroscale momentum equation for the fluid phase, described in section B.2.2.
The microscale stress tensor of Equation B.38 can be averaged to the effective macroscale stress tensor $\mathbf{t}^{\bar{\bar{s}}}$, which builds the macroscale effective stress tensor [44, (eq: 97-101)]

$$\mathbf{t}_{\mathsf{eff}}^{\bar{\bar{s}}} = \mathbf{t}^{\bar{\bar{s}}} + \tilde{\alpha} p^s \mathbf{1} = \mathbf{t}^{\bar{\bar{s}}} + p^s \mathbf{1}.$$

The stress-strain relationship is given as

$$\begin{aligned} \dot{\mathbf{t}}_{\mathsf{eff}}^{\bar{\bar{s}}} &= \mathbf{D}_s : \dot{\mathbf{e}}_{\mathsf{el}}^{\bar{\bar{s}}} = \mathbf{D}_s : (\dot{\mathbf{e}}^{\bar{\bar{s}}} - \dot{\mathbf{e}}_{\mathsf{vp}}^{\bar{\bar{s}}}) \\ &= \mathbf{D}_s : \mathbf{d}_{\mathsf{el}}^{\bar{\bar{s}}} = \mathbf{D}_s : (\mathbf{d}^{\bar{\bar{s}}} - \mathbf{d}_{\mathsf{vp}}^{\bar{\bar{s}}}). \end{aligned} \tag{B.39}$$

with the tangent matrix $\mathbf{D}_s$. The tangent matrix mimics the mechanical properties of the solid scaffold, the strain for the elastic $\mathrm{e}_{\mathsf{el}}^{\bar{\bar{s}}}$, the visco-plastic $\mathrm{e}_{\mathsf{vp}}^{\bar{\bar{s}}}$ and the combined $\mathrm{e}^{\bar{\bar{s}}}$ mechanical strain. When the fluids in the pore space expand and increase the pressure within the deformable ECM scaffold, the scaffold deformes according to the momentum balance equation of the ECM phase. The governing equation for the linear momentum balance equation in rate form is

$$\nabla \cdot \left(\frac{\partial \mathbf{t}_{\mathsf{eff}}^{\bar{\bar{s}}}}{\partial t} - \frac{\partial p^s}{\partial t} \right) = 0 \tag{B.40}$$

and is derived from the momentum closure relatins in Equation B.16. The divergence of total stress is zero $\nabla \cdot \mathbf{t}^{\overline{\overline{s}}} = 0$ to preserve the momentum over the whole system. With the Equations B.37 and B.39, the Equation B.40 changes to

$$\nabla \cdot \left(\mathbf{D}_s : (\mathbf{d}^{\overline{\overline{s}}} - \mathbf{d}_{\mathsf{vp}}^{\overline{\overline{s}}}) - K \cdot (\mathbf{1} : \mathbf{d}_{sp}^{\overline{\overline{s}}}) \right) = 0$$

$$\nabla \cdot \mathbf{D}_s : \mathbf{d}^{\overline{\overline{s}}} = \nabla \cdot \mathbf{D}_s : \mathbf{d}_{\mathsf{vp}}^{\overline{\overline{s}}} + \nabla \cdot \mathrm{K} \cdot (\mathbf{1} : \mathbf{d}_{sp}^{\overline{\overline{s}}}),$$

where the rate of displacement is $\mathbf{d}^{\overline{\overline{s}}} = \frac{\partial \mathbf{e}^{\overline{\overline{s}}}}{\partial t}$. The relationship between displacement and strain is then

$$\mathbf{e}^{\overline{\overline{s}}} = \mathbf{S}\mathbf{u}^s, \qquad \mathbf{S}^{\mathrm{T}} = \begin{bmatrix} \frac{\partial}{\partial x_1} & & & \frac{\partial}{\partial x_2} & & \frac{\partial}{\partial x_3} \\ & \frac{\partial}{\partial x_2} & & \frac{\partial}{\partial x_1} & \frac{\partial}{\partial x_3} & \\ & & \frac{\partial}{\partial x_3} & & \frac{\partial}{\partial x_2} & \frac{\partial}{\partial x_1} \end{bmatrix}. \qquad \text{[465, (p. 8)]}$$

With the Galerkin procedure, explained in the following section, and the transformation $\mathbf{u}^s(t) \cong \mathbf{N}_u \overline{\mathbf{u}}^{\overline{s}}(t)$, the relation

$$\mathbf{d}^{\overline{\overline{s}}} = \mathbf{S}\mathbf{N}_u \frac{\partial \overline{\mathbf{u}}^{\overline{s}}}{\partial t} = \mathbf{B} \frac{\partial \overline{\mathbf{u}}^{\overline{s}}}{\partial t}, \qquad \mathbf{B}^{\mathrm{T}} = \begin{bmatrix} \frac{\partial \mathbf{N}_u}{\partial x_1} & & & \frac{\partial \mathbf{N}_u}{\partial x_2} & & \frac{\partial \mathbf{N}_u}{\partial x_3} \\ & \frac{\partial \mathbf{N}_u}{\partial x_2} & & \frac{\partial \mathbf{N}_u}{\partial x_1} & \frac{\partial \mathbf{N}_u}{\partial x_3} & \\ & & \frac{\partial \mathbf{N}_u}{\partial x_3} & & \frac{\partial \mathbf{N}_u}{\partial x_2} & \frac{\partial \mathbf{N}_u}{\partial x_1} \end{bmatrix} \qquad \text{[465, (p. 20)]}$$

leads to the final form of the momentum balance equation

$$(\mathbf{C}_{uu})_{ij} \frac{\partial \overline{\mathbf{u}}^{\overline{s}}}{\partial t} = \mathbf{f}_u$$

$$-\int_\Omega \mathbf{B}^{\mathrm{T}} \nabla \cdot (\mathbf{D}_s : \mathbf{1}) \mathbf{B} d\Omega \frac{\partial \overline{\mathbf{u}}^{\overline{s}}}{\partial t} = \int_\Omega \mathbf{B}^{\mathrm{T}} \nabla \cdot (\mathbf{D}_s : \mathbf{d}_{\mathsf{vp}}^{\overline{\overline{s}}}) d\Omega + \int_\Omega \mathbf{B}^{\mathrm{T}} \nabla \cdot (\mathrm{K} \cdot (\mathbf{1} : \mathbf{d}_{sp}^{\overline{\overline{s}}})) d\Omega$$

$$-\int_\Omega \mathbf{B}^{\mathrm{T}} \mathbf{D}_s \mathbf{B} d\Omega \frac{\partial \overline{\mathbf{u}}^{\overline{s}}}{\partial t} = \int_\Omega \mathbf{B}^{\mathrm{T}} (\mathbf{D}_s \mathbf{d}_{\mathsf{vp}}^{\overline{\overline{s}}}) d\Omega + \int_\Omega \mathbf{B}^{\mathrm{T}} (\mathbf{D}_\mathbf{s} \mathbf{d}_{sp}^{\overline{\overline{s}}}) d\Omega$$

with $K = \mathbf{D}_s$ and $\mathrm{div}(\mathbf{A} : \mathbf{B}) = \mathrm{div}(\mathrm{tr}(\mathbf{A}^{\mathrm{T}}\mathbf{B})) = \mathrm{tr}(\mathrm{grad}(\mathrm{tr}(\mathbf{A}^{\mathrm{T}}\mathbf{B}))) = \mathbf{AB}$

B.2.8 Galerkin method for space discretisation

Spatial models require specialised and powerful numeric approaches to obtain the solution of the equation set. The model equations are therefore discretised in time with the approach of Crank-Nicolson and the Wilson's Theta method and in space with the Galerkin method. The Galerkin method solves the system in the weak equation form. The example equation $-div(K\nabla u) = f(x)$ is a PDE in the strong and implicit form $div(K\nabla u) + f(x) = 0$. With the use of shape/test functions N, the weak and implicit form is represented over the integral of a particular domain $\int_\Omega \mathrm{N} \cdot (div(K\nabla u) + f(x)) d\Omega = 0$. Shape functions have the value 1 at a point of interest and the value 0 at other points. With a collection of shape functions, the scalar function can be approximated.

■ **Example B.1** The week formulation $\int_0^1(-u''(x) - f(x))N_h(x)\mathrm{d}x = 0$ is an one-dimensional case with $x \in [01]$ and the boundary condition $u(0) = u(1) = 0$. The equation is multiplied with shape functions

$$-\int_0^1 u''(x)\cdot N_h(x)\mathrm{d}x - \int_0^1 f(x)\cdot N_h(x)\mathrm{d}x$$

and become the equation

$$\underbrace{-u'(x)\cdot N_h(x)\Big|_0^1}_{=0} + \int_0^1 u'(x)\cdot N_h'(x)\mathrm{d}x = \int_0^1 f(x)\cdot N_h(x)\mathrm{d}x$$

after integration. With $u(x) \cong \sum_a \overline{u}_a N_a(x),\ u'(x) \cong \sum_a \overline{u}_a N_a'(x)$ and test function $N_h = \sum_b c_b N_b(x),\ N_h' = \sum_b c_b N_b'(x)$, one obtains

$$\int_0^1 \sum_a \overline{u}_a N_a'(x)\cdot\sum_b c_b N_b'(x)\mathrm{d}x = \int_0^1 f(x)\cdot\sum_b c_b N_b(x)\mathrm{d}x$$

$$\sum_a \overline{u}_a \underbrace{\int_0^1 N_a'(x)N_b'(x)\mathrm{d}x}_{\mathrm{k}_{ab}} = \underbrace{\int_0^1 f(x)\cdot\sum_b N_b(x)\mathrm{d}x}_{f_b}$$

with which the differential operator shift from the system equations to the shape functions. Such equation sets can be presented in the matrix form:

$$k_{11} = \int_0^h \frac{1}{h}\cdot\frac{1}{h}\mathrm{d}x + \int_h^{2h}(-\frac{1}{h})\cdot(-\frac{1}{h})\mathrm{d}x = \frac{2}{h} = k_{22}$$

$$k_{12} = \int_0^h \frac{1}{h}\cdot 0\mathrm{d}x + \int_h^{2h}(-\frac{1}{h})\cdot\frac{1}{h}\mathrm{d}x = -\frac{1}{h} = k_{21}$$

$$k\cdot\overline{u} = fh$$

$$\frac{1}{h^2}\underbrace{\begin{bmatrix} 2 & -1 & 0 & 0 & \cdots & 0 \\ -1 & 2 & -1 & 0 & & \vdots \\ 0 & -1 & 2 & -1 & & \vdots \\ \vdots & & \ddots & \ddots & \ddots & \vdots \\ \vdots & & & \ddots & \ddots & -1 \\ 0 & \cdots & \cdots & \cdots & -1 & 2 \end{bmatrix}}_{k}\cdot\begin{bmatrix} u_1 \\ u_2 \\ \vdots \\ \vdots \\ \vdots \\ \vdots \end{bmatrix} = \begin{bmatrix} f_1 \\ f_2 \\ \vdots \\ \vdots \\ \vdots \\ \vdots \end{bmatrix}$$

The function $\mathbf{f}$ has bounded support, and one can take $A = \{x \in \mathbb{R}^2 : |x - x^0| \leq 1/2 + \epsilon\}$ for all $\epsilon \in]0\,;5/2 - \sqrt{2}[$. ■

B.2.9 Governing equation of tumour cells relates to the ECM

After the Equation B.13 is added to the left and right side of Equation B.36, the mass balance equation for the tumour mass is:

$$\begin{aligned}&\left[\frac{S^t}{K}(S^t+p^{th}\frac{\partial S^t}{\partial p^{th}})+\epsilon\frac{\partial S^t}{\partial p^{th}}\right]\frac{\partial p^{th}}{\partial t}+\left[\frac{S^t}{K}(1-S^l-p^{hl}\frac{S^l}{p^{hl}})\right]\frac{\partial p^{hl}}{\partial t}+\left[\frac{S^t}{K}\right]\frac{\partial p^l}{\partial t}\\ =&\nabla\cdot\left[\frac{k^t_{rel}\mathbf{k}}{\mu^t}\cdot\nabla(p^l+p^{hl}+p^{th})\right]-S^t\left[\mathbf{1}:(\mathbf{d}^{\overline{\overline{s}}}-\mathbf{d}^{\overline{\overline{s}}}_{sp})\right]-\epsilon\mathbf{v}^{\overline{s}}\nabla S^t+\frac{1}{\rho^t}\overset{l\to t}{\mathrm{M}}\end{aligned}\tag{B.41}$$

This equation can be seen as weak form for the Galerkin procedure as described in the previous section. The primary variables are chosen as follows:

$$\begin{aligned}p^{th}(t)&\cong\mathbf{N}_t\overline{\mathbf{p}}^{th}(t)\\ p^{hl}(t)&\cong\mathbf{N}_h\overline{\mathbf{p}}^{hl}(t)\\ p^{l}(t)&\cong\mathbf{N}_l\overline{\mathbf{p}}^{l}(t)\\ w^{\overline{nl}}(t)&\cong\mathbf{N}_n\overline{\mathbf{w}}^{\overline{nl}}(t)\\ \mathbf{u}^{s}(t)&\cong\mathbf{N}_u\overline{\mathbf{u}}^{\overline{s}}(t)\end{aligned}$$

The vectors with the nodal values are $\overline{\mathbf{p}}^{th}(t),\overline{\mathbf{p}}^{hl}(t),\overline{\mathbf{p}}^{l}(t),\overline{\mathbf{w}}^{\overline{nl}}(t)$, and $\overline{\mathbf{u}}^{\overline{s}}(t)$. The related vectors of shape functions are $\mathbf{N}_t,\mathbf{N}_h,\mathbf{N}_l,\mathbf{N}_n$, and $\mathbf{N}_u$. The Equation B.41 is then

$$\begin{aligned}&\int_\Omega\mathbf{N}_t^{\mathrm{T}}\left[\frac{S^t}{K}(S^t+p^{th}\frac{\partial S^t}{\partial p^{th}})\mathbf{N}_t+\epsilon\frac{\partial S^t}{\partial p^{th}}\mathbf{N}_t\right]d\Omega\cdot\frac{\partial\overline{\mathbf{p}}^{th}}{\partial t}\\ &+\int_\Omega\mathbf{N}_t^{\mathrm{T}}\left[\frac{S^t}{K}(1-S^l-p^{hl}\frac{S^l}{p^{hl}})\mathbf{N}_h\right]d\Omega\cdot\frac{\partial\overline{\mathbf{p}}^{hl}}{\partial t}\\ &+\int_\Omega\mathbf{N}_t^{\mathrm{T}}\left[\frac{S^t}{K}\mathbf{N}_l\right]d\Omega\cdot\frac{\partial\mathbf{p}^{l}}{\partial t}\\ &-\int_\Omega(\nabla\mathbf{N}_t)^{\mathrm{T}}\left[\frac{k^t_{rel}\mathbf{k}}{\mu^t}\nabla\mathbf{N}_t)\right]d\Omega\cdot\overline{\mathbf{p}}^{th}\\ &-\int_\Omega(\nabla\mathbf{N}_t)^{\mathrm{T}}\left[\frac{k^t_{rel}\mathbf{k}}{\mu^t}\nabla\mathbf{N}_h)\right]d\Omega\cdot\overline{\mathbf{p}}^{hl}\\ &-\int_\Omega(\nabla\mathbf{N}_t)^{\mathrm{T}}\left[\frac{k^t_{rel}\mathbf{k}}{\mu^t}\nabla\mathbf{N}_l)\right]d\Omega\cdot\overline{\mathbf{p}}^{l}\\ =&\int_\Omega\mathbf{N}_t^{\mathrm{T}}\left[\frac{1}{\rho^t}\overset{l\to t}{\mathrm{M}}-S^t\left[\mathbf{1}:(\mathbf{d}^{\overline{\overline{s}}}-\mathbf{d}^{\overline{\overline{s}}}_{sp})\right]-\epsilon\mathbf{v}^{\overline{s}}\nabla S^t\right]d\Omega.\end{aligned}$$

and can be written in the matrix form:

$$\begin{pmatrix}\mathbf{C}_{tt} & \mathbf{C}_{th} & \mathbf{C}_{tl}\end{pmatrix}\begin{pmatrix}\frac{\partial\overline{\mathbf{p}}^{th}}{\partial t}\\ \frac{\partial\overline{\mathbf{p}}^{hl}}{\partial t}\\ \frac{\partial\overline{\mathbf{p}}^{pl}}{\partial t}\end{pmatrix}+\begin{pmatrix}\mathbf{K}_{tt} & \mathbf{K}_{th} & \mathbf{K}_{tl}\end{pmatrix}\begin{pmatrix}\overline{\mathbf{p}}^{th}\\ \overline{\mathbf{p}}^{hl}\\ \overline{\mathbf{p}}^{pl}\end{pmatrix}=\mathbf{f}_t$$

or simply

$$\mathbf{C}_{ij}(\mathbf{x})\frac{\partial \mathbf{x}}{\partial t} + \mathbf{K}_{ij}(\mathbf{x})\mathbf{x} = \mathbf{f}_i(\mathbf{x}).$$

This equation captures the multi-fluid system. This fluid system is a numeric bloc and must be iteratively aligned with the numeric bloc for the ECM momentum equation (deformation of the solid material) and the numeric bloc for the species mass conservation (necrotic part of the tumour cells). This is visualised with three yellow blocks in Figure B.3. The last missing numeric bloc describes necrosis within the tumour phase and motivates the following section.

B.2.10 Necrosis inside the tumour cell phase

The current TCAT systems allows only three immiscible and independently moving liquids beside the solid phase. But it is possible to subdivide each immiscible liquid into miscible liquids as often as desired. The tumour phase can exhibit a certain necrotic part due to oxygen limitation. The mass fraction of the necrotic tumour mass part $\omega^{N\bar{t}} = \frac{\epsilon^{N\bar{t}}\rho^{N\bar{t}}}{\epsilon^t\rho^t}$ is complement to the living tumour mass part $(1-\omega^{N\bar{t}})$. The rate of death $\epsilon^t r^{N\bar{t}}$ describes the exchange of mass between those two miscible liquids as specified on page 230. All miscible liquids move with the same velocity like the phase to which they belong. The mass conservation of the necrotic tumour mass

$$\frac{\partial \epsilon^t\rho^t\omega^{N\bar{t}}}{\partial t} + \nabla\cdot(\epsilon^t\rho^t\omega^{N\bar{t}}\mathbf{v}^{\bar{t}}) - \epsilon^t r^{Nt} = 0 \tag{B.42}$$

is distinguished from the mass conservation of the living tumour mass

$$\frac{\partial \epsilon^t\rho^t(1-\omega^{N\bar{t}})}{\partial t} + \nabla\cdot(\epsilon^t\rho^t(1-\omega^{N\bar{t}})\mathbf{v}^{\bar{t}}) + \epsilon^t r^{Nt} - \overset{l\to t}{\mathrm{M}} = 0 \tag{B.43}$$

The living tumour mass grows at the expense of IF $\mathrm{M}^{l\to t}$ as specified on page 230. The summation of Equations B.42 and B.43 gives the Equation B.27, which were developed on page 221 for the tumour mass conservation equation $\frac{\partial(\rho^t\epsilon^t)}{\partial t} + \nabla\cdot(\rho^t\epsilon^t\mathbf{v}^t) = \mathrm{M}^{l\to t}$. The expansion of Equation B.42 with the product rule[6] results in

$$\epsilon^t\rho^t\frac{\partial\omega^{N\bar{t}}}{\partial t} + \omega^{N\bar{t}}\frac{\partial\epsilon^t\rho^t}{\partial t} + \omega^{N\bar{t}}\nabla\cdot(\epsilon^t\rho^t\mathbf{v}^{\bar{t}}) + \epsilon^t\rho^t\mathbf{v}^{\bar{t}}\cdot\nabla\omega^{N\bar{t}} - \epsilon^t r^{Nt} = 0$$

$$\epsilon^t\rho^t\frac{\partial\omega^{N\bar{t}}}{\partial t} + \omega^{N\bar{t}}\underset{\text{growth}}{\overset{l\to t}{\mathrm{M}}} + \epsilon^t\rho^t\mathbf{v}^t\cdot\nabla\omega^{N\bar{t}} - \epsilon^t r^{Nt} = 0$$

[6] Product rule of divergence: If $\mathbf{v}$ is a vector field and f a scalar valued function than $\nabla\cdot(fv) = \sum\partial_i(fv_i) = \sum(f\partial_i v_i + v_i\partial_i f) = f\sum\partial_i v_i + \sum v_i\partial_i f = f\nabla\cdot v + v\cdot\nabla f$ takes effect. In this case, the mass fraction $\omega^{N\bar{t}} = f$ is the scalar valued function and the velocity term $\epsilon^t\rho^t\mathbf{v}^{\bar{t}} = v$ is the vector field.

with the velocity of the tumour mass $\mathbf{v}^t$, which is described in Equation B.23. With $\epsilon^t = \epsilon S^t$, the final form is

$$\frac{\partial \omega^{N\bar{t}}}{\partial t} = \frac{1}{\epsilon S^t \rho^t}\left[\epsilon S^t r^{Nt} - \omega^{N\bar{t}} \underset{\text{growth}}{\overset{l\to t}{\mathrm{M}}} - \epsilon S^t \rho^t \mathbf{v}^t \cdot \nabla \omega^{N\bar{t}}\right].$$

This equation is solved outside the staggered scheme and does't belong to the governing equations.

B.2.11 Soluble factors: how an oxygen gradient is set

The TCAT Equation B.8 on page 213 is used as starting point for the description of the diffusive species. The species i shall present oxygen and should diffuse within the IF $\alpha = \kappa = l$. With Fick's law $\rho^l \omega^{\overline{ol}} \mathbf{u}^{\overline{\overline{ol}}} = -D^{\overline{ol}}_{\text{eff}} \rho^l \nabla \omega^{\overline{ol}}$ and the effective diffusion coefficient

$$D^{\overline{ol}}_{\text{eff}} = D^{\overline{ol}}_0 (\epsilon S^l)^\sigma,$$

the diffusion is described as a function of basal diffusion coefficient $D^{\overline{ol}}_0$, IF volume fraction ϵS^l, and extracellular space tortuosity assumed to be $\sigma = 2$. The diffusion at the macroscale depends more on the interconnectivity grade of the pore space then on the IF volume fraction [148]. Equation B.8 is modified to

$$\frac{\partial[(\epsilon S^l \rho^l \omega^{o\bar{l}})]}{\partial t} + \nabla \cdot (\epsilon S^l \rho^l \omega^{o\bar{l}} \mathbf{v}^{\bar{l}}) - \nabla \cdot (\epsilon S^l D^{\overline{ol}}_0 (\epsilon S^l)^\sigma \rho^l \nabla \omega^{\overline{ol}}) - \epsilon S^l r^{ol} - \sum_{\kappa \in \mathfrak{I}_{Cl}} \overset{i\kappa\to i\alpha}{\mathrm{M}} = 0.$$

Without internal reactions among the species $r^{ol} = 0$ but with the product rule, an oxygen sink with negative sign, and the oxygen transport from interphase κ to the phase α, the equation changes to

$$\epsilon S^l \rho^l \frac{\partial \omega^{o\bar{l}}}{\partial t} + \omega^{o\bar{l}} \frac{\partial \epsilon S^l \rho^l}{\partial t} + \omega^{o\bar{l}} \nabla \cdot (\epsilon S^l \rho^l \mathbf{v}^{\bar{l}}) + \epsilon S^l \rho^l \mathbf{v}^{\bar{l}} \cdot \nabla \omega^{o\bar{l}} - \nabla \cdot (\epsilon S^l D^{\overline{ol}}_0 (\epsilon S^l)^\sigma \rho^l \nabla \omega^{\overline{ol}}) + \overset{ol\to\varnothing}{\mathrm{M}} = 0.$$

This equation changes with Equation B.27 to the relationship

$$\epsilon S^l \rho^l \frac{\partial \omega^{o\bar{l}}}{\partial t} + \omega^{o\bar{l}} \overset{l\to t}{\mathrm{M}} + \epsilon S^l \rho^l \mathbf{v}^{\bar{l}} \cdot \nabla \omega^{o\bar{l}} - \nabla \cdot (\epsilon S^l D^{\overline{ol}}_0 (\epsilon S^l)^\sigma \rho^l \nabla \omega^{\overline{ol}}) + \overset{ol\to\varnothing}{\mathrm{M}} = 0,$$

where $\omega^{o\bar{l}}\, \mathrm{M}^{l\to t}$ accounts for oxygen consumption due to the tumour growth, and $\mathrm{M}^{nl\to t}$ encompasses the oxygen consumption based on growth independent metabolism. The reordered form is

$$\epsilon S^l \frac{\partial \omega^{ol}}{\partial t} = \underbrace{\nabla \cdot (\epsilon S^l D^{\overline{ol}}_0 (\epsilon S^l)^\sigma \nabla \omega^{ol})}_{\text{oxygen diffusion}} + \underbrace{\frac{1}{\rho^l}(\omega^{ol} \overset{l\to t}{\mathrm{M}} - \overset{ol\to\varnothing}{\mathrm{M}})}_{\text{oxygen consumption}} - \underbrace{\epsilon S^l \mathbf{v}^l \nabla \omega^{ol}}_{\text{IF flow carries oxygen}}$$

where the convective transport is small in comparison to the diffusive part so that the final governing equation is

$$\epsilon S^l \frac{\partial \omega^{ol}}{\partial t} = \nabla \cdot (\epsilon S^l D_0^{\overline{ol}} (\epsilon S^l)^\sigma \nabla \omega^{ol}) + \frac{1}{\rho^l} (\omega^{ol} \overset{l\to t}{\mathrm{M}} - \overset{ol\to\varnothing}{\mathrm{M}}).$$

With the Galerkin procedure and transformation $w^{\overline{ol}}(t) \cong \mathbf{N}_n \overline{\mathbf{w}}^{\overline{ol}}(t)$ the weak form is

$$\mathrm{C}_{nn} \frac{\partial \mathbf{w}^{\overline{ol}}}{\partial t} + \mathrm{K}_{nn} \mathbf{w}^{\overline{ol}} = \mathrm{f}_n$$

$$\int_\Omega \mathbf{N}_n^{\mathrm{T}} (\epsilon S^l \mathbf{N}_n) d\Omega \frac{\partial \mathbf{w}^{\overline{ol}}}{\partial t} + \int_\Omega (\nabla \mathbf{N}_n)^{\mathrm{T}} (\epsilon S^l D_0^{\overline{ol}} (\epsilon S^l)^\sigma \nabla \mathbf{N}_n) d\Omega \mathbf{w}^{\overline{ol}} = \int_\Omega \mathbf{N}_n^{\mathrm{T}} \frac{1}{\rho^l} (\omega^{ol} \overset{l\to t}{\mathrm{M}} - \overset{ol\to\varnothing}{\mathrm{M}}) d\Omega$$

B.2.12 Tissue dynamic with proliferation, metabolism, and death: interphase mass exchange

The previous sections described a tissue model in a steady state without any biological changes. Neither does the tumour growth nor is oxygen consumed, and the tumour cells do not die. Everything, which the biologists and clinicians know, has to be actively described for the model as long as it is crucial for the model purpose. In order to make the model living, rules have to be implemented, which mainly concerns the transfer of mass across phases. These rules are formulated in the form of interphase mass exchange terms. The previously described equations ensure, that the model finds subsequently its new equilibrium after each biological perturbation.
The TCAT tumour growth model has interphase mass exchange terms $\mathrm{M}^{\kappa\to\alpha}$, which transports mass from an immiscible fluid κ to an immiscible fluid α. The transport within one phase and between two miscible fluids is done by the reaction term $\epsilon^{\overline{\overline{\alpha}}} r^{i\alpha}$. The growth of living tumour mass $(1-\omega^{N\bar{t}})\epsilon S^t$ is modelled as mass transfer from IF to the tumour phase

$$\overset{l\to t}{\underset{\text{growth}}{\mathrm{M}}} = [\gamma^t_{\text{growth}} G_1(\omega^{\overline{ol}}) G_2(p^t)](1-\omega^{\overline{Nt}})\epsilon S^t \tag{B.44}$$

and depends on the maximum proliferation rate γ_{growth}, the oxygen concentration $\omega^{\overline{ol}}$, and the local tumour phase pressure p^t. The last two variables additinally affect the oxygen consumption rate

$$\overset{ol\to\varnothing}{\mathrm{M}} = [\gamma^{\overline{ol}}_{\text{growth}} G_1(\omega^{\overline{ol}}) G_2(p^t) + \gamma_0^{\overline{ol}} R(\omega^{\overline{ol}})](1-\omega^{N\bar{t}})\epsilon S^t. \tag{B.45}$$

This equation contains the maximum growth dependant oxygen consumption rate $\gamma^{\overline{ol}}_{\text{growth}}$ and the oxygen consumption due to the basal TC respiration $\gamma_0^{\overline{ol}} R(\omega^{\overline{ol}})$, which in turn depends on the available oxygen level $\omega^{\overline{ol}}$ and the maximum oxygen consumption rate $\gamma_0^{\overline{ol}}$. While the Equation B.44 is related to the mass of the phases averaged over all internal species i, the Equation B.45 accounts only for the species $i = o$ dependent mass

within the phases. The necrotic subfraction appears when oxygen falls below the oxygen depreviation threshold $N_1(\omega^{\overline{nl}}$ and increases to the maximum rate $\gamma^t_{\text{necrosis}}$. Albeight biologically justified, the model assumes necrosis due to high tumour pressure $N_2(p^t)$ with a maximum rate of σ^t_α. The mass transfer within the tumour phase

$$\epsilon S^t r^{N^t} = [\gamma^t_{\text{necrosis}} N_1(\omega^{\overline{ol}}) + \sigma^t_\alpha N_2(p^t)](1-\omega^{N\bar{t}})\epsilon S^t$$

occurs from the living TC fraction $(1-\omega^{N\bar{t}})\epsilon S^t$ to the death TC fraction $\omega^{N\bar{t}}\epsilon S^t$. The related sub functions

$$G_1(\omega^{\overline{ol}}) = \begin{cases} 0 & \text{for } 0 \le \omega^{\overline{ol}} \le \omega^{\overline{ol}}_{\text{crit}} \\ \frac{1}{2} + \frac{1}{2}\cos\left[\pi\left(1 + \frac{\omega^{\overline{ol}} - \omega^{\overline{ol}}_{\text{crit}}}{\omega^{\overline{ol}}_{\text{env}} - \omega^{\overline{ol}}_{\text{crit}}}\right)\right] & \text{for } \omega^{\overline{ol}}_{\text{crit}} \le \omega^{\overline{ol}} \le \omega^{\overline{ol}}_{\text{env}} \\ 1 & \text{for } \omega^{\overline{ol}} \ge \omega^{\overline{ol}}_{\text{env}} \end{cases}$$

$$G_2(p^t) = \begin{cases} 1 & \text{for } 0 \le p^t \le p^t_{\text{cr1}} \\ \frac{1}{2} + \frac{1}{2}\cos\left[\pi\left(1 + \frac{p^t - p^t_{\text{cr1}}}{p^t_{\text{cr2}} - p^t_{\text{cr1}}}\right)\right] & \text{for } p^t_{\text{cr1}} \le p^t \le p^t_{\text{cr2}} \\ 0 & \text{for } p^t \ge p^t_{\text{cr2}} \end{cases}$$

$$R(\omega^{\overline{ol}}) = \begin{cases} \frac{1}{2} + \frac{1}{2}\cos\left[\pi\left(1 + \frac{\omega^{\overline{ol}}}{\omega^{\overline{ol}}_{\text{crit}}}\right)\right] & \text{for } 0 \le \omega^{\overline{ol}} \le \omega^{\overline{ol}}_{\text{crit}} \\ 1 & \text{for } \omega^{\overline{ol}} \ge \omega^{\overline{ol}}_{\text{crit}} \end{cases}$$

$$N_1(\omega^{\overline{ol}}) = \begin{cases} \frac{1}{2} + \frac{1}{2}\cos\left(\frac{\omega^{\overline{ol}}}{\omega^{\overline{ol}}_{\text{crit}}}\pi\right) & \text{for } 0 \le \omega^{\overline{ol}} \le \omega^{\overline{ol}}_{\text{crit}} \\ 0 & \text{for } \omega^{\overline{ol}} \ge \omega^{\overline{ol}}_{\text{crit}} \end{cases}$$

$$N_2(p^t) = \begin{cases} 0 & \text{for } 0 \le p^t \le p^t_{\text{cr1}} \\ \frac{1}{2} + \frac{1}{2}\cos\left[\pi\left(1 + \frac{p^t - p^t_{\text{cr1}}}{p^t_{\text{cr2}} - p^t_{\text{cr1}}}\right)\right] & \text{for } p^t_{\text{cr1}} \le p^t \le p^t_{\text{cr2}} \\ 1 & \text{for } p^t \ge p^t_{\text{cr2}} \end{cases}$$

are visualised in Figure B.5. The threshold parameters within these functions describe the transition zones. Below the threshold $\omega^{\overline{ol}}_{\text{crit}}$, cells have a reduced basic respiratory or metabolic turnover and start to die, while above this threshold, the TC phase growth rate increases up to the maximum proliferation rate at the environmental oxygen concentration $\omega^{\overline{ol}}_{\text{env}}$. The proliferation rate is maximum if the tumour pressure is below p^t_{cr1}. Above this threshold, cells start to grow slower and also start to die. The cancer cells stop grow and die with the maximum necrosis rate above the threshold p^t_{cr2}.

This section summarized the model of Giuseppe Sciumé *et al.* [6, 50, 147, 148]. The model assumes a porous solid ECM material, which harbours HC and TC. The related equations have been derived from principles of TCAT and subsequently adjusted to the needs of cancer growth models.

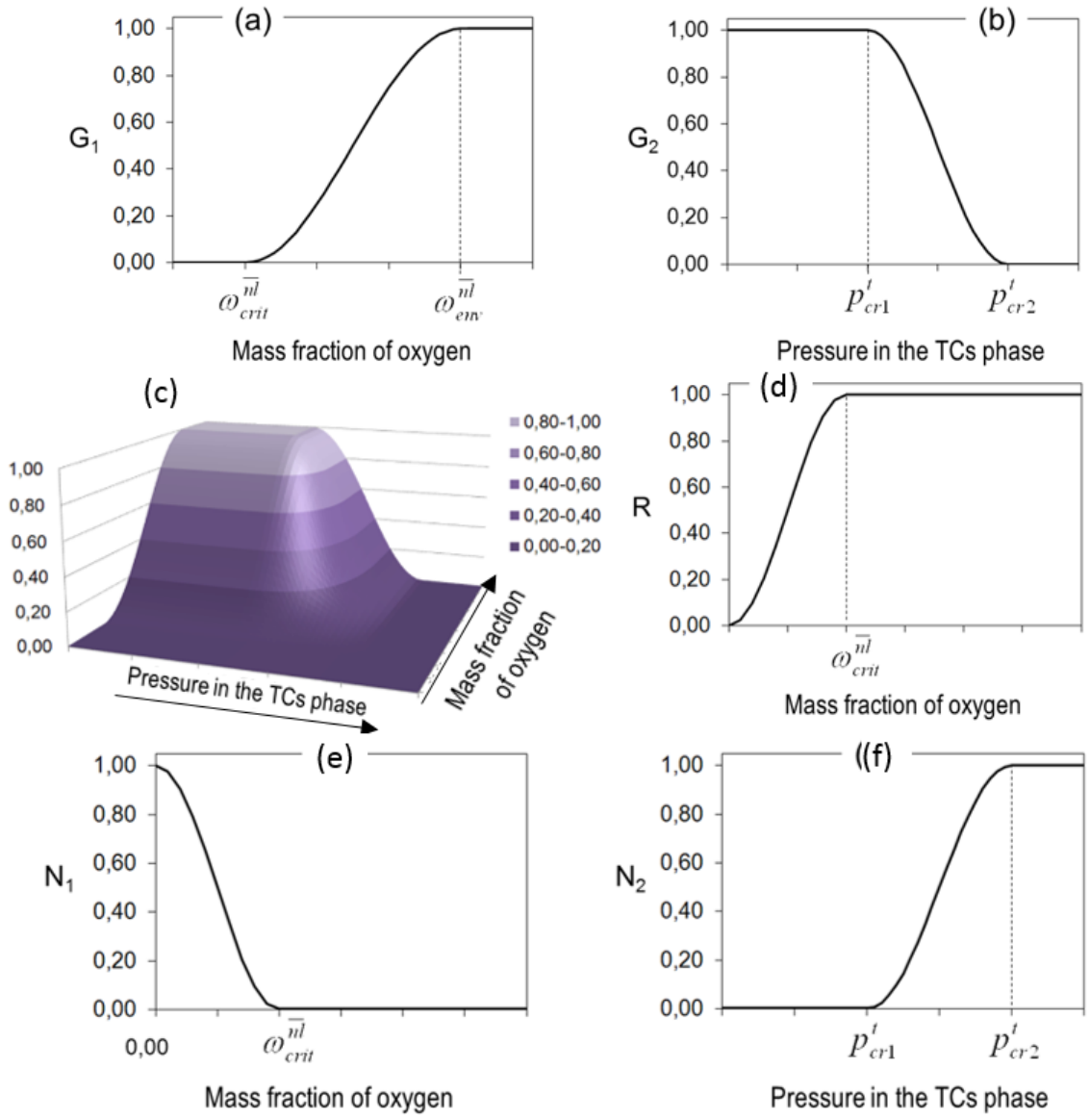

Figure B.5: Proliferation, death, and consumption profiles over increasing pressure and oxygen levels (unpublished records of Giuseppe Sciumé).

C. Swelling glycosaminoglycans

This chapter paraphrases, restructures, and improves a previously published paper [72], which is believed to be the most suitable model for TCAT. This chapter reproduces the model for a PEG cross-linked chondroitin-sulfate (ChS) gel that represents GaG. The chapter abstains from adding the citation to almost any of the following sentences to improve readability. A first overview can be found in Figure C.1.

C.1 Multi-phase characterisation

The volume fractions of cross-linker θ_1, chondroitin sufate θ_2, and solvent θ_3 sum up to unity

$$\theta_1 + \theta_2 + \theta_3 = 1 \tag{C.1}$$

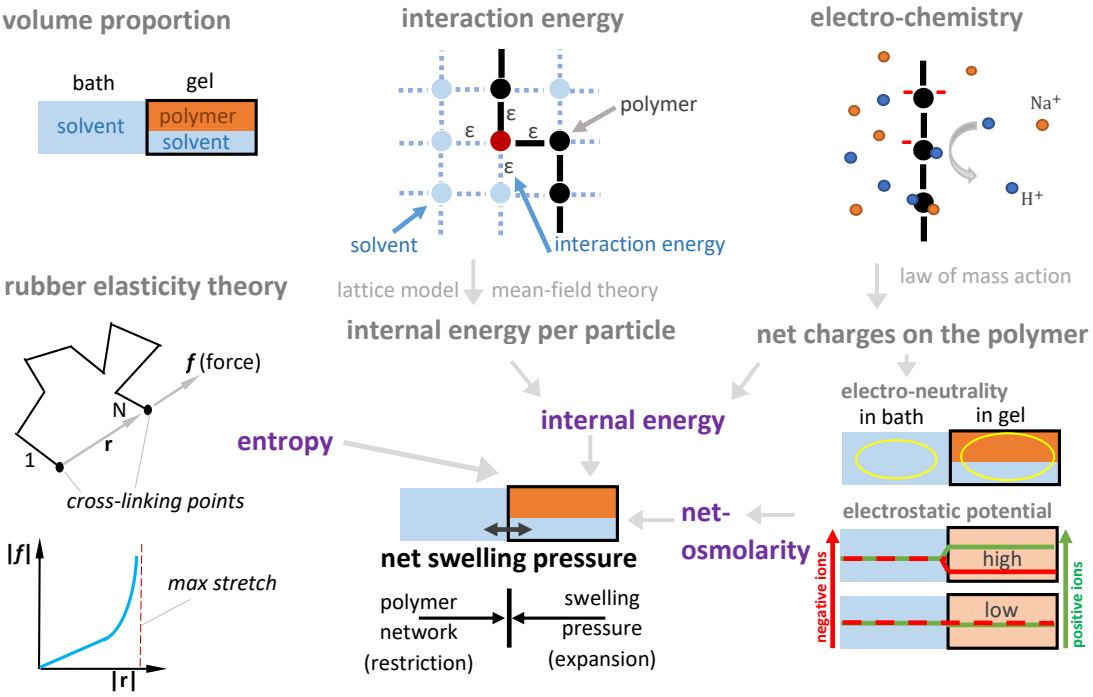

Figure C.1: Swelling poly-electrolyte in a nutshell. The description starts at the bottom left and proceeds clockwise. The **rubber elasticity theory** states that a polymer with N segments between two fixed points with distance r are in a local energy minimum with many possibilities to curl. If the force at one end-point applies, the force needs to be increasingly larger for each incremental extension of r until the free polymer is taut. The polymers tends to retract what can be interpreted as elasticity and is an factor that counteracts swelling. This sub-figure is reproduced [79]. The **volume proportion** defines the proportion of solid polymers, while the rest is solvent. The gel is in contact to a surrounding bath, which is filled with the the same solvent. The **interaction energies** are defined differently for different pairings of particles. The interaction energies are subsequently referred to the internal energy of particles. The **electro-chemistry** determines the number of neutralised negative charges on the polymer, whereby the bound charges set up the Donnan potential. The free movable ions sodium and hydrogen contribute to the net-osmolarity between gel and bath, whereby electro-neutrality is assumed in bath and gel respectively. The bigger the Donnan potential, the more negatively charged ions are ousted and the more positively charged ions are attracted. The terms for entropy, internal energy, and net-osmolarity decide finally whether the **swelling pressure** overcome the restricting polymer network effects or not.

Each volume fraction is created by particle volume ν_i multiplied by the particle number N_i

$$\theta_i = \nu_i N_i \tag{C.2}$$

The particle density for solvent ϕ_s and polymer ϕ_p are defined as

$$\phi_s = \frac{N_s}{N_p + N_s} \qquad \phi_p = \frac{N_p}{N_p + N_s}.$$

C.2 Ion-chemistry

The ion chemistry is a crucial building step to understand the swelling pressure in hydrogels. The aim of this section is the determination of both the ion-balance to understand the net-osmolarity as well as the average charge per monomer z_p to understand the Donnan potential. One has to quantify, therefore, the proportion of both negatively charged ChS monomers and the remaining monomers with charges neutralised by sodium and hydrogen ions.

C.2.1 Balance of charged monomers in equilibrium

The double negative charged ChS monomers M^{-2} bind successively sodium $n = [Na^+]$ and hydrogen $h = [H^+]$, while the counter-ion chloride $c_l = [Cl^-]$ remains unbound in the environment. Consequently, different monomer types appear and one is interested in the different monomer concentrations $m = [\mathrm{M^{2-}}]$, $y = [\mathrm{MH^-}]$, $v = [\mathrm{MNa^-}]$, $w = [\mathrm{MH_2}]$, $x = [\mathrm{MNa_2}]$, $q = [\mathrm{MHNa}]$. The reactions rates for the ion binding an dissociation are

$$\begin{aligned}
\mathrm{M^{2-}} + \mathrm{H^+} &\underset{\mathrm{k_{-h}}}{\overset{\mathrm{k_h}}{\rightleftharpoons}} \mathrm{MH^-} & \qquad \mathrm{m} + \mathrm{h} &\underset{\mathrm{k_{-h}}}{\overset{\mathrm{k_h}}{\rightleftharpoons}} \mathrm{y} \\
\mathrm{M^{2-}} + \mathrm{Na^+} &\underset{\mathrm{k_{-n}}}{\overset{\mathrm{k_n}}{\rightleftharpoons}} \mathrm{MNa^-} & \qquad \mathrm{m} + \mathrm{n} &\underset{\mathrm{k_{-n}}}{\overset{\mathrm{k_n}}{\rightleftharpoons}} \mathrm{v} \\
\mathrm{MH^-} + \mathrm{H^+} &\underset{\mathrm{k_{-h2}}}{\overset{\mathrm{k_{h2}}}{\rightleftharpoons}} \mathrm{MH_2} & \xrightarrow{\text{simplify}} \qquad \mathrm{y} + \mathrm{h} &\underset{\mathrm{k_{-h2}}}{\overset{\mathrm{k_{h2}}}{\rightleftharpoons}} \mathrm{w} \\
\mathrm{MNa^-} + \mathrm{Na^+} &\underset{\mathrm{k_{-n2}}}{\overset{\mathrm{k_{n2}}}{\rightleftharpoons}} \mathrm{MNa_2} & \qquad \mathrm{v} + \mathrm{n} &\underset{\mathrm{k_{-n2}}}{\overset{\mathrm{k_{n2}}}{\rightleftharpoons}} \mathrm{x} \\
\mathrm{MH^-} + \mathrm{Na^+} &\underset{\mathrm{k_{-hn}}}{\overset{\mathrm{k_{hn}}}{\rightleftharpoons}} \mathrm{MHNa} & \qquad \mathrm{y} + \mathrm{n} &\underset{\mathrm{k_{-hn}}}{\overset{\mathrm{k_{hn}}}{\rightleftharpoons}} \mathrm{q}
\end{aligned}$$

with the total monomer concentration

$$m_T = m + y + v + w + x + q. \tag{C.3}$$

Mass action kinetics is used to derive the ODE system. As the ion binding occurs only in the solvent phase, one has to scale the binding reactions with the volume fraction of the solvent θ_s. As soon as ions are bound, the whole hydrogel volume becomes relevant and the monomers are related to the hydrogel space. Two solvent units are needed for the dissociation of an ion binding, so that the dissociation constant is multiplied with ϕ_s^2. The

system at steady state is:

$$\begin{aligned}
\frac{dy}{dt} &= 0 = (k_h mh - k_{h_2} yh - k_{hn} yn)\theta_s + (-k_{-h} y + k_{-h_2} w + k_{-hn} q)\phi_s^2 \\
\frac{dv}{dt} &= 0 = (k_n mn - k_{n_2} vn)\theta_s + (-k_{-n} v + k_{-n_2} x)\phi_s^2 \\
\frac{dw}{dt} &= 0 = k_{h_2} yh\theta_s - k_{-h_2} w\phi_s^2 \\
\frac{dx}{dt} &= 0 = k_{n_2} vn\theta_s - k_{-n_2} x\phi_s^2 \\
\frac{dq}{dt} &= 0 = k_{hn} yn\theta_s - k_{-hn} q\phi_s^2
\end{aligned}$$

The double negative charge is considered, rate constants of the second binding are assumed to be the half of the first binding $k_{i_2} = 0.5k_i$, and the dissociation of the secondly bound molecule is twice as fast as the dissociation of the lastly bound ion $k_{-i_2} = 2k_{-i}$. If another ion type binds in a second step, it binds with the half of the mean first rates $2k_{hn} = {}^1\!/_2(k_h + k_n)$. Accordingly, the dissociation of the second ion occurs with twice the speed of the mean dissociation rate of the last bound ion $k_{-hn} = 2^1\!/_2(k_{-h} + k_{-n})$.

$$0 = (k_h mh - 0.5k_h yh - 0.25(k_h + k_n)yn)\theta_s + (-k_{-h} y + 2k_{-h} w + (k_{-h} + k_{-n})q)\phi_s^2 \tag{C.4}$$

$$0 = (k_n mn - 0.5k_n vn)\theta_s + (-k_{-n} v + 2k_{-n} x)\phi_s^2 \tag{C.5}$$

$$w = \frac{0.5k_h yh\theta_s}{2k_{-h}\phi_s^2} = \frac{yh\theta_s}{4K_h\phi_s^2} \tag{C.6}$$

$$x = \frac{0.5k_n vn\theta_s}{2k_{-n}\phi_s^2} = \frac{vn\theta_s}{4K_n\phi_s^2} \tag{C.7}$$

$$q = \frac{0.25(k_h + k_n)yn\theta_s}{(k_{-h} + k_{-n})\phi_s^2} = \frac{yn\theta_s}{K_{hn}\phi_s^2} \tag{C.8}$$

Rate coefficients have been summarised to the parameter K. Integration of w, x, and y into Equation C.4 and C.5 gives

$$\begin{aligned}
0 =& (k_h mh - 0.5k_h yh - 0.25(k_h + k_n)yn)\theta_s + (-k_{-h} y + 2k_{-h} \frac{0.5k_h yh\theta_s}{2k_{-h}\phi_s^2} \\
&+ (k_{-h} + k_{-n}) \frac{0.25(k_h + k_n)yn\theta_s}{(k_{-h} + k_{-n})\phi_s^2})\phi_s^2 \\
=& (k_h mh - 0.5k_h yh - 0.25(k_h + k_n)yn)\theta_s - k_{-h} y\phi_s^2 + 0.5k_h yh\theta_s + 0.25(k_h + k_n)yn\theta_s \\
=& k_h mh\theta_s - k_{-h} y\phi_s^2
\end{aligned}$$

$$y = \frac{mh\theta_s}{K_h\phi_s^2} \tag{C.9}$$

$$\begin{aligned}
0 =& (k_n mn - 0.5k_n vn)\theta_s + \left(-k_{-n} v + 2k_{-n} \frac{0.5k_n vn\theta_s}{2k_{-n}\phi_s^2}\right)\phi_s^2 \\
v =& \frac{mn\theta_s}{K_n\phi_s^2}
\end{aligned} \tag{C.10}$$

Equations C.9 and C.10 are set into Equations C.6 to C.8.

$$w = \frac{h\theta_s}{4K_h\phi_s^2}\frac{mh\theta_s}{K_h\phi_s^2} = \left(\frac{\theta}{2K_h\phi_s^2}\right)^2 mh^2 \tag{C.11}$$

$$x = \frac{n\theta_s}{4K_n\phi_s^2}\frac{mn\theta_s}{K_n\phi_s^2} = \left(\frac{\theta}{2K_n\phi_s^2}\right)^2 mn^2 \tag{C.12}$$

$$q = \frac{n\theta_s}{K_{hn}\phi_s^2}\frac{mh\theta_s}{K_h\phi_s^2} = \left(\frac{\theta}{\sqrt{K_nK_{hn}}\phi_s^2}\right)^2 mhn \tag{C.13}$$

These terms can be reintroduced into the total monomer Equation C.3 with the assumption that the total monomer concentration m^T is proportional to the particle fraction $\phi_p = v_p N_A m^T$ with the unit-less Avogadro's constant $N_A = 6 \cdot 10^{23}$ and the monomer volume v_p.

$$\begin{aligned}\theta_p &= m + \frac{h\theta_s}{K_h\phi_s^2}m + \frac{n\theta_s}{K_n\phi_s^2}m + \left(\frac{h\theta_s}{2K_h\phi_s^2}\right)^2 m + \left(\frac{n\theta_s}{2K_n\phi_s^2}\right)^2 m + \left(\frac{\theta_s}{\sqrt{K_nK_{hn}}\phi_s^2}\right)^2 hnm \\ m &= \frac{\theta_p}{v_pN_A}\cdot\frac{1}{1+\frac{h\theta_s}{K_h\phi_s^2}+\frac{n\theta_s}{K_n\phi_s^2}+\left(\frac{h\theta_s}{2K_h\phi_s^2}\right)^2+\left(\frac{n\theta_s}{2K_n\phi_s^2}\right)^2+\left(\frac{\theta_s}{\sqrt{K_nK_{hn}}\phi_s^2}\right)^2 hn}\end{aligned} \tag{C.14}$$

Equations C.9 to C.14 provide the monomer type concentrations. This will help determining the charge concentrations in a hydrogel volume element as described in the next section.

C.2.2 Charge difference between glycan gel and interstitial fluid

In this section, the Donnan potential and the osmotic potential are tackled. The Donnan potential is the charge that is bound to the polymer network, whereas the osmotic potential is related to the solution. The bigger the Donnan potential is ($z_p\Psi_e$), with the electrostatic potential Ψ_e, the less freely movable ions are present within the gel

$$c = c_b e^{-z_c\Psi_e} \tag{C.15}$$

compared to the interstitial fluid (b, bath) outside the gel. If the Donnan potential vanishes, the ion charge concentration in the gel equals the concentration outside. The concentration c stands for hydrogen h, sodium n, or chloride c_l, whereby the ion charge is $z_n = z_h = 1$ and $z_{cl} = -1$.

Osmotic potential

This section deals with the 'net-osmolarity' representing the difference between the ion charge in the gel and the ion charge in the interstitial fluid (b, bath). With Equation C.15, the net-osmolarity depends only on the ion-concentrations in the interstitial fluid and the electrostatic potential Ψ_e with the equation

$$\begin{aligned}\Delta\Sigma_I &= (n+h+c_l) - (n_b+h_b+c_{l_b}) = (n_be^{-z_n\Psi_e} + h_be^{-z_h\Psi_e} + c_{l_b}e^{z_{c_l}\Psi_e}) - (n_b+h_b+c_{l_b}) \\ &= (n_be^{-\Psi_e} + h_be^{-\Psi_e} + (n_b+h_b)e^{\Psi_e}) - (n_b+h_b+n_b+h_b)\end{aligned}$$

$$
\begin{aligned}
&= (n_b e^{-\Psi_e} + n_b e^{\Psi_e} + h_b e^{-\Psi_e} + h_b e^{\Psi_e}) - 2(n_b + h_b) \\
\Delta\Sigma_I &= (n_b + h_b)(e^{-\Psi_e} + e^{\Psi_e} - 2),
\end{aligned} \tag{C.16}
$$

whereby it is assumed that the ions in the solution respect the electroneutrality assumption $n_b + h_b - c_{l_b} = 0$.

Donnan potential

The Donnan potential is the charge that is bound to the polymers. The previously described mass action balance gives the concentrations of the double charged monomers $m = [\mathrm{M}^{2-}]$ and the two single charged monomer types $y = [\mathrm{MH}^{-}]$ and $v = [\mathrm{MNa}^{-}]$. With the allocated Equations C.9, C.10, and C.14 as well as with the relationship $\phi_p = v_p N_A m^T$, the average charge per monomer z_p

$$
\begin{aligned}
z_p m_T &= -(2m + y + v) \\
z_p &= -\frac{v_p N_A}{\phi_p}\left(2 + \frac{h\theta_s}{K_h \phi_s^2} + \frac{n\theta_s}{K_n \phi_s^2}\right) m
\end{aligned} \tag{C.17}
$$

can be obtained. The next step is the calculation of the electrostatic potential with Equation C.19. Therefore, one assumes electroneutrality within the gel with Equation C.18.

$$
\begin{aligned}
0 &= (n + h - c_l)\theta_s + z_p m_T \\
0 &= (n_b e^{-\Psi_e} + h_b e^{-\Psi_e} - (n_b + h_b) e^{\Psi_e})\phi_s + z_p m_T \\
0 &= ((n_b + h_b)(1 - (e^{\Psi_e})^2)\phi_s + z_p m_T e^{\Psi_e} \\
0 &= (e^{\Psi_e})^2 - \frac{z_p m_T}{(n_b + h_b)\phi_s} e^{\Psi_e} - 1 \\
\Psi_e &= \ln\left(\underbrace{\underbrace{\frac{z_p m_T}{2(n_b + h_b)\phi_s}}_{<0 \text{ as } z_p<0} \pm \sqrt{\underbrace{\left(\frac{z_p m_T}{2(n_b + h_b)\phi_s}\right)^2}_{>0} + 1}}_{\text{must be positive}}\right) \\
\Psi_e &= \ln\left(\frac{z_p m_T}{2(n_b + h_b)\phi_s} + \sqrt{\left(\frac{z_p m_T}{2(n_b + h_b)\phi_s}\right)^2 + 1}\right)
\end{aligned} \tag{C.18, C.19}
$$

In summary, this section delivered the net-osmolarity $\Delta\Sigma_I$ in Equation C.16, the average charge of a monomer z_p in Equation C.17, and the electrostatic potential Ψ_e in Equation C.19. The average charge of a monomer appears in the term for the internal energy

$$
U_e = z_p N_p \Phi_e
$$

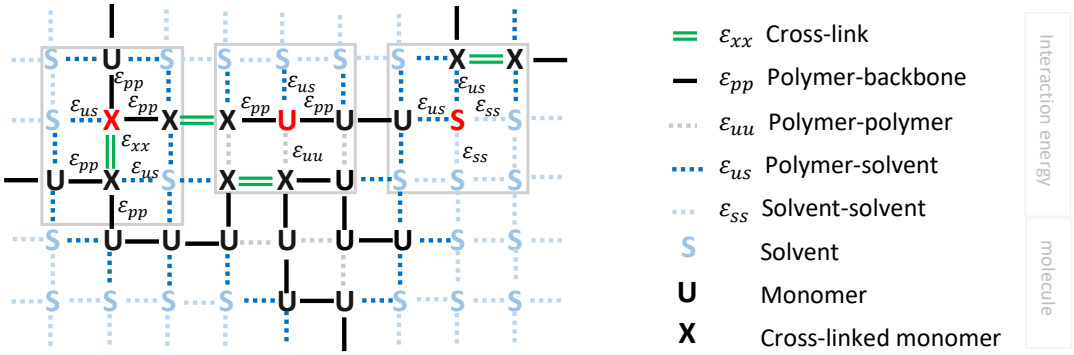

Figure C.2: Lattice model for polymer solutions. The red indicated species represent cross-linked monomers, X, uncrosslinked monomers, U, and solvent molecules, S, with their expected interaction energies ϵ. Each species has $z = 4$ (in 2D) or $z = 6$ (in 3D) free interaction sites. If a middle piece monomer has covalent bounds to it neighbours, two of the free sites get lost $z - 2$. One get lost if it is an end piece $z - 1$. Cross-linked molecules are seen as a pair with $2z$ free sides, which are however reduced by the crosslink itself $2z - 2$. Cross-linked monomers in the middle of each polymer loose four further free sides $2z - 6$. If one cross-linked monomer is an end piece, it has one side more $2z - 5$. If booth are end pieces two additional sides are free $2z - 4$. The figures is inspired by Sircar *et al.* [72, 343] and was extended.

with the number of monomers per volume N_p and the electric potential Φ_e. The electric potential relates to the electrostatic potential $\Psi_e = {}^{\Phi_e}/_{k_B T}$ via the Boltzmann's constant k_B and Kelvin's temperature T. This results in the equation

$$U_e = z_p N_p \Psi_e k_B T. \tag{C.20}$$

C.3 Polymer network structure: inner energy

The internal energy U is made by two elements: electrostatic interactions, which act in long range U_e and molecular interactions considering the direct neighbours $\tilde{U}$. The long range electrostatic interactions are given with the simple Equation C.20. The short range interactions have to be derived with the lattice model for polymer solutions and the mean field theory [79]. The lattice model can be found in Figure C.2. The assumptions are that all cross-links are covalently bound and are identical, that the polymers are long enough to ignore end-effects, and that the monomer type does not change interactions to solvents or influence the binding among them. The aim is determining the interaction energy F between the species. Subsequently, the interaction energy is related to the species as per particle interaction energy or internal energy $\tilde{u}$. The interaction energy is not identical with the Helmholtz free energy F.

C.3.1 Setting the equations with the lattice model

Between the cross-linked species, x, the uncross-linked species, u, and the solvent particles, s, appear the interaction energies $k_B T_0 \epsilon_{xx}$, $k_B T_0 \epsilon_{uu}$, $k_B T_0 \epsilon_{pp}$, $k_B T_0 \epsilon_{us}$, $k_B T_0 \epsilon_{ss}$

with Kelvin's reference temperature T_0 as specified in Figure C.2. In a three-dimensional cubic lattice, one assumes the coordination number $z = 6$, with which the cross-linked particle pair has $2z - 6 = 6$ and the uncross-linked monomer has $z - 2 = 4$ free interaction sites in the middle of a polymer. End-effects are neglected, because the gel is composed of two different monomer species PEG and ChS, with which equations would become too extensive.

According to Figure C.2, the cross-linked monomer-pair between two polymers has $2z - 6$ free sides E_{us}, which are to the likelihood ${}^{N_p}/_{N_t}$ non-covalently interacting ϵ_{uu} with other monomers and to the likelihood ${}^{N_s}/_{N_t}$ non-covalently interacting ϵ_{us} with solvent particles. In addition, two of the available sides are spend for the cross-link itself with the covalent interaction ϵ_{xx}, and four of the available sides are blocked by the adjacent monomers covalently interacting ϵ_{pp} with the cross-linked monomer-pair. And lastly, the solvent acts to the likelihood of ${}^{N_s}/_{N_t}$ with other solvent molecules ϵ_{ss}.

The cross-liked fraction for each monomer-type is important. The number of PEG particles n_1 is to the fraction of k_1 cross-linked. The number of ChS particles n_2 is to the fraction of k_2 cross-linked. Each cross-linked pair consists to a likelihood of k_1^2 only of PEG, to a likelihood of k_2^2 only of ChS, and to a likelihood of $k_1 k_2$ exactly of one PEG and one ChS monomer. This is valid for a cross-linked pair that can be divided by two to obtain the interaction energy for a cross-linked monomer. The uncross-linked monomer, which interacts with neighbours, is to a likelihood of $(1 - k_1)$ a PEG and to a likelihood of $(1 - k_2)$ a ChS monomer. Solvent molecules, however, are not further distinguished and are considered only as the particle number of solvent molecules N_s.

In conclusion and in the averaged sense of the mean field theory, the equations for the interaction energy are:

$$F_x = \underbrace{{}^1/_2}_{\text{pair}} \underbrace{\left(n_1 k_1^2 + n_2 k_2^2 + (n_1 + n_2) k_1 k_2\right)}_{\text{monomer type proportions}} \underbrace{(2\epsilon_{xx} + (2z-6)(\epsilon_{uu}\frac{N_p}{N_t} + \epsilon_{us}\frac{N_s}{N_t}) + 4\epsilon_{pp}) k_B T_0}_{\text{interaction energy with neighbours in lattice}}$$

$$F_u = (n_1(1-k_1) + n_2(1-k_2))((z-2)(\epsilon_{uu}\frac{N_p}{N_t} + \epsilon_{us}\frac{N_s}{N_t}) + 2\epsilon_{pp}) k_B T_0$$

$$F_s = N_s \cdot z \left(\epsilon_{us}\frac{N_p}{N_t} + \epsilon_{ss}\frac{N_s}{N_t}\right) k_B T_0$$

The proportion of cross-linked monomers of either PEG k_1 or ChS k_2 is contemplated by the ChS fraction of all monomers $n_1 + n_2 = N_p$, $n_2 = \alpha N_p$, and $n_1 = (1-\alpha)N_p$. Additionally, the particle densities are reintroduced $\phi_p = \frac{N_p}{N_t}$,$\phi_s = \frac{N_s}{N_t}$. The following equations

$$F_x = N_p \left((1-\alpha)k_1^2 + \alpha k_2^2 + k_1 k_2\right)(\epsilon_{xx} + (z-3)(\epsilon_{uu}\phi_p + \epsilon_{us}\phi_s) + 2\epsilon_{pp}) k_B T_0 \quad \text{(C.21)}$$

$$F_u = N_p((1-\alpha)(1-k_1) + \alpha(1-k_2))((z-2)(\epsilon_{uu}\phi_p + \epsilon_{us}\phi_s) + 2\epsilon_{pp}) k_B T_0 \quad \text{(C.22)}$$

$$F_s = N_s \cdot z\,(\epsilon_{us}\phi_p + \epsilon_{ss}\phi_s)\, k_B T_0 \quad \text{(C.23)}$$

are transferred to the equation for internal energy

$$\tilde{U} = \frac{1}{2}(F_x + F_u + F_s) = k_B T_0 \left[\chi N_p N_s + \mu_0^s N_s + \mu_0^p N_p + C\right]$$

and the transformed to the internal energy per particle $\tilde{u}$.

$$\tilde{u} = \frac{1}{2N_t}(F_x + F_u + F_s) = k_B T_0 \left[\chi \phi_p \phi_s + \mu_0^s \phi_s + \mu_0^p \phi_p + c\right] \tag{C.24}$$

The internal energy is an extensive variable and is transformed to a molar variable due to division by the number of all particles N_t. To emphasize the intensive character and in contrast to the original publication, the symbol is written lower cased according to the convention of Wallace and Hobbs. The deviation by two transfers the reference from the interaction between two species to the particles themselves, and c is a constant. The equation defines the Flory interaction parameter χ between solvent and polymer as well as the chemical potential for either polymer μ_0^p in a separated phase or solvent species μ_0^s as independent phase. The chemical potential for polymer $\tilde{\mu}_p$ and solvent $\tilde{\mu}_s$ in the gel mixture will be determined later. Combining the Equations C.21 to C.24 with the relationships

$$\phi_p^2 = \phi_p(1 - \phi_s) = \phi_p - \phi_p\phi_s$$
$$\phi_s^2 = \phi_s(1 - \phi_p) = \phi_s - \phi_p\phi_s$$

delivers

$$\begin{aligned}
\frac{2u}{k_B T_0} = &+ \Bigg[\underbrace{(\epsilon_{xx} + 2\epsilon_{pp})((1-\alpha)k_1^2 + \alpha k_2^2 + k_1 k_2)}_{\text{from } F_x} + \underbrace{2\epsilon_{pp}(1 - (1-\alpha)k_1 - \alpha k_2)}_{\text{from } F_u}\Bigg]\phi_p \\
&+ \left[\epsilon_{uu}(z-3)((1-\alpha)k_1^2 + \alpha k_2^2 + k_1 k_2) + \epsilon_{uu}(z-2)(1-(1-\alpha)k_1 - \alpha k_2)\right](\phi_p - \phi_p\phi_s) \\
&+ \left[\epsilon_{us}(z-3)((1-\alpha)k_1^2 + \alpha k_2^2 + k_1 k_2) + \epsilon_{us}(z-2)(1-(1-\alpha)k_1 - \alpha k_2) + z\epsilon_{us}\right]\phi_p\phi_s \\
&+ \left[\epsilon_{ss} z\right](\phi_s - \phi_p\phi_s) \\
= &+ [(\epsilon_{xx} + 2\epsilon_{pp} + \epsilon_{uu}(z-3))((1-\alpha)k_1^2 + \alpha k_2^2 + k_1 k_2) \\
&+ (2\epsilon_{pp} + \epsilon_{uu}(z-2))(1-(1-\alpha)k_1 - \alpha k_2)]\phi_p \\
&+ [(\epsilon_{us} - \epsilon_{uu})(z-3)((1-\alpha)k_1^2 + \alpha k_2^2 + k_1 k_2) \\
&+ (\epsilon_{us} - \epsilon_{uu})(z-2)(1-(1-\alpha)k_1 - \alpha k_2) + z\epsilon_{us} - \epsilon_{ss} z]\phi_p\phi_s \\
&+ [\epsilon_{ss} z]\phi_s
\end{aligned}$$

The original paper [72] claimed to reduce the number of parameter from five to four, however, this was not reproducible, it causes an unnecessary residual C, and did not

result in fewer parameter[1]. Therefore, this thesis directly compares the internal energy equation

$$\frac{\tilde{u}}{k_B T_0} = [\chi\phi_p\phi_s + \mu_0^s\phi_s + \mu_0^p\phi_p + C]$$

with the following equation.

$$\begin{aligned}
\chi =& \frac{1}{2}(\epsilon_{us} - \epsilon_{uu})(z-3)((1-\alpha)k_1^2 + \alpha k_2^2 + k_1k_2) \\
&+ \frac{1}{2}(\epsilon_{us} - \epsilon_{uu})(z-2)(1-(1-\alpha)k_1 - \alpha k_2) + \frac{\epsilon_{us} - \epsilon_{ss}}{2}z \\
\mu_0^s =& \frac{\epsilon_{ss}}{2}z \\
\mu_0^p =& \frac{1}{2}(\epsilon_{xx} + 2\epsilon_{pp} + \epsilon_{uu}(z-3))((1-\alpha)k_1^2 + \alpha k_2^2 + k_1k_2) \\
&+ \frac{1}{2}(2\epsilon_{pp} + \epsilon_{uu}(z-2))(1-(1-\alpha)k_1 - \alpha k_2)
\end{aligned}$$

[1] With $\epsilon_1 = \epsilon_{us} - \epsilon_{uu}$, $\epsilon_2 = \epsilon_{us} - \epsilon_{ss}$, $\epsilon_3 = \epsilon_{xx} - \epsilon_{uu}$, $\epsilon_4 = \epsilon_{pp} - \epsilon_{uu}$

$$\begin{aligned}
=& + [((\epsilon_3 + \epsilon_{uu}) + 2(\epsilon_4 + \epsilon_{uu}) - 3\epsilon_{uu} + (\epsilon_{us} - \epsilon_1)z))((1-\alpha)k_1^2 + \alpha k_2^2 + k_1k_2) \\
&+ (2\epsilon_4 + (\epsilon_{us} - \epsilon_1)z)(1-(1-\alpha)k_1 - \alpha k_2)]\phi_p \\
&+ [\epsilon_1(z-3)((1-\alpha)k_1^2 + \alpha k_2^2 + k_1k_2) \\
&+ \epsilon_1(z-2)(1-(1-\alpha)k_1 - \alpha k_2) + z(\epsilon_2 + \epsilon_{ss}) - z\epsilon_{ss}]\phi_p\phi_s \\
&+ [-\epsilon_2 z]\phi_s + \epsilon_{us}z(1-\phi_p)
\end{aligned}$$

$$\begin{aligned}
\frac{2U}{k_B T_0} =& + [(\epsilon_3 + 2\epsilon_4 - \epsilon_1 z)((1-\alpha)k_1^2 + \alpha k_2^2 + k_1k_2) + (2\epsilon_4 - \epsilon_1 z)(1-(1-\alpha)k_1 - \alpha k_2) \\
&+ \epsilon_{us}z((1-\alpha)k_1^2 + \alpha k_2^2 + k_1k_2 - (1-\alpha)k_1 - \alpha k_2) + (\epsilon_{us}z - \epsilon_{us}z)]\phi_p \\
&+ [\epsilon_1(z-3)((1-\alpha)k_1^2 + \alpha k_2^2 + k_1k_2) + \epsilon_1(z-2)(1-(1-\alpha)k_1 - \alpha k_2) + z\epsilon_2]\phi_p\phi_s \\
&- [\epsilon_2 z]\phi_s + \epsilon_{us}z
\end{aligned}$$

Coefficient comparison with

$$\frac{\tilde{U}}{k_B T_0} = [\chi\phi_p\phi_s + \mu_0^s\phi_s + \mu_0^p\phi_p + C]$$

gives

$$\begin{aligned}
\chi =& \frac{z}{2}\epsilon_1(((1-\alpha)k_1^2 + \alpha k_2^2 + k_1k_2 + 1 - (1-\alpha)k_1 - \alpha k_2) + \frac{z\epsilon_2}{2} \\
&- \frac{3\epsilon_1}{2}((1-\alpha)k_1^2 + \alpha k_2^2 + k_1k_2) - \epsilon_1(1-(1-\alpha)k_1 - \alpha k_2) \\
\chi =& \frac{z}{2}\epsilon_1(k_1k_2 - (1-\alpha)k_1(1-k_1) - \alpha k_2(1-k_2) + 1) + \frac{z\epsilon_2}{2} \\
&+ \epsilon_1(k_1(1-\alpha)(1 - \frac{3}{2}k_1 + \alpha k_2(1 - \frac{3}{2}k_2) - \frac{3}{2}k_1k_2 - 1) \\
\mu_0^s =& -\epsilon_2\frac{z}{2} \\
\mu_0^p =& \frac{\epsilon_3 + 2\epsilon_4 - \epsilon_1 z}{2}((1-\alpha)k_1^2 + \alpha k_2^2 + k_1k_2) + \frac{1}{2}(2\epsilon_4 - \epsilon_1 z)(1-(1-\alpha)k_1 - \alpha k_2) \\
&+ \frac{\epsilon_{us}}{2}z((1-\alpha)k_1^2 + \alpha k_2^2 + k_1k_2 - (1-\alpha)k_1 - \alpha k_2) \\
\neq& \frac{\epsilon_3 + \epsilon_4 - \epsilon_1 z}{2}((1-\alpha)k_1^2 + \alpha k_2^2 + k_1k_2) + (z-2)\left(\epsilon_4 - \frac{3}{2}\epsilon_1\right)(1-(1-\alpha)k_1 - \alpha k_2) \\
C =& \frac{z}{2}\epsilon_{us}
\end{aligned}$$

Red marked parts show the differences between this calculation and the published equations.

$$c = 0$$

C.3.2 Parameter estimation

The parameters can be estimated with the relationship between standard free energies and solubility parameters with the equations

$$\begin{aligned} -k_B T_0 \mu_p^0(\alpha = 0) &= \nu_1 \delta_1^2 && \text{PEG cross-linker} \\ -k_B T_0 \mu_p^0(\alpha = 1) &= \nu_2 \delta_2^2 && \text{ChS monomers} \\ -k_B T_0 \mu_s^0 &= \nu_w \delta_w^2 && \text{Solvent.} \end{aligned}$$

These equations contain the monomer volumes $\nu_i = {}^{M_i}/_{\rho_i \cdot N_A}$ and the Hildebrand solubility values δ_i. The standard free energies are based on experimentally determined values [72] and result in $\mu_p^0(\alpha = 0) = -525.05$, $\mu_p^0(\alpha = 1) = -529.23$, and $\mu_s^0 = -11.238$ without units. The Flory-Huggins parameter for PEG4000 in water is expected to be around $\chi(\alpha = 0) \approx 0.5$ [466, 467] in contrast to the non-physical parameter value $\chi = 11.22$ from the paper [72].

C.3.3 Chemical potential of polymer and solution in a mixture

The final aim of the section is the determination of the chemical potential within a polymer mixture $\tilde{\mu}_p$ & $\tilde{\mu}_s$ and not related to separate pure conditions μ_0^s & μ_0^p. The internal energy is defined in Equation C.24 and is

$$\tilde{u} = k_B T_0 \left[\chi \phi_p (1 - \phi_p) + \mu_0^s (1 - \phi_p) + \mu_0^p \phi_p\right] = k_B T_0 [\chi \phi_p - \chi \phi_p^2 + \mu_0^s - \mu_0^s \phi_p + \mu_0^p \phi_p],$$

whereby the intensive variable $\tilde{u}$ can be expressed as extensive variable in the derivative

$$\frac{\partial \tilde{U}}{\partial N_p} = \frac{\partial \frac{\tilde{U}}{N_t}}{\partial \frac{N_p}{N_t}} = \frac{\partial \tilde{u}}{\partial \phi_p} = k_B T_0 \left[\chi - 2\chi \phi_p - \mu_0^s + \mu_0^p\right]$$

However, the pure chemical potentials μ_0^p & μ_0^s do no represent chemical potentials in a mixture. Therefore, the definitions of chemical potentials must relate changes of the internal energy with the changes in the polymer, which is proportionately added to the internal energy of either polymer or solution [468].

$$\begin{aligned} \tilde{\mu}_p &= \tilde{u} + (1 - \phi_p) \frac{\tilde{u}}{\phi_p} = k_B T_0 [\chi \phi_p - \chi \phi_p^2 + \mu_0^s - \mu_0^s \phi_p + \mu_0^p \phi_p + (1 - \phi_p)(\chi - 2\chi \phi_p - \mu_0^s + \mu_0^p)] \\ &= k_B T_0 [\chi \phi_p^2 - 2\chi \phi_p + \chi + \mu_0^p] = k_B T_0 [\chi (1 - \phi_p)^2 + \mu_0^p] \\ &= k_B T_0 [\chi \phi_s^2 + \mu_0^p] \qquad \text{(C.25)} \\ \tilde{\mu}_s &= \tilde{u} - \phi_p \frac{\tilde{u}}{\phi_p} = k_B T_0 [\chi \phi_p - \chi \phi_p^2 + \mu_0^s - \mu_0^s \phi_p + \mu_0^p \phi_p - \phi_p (\chi - 2\chi \phi_p - \mu_0^s + \mu_0^p)] \\ &= k_B T_0 [\chi \phi_p^2 + \mu_0^s] \qquad \text{(C.26)} \end{aligned}$$

C.4 Polymer flexibility between cross-links: rubber elasticity theory

An important characteristic in polymers is the flexibility in the chains and their tendency to reorganise themselves in the available space. The random organisation within the space is controlled by a local energy minimum that resist change. Thus, polymer networks develop resisting force against extension and create elasticity to return to the local energy minimum [79]. The rubber elasticity theory help modelling this effect. However, it might be more logical to name it gel elasticity theory. Rubber does not usually contain solvents within the polymer network. Polymer-networks without solvent might be classified as rubber, whereas polymer-networks with solvent might be classified as gels [79]. The difference between a solvent and a gel is the presence of a often small number of crosslinks between the polymer fibres [79].
After the investigation of the average behaviour of the chains with statistical mechanics, one can determine the entropy. The entropy $S = \sum N_i \omega_i$ is number of particles N_i times the entropy per particle ω_i. For solvents j, the entropy per particle is

$$\omega_i = -ln(\phi_j) \qquad j \geq 3 \tag{C.27}$$

and for interconnected monomers i

$$\omega_i = -\frac{3k_i}{2N_i}\left[(\phi_i)^{-2/3} - 1\right], \qquad i = 1, 2. \tag{C.28}$$

The general entropy equation for the whole polymer is

$$S = -\underbrace{n_1 \frac{3k_1}{2N_1}\left[\phi_1^{-2/3} - 1\right]}_{\text{PEG}} - \underbrace{n_2 \frac{3k_i}{2N_i}\left[\phi_2^{-2/3} - 1\right]}_{\text{ChS}} - \underbrace{N_s \ln(\phi_s)}_{\text{solvent}} - \underbrace{\sum n_j \ln(\phi_j)}_{\text{Ion}}. \tag{C.29}$$

With the Equations

$$n_1 = (1-\alpha)N_p \qquad n_2 = \alpha N_p \qquad \phi_1 = (1-\alpha)\phi_p \qquad \phi_1 = \alpha\phi_p \qquad \phi_p = \frac{N_p}{N_p + N_s},$$

the Equation C.29 is transformed[2] and results in the following derivatives

$$S = \underbrace{-\frac{3k_1}{2N_1}(1-\alpha)^{\frac{1}{3}} N_p \left(\frac{N_p}{N_t}\right)^{-\frac{2}{3}}}_{S_1} + \frac{3k_1}{2N_1}(1-\alpha)N_p$$

[2]The derivative of S_1:

$$\begin{aligned}
\frac{\partial S_1}{\partial N_p} &= -\frac{3k_1}{2N_1}(1-\alpha)^{\frac{1}{3}}\left[\phi_p^{-\frac{2}{3}} - \frac{2}{3}N_p\phi_p^{-\frac{5}{3}}\frac{N_t - N_p}{N_t^2}\right] \\
&= -\frac{3k_1}{2N_1}(1-\alpha)^{\frac{1}{3}}\left[\phi_p^{-\frac{2}{3}}\left(1 - \frac{2}{3}(1-\phi_p)\right)\right] \\
&= -\frac{k_1}{N_1}(1-\alpha)^{\frac{1}{3}}\phi_p^{-\frac{2}{3}}\left[\frac{1}{2} + \phi_p\right]
\end{aligned}$$

$$
\begin{aligned}
&- \frac{3k_2}{2N_2}\alpha^{\frac{1}{3}} N_p \left(\frac{N_p}{N_t}\right)^{-\frac{2}{3}} + \frac{3k_2}{2N_2}\alpha N_p \\
&- N_s \ln\left(\frac{N_s}{N_t}\right) - \sum n_j \ln(\phi_j) \\
\frac{\partial S}{\partial N_p} =& - \frac{k_1}{N_1}\phi_1^{-\frac{2}{3}}\left[\phi_1 + \frac{1-\alpha}{2}\right] - \frac{k_2}{N_2}\phi_2^{-\frac{2}{3}}\left[\phi_2 + \frac{\alpha}{2}\right] + \frac{3}{2}\left[\frac{k_1}{N_1}(1-\alpha) + \frac{k_2}{N_2}\alpha\right] + \phi_s
\end{aligned}
\tag{C.30}
$$

$$
\frac{\partial S}{\partial N_s} = - \frac{k_1}{N_1}\phi_1^{\frac{1}{3}} - \frac{k_2}{N_2}\phi_2^{\frac{1}{3}} - \ln\phi_s - \phi_p + \sum_{i\geq 4}\phi_i \tag{C.31}
$$

$$
\frac{\partial S}{\partial N_i} = - \ln\phi_i - 1 + \sum_{i\geq 4}\phi_i \tag{C.32}
$$

C.5 Merging the parts to obtain the swelling pressure

After the different elements were set, the equations can be assembled to represent a generic polyelectrolyte gel. In context of the TCAT framework, the gel is assumed to dynamically swell and deswell within the pericellular space. Albeit the model contains PEG, one might assume that collagen has a similar effect in retracting GaG. A majority of the gel system properties might be experimentally determined outside of the tissue system. The water holding capacity and the mechanical response of the GaG gel in the pore space is the purpose of this section.

In order to find the equilibrium within a semi-diluted pericellular gel, equilibrium conditions have to be considered with the chemical potential [72]

$$
\mu_j = \frac{\partial G}{\partial n_j} = \underbrace{\underbrace{-k_B T \frac{\partial S}{\partial n_j}}_{\mu_j^S} + \underbrace{\frac{\partial U_{sr}}{\partial n_j}}_{\mu_j^I}}_{M} + \underbrace{\frac{\partial U_{lr}}{\partial n_j}}_{z_j\phi_e} + \nu_j P, \tag{C.33}
$$

which is defined by the Gibb's free energy G derived after the number n_j of a chemical particle j. Each particle has a related volume ν_j at reference temperature T_0. A pressure P can act on the system.

The entropy S related part $\mu_j^S(\phi_j, k_i, N_i)$ can account for the rubber elasticity theory. Both polymer types $i \in 1, 2$ are characterized by the total monomer length N_i and the averaged number of monomers being cross-linked with others k_i.

The inner energy term of the chemical potential μ_i^I has two contributors. The long range inner energy $U_{lr} = \sum_i z_i n_i \phi_e$ is based on the charge per ion particle z_i multiplied with the abundance of an ion n_i and the electronic potential ϕ_e. The short range inner energy U_{sr} describes the interaction between polymers, polymer and solvent, and solvent to solvent. The resulting modified Flory-Huggins parameter $\chi(k_i, \alpha, z, \check{\epsilon})$ and the chemical potentials of pure polymer $\mu_0^s(k_i, \alpha, z, \check{\epsilon})$ respective pure fluid $\mu_0^l(z, \check{\epsilon})$ are based on z interaction sides of a polymeric monomer and related interaction energies between particles, adjusted via

the Hildebrand solubility. The chemical potential of the inner energy for the polymer p and bound water yields

$$\mu_s^I = k_B T_0(\chi\phi_l^2 + \mu_0^s) \tag{C.34}$$

$$\mu_l^I = k_B T_0(\chi\phi_s^2 + \mu_0^l) \tag{C.35}$$

The inner energy and entropy contributions are summarized to the term $M_j(\mu_j^S, \mu_j^I)$. The cross-linked polymer network of an electrolyte can be described with equations for the polymer phase and the solvent phase [72]

$$\begin{aligned}\frac{1}{\nu_s}\mu_s^-\mathbf{n} = \frac{k_B T}{\nu_s}(M_s^- + z_s\Psi_e \\ + \nu_s\frac{P^-}{k_B T} - \nu_s\frac{\mathbf{t}^{\bar{\bar{s}}}}{k_B T})\end{aligned} \tag{C.36}$$

$$\begin{aligned}\frac{1}{\nu_l}(\mu_l^+ - \mu_l^-)\mathbf{n} = \frac{k_B T}{\nu_l}(M_l^+ - M_l^- \\ + (n_b + h_b)(e^{-\psi_e} + e^{\psi_e} - 2) \\ + \nu_l\frac{P^f}{k_B T} - \nu_l\frac{P^-}{k_B T})\end{aligned} \tag{C.37}$$

as well as with the combined system after elimination

$$\begin{aligned}\frac{P^s}{k_B T} &= \frac{\mu_p^-}{\nu_p} + \frac{\mu_{fw}^+}{\nu_{fw}} - \frac{\mu_{fw}^-}{\nu_{fw}} \\ &= \frac{M_p^-}{\nu_p} + \frac{M_{fw}^+}{\nu_{fw}} - \frac{M_{fw}^-}{\nu_{fw}} + \frac{z_p}{\nu_p}\Psi_e \\ &+ \frac{(n_b + h_b)}{\nu_{fw}}(e^{-\psi_e} + e^{\psi_e} - 2) \\ &+ \frac{P^f - \mathbf{t}^{\bar{\bar{s}}}}{k_B T}\end{aligned} \tag{C.38}$$

with negative superscript for constituents for the pericellular gel ϵ^s and positive superscript for fluid constituents outside the gel ϵ^l. The pericellular gel has a moving edge with normal $\mathbf{n}$ to the interphase, which is cancelled out $P^s\mathbf{n} = 0$ in the equilibrium. The differences between the chemical potentials μ define the net swelling pressure of the solid phase P^s. The osmotic pressure $(n_b + h_b)\cdot\ (e^{-\psi_e} + e^{\psi_e} - 2)$ is created by the potential of hydrogen pH h_b and salt concentration n_b. Polyelectrolytes generate with the Donnan potential $z_s\Psi_e$ an additional water attracting force depending on the average charge per monomer z_s, the electrostatic potential $\Psi_e = \Phi_e/k_B T$, the electric potential Φ_e, the Boltzmann constant k_B, and the temperature T. The Equation C.38 delivers an direct linkage between the pressure of the solid phase P^s and IFP p^f. Thus, a part of the external pressure can be discharged by IFF. Further explanations can be found in the work of Sircar *et al.* [72].

The net swelling pressure replaces the pressure-saturation relationship in TCAT tissue models for not miscible fluids $\Delta p^{th}(S^l)$, $\Delta p^{th}(S^l)$ and its simplified version for partly miscible fluids $\Delta p(S^l)$ [147]. The former pressure-saturation relationships are based on geomechanics and consider interfacial tension in the pore space [418]. Interfacial tension between IF and ECM phase correlates here with the Flory-Huggins Parameter χ [469]. The difference between the osmotic pressure of the stroma and the osmotic pressure of the cell phases affect the interfacial membrane tension, and the membrane area is regulated to compensate the forces [470].

D. Growth model associated parameters

A typical TCAT model has many parameters and even more if the represented tissue suffers from malignant transformations representing cancer. Three parameter classes are most important. First, the initial condition and the question which volume distribution of IF, ECM, and cells make up the host tissue, and which parameter for the geometry are required. Second, how oxygen is delivered and consumed at the cellular and tissue scale. And finally, which mechanical parameters at the microscale and macroscale are relevant to understand the restriction of tumour expansion.

D.1 Volume distribution

Reported values are often in mass unites related to dry or wet tissue. Therefore, density values are necessary to obtain the volume fractions within the tissue, whereby the density of skin is 1.06 g/cm^3 [471].

D.1.1 Body fluid volume fractions

The distribution volume is the volume that permeates the tissue and is dissected in IF volume and blood plasma volume. In order to differentiate between the two volumes, the distribution volume is labelled with isotopes of ^{51}Cr-EDTA and ^{125}I-BSA, whereby ^{125}I-BSA remains within the blood plasma [105]. The IF volume in rat skin is 0.425 $^{mL}/_{g}$ wet wt, while the total tissue water is around 0.6 $^{mL}/_{g}$ wet wt. In the muscle of rat, the IF volume is much smaller with 0.062 $^{mL}/_{g}$ wet wt, while the total tissue water is with 0.75 $^{mL}/_{g}$ wet wt more abundant [105]. Muscles have a higher cellularity and such tissues are expected to be more responsive to cell volume regulation changes [105].

D.1.2 Polymer densities

Polymers can occupy two different amounts of volume per weight unit, with a higher value for hydrated polymers. The specific volume of collagen with bound water is $1.87\ \mathrm{cm}^3/\mathrm{g}$ [95, 472], while without bound water the specific volume spans from $0.695\ \mathrm{cm}^3/\mathrm{g}$ for more glycosylated collagen 2 and $0.709\ \mathrm{cm}^3/\mathrm{g}$ for more skin related collagen 1 [473]. The bound water is also a space that is not assessable by larger molecules such as albumin. Each gram collagen bind $1.57\ \mathrm{g}$ fluid, which reduces the space for albumin movements [474]. The value is similar to the specific volume of hydrated collagen mentioned above. Macromolecular crowding of polymers consequently reduce the IF space and build exclusion volumes that are not accessible for drugs and molecules [475]. The specific density of most proteins vary within 5% of the above mean values [473]. The mean specific volume of dry noncollagenous proteins in cartilage is $0.74\ \mathrm{cm}^3/\mathrm{g}$ and $0.54\ \mathrm{cm}^3/\mathrm{g}$ for GaG [473]. The protein density is constantly $1.41\ \mathrm{g}/\mathrm{cm}^3$ for polymers with a weight of more than $30\mathrm{kDa}$ [476].

D.1.3 Cell size

Because TCAT works with cell phases, the average cell volume is necessary to integrate cell related parameter and to understand how many cells are represented by a particular volume fraction. The diameter of SK-mel-28 is $19.40 \pm 2.72\ \mu\mathrm{m}$ detected with Cellometer image cytometry and analysed using the Cellometer T4 (Nexcelom Bioscience: www.nexcelom.com). This gives a volume of $3823\ \pm 402\ \mu\mathrm{m}^3$ assuming a sphere. This is close to other observations made with trypsinized cells (*i.e.*,suspension with single cells). The keratinocyte volume is $3054 \pm 339\ \mu\mathrm{m}^3$ (diameter $18 \pm 2\ \mu\mathrm{m}^3$) [477], but the median diameter increases upon confluence with increasing oxygen concentration from 16 to $25\ \mu m^3$ [478]. Human fibroblasts have a volume of $3414\ \mu m^3$ [479]. A 3D reconstruction of mouse melanoma cellline B16F10 calculated a volume of $3427 \pm 1275\ \mu\mathrm{m}^3$ [480]. A better determination of the volume of each single cell can be reached with confocal microscopy and 3D-image reconstruction [481].

D.1.4 Vessel volume

The vessel volume fraction can be determined with immunohistochemistry. In the papillary dermis, 4.4% (0.35%) account for blood vessels (blood) and 0.3% (0.044%) for the lymphatic vessels (lymph) while in the reticular dermis, 2.2% (0.24) of the tissue account for blood vessels (blood) and 0.4% (0.064%) for lymphatic vessels (lymph) [482]. Numbers in brackets indicate the luminal part related to tissue, without endothelial cells. Non-invasive measurements with reflectance spectroscopy *in vivo* lead to a ratio of blood volume to tissue volume between 0.78% and 2.06% depending on tanning status and skin type [483]. Assuming that values for blood volume in histochemistry are underestimated, because the vessels are not under pressure and in spectroscopy overestimated because of light scattering, a general blood volume proportion of 0.9% might be a justified orientation

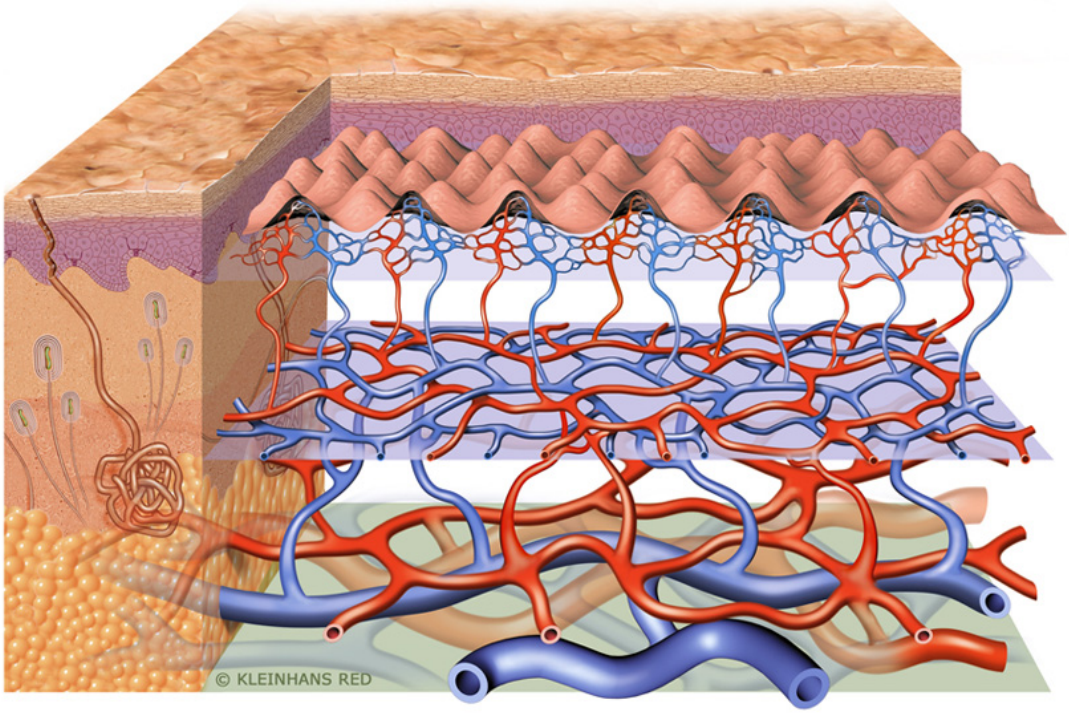

Figure D.1: Skin anatomy with papillary loops in the papillary dermis, called superficial plexus, and the deep vascular plexus in the dermis (blue planes). Large vessels reside in the hypodermis. Figure source is pinterest.

point. It is thereby important to take the bloodvessel system into account that is depicted in Figure D.1. The epidermis is avascular. Capillaries occur in the papillary dermis as papillary loops called papillary plexus [1], while supply arterioles occur in the deep reticular dermis, and large blood vessels occur in the hypodermis.

D.2 Oxygen

The current TCAT model assumes that only tumour cells and not host cells consume oxygen and that oxygen levels decline as soon tumour cells are present. The only oxygen source considered for the skin is the cutaneous plexus without consideration of the papillary plexus or atmospheric oxygen [6].

Moreover, the TCAT model works with mass units and treat oxygen as unit-less mass fraction of the IF [148]. On the one hand, the modelling community requires extensive quantities such as mass [451], on the other hand, oxygen is a dissolved gas and obeys partial pressure for dissolution, diffusion, and reactions. However, partial pressure is an intensive quantity which might work well for open systems being in exchange with the atmosphere. Medical models of tissue oxygenation and both respiratory and cardiovascular system are based on partial pressures and rely in addition on saturation degrees of oxygen binding molecules, which mediate 98% of transported oxygen [484]. A proper update of the

[1] A plexus is a network of vessels or nerves

oxygenation terms in TCAT models is necessary and might also come up with solutions for unsolved problems, such as the oxygen diffusion from arterioles or the oxygen permeation in the perivascular stroma [484]. An question to be addressed might be the appropriate quantity for the interface transport to ensure thermodynamically correct simulations of gas transport within tissues.
Integrated tissue oxygenation models are necessary for clinical approaches and single measurements are not sufficient [485, 486]. Optical oxygen measurements in life science are a fast developing research field [487] and might at least improve the available data base. However, it is known that the oxygen related components cannot be measured separately and can then be subsequently merged to one model as too many relationships influence the oxygenation in tissues [484]. For example, the oxygen permeability depends also on skin humidity, and sun exposure related alterations such as keratoses or elastosis [240]. However, this section provides some orientation points in mass units to model skin oxygenation with TCAT without claiming to have reached a satisfactory solution of this matter.

D.2.1 Solubility of oxygen in blood

Oxygen binds the metalloprotein heamoglobin on red blood cells (erythrocytes) and dissolves in blood plasma to a lower degree. The solubility of oxygen in blood is calculated as follows [488]:

$$C_b = C_P + \frac{[\mathrm{Hb}] \cdot \mathrm{PO}}{(1 + (\frac{\alpha_{O2sol} \cdot P_{50}}{C_p})^h)}$$

with tetramer hemoglobin concentration $[\mathrm{Hb}] = 2.3\ {}^{mmol}/_{\mathrm{L}}$, oxyphoric power $\mathrm{PO} = 4$, hill coefficient $h = 2.73$, oxygen concentration with 50% oxygen saturation $\mathrm{P}_{50} = 26\ \mathrm{mmHg}$ and the solubility of oxygen $\alpha_{O2sol} = 1.39 \cdot 10^{-3}\ {}^{\mathrm{mmol}}/_{\mathrm{L \cdot mmHg}}$. In addition, Henry's law $C_p = \alpha_{\mathrm{O2sol}} P_{O2}$ considers the physical solubility of oxygen in the blood plasma. The oxygen partial pressure is $\mathrm{P}_{\mathrm{O2}} = 35.2\ \mathrm{mmHg}$ ($C_b = 6.449\ {}^{\mathrm{mmol}}/_{\mathrm{L}}$) within the skin microvasculature [241] and does only measure the oxygen in the blood plasma without the oxygen bound to haemoglobin [484]. A 0.9% sterile saline solution at $35\ ^\circ$C body temperature has a oxygen solubility of $\alpha_{\mathrm{solv}} = 4.4\ {}^{\mathrm{mL}}/_{\mathrm{L}}$ under atmospheric pressure [489] and might be an orientation point for comparison.

D.2.2 Absolute oxygen delivery capacity after blocked blood flow

A static condition is an good orientation point, but as a neoplasm might increase oxygen demand, it would be interesting to get an impression of the delivery capacity of the microvasculature. Therefore, one can look at what happens if the blood flow is interrupted. If the blood flow is interrupted for one minute, the oxygen partial pressure drops to $\mathrm{P}_{\mathrm{O2}} = 19.2\ \mathrm{mmHg}$ ($C_b = 2.82\ {}^{\mathrm{mmol}}/_{\mathrm{L}}$). If the blockade is removed, the oxygen partial pressure jumps up to $43.2\ \mathrm{mmHg}$ ($C_b = 7.42\ {}^{\mathrm{mmol}}/_{\mathrm{L}}$) after re-perfusion, which is above the

normal value $\mathrm{P_{O2}} = 35.2\ \mathrm{mmHg}$ ($C_b = 6.449\ ^{\mathrm{mmol}}/_{\mathrm{L}}$) [241]. This results in the bottom and the top oxygen partial pressure for oxygen delivery. An oxygen partial pressure below that range is too low to constitute a gradient that results in oxygen transport.
Having that range, the maximal transferred mass of oxygen can be estimated. The standard TCAT model uses mass as extensive quantity wherefore the oxygen density in blood $\rho_{\text{b-norm}} = 6.449\ ^{\mathrm{mmol}}/_{\mathrm{L}} \cdot 32^{\mathrm{mg}}/_{\mathrm{mmol}} = 206.368\ ^{10^{-6}\mathrm{Kg}}/_{0.001\mathrm{m}^3} = 0.206^{\mathrm{Kg}}/_{\mathrm{m}^3}$ is determined using the specific molecular oxygen weight $32\ ^{\mathrm{mg}}/_{\mathrm{mmol}}$. The same calculation is done for the oxygen density in the interrupted blood stream, which is $\rho_{\text{b-min}} = 0.09024\ ^{\mathrm{Kg}}/_{\mathrm{m}^3}$. This gives an oxygen density drop of $0.116\ \frac{\mathrm{Kg}}{\mathrm{m}^3}$ in the blood. For comparison, the oxygen density is $1.429\ ^{\mathrm{Kg}}/_{\mathrm{m}^3}$ in pure gas form and $0.01\ ^{\mathrm{Kg}}/_{\mathrm{m}^3}$ if dissolved in water at room temperature (declining density with increasing temperature). With an tissue blood volume fraction of $\epsilon S^b = 0.009$ and the time needed until the blood oxygen reaches its steady state bottom value after blood flow interruption $\tilde{\tau} = 8.44 \pm 1.53\ s$ [241], the oxygen delivery rate (ODR) within skin can be estimated to be $1.24 \cdot 10^{-4}\ ^{\mathrm{Kg}}/_{\mathrm{m}^3\mathrm{s}}$.

D.2.3 Tissue oxygen consumption

The skin oxygen consumption is much lower and delivery parameters, such as the oxygen permeation, is one order of magnitude higher than the consumption [240, 484]. This makes sense as the system has also to work in times of high oxygen demand[2], *e.g.*, while doing sport. However, it also means that oxygen supply of a tumour is not critical until the tumour has reached a certain size that transcends the buffer capacity. The default oxygen consumption is also not equal in all skin layers. The oxygen consumption is highest at the papillary dermis with $0.5 \cdot 10^{-4}{}^{\mathrm{Kg}}/_{\mathrm{m}^3\mathrm{s}}$ ($2110\ ^{\mathrm{mL_{O_2}}}/_{\mathrm{m}^3\mathrm{min}} \cdot 1.429^{\mathrm{kg}}/_{\mathrm{m}^3}$) [240, 490] and reduces to $0.47 \cdot 10^{-4}{}^{\mathrm{Kg}}/_{\mathrm{m}^3\mathrm{s}}$ at the upper epidermis [240, 490] and $0.35 \cdot 10^{-4}{}^{\mathrm{Kg}}/_{\mathrm{m}^3\mathrm{s}}$ intra-dermal [240, 491]. The oxygen consumption rate for brain tissue is $1.27 \pm 0.07\ ^{\mu\mathrm{mol}}/_{min \cdot g}$ [492].

D.2.4 Cellular oxygen consumption

The Warburg effect describes the increased production of lactic acid from glucose in tumour tissues in comparison to normal tissues under non-hypoxic conditions [493, 494]. In the last decades more and more findings show that mutations in oncogenes and tumour suppressor genes can directly alter metabolism [495] and metabolism is also suspected to be altered by environmental mechanics [496], which would explain glycolysis in well oxygenated but crowded cancer tissues. The $\mathrm{BRAF}^{\mathrm{V600E}}$ mutation in two malignant melanoma celllines (FM55-M2 and SK-MEL-28) impairs oxidative phosphorylation and makes the cell-lines addicted to glycolysis and thus addicted to BRAF dependent signalling [248]. This is connected to 14 or 16 fold increase of the extracellular acidification rate (ECAR). Inhibition of glycolysis or knock-down of BRAF shows a certain shift back to the impaired oxidative phosphorylation. As shown in Figure D.2 E-F, the OCR doubles within 120 hours following BRAF inhibition but the adenosine triphosphate (ATP)-level decreases. The sensor for

[2] One has also to differentiate between systemic regulation (heart) and local regulation (Vasodilation, vasoconstriction), which makes the regulation even more complicated.

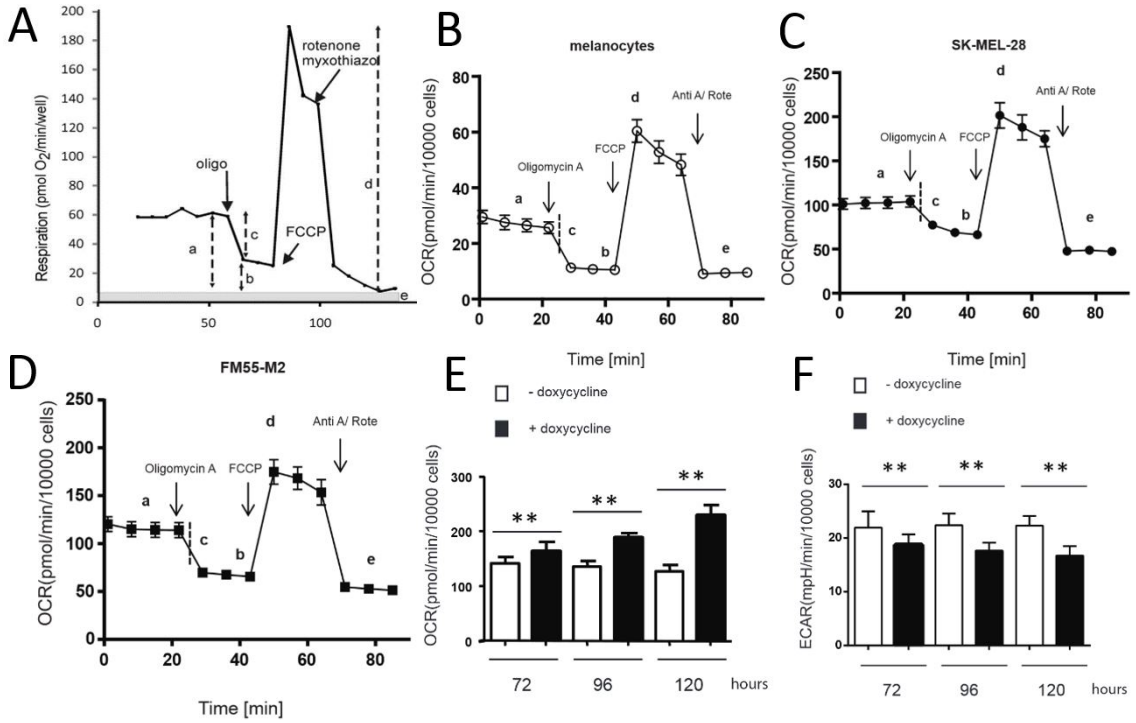

Figure D.2: A: Sheme for cell respiratory control: Oligomycin A (oligo) blocks oxidative phosphorylation and ATPase, FCCP unsets the proton gradient, which makes the system highly inefficient. Rotenone unsets the electron transport chain and stops the processing of oxygen. Marks: a, basal respiration; b, proton leak; c, ATP-turnover; d, maximum respiration; e, non-mitochondrial respiration [247]. B-D: OCR of melanocytes, SK-MEL-28, FM55-M2. E-F: OCR and ECAR of FM55-M2 without and after $BRAF^{V600E}$ knock-down with doxycycline. B-F: Figure source [248].

bioenergetic stress protein kinase AMP-activated catalytic subunit alpha 2 (PRKAA2)[3] indicates the importance of glycolysis for cells [248]. Another study shows that melanoma cells rely on solute carrier family 16 member 1 (SLC16A1)[4] to transport protons and lactate out of the cell, while melanocytes and keratinocytes depend on SLC16A1[5] in acidic environments to maintain the intracellular pH value [497]. Independent of the ongoing discussion about the existence of the Warburg effect in non-hypoxic conditions, the model requires parameter for the oxygen consumption so that the necrotic core arises naturally. Furthermore, it might be useful for the future to implement the acidification rate in hypoxic conditions depending on the research question. With the molar mass $\mathrm{M} = 32\ \mathrm{g/mol}$ and the cell size, following oxygen consumption of SK-mel-28 cells can be obtained in international system of units (SI)-standard for the tumour cell phase:

$$y_{t0}^{nl} = 100 \frac{\mathrm{pmol}}{\mathrm{min} \cdot 1000\ \mathrm{cells}} \cdot 32 \cdot 10^{-3} \frac{\mathrm{kg}}{\mathrm{mol}} = 100\ \frac{10^{-12}\mathrm{mol} \cdot 32 \cdot 10^{-3}\ \frac{\mathrm{kg}}{\mathrm{mol}}}{60\mathrm{s} \cdot 1000 \cdot 3823 \cdot 10^{-18}\mathrm{m}^3}$$

[3] Also known as AMPK

[4] Also known as MCT1

[5] Also known as cation proton antiporter 1 NHE1, which was already mentioned in the mechano regulation section

$$= 139.6 \cdot 10^{-4} \frac{\mathrm{Kg}}{\mathrm{m}^3 \cdot \mathrm{s}}$$

A TCAT cancer growth model requires an oxygen consumption rate for the basic metabolism and the growth dependent metabolism. The oxygen consumption rate (OCR) can be divided in different elements [247], like mitochondria independent oxygen consumption with or without oxidative phosphorylation, as shown in Figure D.2 A-D. Two melanoma celllines show an increased overall OCR in comparison to melanocytes. The absolute level before deactivation of the ATPase with oligomycin A is assumed to be the basic metabolic turnover $y_0^{nl} = 140 \cdot 10^{-4}\ {}^{\mathrm{Kg}}/_{\mathrm{m}^3 \cdot \mathrm{s}}$, while the maximum rate after breakdown of the proton gradient with FCCP is assumed to be the growth depended capacity $y_{growth}^{nl} = 140 \cdot 10^{-4}\ {}^{\mathrm{Kg}}/_{\mathrm{m}^3 \cdot \mathrm{s}}$, which is added to the basic OCR. The SK-MEL-28 cellline is used as reference.
These values for the oxygen consumption are restricted to the cell phase and are much higher than the OCR measured for the different skin layers. But these values are specific to melanocytes and melanoma cells and reflect their high metabolic activity. For instance, the colon cancer cellline RKO has a OCR of $2 \cdot {}^{\mathrm{pmol}}/_{\mathrm{min} \cdot 1000\ \mathrm{cells}}$ [498] reaches only 5% of the melanocyte and 2% of the melanoma cell oxygen consumption rate. The consumption rate of fibroblasts is $1.1 \cdot 10^{-4} {}^{\mathrm{Kg}}/_{\mathrm{m}^3 \cdot \mathrm{s}}$ ($1.19 \cdot 10^{-17} {}^{\mathrm{mol}}/_{\mathrm{cell} \cdot \mathrm{s}}$) [499]. Via the nicotinamide adenine dinucleotide (NADH) in mitochondria, the OCR of keratinocytes at the basal layer is calculated to be $0.91 \cdot 10^{-4} {}^{\mathrm{Kg}}/_{\mathrm{m}^3 \cdot \mathrm{s}} (0.035 \mu \mathrm{moles}/10^6 \mathrm{cells}/\mathrm{h})$ [500]. The brain consumption rate after transformation is $7 \cdot 10^{-4} {}^{\mathrm{Kg}}/_{\mathrm{m}^3 \cdot \mathrm{s}}$ [492]. In general, cells consume $1.55 \cdot 10^{-9}$ to $3.8 \cdot 10^{-9}\ {}^{\mathrm{mmolO_2}}/_{\mathrm{h} \cdot \mathrm{cell}}$ [501].

D.2.5 Extracellular acidification rate of cells

The ECAR is given in the unit ${}^{\mathrm{mpH}}/_{\mathrm{min} \cdot 1000 \mathrm{cells}}$. 30000 melanoma cells were seeded per well [248] and each reaction well captures $80\ \mu\mathrm{l}$ medium (XF96 V3 microplates Seahorse Bioscience). The ECAR can be translated in the proton production rate (PPR) with $\mathrm{PPR}_{\mathrm{total}} = \mathrm{ECAR}_{\mathrm{tot}}/\mathrm{BP}$, whereby BP is the buffering power. For $7\ \mu l$ DMEM medium, the buffering power is $\mathrm{BP} = 0.1\ \mathrm{mpH}/\mathrm{pmol}/7\mu\mathrm{l}$ [502]. A proton has a weight of $1.672 \cdot 10^{-27} \mathrm{kg}$ and one mol encompasses $6.02214 \cdot 10^{23}$ particles. The ECAR of SK-MEL-28 is $51\ {}^{\mathrm{mpH}}/_{\mathrm{min} \cdot 1000\ \mathrm{cells}}$ [248]. The following translation into SI standard can be made:

$$\begin{aligned}
\mathrm{PPR}_{\mathrm{total}} &= 51 \frac{\mathrm{mpH}}{\mathrm{min} \cdot 1000\ \mathrm{cells}} \cdot \frac{\mathrm{pmol}}{0.1 \mathrm{mpH} \cdot 7 \mu \mathrm{m}} \cdot 80 \mu l \cdot M \\
&= 51 \frac{10^{-12} \cdot 6.02214129 \cdot 10^{23} \cdot 1.672621898 \cdot 10^{-27} \mathrm{kg} 80}{60\mathrm{s} \cdot 1000 \cdot 3823 \cdot 10^{-18} \mathrm{m}^3 7} \\
&= 25.6 \cdot 10^{-4} \frac{\mathrm{Kg}}{\mathrm{m}^3 \cdot \mathrm{s}}.
\end{aligned}$$

Also the ratio of OCR/ECAR may be used as orientation point with $14.8\ {}^{\mathrm{pMol}}/_{\mathrm{mpH}}$ for melanocytes, $2.74\ {}^{\mathrm{pMol}}/_{\mathrm{mpH}}$ for the FM-55-M2 melanoma cellline, and $2.21\ {}^{\mathrm{pMol}}/_{\mathrm{mpH}}$ for the SK-MEL-28 melanoma cellline [248].

D.2.6 Oxygen affects the cell type specific proliferation rate

Melanocytes prefere the partial oxygen pressure range of $\mathrm{PO2} = 6 - 34\ \mathrm{mmHg}$, which is in the range of PO2 at the dermal-epidermal junctions with $\mathrm{PO2} = 15\ \mathrm{mmHg}$ $(1-3\%$ Oxygen) [242]. This range is close to the preferred region for fibroblasts with $\mathrm{PO2} = 9 - 16\ \mathrm{mmHg}$ [503]. Keratinocytes prefere a region of $\mathrm{PO2} = 36 - 133\ \mathrm{mmHg}$ [504]. The proliferation rate over the oxygen pressure is shown in D.3 A. The curve fitting toolbox of Matlab R2015a was used to derive following equation for melanocyte proliferation

$$y_2 = 1.023 \cdot \exp(-0.005022 \cdot PO_2) - 1.82 \cdot \exp(-6.791 \cdot PO_2), \tag{D.1}$$

assuming cell death at zero oxygen, which is not confirmed. For keratinocytes the fitting curve is

$$y_1 = 4.417 \cdot \sin(0.007357 \cdot PO_2 - 1.326) + 4.38 \cdot \sin(0.0082 \cdot PO_2 + 7.725). \tag{D.2}$$

The oxygen concentration in IF can be calculated from the partial pressure with the Henry constant for oxygen in water $H^{cp} = 1.3 \cdot 10^{-5\mathrm{mol}/\mathrm{m^3 \cdot Pa}}$ and the equation $c = H^{cp} \cdot p$ [505]. For the molar mass of oxygen and the application on pressure values in mmHg the Henry constant is $H^{cp} = 1.3 \cdot 10^{-5\mathrm{mol}/\mathrm{m^3 Pa}} \cdot {}^{\mathrm{Pa}}/_{0.0075\mathrm{mmHg}} \cdot 32 \cdot 10^{-3\mathrm{Kg}/\mathrm{mol}} = 0.5546 \cdot 10^{-4\mathrm{Kg}/\mathrm{m^3 \cdot mmHg}}$. However, this is an extremely simplified assumption as the *stratum corneum* differs in thickness and is much thinner at the forehead in comparison to acral skin. The oxygen conductivity is $\mathrm{K_{ox}} = 3.7 \cdot 10^{-7}\ {}^{mL\ O_2}/_{\mathrm{m \cdot min \cdot Torr}}$ in the stratum corneum and $\mathrm{K_{ox}} 1.3 \cdot 10^{-6}\ {}^{mL\ O_2}/_{\mathrm{m \cdot min \cdot Torr}}$ in living tissue [240].

D.2.7 Atmospheric and vascular boundary condition for oxygen

The oxygen pressure at the skin surface is $163 \pm 9\ \mathrm{mmHg}$ or Torr and decreases with the skin depth as shown in Figure D.3 B. If one ignores the *stratum corneum*, one can assume a boundary oxygen pressure for the skin surface of $135\mathrm{mmHg}$ [240] which is $74.9 \cdot 10^{-4\mathrm{Kg}/\mathrm{m^3}}$ using the Henry constant $H^{cp} = 0.5546 \cdot 10^{-4\mathrm{Kg}/\mathrm{m^3 \cdot mmHg}}$ for water. The mass fraction of oxygen is

$$\omega_{env}^{nl} = \frac{74.9 \cdot 10^{-4}\,\frac{\mathrm{Kg}}{\mathrm{m^3}}}{1000\,\frac{\mathrm{Kg}}{\mathrm{m^3}}} = 7.5 \cdot 10^{-6} \tag{D.3}$$

with water as reference. The boundary condition for the dermis blood vessel relates to the highest tissue partial pressure close to the base of the capillary loop with $40\ \mathrm{mmHg}$ [241]. This gives a value of $\omega_{env}^{nl} = 2.2 \cdot 10^{-6}$, which is similar to the value in the work of Sciumé *et al.* [6]. The blood contributes to the oxygen profile as shown in Figure D.3 D. The atmospheric oxygen uptake is $0.53 \pm 0.27\ \mathrm{ml\ O_2\ min^{-1}\ m^{-2}}$ during normal blood flow, and increases by $9.5 \pm 6.3\%$ after 5 min blood flow interruption [240]. Tissue solubility is anisotropic in tissues and the linkage between pressure and concentration is disbelieved in this application area [507]. If no data is available, orientation might also be obtained

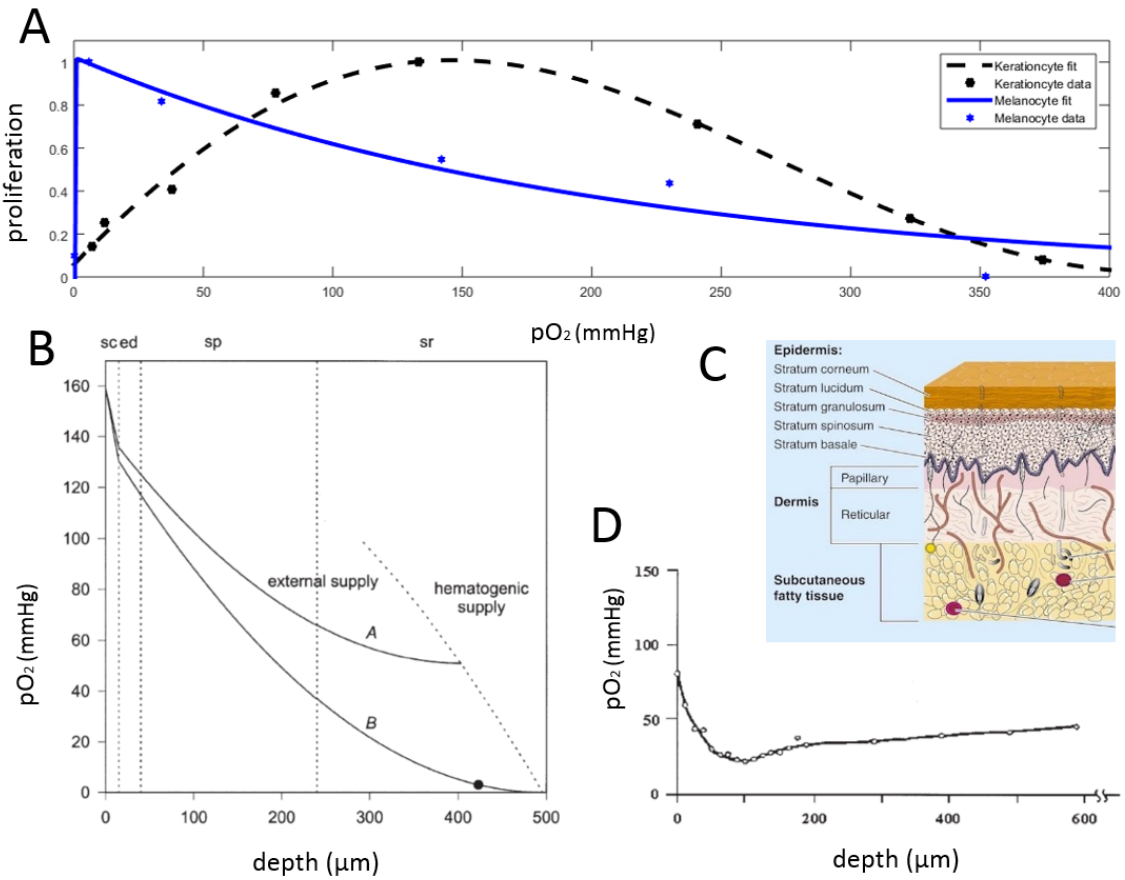

Figure D.3: Oxygen profiles in skin. A: Relative proliferation rate of keratinocytes [504] (black) and melanocytes (blue) [242] over oxygen partial pressure. B: Penetration depth of atmospheric oxygen, measured with oxygen fluxoptode, from skin surface on the left side to deeper parts supplied mainly over blood vessels (hematogenic supply) on the right side. Assumed basic oxygen pressure in profile A of $51\ \mathrm{mmHg}$ and profile B of $0\ \mathrm{mmHg}$. sc: *stratum corneum* (dead keratinocytes); ed: viable epidermis; sp: *stratum papillare*; sr: *stratum reticulare* [240]. C: Skin architecture as orientation for Subfigure B (Figure source: cosmotruth.wordpress.com). D: Oxygen profile of capillary and atmospheric oxygen measured with invasive needle electrodes [240, 506].

with measurements in food [508].

D.2.8 Oxygen diffusion is reduced in interstitial fluid

The diffusion coefficient for oxygen at 37 °C in pure water is between $3 \cdot 10^{-9} m^2/\mathrm{s}$ [509] and $3.83 \cdot 10^{-9} m^2/\mathrm{s}$ [501]. With cross-multiplication we assume a diffusion reduction by factor 1.3 because of increased viscosity. The viscosity of IF of rabbits is 90% higher than of water [510] and the 160% increased viscosity using glycerol decreased the diffusion coefficient by factor 2.3 [511]. This lead to the start value of $2.3 \cdot 10^{-9} m^2/\mathrm{s}$, close to the measured diffusion coefficient of $2.69 \cdot 10^{-9} m^2/\mathrm{s}$ in protein solution at 37 °C [501, 512]. In addition, the diffusion coefficient is affected by the solubility of oxygen in water but not by the salinity, but is neglected here [509].

D.2.9 Permeability and diffusion is reduced in polymers

Besides the diffusion coefficient for oxygen in water at the microscale, the diffusion coefficient in cell free porous extracellular matrix is available at the macroscale. With a collagen volume fraction 0.17 [513], processed acellular dermal matrix AlloDerm® from LifeCell Cooperation has an effective diffusion coefficient of $2.5 \cdot 10^{-9} m^2/s$ which is restricted in comparison to their baseline diffusion coefficient of $8.5 \cdot 10^{-8} m^2/s$ [501]. With the equation for the tortuosity of the tissue

$$\sigma = \log_{\epsilon S^l} \frac{D_{\text{eff}}^{\overline{ol}}}{D_0^{\overline{ol}}} \tag{D.4}$$

one gets $\sigma = \log_{0.79} {}^{2.5 \cdot 10^{-9} m^2/s} / _{8.5 \cdot 10^{-8} m^2/s} = 14.96$ assuming an additional GaG and elastin volume fraction of 0.04 added to the collagen volume fraction. The same calculation is done for the experiment from Cheema *et al.* [514]. With saline at $37\ ^\circ\mathrm{C}$, which has an diffusion coefficient $3 \cdot 10^{-9} \frac{\mathrm{m}^2}{\mathrm{s}}$ [509], they measured the effective diffusion coefficient of $4.5 \cdot 10^{-10} m^2/s$ and $1.7 \cdot 10^{-10} m^2/s$ in collagen matrices ($2.035\ \mathrm{mg/ml}$) with 11% and 34% compression [514]. Without bound water, collagen makes 1.42% of the available space. This volume fraction increases by 11% compression to 1.56% and with 34% compression to 2.15%. $\sigma = \log_{0.984} {}^{4.5 \cdot 10^{-10} m^2/s} / _{3 \cdot 10^{-9} m^2/s} = 117.6$ and $\sigma = \log_{0.9785} {}^{1.7 \cdot 10^{-10} m^2/s} / _{3 \cdot 10^{-9} m^2/s} = 131.8$. The oxygen diffusion coefficient also depends on the water content in tissues [515] but it might be a good orientation mark for the beginning. However, a gel cross-links more homogeneously than a cell-free tissue ECM, where the removed cells leaved holes and the ECM is more clumped. The permeability of skin for different substances is well studied elsewhere [516, 517].

D.3 Mechanical parameter

If the extracellular matrix is responsible to give tissue stability, it also means that it will restrict the expansion of neoplasms. Finding parameters that explain the restrictive characteristics is key to understand the balance between tumour growth pressure and counteracting pressure.

D.3.1 Viscosity of cells, membranes, and interstitial fluid

The viscosity describes the resistance of a fluid, which is exposed to tensile or shear stress. This parameter influences the diffusion of molecules and is highly heterogeneous inside cells, spanning a range from 0.001 to $0.9\ \mathrm{Pa \cdot s}$ measured with molecular rotors [518, 519]. Viscosity can be quantitatively mapped with spatial resolution of a cell across different organelles with photo induces electron transfer (PET) [520]. The lysosome is the organelle with the highest viscosity in a cell with 0.130 to $0.175\ \pm 0.02\ \mathrm{Pa \cdot s}$ [520]. The viscosity increases after photo induced cell death to $0.35\ \pm 0.05\ \mathrm{Pa \cdot s}$ [518]. The viscosity of kerationcytes' plasma membrane varies between 0.03 to $0.1\ \mathrm{Pa \cdot s}$ measured by

electron paramagnetic resonance spectroscopy. The viscosity of IF of rabbits is 90% and the viscosity of blood plasma is 58% higher than of water [510]. The viscosity of human oedema is $34 \pm 16\%$ higher than of water [521]. The viscosity of water is $0.69 \cdot 10^{-3}\mathrm{Pa} \cdot \mathrm{s}$ by $37\ ^{\circ}\mathrm{C}$. The highest viscosity of the cytosol was found in a publication about drosophila embryo with a viscosity of $3.6\ \pm 0.1\ \mathrm{Pa} \cdot \mathrm{s}$, tested with $0.46\ \mu$-m-diameter beads [522]. The bead might be too big to measure viscosity in a cell accurately.

D.3.2 Pressure affects the proliferation rate but does not affect cell death

Proliferation rates change with tumour pressure and highly depends on the cellline as shown in Figure D.4 [523]. Measurements for melanoma or melanocytes are not available. The dependency of cell death on hydrostatic pressure plays a role in the eye but not in cancer. A pressure of around $50\ \mathrm{mmHg}$ in eye triggers apoptotic cell death in retina-ganglion cells (RGT-5) due to cytochrome c release after mitochondrial cristae compression [524]. A pressure of 130 to $193\ \mathrm{MPa}$ was necessary to induce 50% cell death in non-melanoma cancer celllines [525, 526], what is 1000-fold atmosphere pressure and is consequently not physiologically relevant.

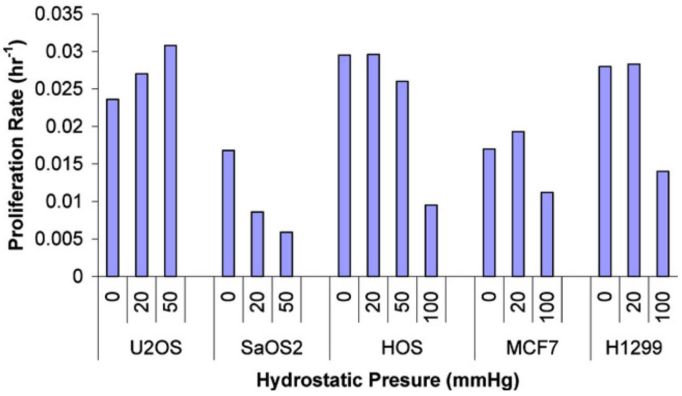

Figure D.4: Proliferation rate versus hydrostatic pressure. Osteosarcoma cells: U2OS, SaOS2, HOS; breast cancer cellline: MCF7; lung cancer cellline: H1299 [523].

D.3.3 Hydrogel systems for cell culture labs and related parameter

Since the experimental field of biology realises evermore tremendous differences in results from 2D cell culture to the *in vivo* situation, scientists have been examining several scaffolds for colonisation with cells in 3D. Synthetic water-rich hydrogels with biological functionalisation proofed to be best reproducible, scalable, and animal-free 3D cell culture systems [527, 528]. While polyacrylamide is used only for 2D cell culture systems, PEG based systems like the following allow three dimensions [278]: HyStem® offers a combination of gelatin and hyaluronan with a shear modulus[6] of $G = 1.6 - 21$ kPa for clinical applications [529]. QGel offers a wide range of tissue specific and predefined powders for hydrogel formation. Gelation is based on vinyl sulfone groups reacting with cysteines of a cross-linker [531]. QGel provides no credible published mechanical data. Cellendes uses

[6] Only compression modulus K of 120 to $370\ \mathrm{kPa}$ reported [529]. Conversion of bulk to shear modulus $G = {}^{3 \cdot K(1-2\nu)}/_{2(1+\nu)}$ gives a rough range of $G = 1.6 - 21$ kPa with assumed Poisson ratio $\nu = 0.4498 \pm 0.0305$ [530].

		SHEAR E_{shear} [kPa]	INDENTATION E_{indent} [kPa]	TENSILE $E_{uniaxial}$ [kPa]
Stratum corneum	*25% RH*	**30**	**600**	$0.04\text{-}10\cdot10^6$
	98% RH	**10**	n.a.*	$6\text{-}10\cdot10^4$
(Viable) epidermis	*25% RH*	**30**	**600**	n.a.*
	98% RH	**10**	n.a.*	n.a.*
Dermis		**8**	1-10[100,110]	$1\text{-}20\cdot10^3$ [5,139]
Hypodermis		**24**	20-30[41]	n.a.*

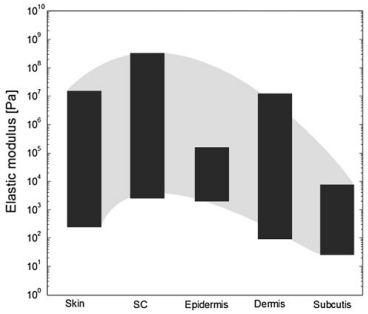

Figure D.5: Different Young's moduli for the skin layers. **Left:** selected experimental values with different mechanical tests under differed relative humidity settings (RH). Table from [533]. Other citations: ([5]:→[534]), ([41]&[110]:→[535]), ([100]:→[536]), ([139]:→ [537]). **Right:** mechanical parameter ranges with the abbreviation SC indicating the *stratum corneum* [68].

dextran and polyvinyl alcohol as polymers, altered either with fast or slow reacting groups for gelation within seconds or within minutes, respectively [532]. Gelation starts after adding cross-linker without cell-damaging chemicals, UV light, or temperature changes. The final gel obtains a selectable shear modulus within the range of $G' = 0.3 - 6\ kPa$ and is cell-impenetrable in its polymeric architecture with a mesh size of $5 - 10$ nm. Hydrogels are not enzymatically degradable if cross-linked with PEG-link and degradable if cross-linked with CD-link, a PEG-link modified with a MMP-cleavable motif. Dextran can be degraded by the user with dextranase. The hydrogel can be functionalized with thiol carrying peptides and soluble long-chain ECM-proteins like fibronectin. Cellendes' transparent information policy about rheometric properties and the number of reactive groups allows decoupled control of biomimetic functionalization and mechanical stiffness by the user. Moreover, the transparent hydrogel is suitable for imaging and can be used for high throughput applications [279].

D.3.4 Elastic moduli are skin layer specific

The determination of mechanical parameters suffers from the highly dynamic nature of the healthy skin anatomy. Composition, structure, volume, and mechanical properties of skin change with body location, race, sex and age of the human [538] as well as with tissue hydration [68, 539]. A comprehensive overview of the skin-layer mechanics can be found in Figure D.5. The mechanical measurements of tissues are highly context-specific, and the elastic modulus can range up to 5 log steps $(4.4\ \text{kPa} - 57\ \text{Mpa})$ depending on moisture [68] or whether the collagen is forced into enthalpic stretching following uniaxial stress or not.

Entropic and not enthalpic stretching is expected in a frequency sweep test. The sweep test measures the shear modulus, which can be used to calculate the elastic modulus. The elastic modulus declines from the *stratum corneum* $(10\ \text{kPa} - 1\ \text{GPa})$ over the dermis $(0.5\ \text{kPa} - 45\ \text{kPa})$ to the subcutaneous fat tissue $(0.12\ \text{kPa} - 30\ \text{kPa})$ [68]. An indentation

test gives a Young's modulus for the dermis of $35\ \mathrm{kPa}$ and the hypodermis of $2\ kPa$ *in vivo* condition [540], while a suction test indicates $120 \pm 88\ kPa$ of the skin [541].
Enthalpic stretching along Langer's lines result in higher Young's moduli than tests, which accesses polymers during entropic stretching [542, 543]. The elastic modulus of stretched human cadaver skin depends on the direction of the Langer lines and is thus anisotropic. In parallel to the Langer lines, the elastic modulus is $127 \pm 36\ \mathrm{MPa}$. In perpendicular direction it is $117 \pm 59\ \mathrm{MPa}$ and in $45°$, it is only $73 \pm 16\ \mathrm{MPa}$ [542, 543]. Tensile stress can result in a Young's modulus of around $83.3 \pm 34.9\ \mathrm{MPa}$ for the high-strain range, with mean ultimate tensile strength $21.6 \pm 8.4\ \mathrm{MPa}$ and mean failure strain $54 \pm 17\%$ [542]. The initial slope value of around $1.18 \pm 0.88\mathrm{MPa}$ in tensile testing is more comparable to torsion [533], suction [541] or indentation [533, 540] measurements *in vivo* [542].

E. PK paper: supp. inf.

Supplementary Information: Quantitative systems pharmacology of dabrafenib metabolism: drug interaction, CYP3A4 enzyme induction, and efficiency loss in hydrogels

Marco Albrecht[1], Yuri Kogan[2], Dagmar Kulms[3], and Thomas Sauter[4]

[1]*Université du Luxembourg; Systems Biology Group; 4367 Belvaux; Luxembourg; Tel.: (+352) 46 66 44 5143; Email: marco.albrecht@uni.lu, marco.albrecht@posteo.eu*
[2]*Institute for Medical Biomathematics (IMBM); 60991 Bnei Atarot; Israel; Email: yurikogan@optimata.com*
[3]*Dresden University of Technology; Experimental Dermatology; 01307 Dresden; Germany; Tel.: +49 (0)351 458-18973 ; Email: dagmar.kulms@uniklinikum-dresden.de*
[4]*Université du Luxembourg; Systems Biology Group; 4367 Belvaux; Luxembourg; Tel.: (+352) 46 66 44 6296; Email: thomas.sauter@uni.lu*

1 Reproduction of the original model

The current standard PK model [1]

$$\frac{dD_{0c}}{dt} = -\frac{\frac{Q}{F}}{\frac{V_c}{F}}(D_{0c} - D_{0p}) - \frac{\frac{CL}{F}}{\frac{V_c}{F}} \cdot D_{0c} + \frac{k_D \cdot D_{0c}}{\frac{V_c}{F}} \cdot e^{-k_D \cdot (t_{ld} - t_{\text{lag}})}$$
$$\frac{dD_{0p}}{dt} = +\frac{\frac{Q}{F}}{\frac{V_p}{F}}(D_{0c} - D_{0p}) - \frac{\frac{CL_{ind}}{F}}{\frac{V_p}{F}} \cdot D_{0p}.$$

describes the central dabrafenib concentration D_{0c} in the central compartment volume V_c and the peripheral dabrafenib concentration D_{0p} in the peripheral compartment volume V_p [1]. The index 0 indicates unmodified dabrafenib in its original form. The equation of the oral compartment is analytically solved and appears

as last first-order term in the central dabrafenib compartment. This term is influenced by the adsorption constant k_D and the time point of last administered dose t_{ld}. The time lag t_{lag} accounts for the delay in transition from the oral compartment. The transfer between central and peripheral compartment is mediated via the distribution clearance Q corrected by the bioavailability change from gelatin capsule to hypromellose (HPMC) capsule F and F_{Gel}. The oral clearance

$$\frac{CL}{F} = \frac{CL_0}{F} + \frac{CL_{ind}}{F}$$
$$\frac{CL_{ind}}{F} = CL_{ind,ss} \cdot \left(\frac{D \cdot F_{\text{Gel}}}{D_{Ref}}\right)^{\gamma} \left(1 - e^{\frac{-\log(2)t}{T_{50}}}\right).$$

sums up the initial oral clearance CL_0 and the inducible oral clearance CL_{ind}. The inducible clearance includes a time-dependent term with drug half-life T_{50} and the last administered drug dose D relative to the reference dose of 150 mg BID dabrafenib D_{ref}, adjusted via exponent γ. The additional inducible clearance for the peripheral compartment has been introduced to mimic both the steep decline in the trough concentration and the alignment of the curves in the steady state according to the original paper [1]. We reproduced the original work [1] shown in Supplemental Figure 1 with additional information, such as the concentration in the peripheral compartment. The code can be found in the supplemental files: *SupplementalCode1.m*. Because the original model does not provide information about dabrafenib metabolites and because the clearance term is artificially time and dose dependent, we created a new model that explicitly addresses those issues. The proposed model uses the parameters of the original model listed in Table 1.

The molecular weight of the dabrafenib molecule is 519.56 g/mol [2]. The units from the the original work [1] in ng/mL can be translated as follows

$$1\frac{\text{ng}}{\text{mL}} = \frac{10^{-9}\text{g} \cdot \text{mol}}{10^{-3}\text{L} \cdot 519.56\text{g}} = 1.925 \cdot 10^{-9}\frac{\text{mol}}{\text{L}} = 1.925\text{nM}$$

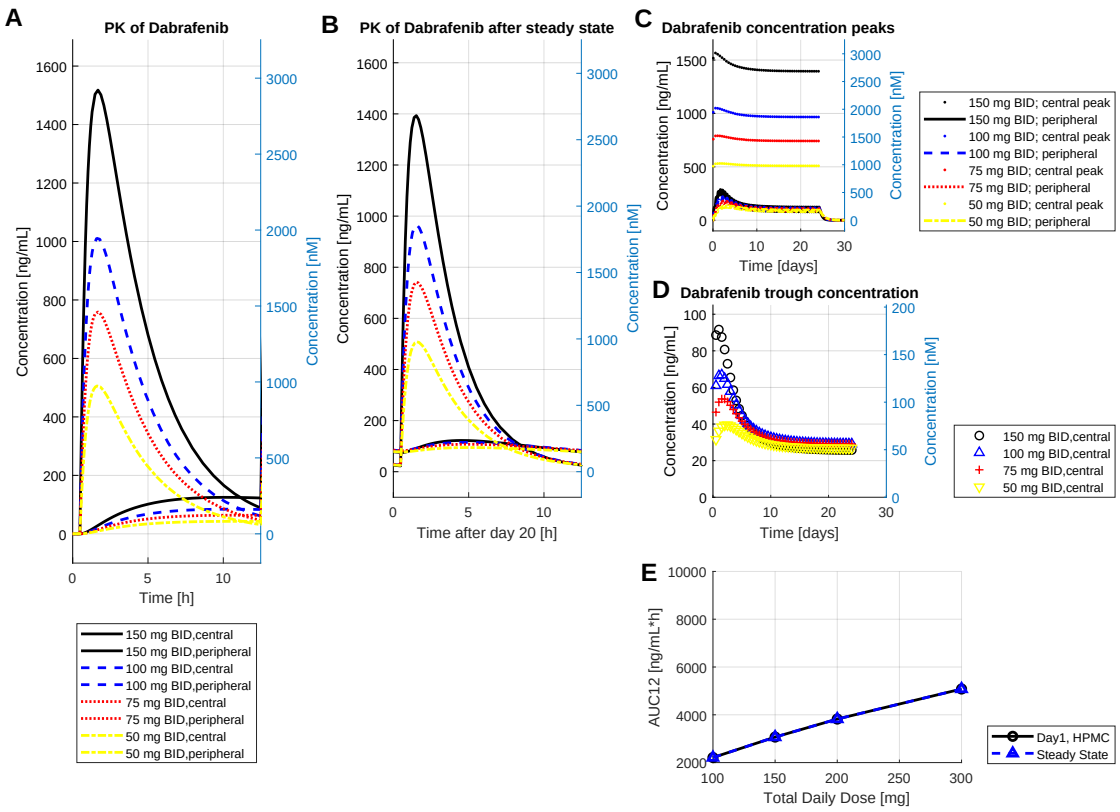

Figure 1: **Reproduction of the original model [1].** A: Dabrafenib concentration pattern for a single dose. B: Dabrafenib concentration pattern after periodic drug administration. C: Peak values of dabrafenib PK after periodic dabrafenib administration. D: Trough concentration of dabrafenib PK after periodic dabrafenib administration. E: Drug exposure as area under the curve (AUC). All profiles are shown for 150 mg, 100 mg, 75 mg, and 50 mg dabrafenib. We show additionally the peripheral compartment and the related concentration in nanomolar nM.

Table 1: Parameter transferred from previous publication [1]

parameter	value	unit	Description
$tlag$	0.482	[h]	absorption lag-time Dabrafenib
$Fgel$	0.555	[-]	relative bioavailability of gelatin capsule to HPMC capsule
K_D	1.88	[L/h]	absorption rate
$CL0F$	17.0	[L/h]	apparent initial clearence
$CLindSS$	17.3	[L/h]	apparent inducible clearence at steady state
$Dref$	170.0	[mg]	reference dose
y	0.927	[-]	power of dependence of CLindSS on absorbed dose (LDOS X Fgel)
$T50$	67.3	[h]	half-life of clearance induction
$tlag$	0.482	[h]	absorption lag-time
VcF	70.3	[L]	apparent volume of central compartment
VpF	174.0	[L]	apparent volume of peripheral compartment
QF	3.3	[L/h]	apparent inter-compartmental

2 Model fit without enzyme induction

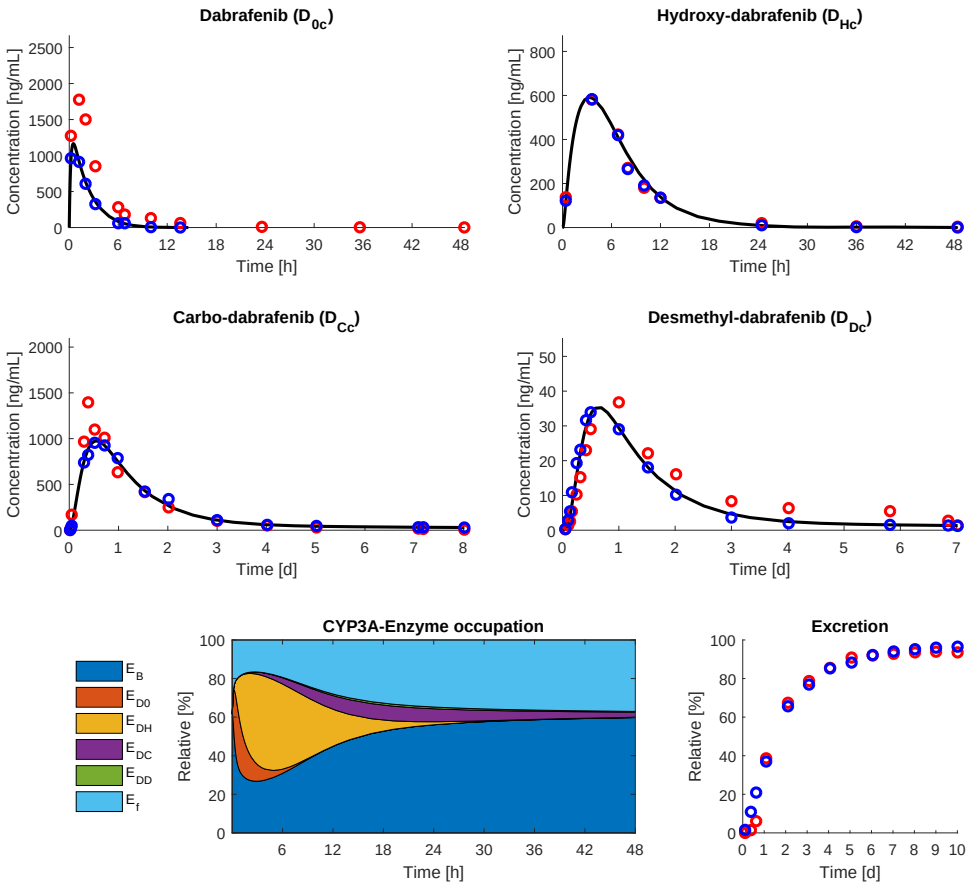

Figure 2: Data fit without enzyme induction. This Figure might be compared with Figure 3 A-D,G and H. The PK profile for dabrafefenib is underestimated probably because of too relative excess of CYP3A4 enzyme. Data source: [3].

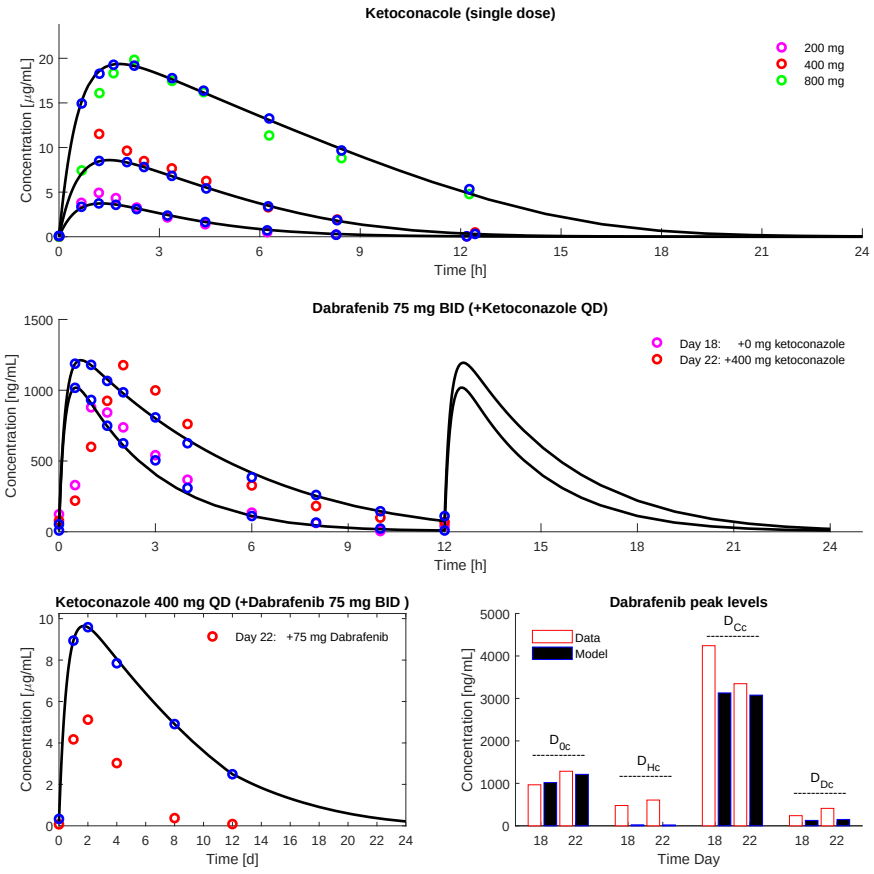

Figure 3: Data fit without enzyme induction. This Figure might be compared with Figure 3 I-L. Overestimated abundance of Dabrafenib and ketoconazole at day 18 and at day 22 probably because of relative lack of enzyme. Data source: [4, 5]

Enzyme pattern after work flow step two

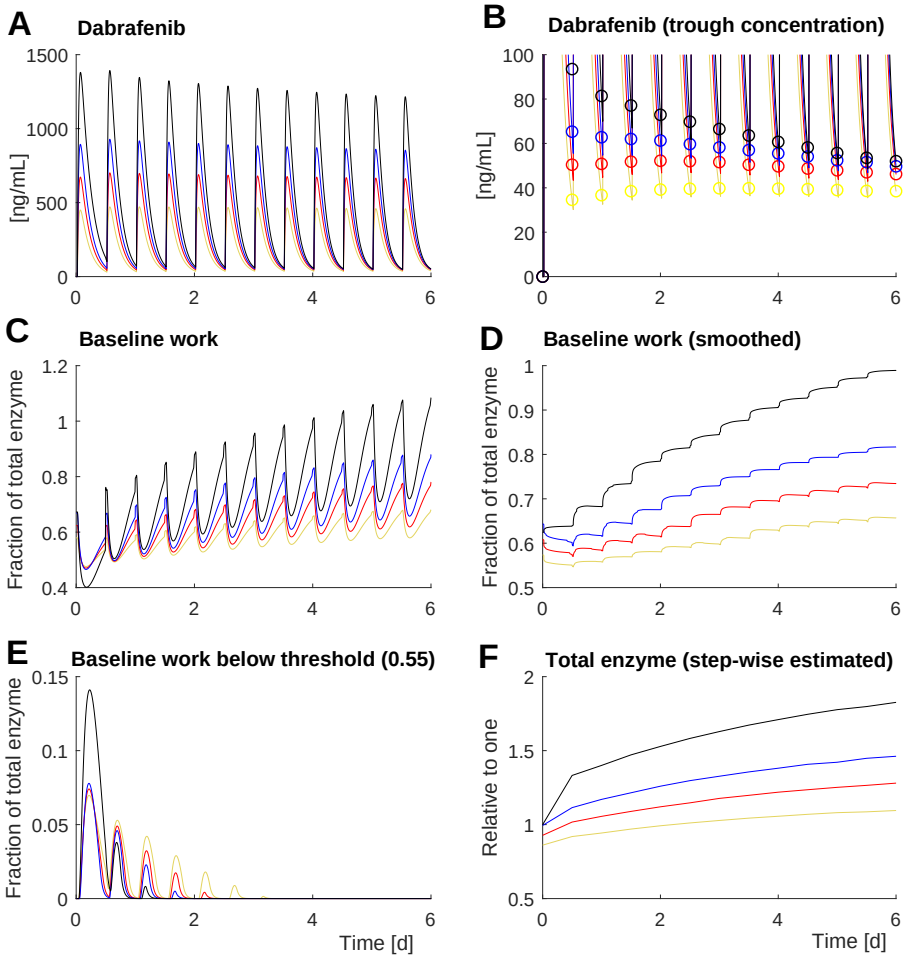

Figure 4: Step-wise optimisation of CYP3A4 level. A: the dabrafenib model without enzyme induction is used with fixed parameters. B: the algorithm optimises the enzyme concentration for each dose period to reach the reported trough level. C: The enzyme dependent baseline work is increasing with the increase of total enzyme (F). D: as C but with smoothed time course. E: difference between CYP3A4 that performs baseline work and the minimal accepted concentration level of it. F: total enzyme calculated for each dose period.

Image quantification

The spheroid areas where recorded as shown in Supplementary Figure 5. Image quantification was performed with Fiji in batch process using the following code:

```
t=getTitle();
Stack.setChannel(2)
run("Delete Slice", "delete=channel");
run("Z Project...", "projection=[Max Intensity]");
run("16-bit");
run("Green");
run("Gamma...", "value=0.50");
close("\\Others")
run("Enhance Contrast", "saturated=0.35");
run("Apply LUT", "slice");
run("8-bit");
run("Duplicate...", " ");
run("Smooth", "slice");
run("Smooth", "slice");
run("Smooth", "slice");
run("Smooth", "slice");
setAutoThreshold("Intermodes dark");
run("Convert to Mask");
run("Analyze Particles...", "size=2-Infinity show=Outlines clear include summarize");
run("Images to Stack", "name=Stack title")
run("Next Slice [>]");
run("Delete Slice");
run("Z Project...", "projection=[Sum Slices]");
rename(t);
saveAs("Jpeg", "E:\\ResultImageQuant\\");
```

The performance of the code can be seen in Figure 5 by comparing the original image with the detected boundary.

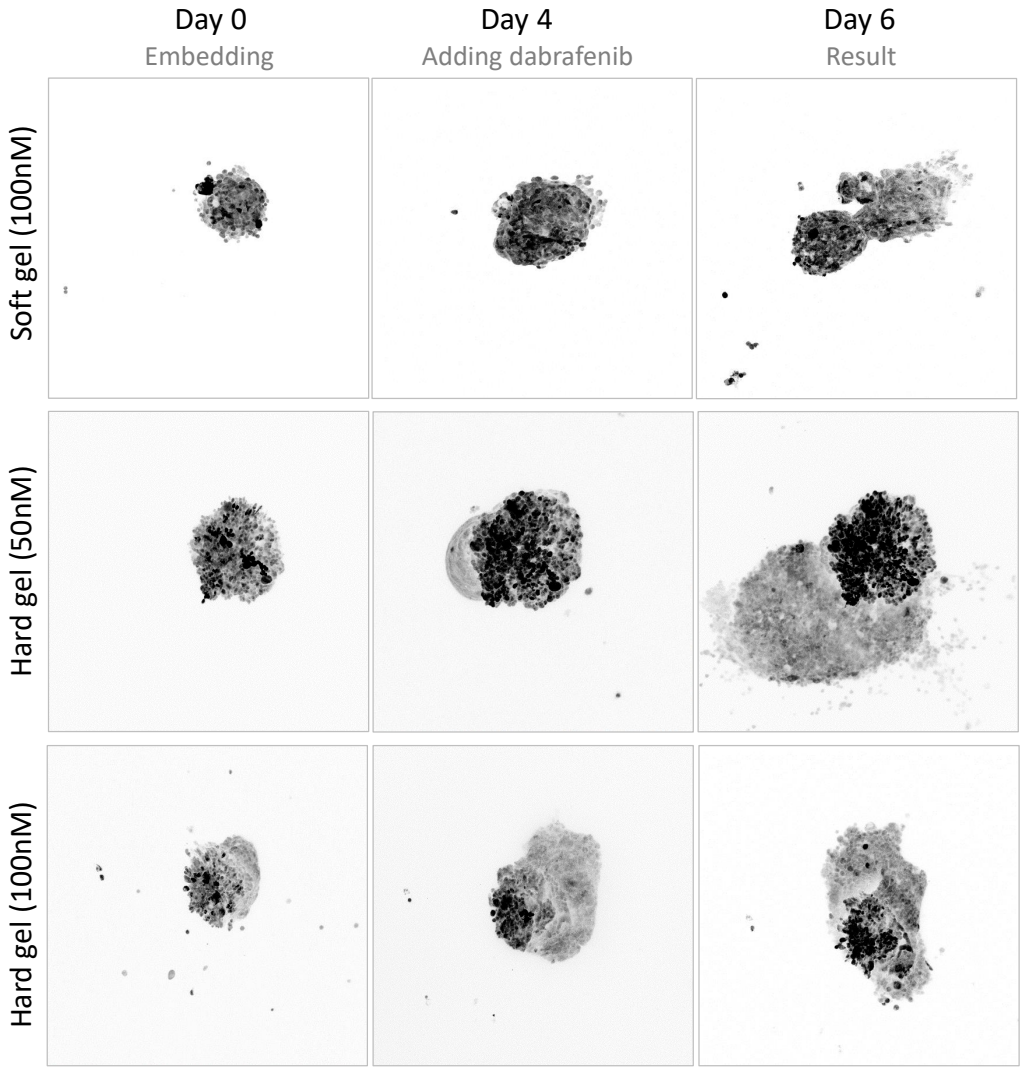

Figure 5: Three spheroids with unexpectedly high growth rate, despite or because of the high dabrafenib concentration. Spheroids were treated at day 4 and evaluated at day 6. The occasional outburst of growth above the related control values was observed for two samples exposed to high drug concentrations. The spheroid at the bottom was not striking in area growth but seemed to grow toward the background.

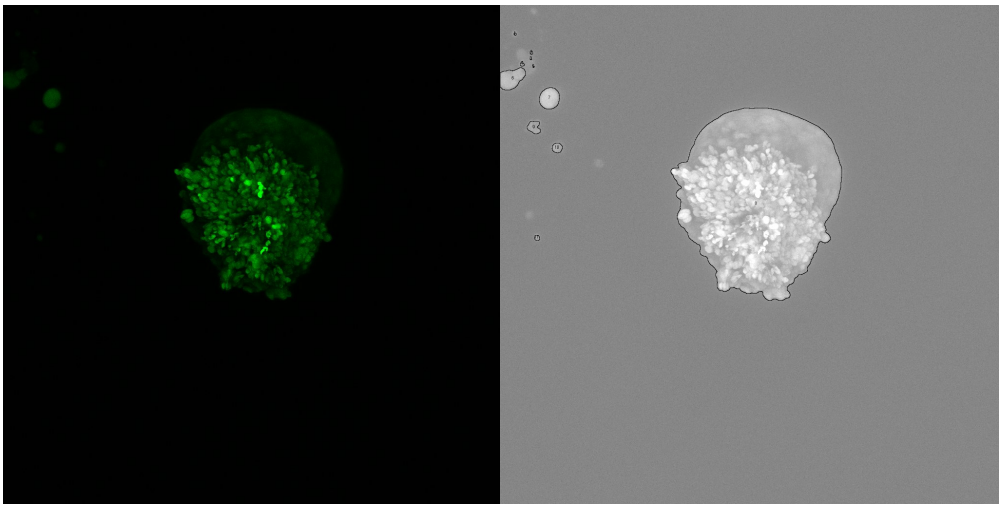

Figure 6: Image quantification returns from the original image (left) the control figure (right). The control figure contains the original image and the boundary of the image segmentation for a fast visual quality check.

References

1. Ouellet, D. *et al.* Population pharmacokinetics of dabrafenib, a BRAF inhibitor: effect of dose, time, covariates, and relationship with its metabolites. *The Journal of Clinical Pharmacology* **54,** 696–706 (2014).
2. Huynh, H. H. *et al.* Development and validation of a simultaneous quantification method of 14 tyrosine kinase inhibitors in human plasma using LC-MS/MS. *Therapeutic drug monitoring* **39,** 43–54 (2017).
3. Bershas, D. A. *et al.* Metabolism and disposition of oral dabrafenib in cancer patients: proposed participation of aryl nitrogen in carbon-carbon bond cleavage via decarboxylation following enzymatic oxidation. *Drug Metabolism and Disposition* **41,** 2215–2224 (2013).
4. Heel, R. *et al.* Ketoconazole: a review of its therapeutic efficacy in superficial and systemic fungal infections. *Drugs* **23,** 1–36 (1982).
5. Suttle, A. B. *et al.* Assessment of the drug interaction potential and single-and repeat-dose pharmacokinetics of the BRAF inhibitor dabrafenib. *The Journal of Clinical Pharmacology* **55,** 392–400 (2015).

Sensitivity analysis

Impact on dabrafenib PK profile

The following sensitivity plots were computed with the Supplementary Code 5 (Supplementary-Code-5.m). Not all parameter influence all time profiles with the consequence that some plots are flat and the heat-maps are empty. A parameter is considered valuable if it influences at least one of the tested profiles.

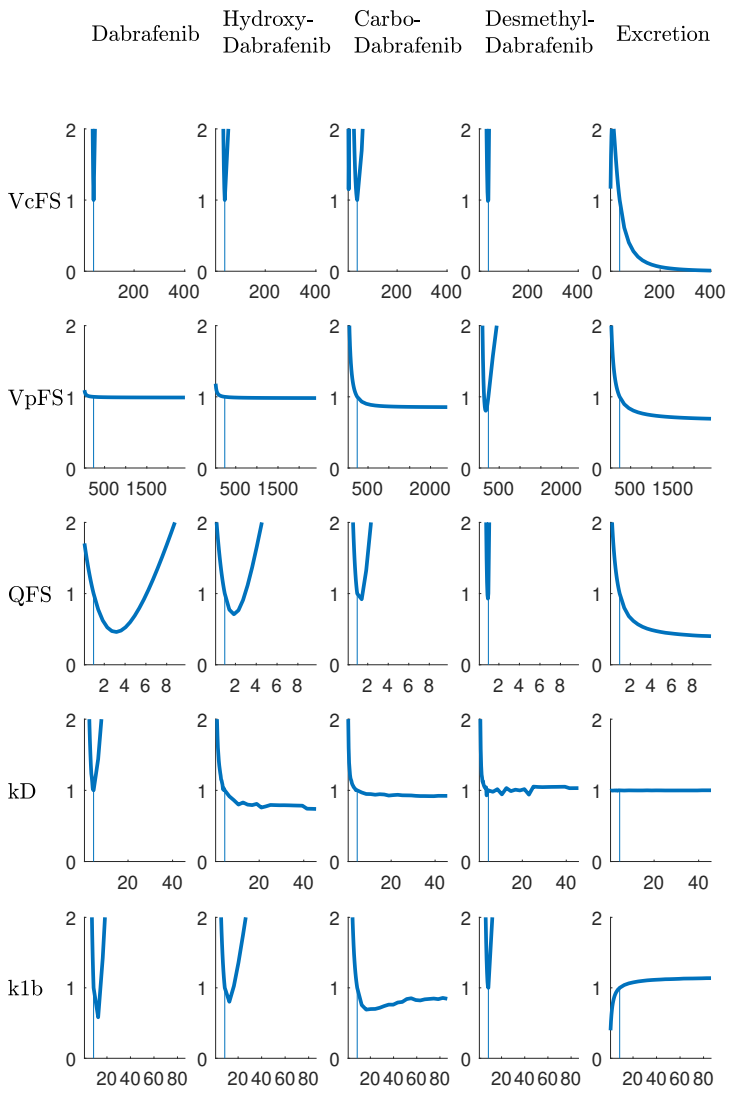

Figure 7: Sensitivity-analysis: relative change of fitting quality (RSS) if parameter value is changed.

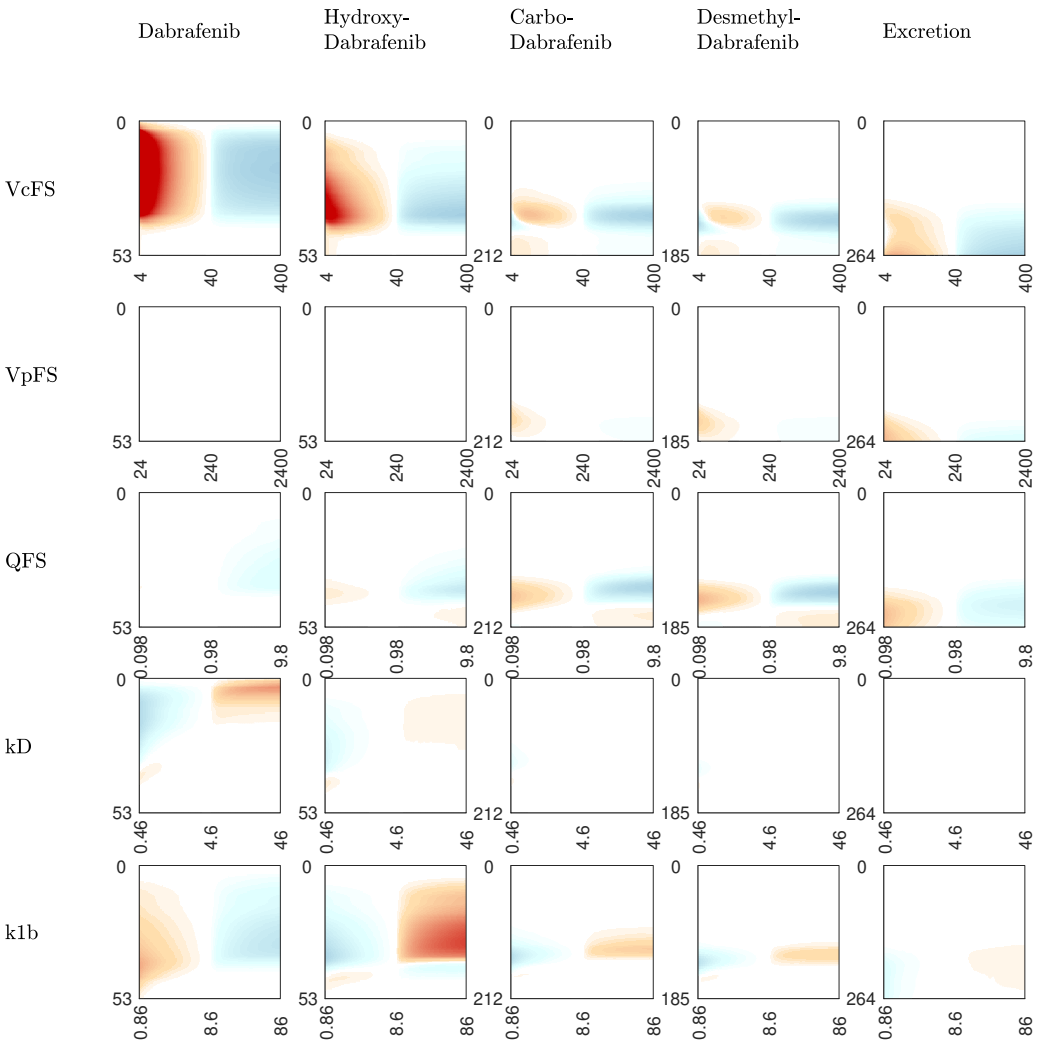

Figure 8: Sensitivity-analysis: time course change over different parameter values. Red areas indicate that these periods the time-course is above the original dynamic. Cyan areas indicate that the dynamic descend below the original dynamic.

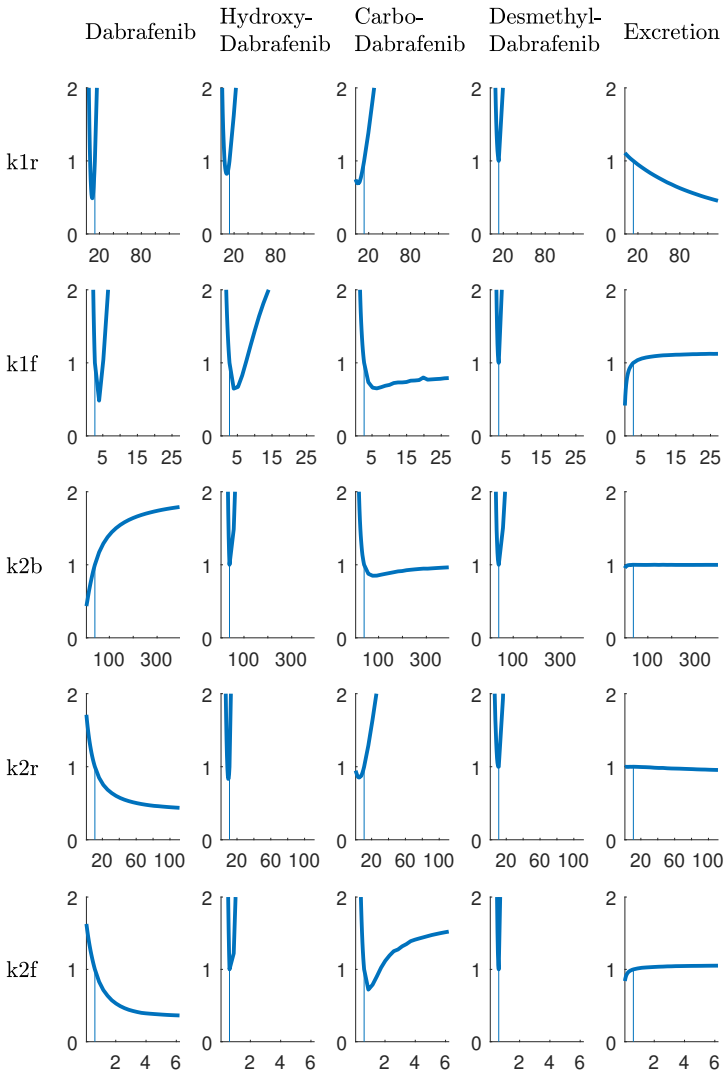

Figure 9: Sensitivity-analysis: relative change of fitting quality (RSS) if parameter value is changed.

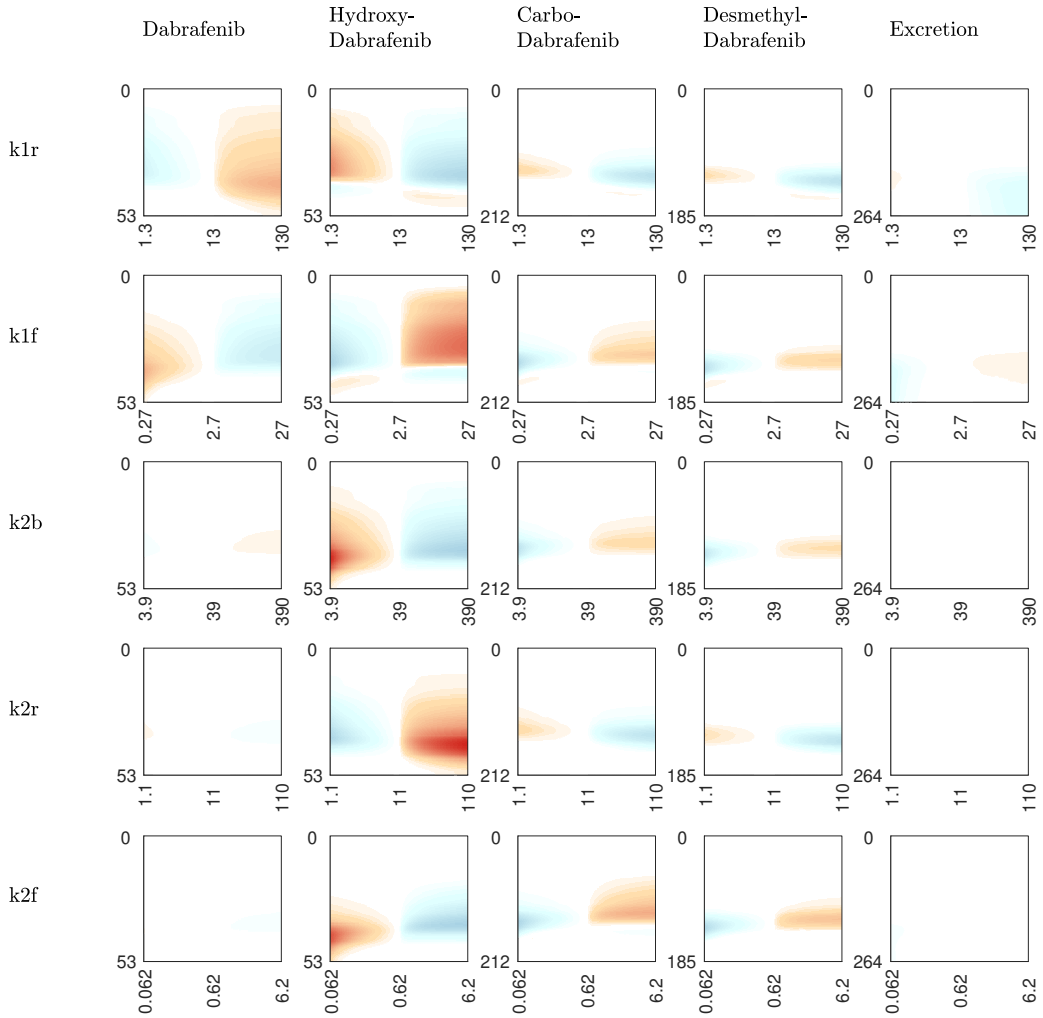

Figure 10: Sensitivity-analysis: time course change over different parameter values. Red areas indicate that these periods the time-course is above the original dynamic. Cyan areas indicate that the dynamic descend below the original dynamic.

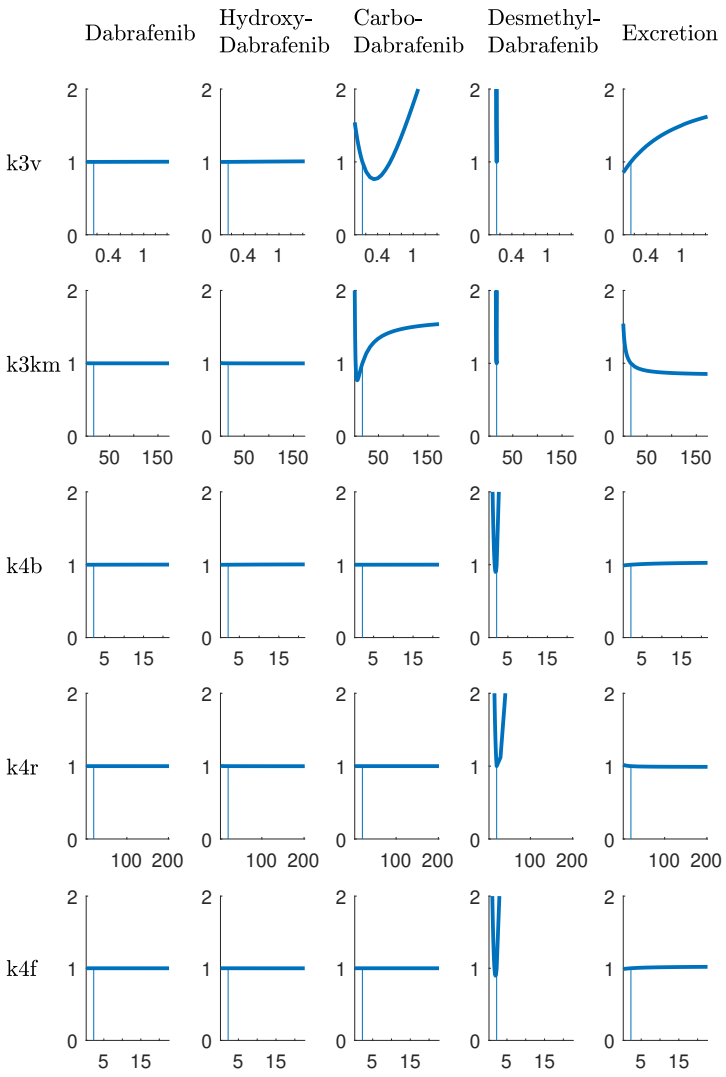

Figure 11: Sensitivity-analysis: relative change of fitting quality (RSS) if parameter value is changed.

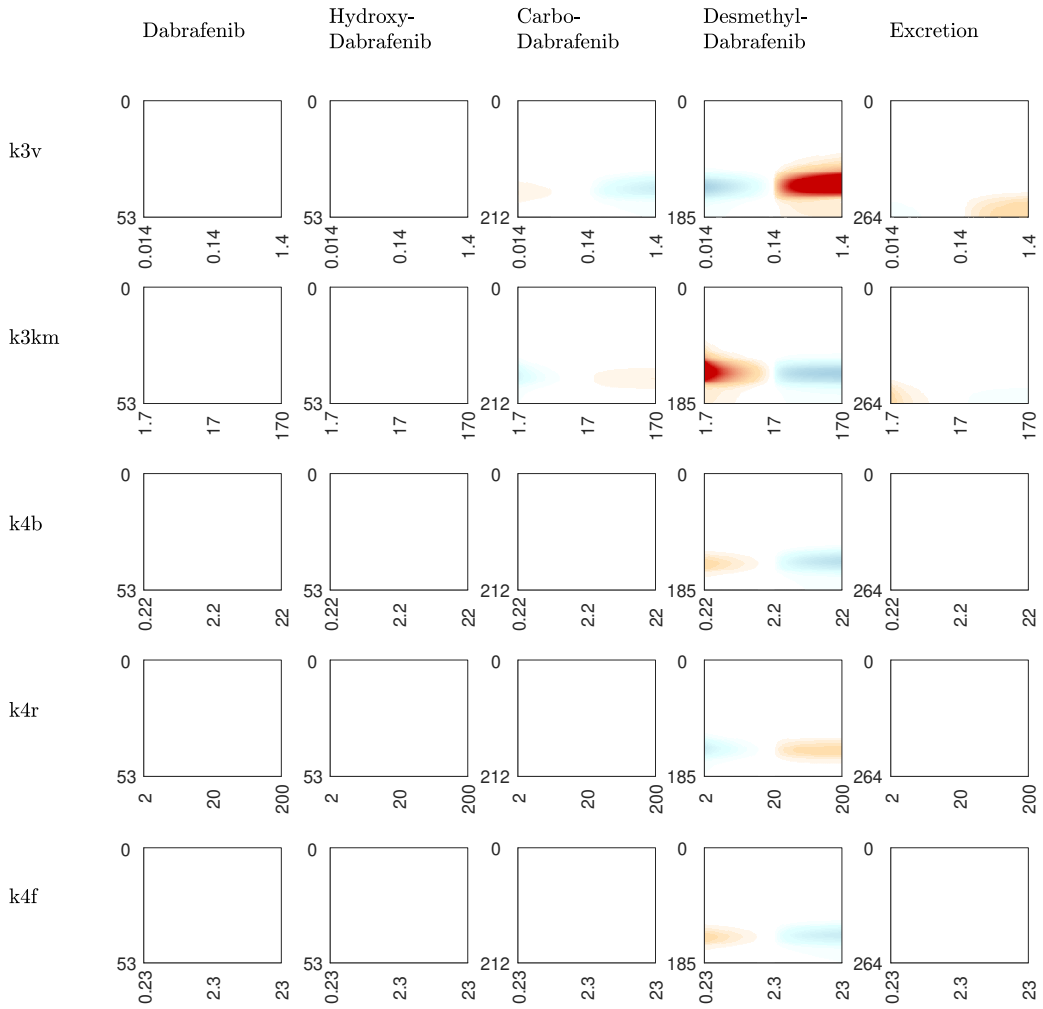

Figure 12: Sensitivity-analysis: time course change over different parameter values. Red areas indicate that these periods the time-course is above the original dynamic. Cyan areas indicate that the dynamic descend below the original dynamic.

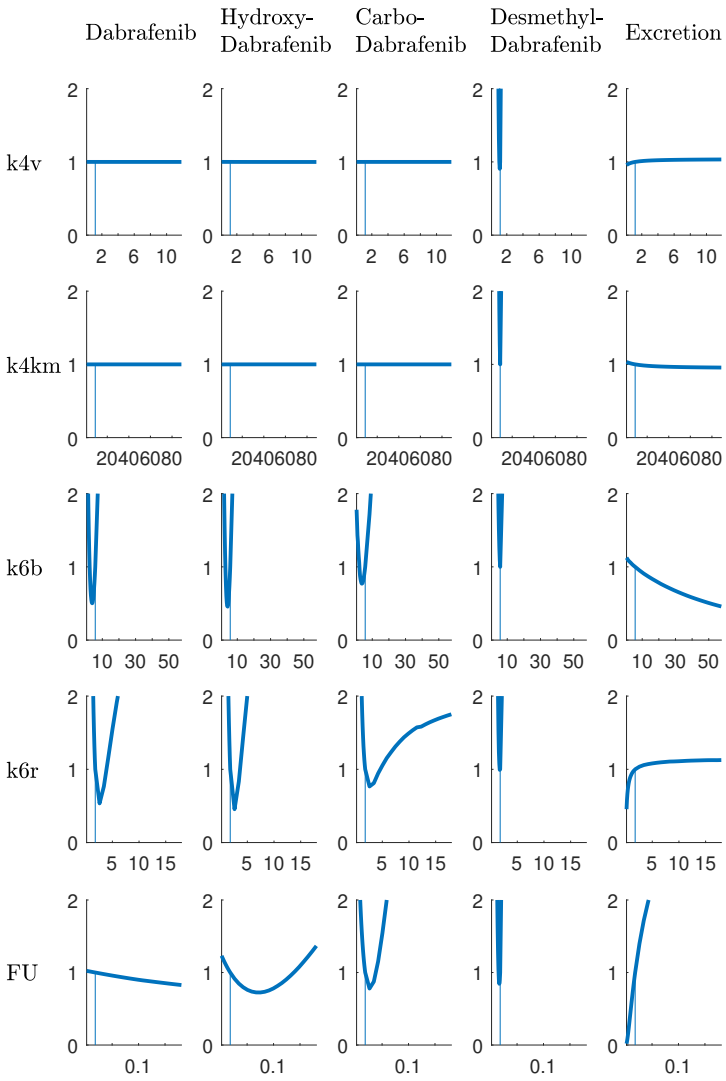

Figure 13: Sensitivity-analysis: relative change of fitting quality (RSS) if parameter value is changed.

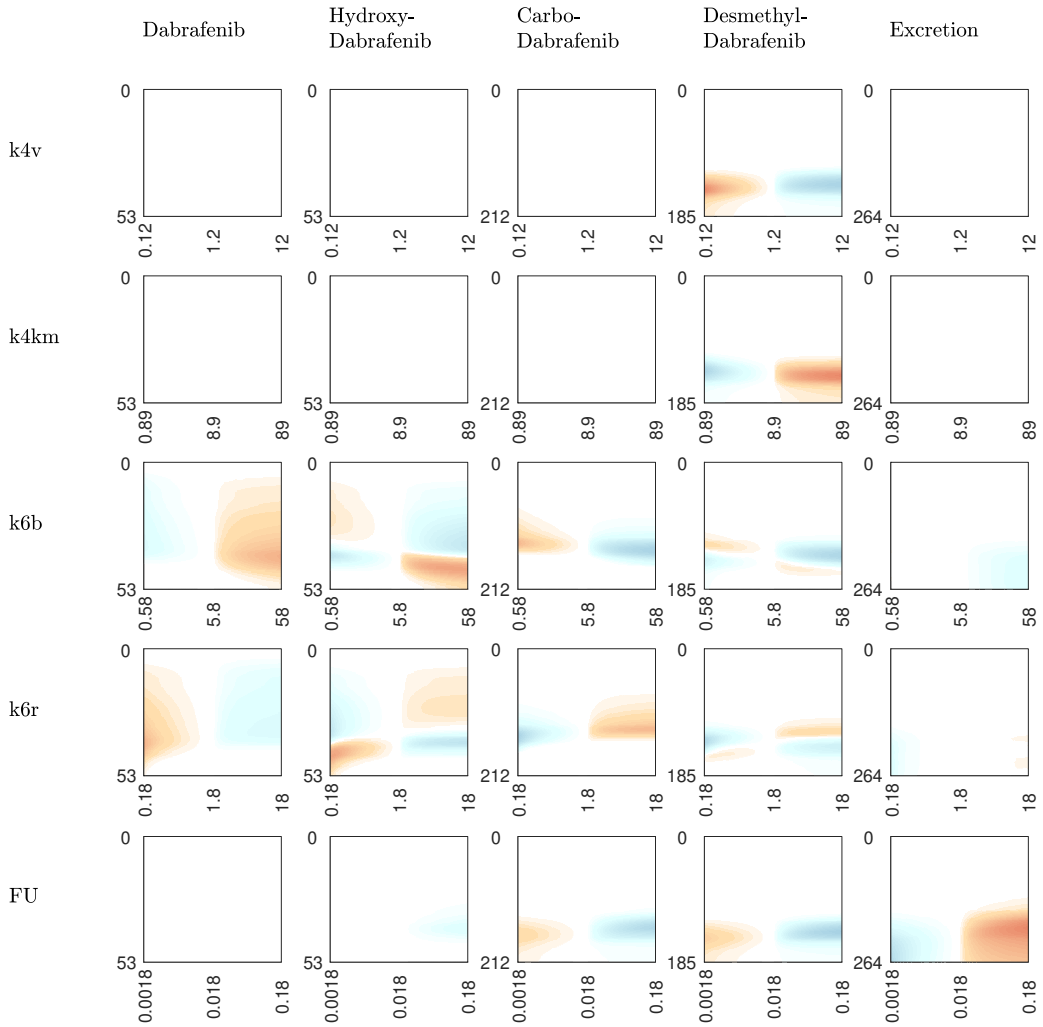

Figure 14: Sensitivity-analysis: time course change over different parameter values. Red areas indicate that these periods the time-course is above the original dynamic. Cyan areas indicate that the dynamic descend below the original dynamic.

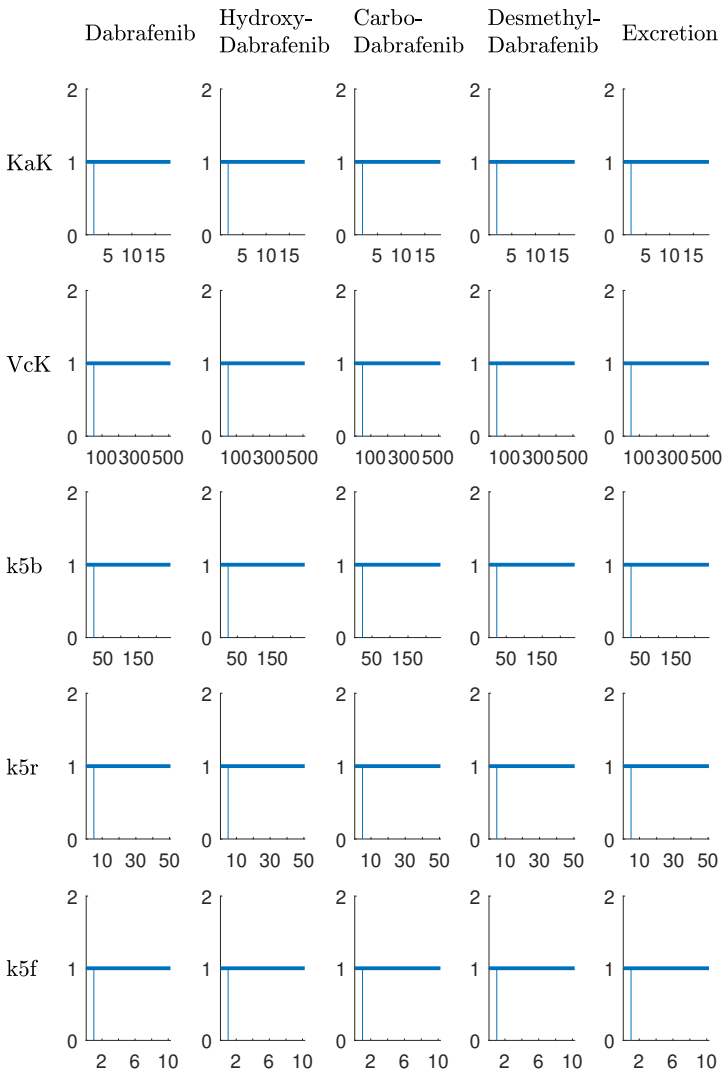

Figure 15: Sensitivity-analysis: relative change of fitting quality (RSS) if parameter value is changed.

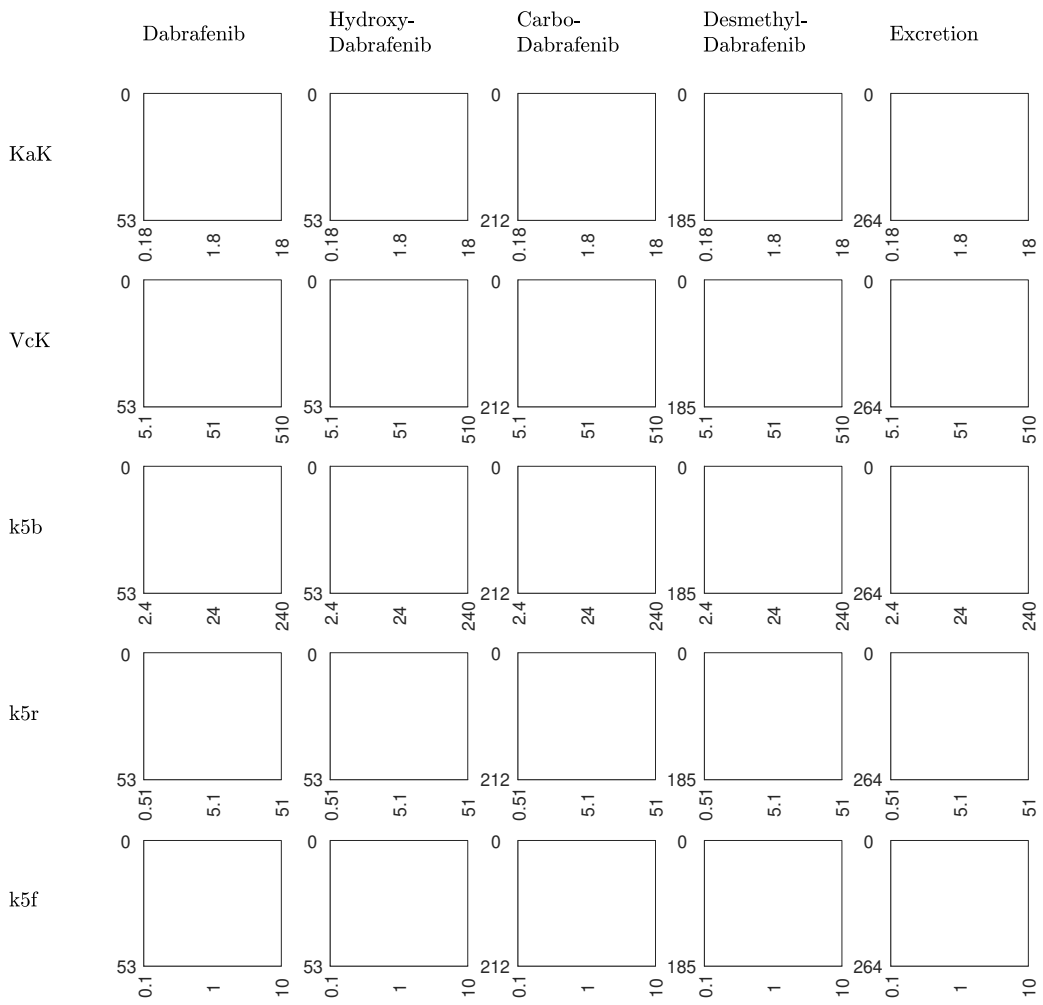

Figure 16: Sensitivity-analysis: time course change over different parameter values. Red areas indicate that these periods the time-course is above the original dynamic. Cyan areas indicate that the dynamic descend below the original dynamic.

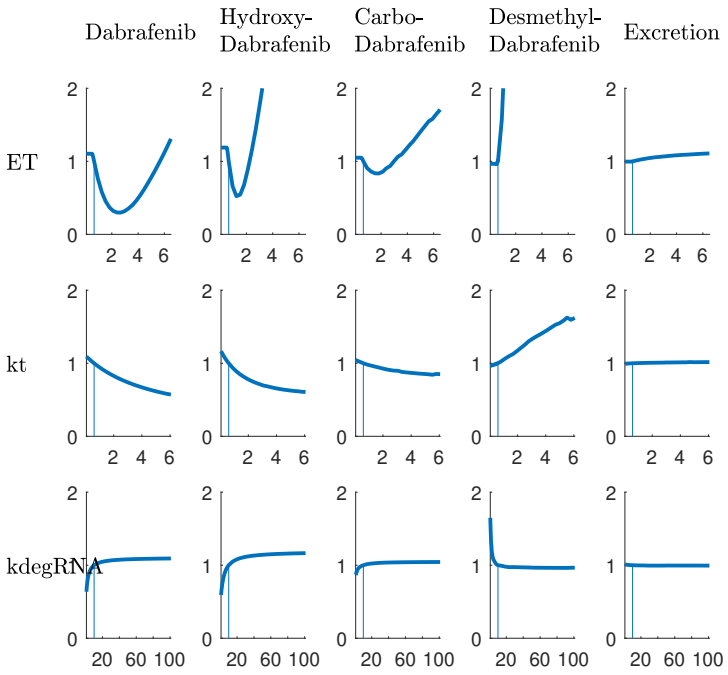

Figure 17: Sensitivity-analysis: relative change of fitting quality (RSS) if parameter value is changed.

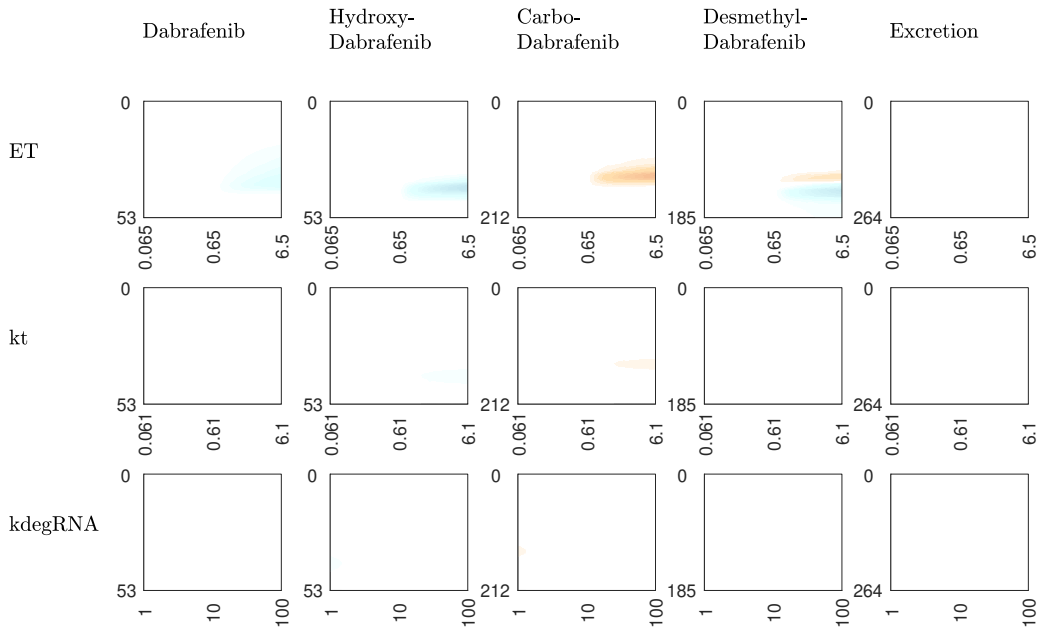

Figure 18: Sensitivity-analysis: time course change over different parameter values. Red areas indicate that these periods the time-course is above the original dynamic. Cyan areas indicate that the dynamic descend below the original dynamic.

Impact on ketoconazole PK profile

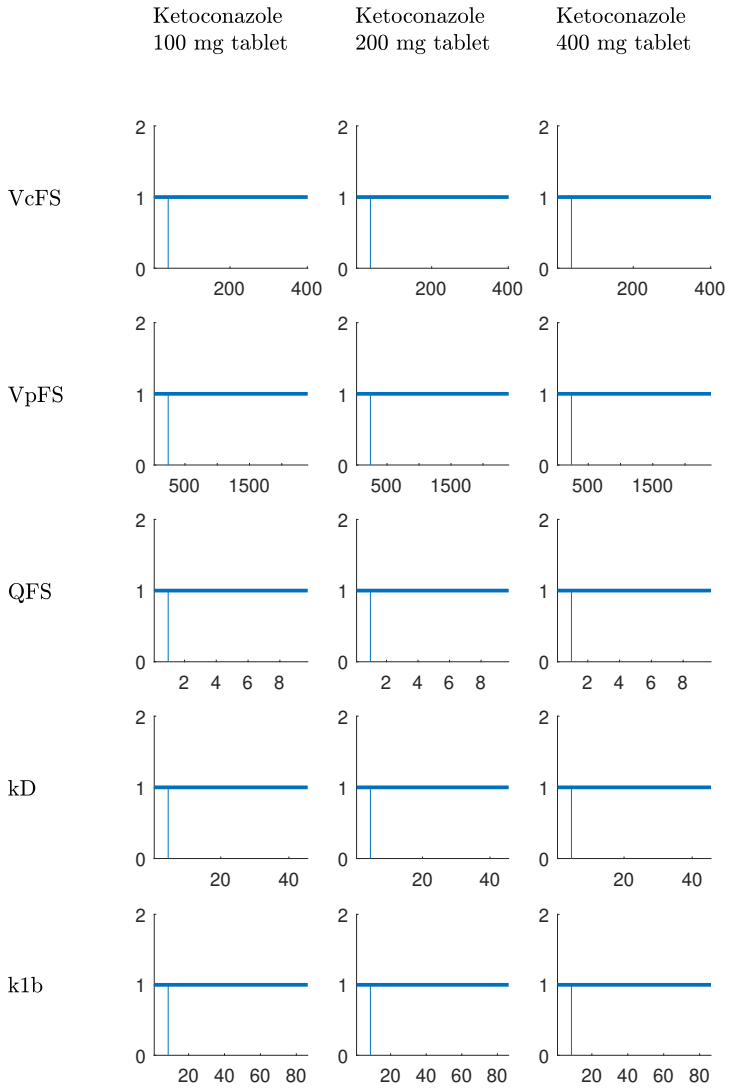

Figure 19: Sensitivity-analysis: relative change of fitting quality (RSS) if parameter value is changed.

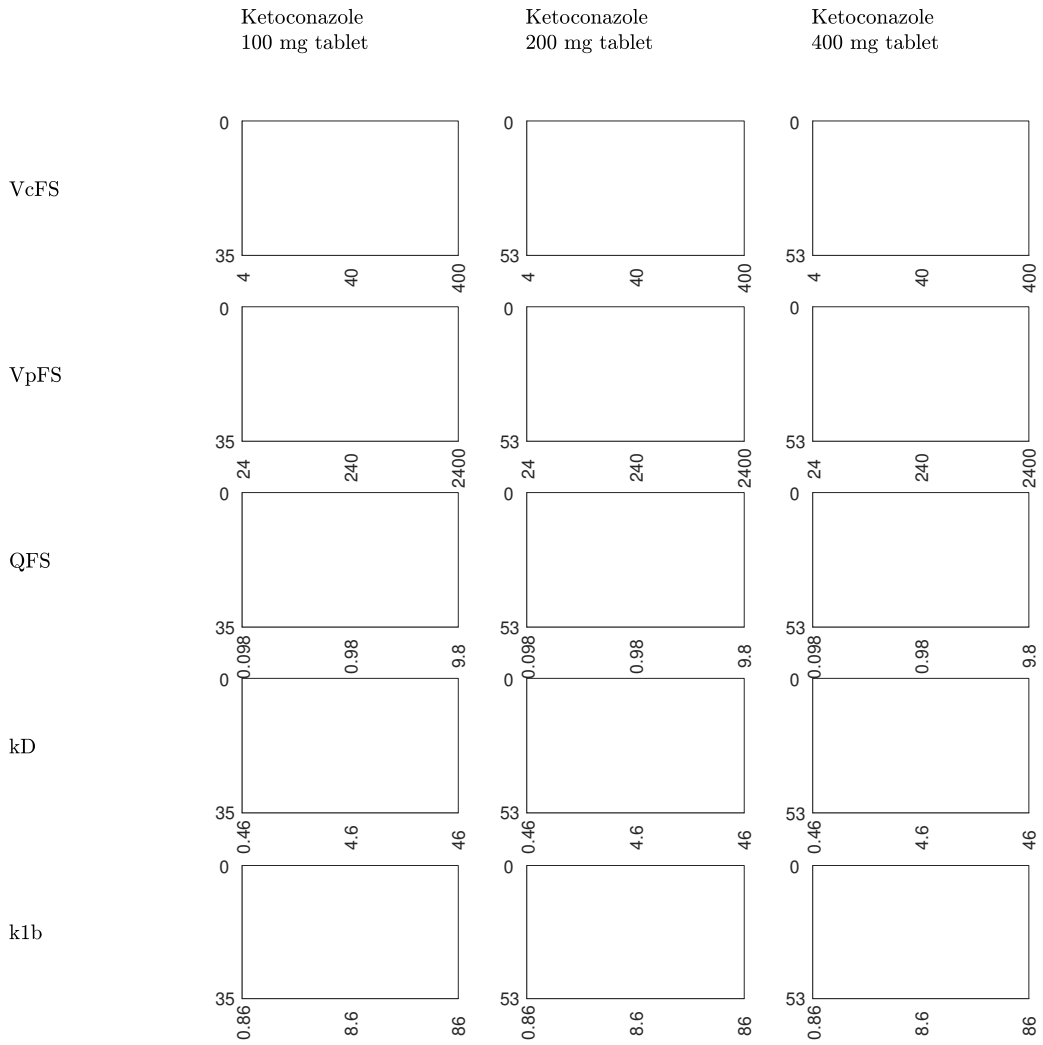

Figure 20: Sensitivity-analysis: time course change over different parameter values. Red areas indicate that these periods the time-course is above the original dynamic. Cyan areas indicate that the dynamic descend below the original dynamic.

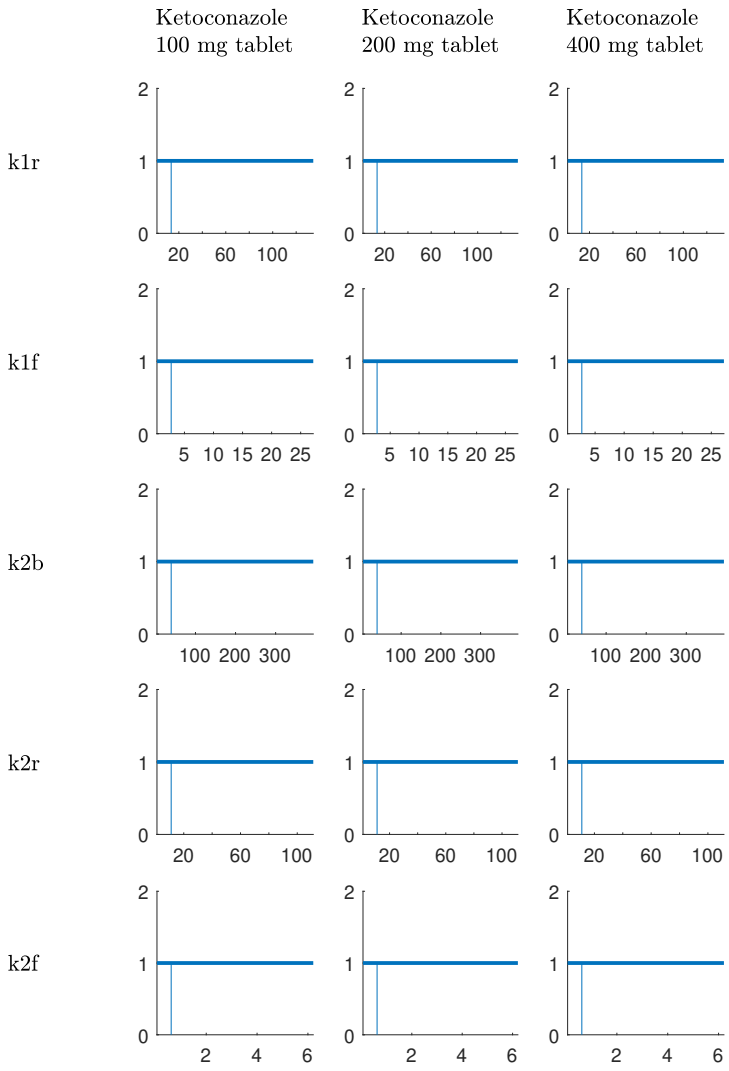

Figure 21: Sensitivity-analysis: relative change of fitting quality (RSS) if parameter value is changed.

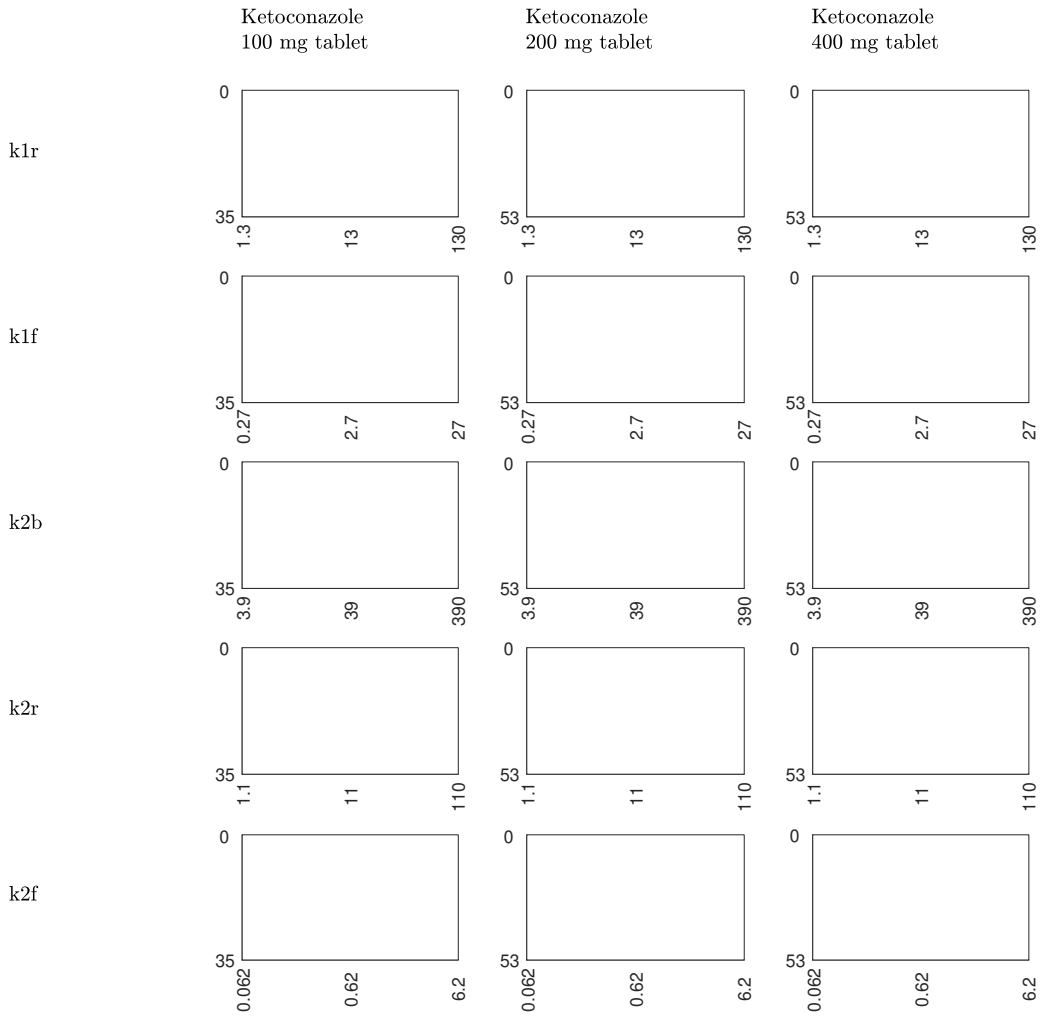

Figure 22: Sensitivity-analysis: time course change over different parameter values. Red areas indicate that these periods the time-course is above the original dynamic. Cyan areas indicate that the dynamic descend below the original dynamic.

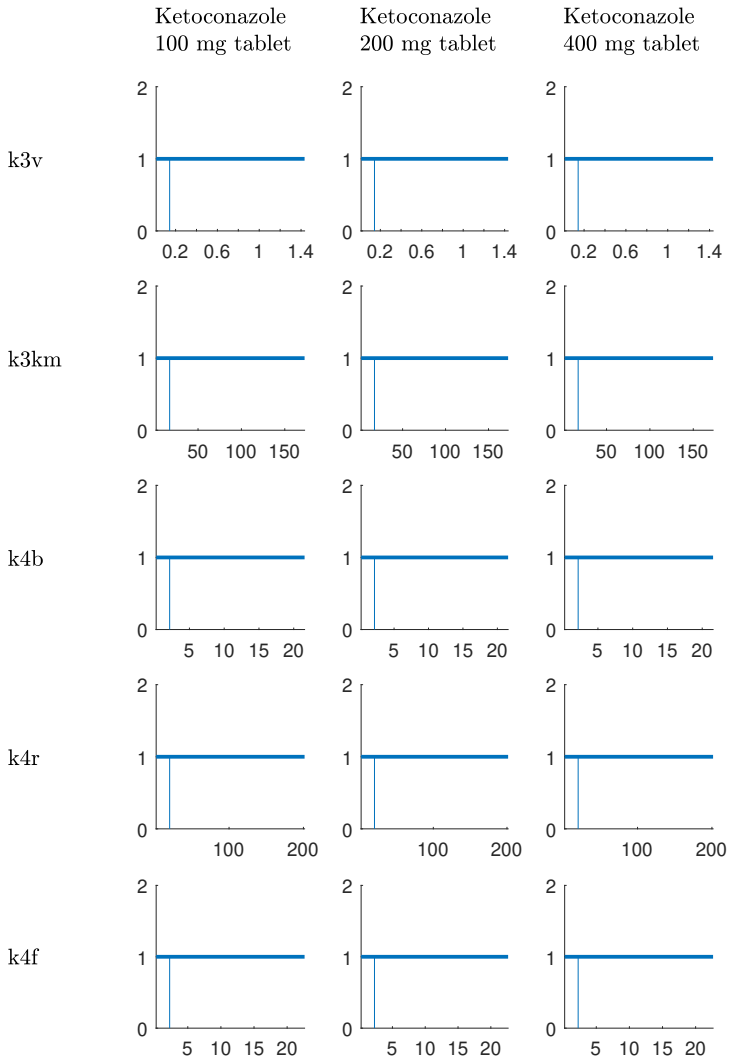

Figure 23: Sensitivity-analysis: relative change of fitting quality (RSS) if parameter value is changed.

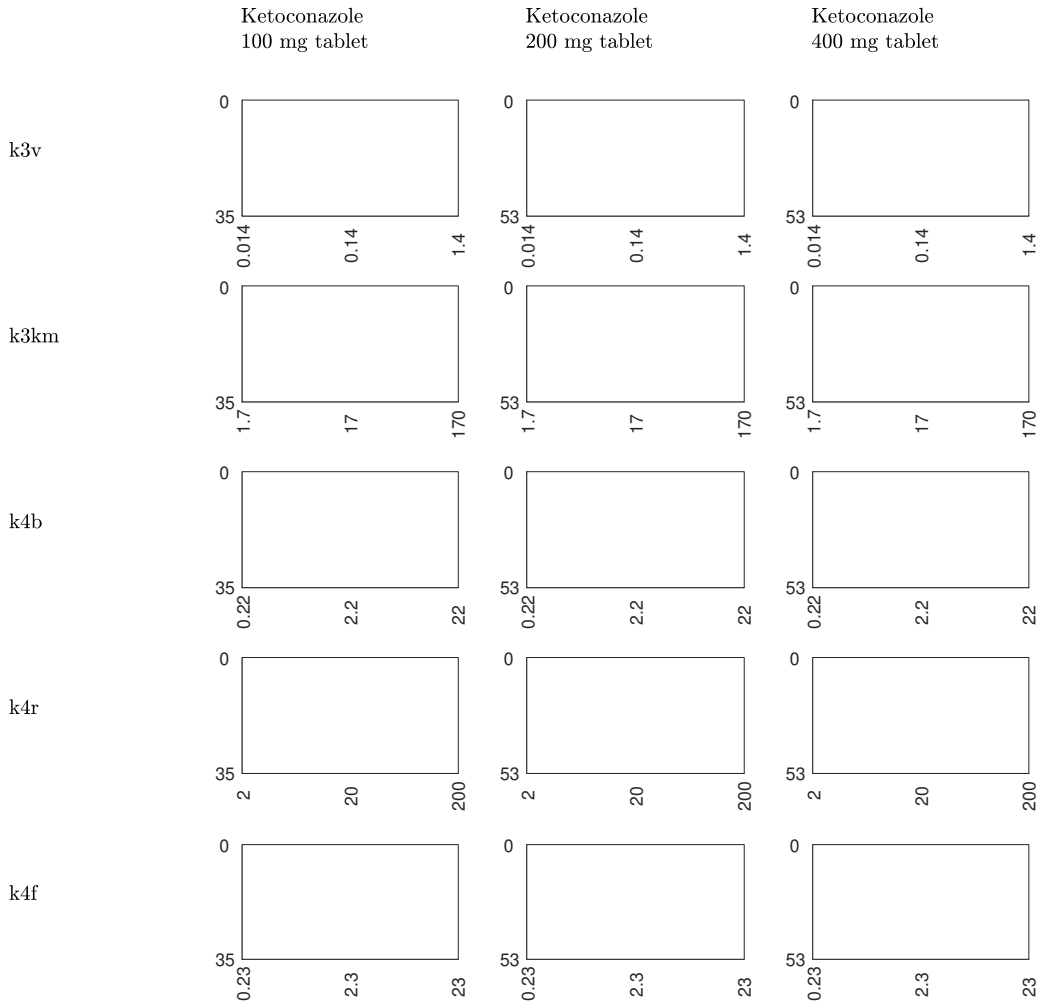

Figure 24: Sensitivity-analysis: time course change over different parameter values. Red areas indicate that these periods the time-course is above the original dynamic. Cyan areas indicate that the dynamic descend below the original dynamic.

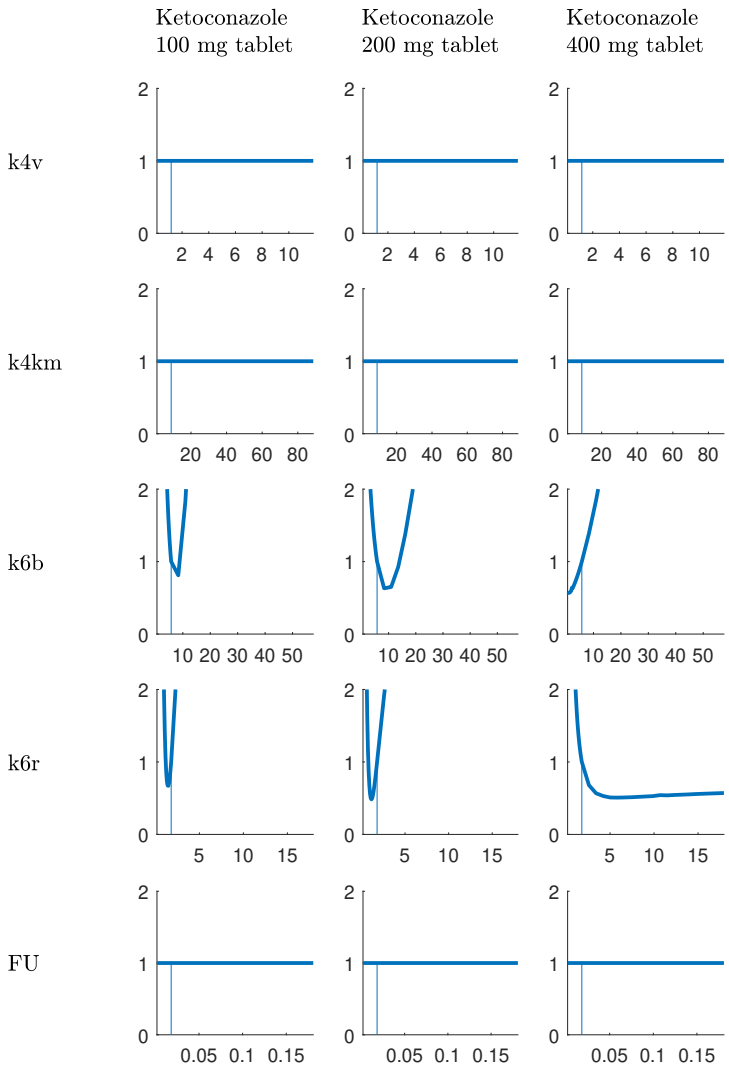

Figure 25: Sensitivity-analysis: relative change of fitting quality (RSS) if parameter value is changed.

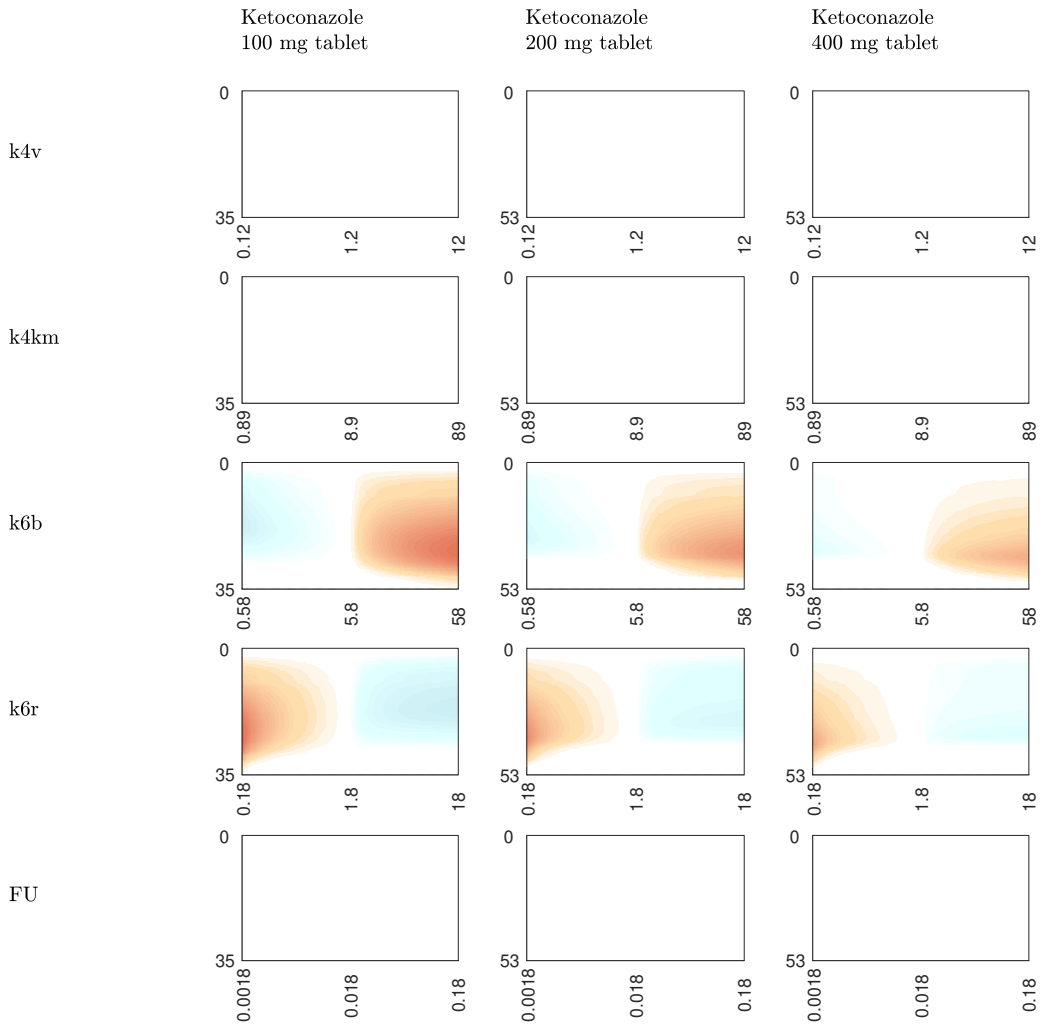

Figure 26: Sensitivity-analysis: time course change over different parameter values. Red areas indicate that these periods the time-course is above the original dynamic. Cyan areas indicate that the dynamic descend below the original dynamic.

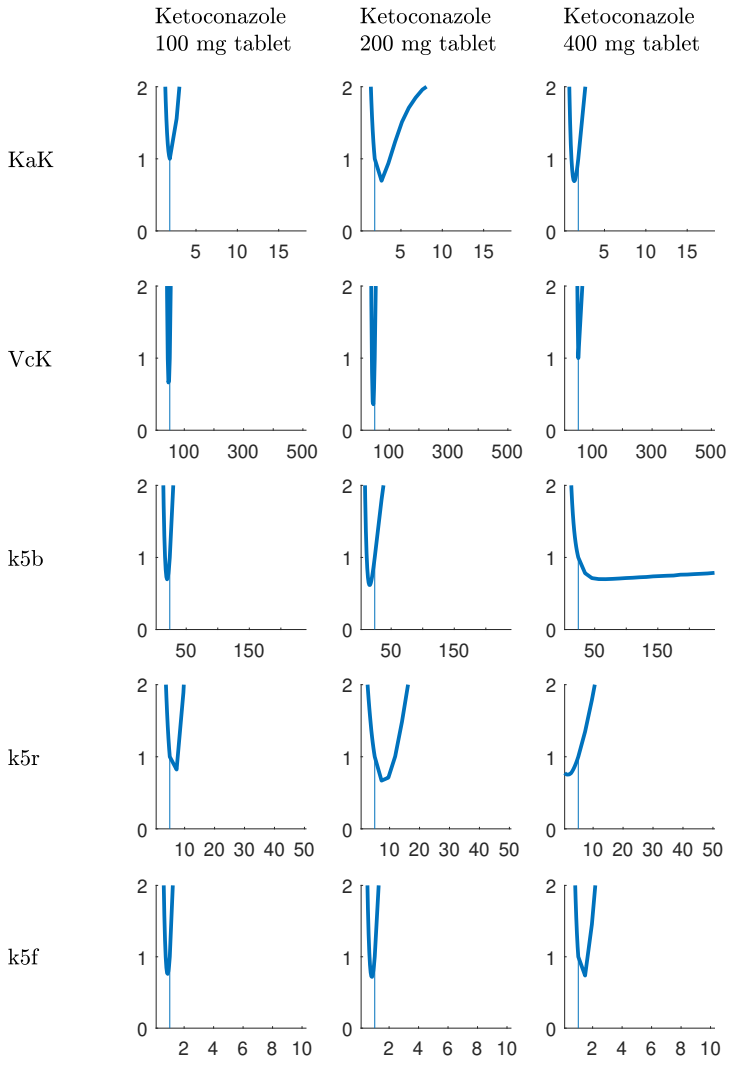

Figure 27: Sensitivity-analysis: relative change of fitting quality (RSS) if parameter value is changed.

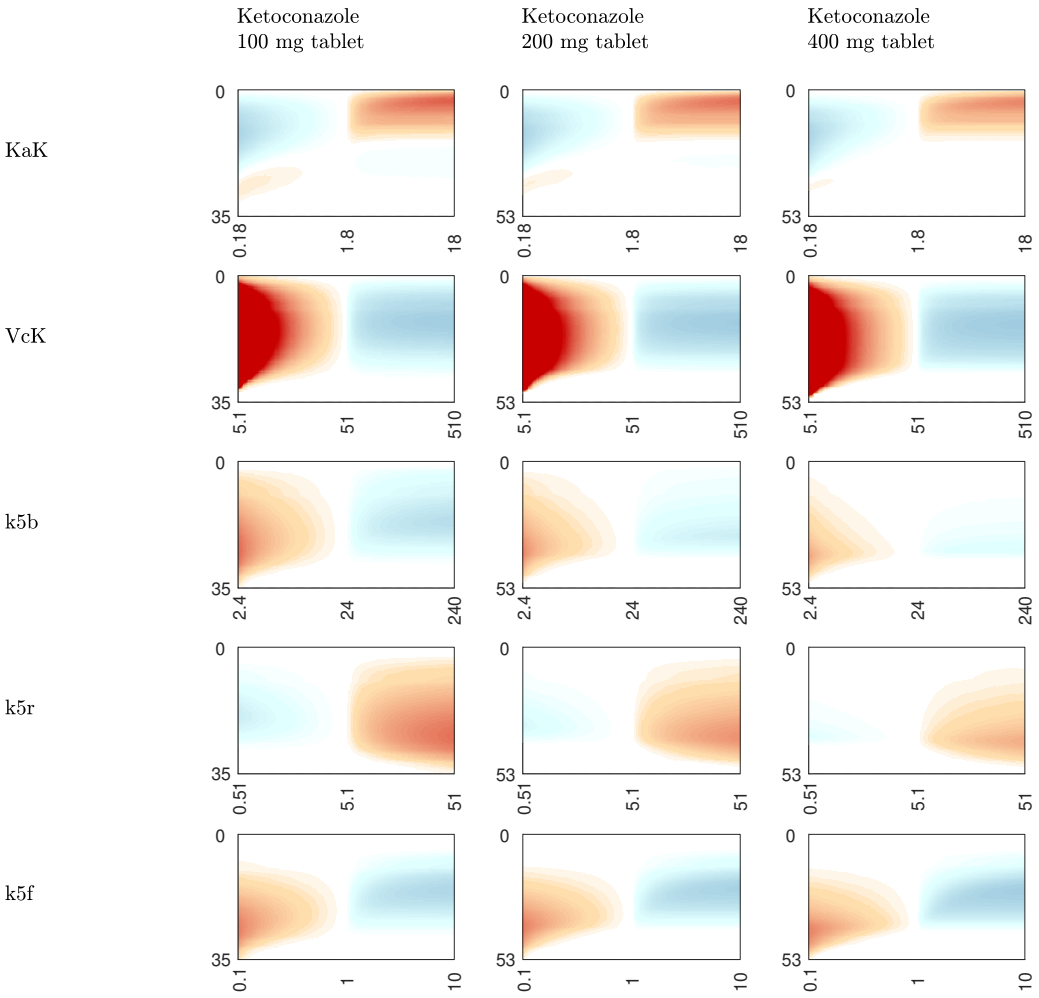

Figure 28: Sensitivity-analysis: time course change over different parameter values. Red areas indicate that these periods the time-course is above the original dynamic. Cyan areas indicate that the dynamic descend below the original dynamic.

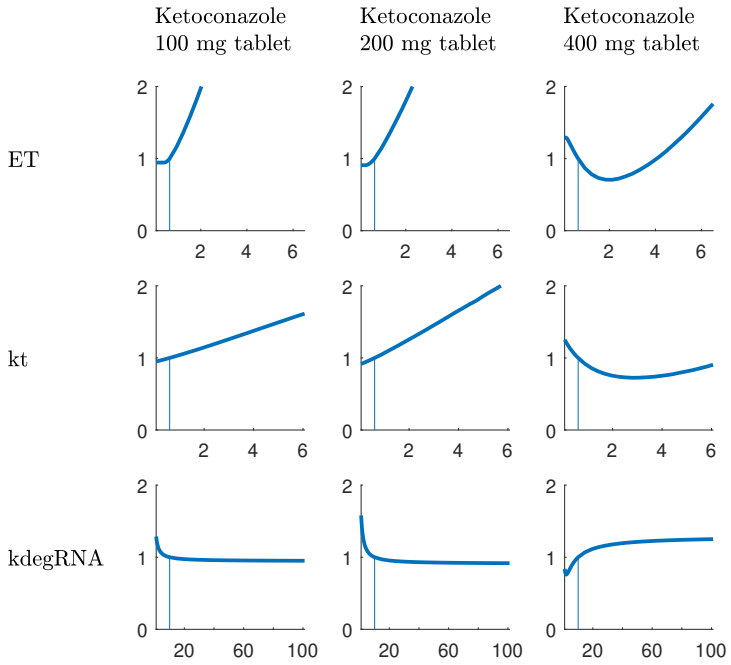

Figure 29: Sensitivity-analysis: relative change of fitting quality (RSS) if parameter value is changed.

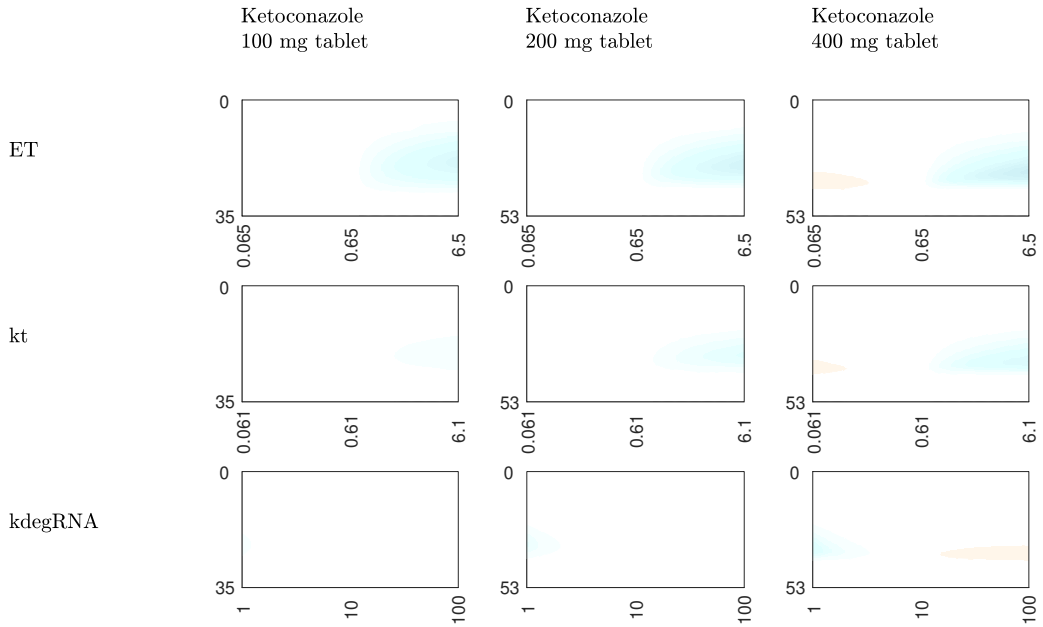

Figure 30: Sensitivity-analysis: time course change over different parameter values. Red areas indicate that these periods the time-course is above the original dynamic. Cyan areas indicate that the dynamic descend below the original dynamic.

Impact on ketoconazole dabrafenib interaction

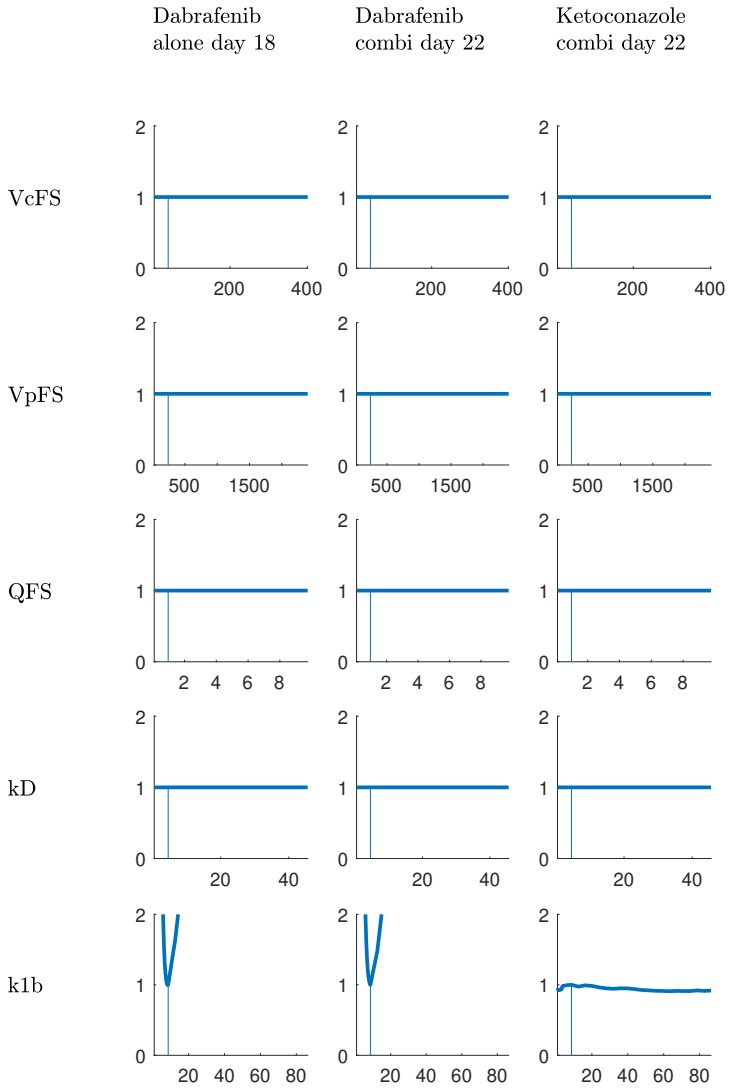

Figure 31: Sensitivity-analysis: relative change of fitting quality (RSS) if parameter value is changed.

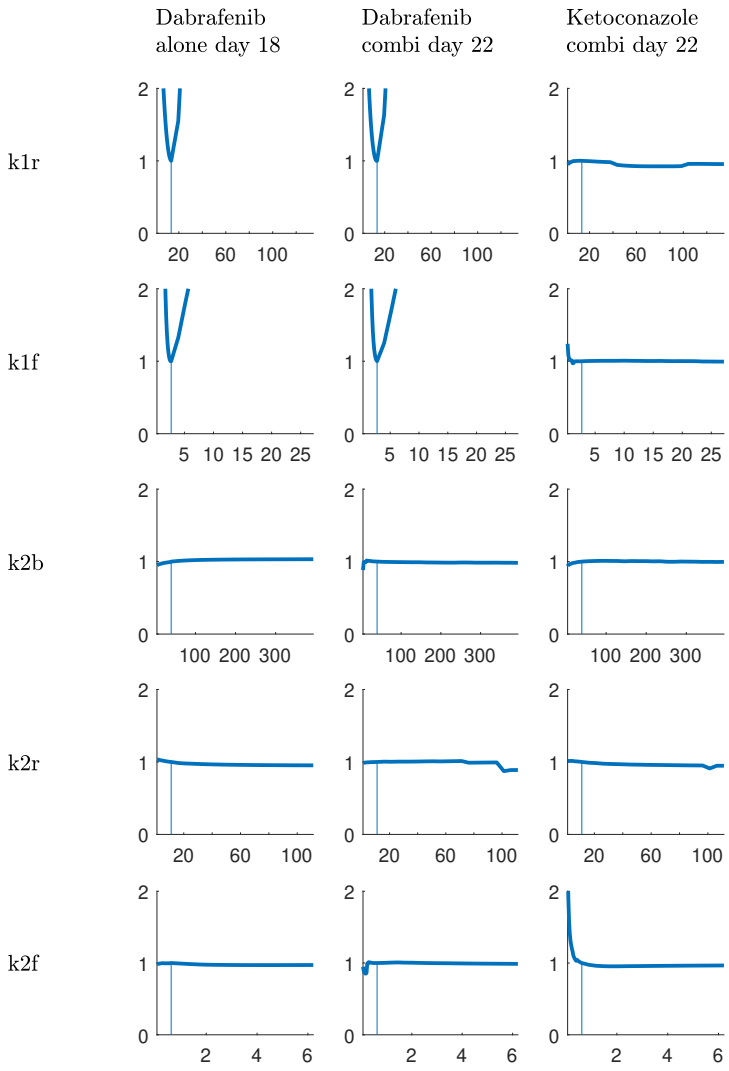

Figure 32: Sensitivity-analysis: relative change of fitting quality (RSS) if parameter value is changed.

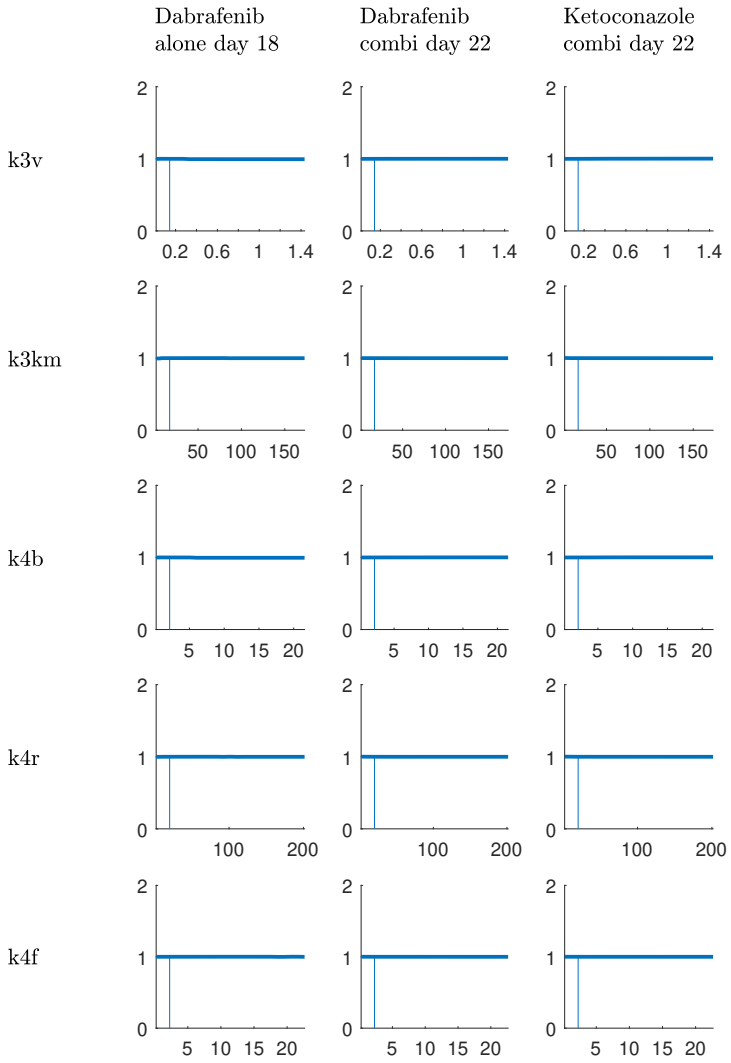

Figure 33: Sensitivity-analysis: relative change of fitting quality (RSS) if parameter value is changed.

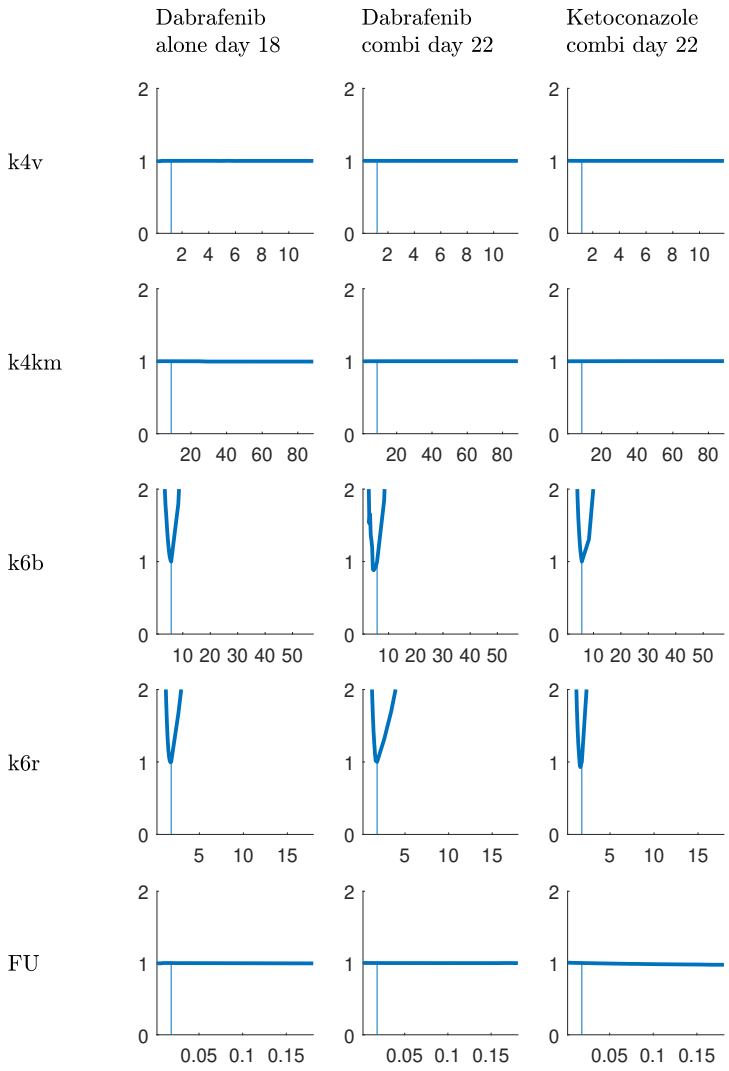

Figure 34: Sensitivity-analysis: relative change of fitting quality (RSS) if parameter value is changed.

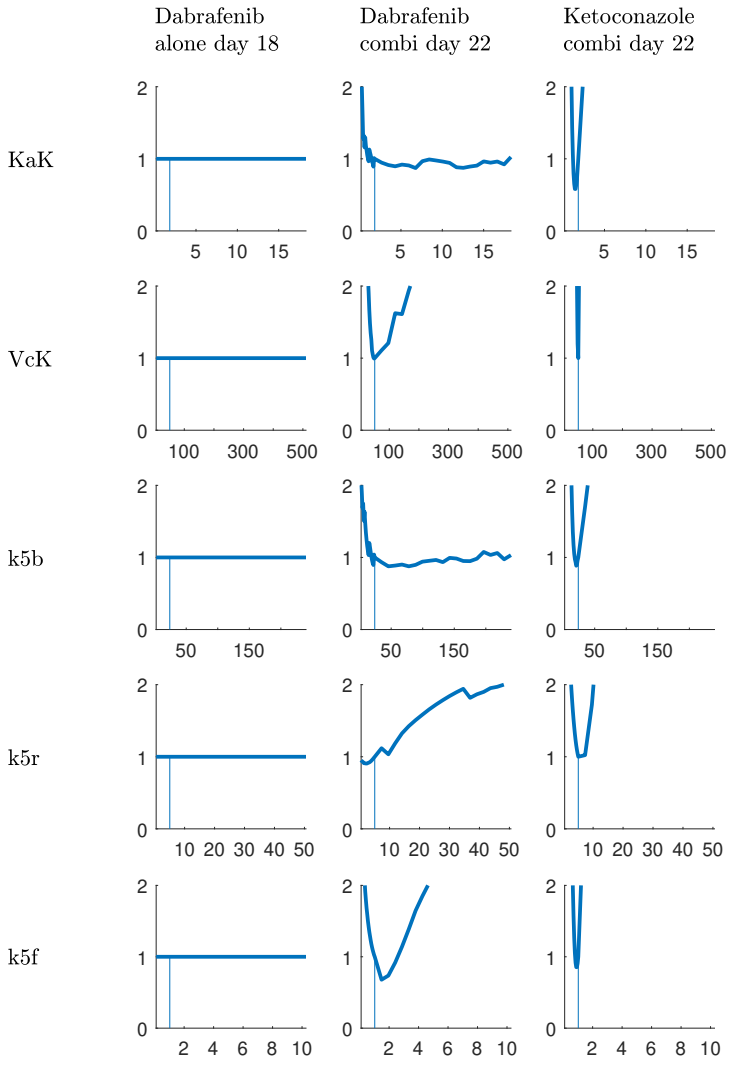

Figure 35: Sensitivity-analysis: relative change of fitting quality (RSS) if parameter value is changed.

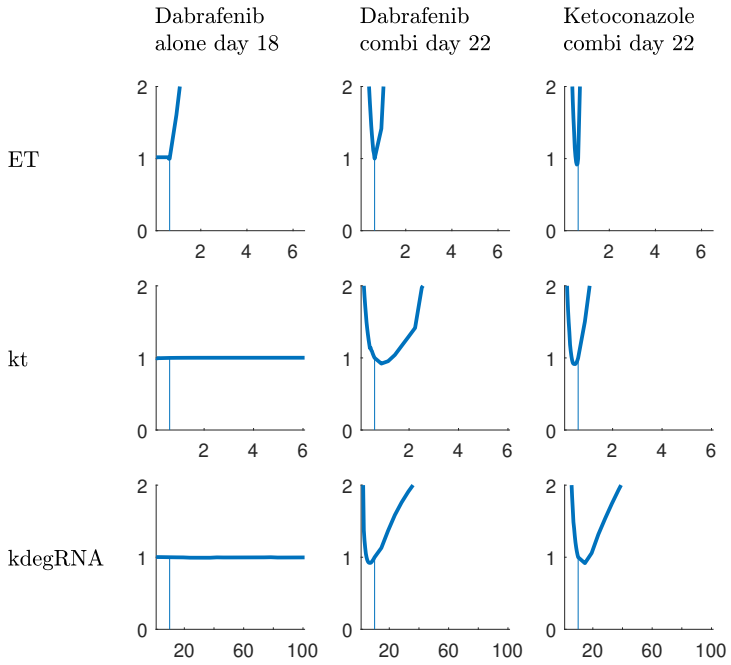

Figure 36: Sensitivity-analysis: relative change of fitting quality (RSS) if parameter value is changed.